

**MICROBIAL MEDIATED SYNTHESIS OF  
VISIBLE LIGHT ACTIVE SILVER BASED  
TITANIA NANOCOMPOSITES AND THEIR  
PHOTOCATALYTIC APPLICATIONS IN  
DEGRADATION OF AZO DYES**

Thesis

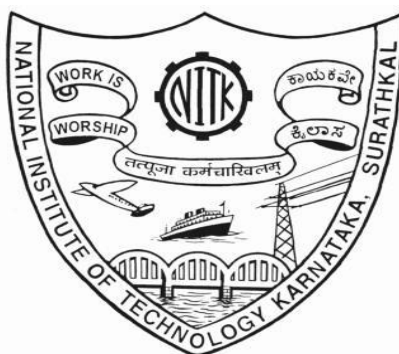
Submitted in partial fulfillment of the requirements for the  
degree of

**DOCTOR OF PHILOSOPHY**

by

**DEEKSHITHA**

Registration No. 155137CH15F02



DEPARTMENT OF CHEMICAL ENGINEERING  
NATIONAL INSTITUTE OF TECHNOLOGY KARNATAKA  
SURATHKAL, MANGALORE  
NOVEMBER, 2023

## DECLARATION

I hereby *declare* that the Research Thesis entitled “**Microbial mediated synthesis of visible light active silver based titania nanocomposites and their photocatalytic applications in degradation of azo dyes**” which is being submitted to the **National Institute of Technology Karnataka, Surathkal** in partial fulfillment of the requirements for the award of the Degree of **Doctor of Philosophy** in the Department of Chemical Engineering, *is a bonafide report of the research work carried out by me*. The material contained in this Research Thesis has not been submitted to any University or Institution for the award of any degree.

*Deekshitha*

DEEKSHITHA

Register No. 155137CH15F02

Department of Chemical Engineering

Place: NITK, Surathkal

Date: 1/12/2023

## CERTIFICATE

This is to *certify* that the Research Thesis entitled “**Microbial mediated synthesis of visible light active silver based titania nanocomposites and their photocatalytic applications in degradation of azo dyes**” submitted by **DEEKSHITHA (Register Number: 155137CH15F02)** as the record of the research work carried out by her, *is accepted as the Research Thesis submission* in partial fulfillment of the requirements for the award of degree of **Doctor of Philosophy**.


  
**Research Guide**

Prof. Vidya Shetty K

Professor,

Department of Chemical Engineering

NITK, Surathkal



**Chairman-DRPC**

Department of Chemical Engineering

NITK, Surathkal



## ACKNOWLEDGEMENT

The route I took to complete this doctoral research has been a highly illuminating stage in my life's journey. I will always be grateful to many people who helped me to complete this and left behind the beautiful experience.

First and foremost, with great respect and love I wish to thank my guide, my Guru **Prof. Vidya Shetty K.**, for her motivational supervision, enthusiasm, boosting and in-depth conversation in assisting to stay motivated and constant support at every step throughout the years of my PhD research pursuit, as well as her significant contributions in shaping of the thesis. She has been and always will be a role model for me in NITK and my Life. I thank her from my bottom of heart for giving me the courage and the knowledge I needed to alter both my career and personal lives.

I am very much thankful to my RPAC members **Dr. Uday Kumar Dalimba**, Associate Professor, Department of Chemistry and **Dr. Jagannathan T. K.** Assistant Professor, Department of Chemical Engineering, NITK, Surathkal for their valuable advice and suggestions that enabled me to improve my research work based on their insights and comments.

I humbly express my sincere gratitude to The Director, NITK Surathkal, and the former and present Academic Dean. I wish to thank our former H.O.D.s Dr. Vidya Shetty K, Dr. Rajmohan B, Dr. Hari Mahalingam, Dr. Prasanna B. D and present H.O.D Dr. Jagdeeshbabu, Department of Chemical Engineering, NITK Surathkal for providing me necessary facilities, funding, and support during the phase of this research work. I would also like to thank all the faculty members of the Department of Chemical Engineering, NITK Surathkal for their valuable support and encouragement. I would like to thank MoE, GOI for providing stipend throughout my research work.

I would as well like to express my sincere thanks to Mrs. Bhavyashree Suvarna, Mrs. Thrithila Shetty, Mrs. Vijetha, Mr. Sadashiva, Mrs. Shashikala S, Mrs. Shashikala Mohan, Mrs. Sandhya, Mr. Jnaneshwar, Mr. Suresh, Mr. Mahadev, Mr. Harish, Mr. Ramesh, Mr. Sukesh, and all other non-teaching staffs for their helpful suggestions and timely maintenance of the laboratory equipment and all the official documentation required.

I gratefully acknowledge my friends Dr. Manjula P, Dr. Shankaramma S. Dr. Aishwarya D, Ms. Deeksha Mathew, Dr Smitha, Mrs. Revathy, Mrs. Preethi Shetty, Mrs. Minimol, Ms. Sedevino Sophia, Dr. Smruthi, Dr. Archana and **Mrs. Shravya P** for their love, care, support, and continuous encouragement.

Words fall short to express my gratitude to my strength, my Family who has encouraged me to start this journey and to reach the goal. My heartfelt gratitude to my Father **Mr. Ganesh Ram B**, who have always encouraged me through this difficult times and my Mother **Mrs. Malathi B** without whose love and care throughout my research work, this journey wouldn't be possible. My special and heartfelt thanks to my sister **Mrs. Shanthala Rohith** for her immense support and my brothers **Mr. Yathish B** and **Mr. Mahesh B** for their constant love, care and encouragement throughout this difficult time of my journey. I would also like to thank my brother in-law Mr. Rohith J, sister-in-law Mrs. Chethana M and my nieces Maanvi, Dhrithi and Gahana for their love and care in my Ph.D journey.

Above all, I am indebted to Almighty God for bestowing upon me the intelligence, health, and courage necessary to complete this research work.

**DEEKSHITHA**

## ABSTRACT

A large quantity of dyes released with textile industry effluents has raised a lot of concern due to their harmful and toxic effects on the ecosystem. Heterogeneous photocatalysis with TiO<sub>2</sub> has been reported to decontaminate these effluents by mineralization of these dyes. However, owing to its limitations such as the wide band gap and high charge recombination rate, TiO<sub>2</sub> is less effective and solar light cannot be utilized as the irradiation source. The modification of TiO<sub>2</sub> with oxides of silver and copper can overcome these limitations. Microbial synthesis of nanoparticles is a greener approach. The present study reports a new method for the synthesis of silver-based TiO<sub>2</sub> and silver-based TiO<sub>2</sub> modified with Cu nanocomposites extracellularly using cell free culture supernatant (CFS) of *Alcaligenes aquatilis* under ambient conditions and their application in the degradation of Reactive Blue 220 (RB 220) and Acid Yellow 17 (AY 17) dyes under visible and solar light. Two step method of synthesis of Ag based TiO<sub>2</sub> nanocomposites was developed to achieve maximum photocatalytic activity under visible light. The optimum synthesis conditions were found to be molar ratio of Ag to Ti of 1:1.6, CFS pH of 7, synthesis time of 4 h for silver ion reduction and 4 h after the addition of Ti precursor. AgO/Ag<sub>2</sub>O@TiO<sub>2</sub> nanocomposites thus formed were spherical with AgO/Ag<sub>2</sub>O embedded in TiO<sub>2</sub> and average particle size of 39.6 nm. Around 99% of 100 ppm RB 220 could be degraded in 90 min with AgO/Ag<sub>2</sub>O@TiO<sub>2</sub>. It showed better activity than Bio-TiO<sub>2</sub> and AgO/Ag<sub>2</sub>O, found to be active under visible as well as solar light. It did not exhibit appreciable activity in the degradation of AY-17. AgO/Ag<sub>2</sub>O@TiO<sub>2</sub> was further modified with Cu by microbial synthesis and the nanocomposites synthesized with molar ratio of Ag:Ti:Cu of 1:1.6:0.7 and calcined at 400°C was found to be the optimum to achieve maximum dye degradation. AgO/Ag<sub>2</sub>O@TiO<sub>2</sub> modified with Cu (ATC-75) was with average particle size of 14.3 nm and showed the presence of Cu as CuO. ATC-75 nanocomposites could degrade 100 ppm RB 220 completely in 45 minutes under visible light and >95 % degradation in 90 min under solar light, whereas it could degrade 90 % of 100 ppm of AY17 dye in 90 min under visible and solar light. The degradation of AY-17 was greatly affected by the presence of RB-220 in mixed dye solution. ATC-75 showed a good reusability potential. These photocatalysts can be used in the treatment of wastewater containing dyes by harnessing solar energy. The synthesis is green, environmental friendly and energy efficient method.

**Keywords:** AgO/Ag<sub>2</sub>O@TiO<sub>2</sub>, *Alcaligenes aquatilis*, dye degradation, microbial synthesis, nanocomposites, photocatalysis.

## CONTENTS

	TITLE	PAGE NO.
	<b>ABSTRACT</b>	i
	<b>CONTENTS</b>	ii
	<b>LIST OF TABLES</b>	vi
	<b>LIST OF FIGURES</b>	vii
	<b>NOMENCLATURE</b>	xiii
<b>CHAPTER 1</b>	<b>INTRODUCTION</b>	1
<b>CHAPTER 2</b>	<b>LITERATURE REVIEW</b>	7
2.1	<b>Heterogeneous Photocatalysis</b>	7
2.1.1	TiO <sub>2</sub> as a photocatalyst	9
2.1.2	Modified TiO <sub>2</sub> photocatalysts	9
2.2	<b>Biosynthesis of Nanoparticles</b>	18
2.2.1	Factors affecting biosynthesis of nanoparticles	31
2.3	<b>Reaction parameters affecting degradation process</b>	33
2.4	<b>Research gaps, scope and objectives of the research work</b>	36
<b>CHAPTER 3</b>	<b>MATERIALS AND METHODS</b>	39
3.1	<b>Materials</b>	39
3.2	<b>Preparation of cell free supernatant (CFS)</b>	40
3.3	<b>Biosynthesis of Ag based TiO<sub>2</sub> nanocomposites</b>	40
3.3.1	Method A	41
3.3.2	Method B (One pot synthesis method with consecutive addition of precursors with time gap between the additions)	42
3.3.3	Method C (One pot synthesis method with simultaneous addition of precursors)	42
3.4	<b>Choice of method of synthesis</b>	43
3.5	<b>Optimization of synthesis parameters for Ag based TiO<sub>2</sub> nanocomposites</b>	43
3.5.1	Optimization of molar ratio of Ag to Ti	44
3.5.2	Optimization of pH of cell free supernatant	44

3.5.3	Optimization of reaction time after the addition of Ag precursor, $t_{\text{step 1}}$ and after the addition of $\text{K}_2\text{TiF}_6$ salt, $t_{\text{step 2}}$ )	44
3.6	<b>Biosynthesis of <math>\text{TiO}_2</math> (Bio-<math>\text{TiO}_2</math>) and <math>\text{AgO}/\text{Ag}_2\text{O}</math> nanoparticles</b>	45
3.7	<b>Synthesis of Ag based <math>\text{TiO}_2</math> modified with Cu nanocomposites (ATC) with optimization of synthesis and calcination conditions</b>	45
3.8	<b>Photocatalytic degradation studies on RB 220 and AY 17 using the biosynthesized nanoparticles as catalyst under visible light</b>	48
3.9	<b>Photocatalytic degradation studies of RB 220 and AY-17 dye using biosynthesized nanocomposite under solar light</b>	50
3.10	<b>Characterization of the biosynthesized nanoparticles</b>	51
3.11	Preparation of RB-220 and AY-17 dye solutions and analysis of their concentrations	52
<b>CHAPTER 4</b>	<b>RESULTS AND DISCUSSION</b>	54
4.1	<b>Biological Synthesis of Ag Based <math>\text{TiO}_2</math> Nanocomposites</b>	54
4.1.1	Selection of method of synthesis	54
4.1.1.1	Characterization of the biosynthesized Ag-based $\text{TiO}_2$ nanocomposite	58
4.1.1.2.	Characterization of the $\text{AgO}/\text{Ag}_2\text{O}-\text{TiO}_2$ nanocomposite synthesized by Method A	64
4.1.2	Optimization of synthesis parameters for $\text{AgO}/\text{Ag}_2\text{O}-\text{TiO}_2$ nanocomposites synthesized by Method A	70
4.1.2.1	Optimization of molar ratio of Ag:Ti in the synthesis mixture	70
4.1.2.2	Optimization of pH of the supernatant used for the synthesis	76
4.1.2.3	Optimization of synthesis time after the addition of silver precursor (step 1)	81
4.1.2.4	Optimization of synthesis time after the addition of Ti precursor (step 2)	85
4.1.2.5	Characterization of the $\text{AgO}/\text{Ag}_2\text{O}@-\text{TiO}_2$ nanocomposite synthesized under optimum synthesis condition	92

4.1.3	Comparison of photocatalytic activity of biosynthesized AgO/Ag <sub>2</sub> O@TiO <sub>2</sub> nanocomposites with biosynthesized AgO/Ag <sub>2</sub> O and Bio-TiO <sub>2</sub>	98
4.2	<b>Optimization of photocatalytic process parameters</b>	101
4.2.1	Optimization of dye solution pH	101
4.2.2	Effect of Catalyst loading	103
4.2.3	Effect of initial dye concentration	104
4.3	<b>Photocatalytic activity of the AgO/Ag<sub>2</sub>O@TiO<sub>2</sub> nanocomposite on RB 220 dye degradation under solar light</b>	106
4.4	<b>Photocatalytic degradation of Acid yellow 17 (AY 17) dye using AgO/Ag<sub>2</sub>O@TiO<sub>2</sub> under visible and solar light</b>	109
4.5	<b>Photocatalytic degradation studies using AgO/Ag<sub>2</sub>O@TiO<sub>2</sub> modified with Cu (ATC) nanocomposite</b>	110
4.5.1	Effect of Cu loading in AgO/Ag <sub>2</sub> O@TiO <sub>2</sub> modified with Cu (ATC) nanocomposite on its photocatalytic activity under visible light	110
4.5.2	Effect of calcination temperature on the photocatalytic activity of AgO/Ag <sub>2</sub> O@TiO <sub>2</sub> modified with Cu (ATC) nanocomposite under visible light	112
4.5.3	Photocatalytic degradation studies of RB-220 using AgO/Ag <sub>2</sub> O@TiO <sub>2</sub> modified with Cu nanocomposite under solar light	115
4.5.4	Photocatalytic degradation studies of AY 17 dye using AgO/Ag <sub>2</sub> O@TiO <sub>2</sub> modified with Cu nanocomposite under visible and solar light	116
4.5.5	Characterization of AgO/Ag <sub>2</sub> O@TiO <sub>2</sub> modified with Cu nanocomposite	120
4.6	<b>Mechanism of photocatalytic degradation of RB 220 and AY 17 dyes by AgO@TiO<sub>2</sub> modified with Cu nanocomposite (ATC-75)</b>	124

4.7	<b>Studies on degradation of dyes in a mixed dye system of RB-220 and AY 17 with AgO/Ag<sub>2</sub>O@TiO<sub>2</sub> modified with Cu (ATC 75) nanocomposite</b>	125
4.8	<b>Reusability studies of AgO/Ag<sub>2</sub>O@TiO<sub>2</sub> modified with Cu (ATC 75) nanocomposite in RB 220 dye degradation</b>	129
<b>CHAPTER 5</b>	<b>SUMMARY AND CONCLUSION</b>	131
	<b>REFERENCES</b>	135
	<b>RESEARCH PUBLICATIONS</b>	167

## LIST OF TABLES

TABLE NO.	TABLE CAPTION	PAGE NO.
2.1	Modified TiO <sub>2</sub> photocatalysts and their photocatalytic application	13
2.2	Nanoparticles synthesized using microbial based synthesis method	24
3.1	Optimization of molar ratio of Ag:Ti:Cu	46
4.1	Band gap energy values of different nanocomposites containing TiO <sub>2</sub>	63
4.2	Initial degradation rate and percentage dye degradation at the end of 15 min, band-gap and crystallite size of nanocomposites synthesized with different methods.	64
4.3	Effect of Ag to Ti molar ratio on percentage dye degradation, initial degradation rate band gap and crystallite size	75
4.4	Effect of CFS pH used in the synthesis on dye degradation, initial rate, band-gap energy and crystallite size of synthesized nanocomposites	81
4.5	Effect of $t_{\text{step 1}}$ on dye degradation, initial dye degradation rate, band-gap energy and crystallite size of nanocomposites synthesized at different time periods	84
4.6	Effect of $t_{\text{step 2}}$ on dye degradation, initial rate of dye degradation, band-gap energy and crystallite of the synthesized nanocomposites	88
4.7	The initial rates of degradation with AgO/Ag <sub>2</sub> O@TiO <sub>2</sub> (AAT), ATC nanocomposites and calcination temperatures of ATC-75	114

## LIST OF FIGURES

FIG. NO.	FIGURE CAPTION	PAGE NO.
2.1	Schematic representation of photocatalytic process	8
3.1	Chemical structure of RB 220 and AY 17	40
3.2	Schematic representation of Method A for synthesis of the nanocomposites.	41
3.3	Schematic representation of Method B for synthesis of the nanocomposites	42
3.4	Schematic representation of Method C for synthesis of the nanocomposites	43
3.5	Schematic representation of the synthesis process for Ag based TiO <sub>2</sub> modified with Cu nanocomposite (ATC)	47
3.6	Schematic diagram of the annular glass photoreactor and Photographic image of the reactor	50
3.7	Schematic diagram of the batch stirred reactor set-up for solar photocatalysis	51
3.8	Calibration plot for the estimation of Acid Yellow 17 dye	53
3.9	Calibration plot for the estimation of Reactive Blue 220 dye	53
4.1	Percentage dye degradation using nanocomposites synthesized by Method A, Method B and Method C	55
4.2	Percentage dye removal using Ag based TiO <sub>2</sub> nanocomposite (synthesized by Method A) in the presence of (i) nanocomposite and light (ii) only visible light without nanoparticles	56
4.3	Effect of calcination on Ag-based TiO <sub>2</sub> nanocomposite synthesized by Method A	57
4.4	XRD pattern of the nanocomposites synthesized by Method A, B and C.	59
4.5	UV-Vis absorption spectra of Ag based TiO <sub>2</sub> nanocomposites synthesized by Method A, Method B and Method C	60

4.6	Tauc plots for the nanocomposites synthesized by Method A, B and C	61
4.7	Colour change of culture supernatant after the addition of the precursor from light yellow (left) to brown (right) (b) TEM image (c) SAED pattern (d) Particle size histogram of the nanocomposites	65
4.8	XRD pattern of the nanocomposites synthesized by Method A	66
4.9	FTIR spectra of the AgO/Ag <sub>2</sub> O-TiO <sub>2</sub> nanocomposite	67
4.10	XPS spectra of (a) AgO/Ag <sub>2</sub> O-TiO <sub>2</sub> nanocomposite (b) O1s (c) Ag3d (d) Ti2p (e) C1s	68
4.11	(a) Time course of variation of percentage dye degradation obtained with AgO/Ag <sub>2</sub> O-TiO <sub>2</sub> nanocomposite synthesized with different molar ratio of Ag to Ti. (b) Pseudo-first order kinetics plot for 1:1.6 ratio	71
4.12	XRD pattern of the nanoparticles synthesized at different ratios (a) 1:0.4 (b) 1:0.8 (c) 1:1.2 (d) 1:1.6 (e) 1:2.0	74
4.13	Tauc plot of the nanocomposites synthesized at different molar ratio	75
4.14	Time course of variation of percentage dye degradation obtained with nanocomposites synthesized at different pH (b) Pseudo first-order kinetics plot for nanocomposite synthesized at pH 7	77
4.15	XRD pattern of Ag-TiO <sub>2</sub> nanocomposites synthesized at different pH (a) pH 5, (b) pH 7, (c) pH 9, (d) pH 11 and (e) pH 13	79
4.16	Tauc plot displaying band-gap energy of the nanocomposites synthesized at different pH	80
4.17	(a) Time course of variation of percentage dye degradation obtained with nanocomposite synthesized with varying $t_{\text{step1}}$ and constant $t_{\text{step2}}$ of 24 h (b) Pseudo first-order kinetics plot for $t_{\text{step1}} = 4$ h	82
4.18	XRD pattern of the nanocomposites synthesized with varying $t_{\text{step1}}$ and constant $t_{\text{step2}}$ of 24 h	83

4.19	Tauc plot showing band-gap energy for Ag <sub>2</sub> O/AgO-TiO <sub>2</sub> nanocomposite synthesized at varying t <sub>step 1</sub> and constant t <sub>step 2</sub> of 24 h	84
4.20	(a) Time course of variation of percentage dye degradation obtained with nanocomposite synthesized with varying t <sub>step 2</sub> and constant t <sub>step 1</sub> of 4 h (b) Pseudo first-order kinetics plot for t <sub>step 2</sub> = 4	86
4.21	XRD pattern of the nanocomposites synthesized with varying t <sub>step 2</sub> and constant t <sub>step 1</sub> of 4 h	87
4.22	Tauc plot for the nanocomposites synthesized at varying t <sub>step 2</sub> with t <sub>step 1</sub> of 4 h	88
4.23	Mass spectrum of the reactor samples (a) before the start of photocatalysis experiment (b) after 30 min of photocatalytic reaction under visible light irradiation (c) after 60 min of photocatalytic reaction under visible light irradiation	90
4.24	(a) and (b) Possible degradation pathways of RB 220 dye	91
4.25	XRD pattern of the AgO/Ag <sub>2</sub> O@TiO <sub>2</sub> nanocomposite synthesized at optimum condition of total 8 h synthesis time	92
4.26	(a) SEM and (b) EDX of the nanocomposites synthesized under optimized condition	93
4.27	TEM image (a) and (b) of the nanocomposites at different magnification (c) Particle size distribution (d) SAED image of the nanocomposites synthesized under optimized condition.	94
4.28	FTIR spectra of the nanocomposites	95
4.29	(a) XPS spectra of the nanocomposite, (b) O1s, (c) C1s, (d) Ag3d, (e) Ti2p	97
4.30	XRD analysis of Bio-TiO <sub>2</sub> , AgO/Ag <sub>2</sub> O and AgO/Ag <sub>2</sub> O@TiO <sub>2</sub> nanocomposite	98
4.31	(a) Colour change of RB 220 dye solution from initial till the end of 90 min using AgO/Ag <sub>2</sub> O@TiO <sub>2</sub> nanocomposite under light (b) Percentage dye (RB 220) degradation using AgO/Ag <sub>2</sub> O, Bio-TiO <sub>2</sub> and AgO/Ag <sub>2</sub> O@TiO <sub>2</sub> nanocomposite (c) Pseudo first-order kinetics plot for AgO/Ag <sub>2</sub> O, Bio-TiO <sub>2</sub>	99

	and AgO/Ag <sub>2</sub> O@TiO <sub>2</sub> nanocomposite (d) Rate constants (k) for the nanocomposites	
4.32	Photoluminescence spectroscopy of Bio-TiO <sub>2</sub> , AgO/Ag <sub>2</sub> O and AgO/Ag <sub>2</sub> O@TiO <sub>2</sub> nanocomposite	101
4.33	Percentage dye degradation at different dye pH with initial dye concentration of 100 ppm and catalyst loading of 0.1 g/l.	102
4.34	Percentage dye degradation at different catalyst loading with initial dye concentration – 100 ppm and pH 3	104
4.35	(a) Percentage dye degradation at different initial concentration at different time intervals (b) Percentage dye degradation at 90 min	105
4.36	(a) Pseudo first-order kinetics plot for dye degradation at different initial dye concentration (b) rate constants for different initial concentrations of dye	106
4.37	(a) Absorption spectra of RB 220 dye from 0 <sup>th</sup> min till 90 min under solar light (b) Dye removal using (i) AgO/Ag <sub>2</sub> O@TiO <sub>2</sub> nanocomposite under solar light (ii) under light (without nanocomposite) (c) Pseudo-first-order kinetic plot for dye degradation	108
4.38	Possible RB 220 degradation mechanism by AgO/Ag <sub>2</sub> O@TiO <sub>2</sub> nanocomposite under solar light	109
4.39	Photocatalytic degradation of AY-17 dye using AgO/Ag <sub>2</sub> O@TiO <sub>2</sub> nanocomposite under visible and solar light	110
4.40	Percentage dye degradation using AgO/Ag <sub>2</sub> O@TiO <sub>2</sub> and AgO/Ag <sub>2</sub> O@TiO <sub>2</sub> modified with Cu (ATC) with varying Cu loading	112
4.41	Percentage dye degradation using ATC-75 nanocomposite calcined at varied temperature	113
4.42	Percentage dye degradation using AgO/Ag <sub>2</sub> O@TiO <sub>2</sub> , ATC-75, AC and TC nanocomposites under visible light	114
4.43	Comparison of RB 220 dye degradation with ATC-75 and AgO/Ag <sub>2</sub> O@TiO <sub>2</sub> nanocomposite under solar light	115

4.44	Absorption spectra of AY 17 dye displaying reduction in the dye concentration from initial to 90 min irradiation time under visible light (Inset) Colour change of AY 17 dye from initial to 90 min	116
4.45	(a) Time course variation of percentage dye degradation using AgO/Ag <sub>2</sub> O@TiO <sub>2</sub> and AgO/Ag <sub>2</sub> O@TiO <sub>2</sub> modified with Cu (ATC-75) nanocomposite (b) Pseudo first-order kinetics plot for AY-17 degradation using ATC-75 nanocomposite	117
4.46	(a) Time course of variation of percentage dye degradation using AgO/Ag <sub>2</sub> O@TiO <sub>2</sub> and Cu-based AgO/Ag <sub>2</sub> O@TiO <sub>2</sub> nanocomposite under solar light (b) Pseudo first-order kinetics plot for AgO/Ag <sub>2</sub> O@TiO <sub>2</sub> modified with Cu (ATC-75) nanocomposites	118
4.47	XRD pattern of the AgO/Ag <sub>2</sub> O@TiO <sub>2</sub> nanocomposite with different Cu loaded samples	119
4.48	Tauc plot displaying the band-gap energy of varied Cu loaded AgO/Ag <sub>2</sub> O@TiO <sub>2</sub> samples	120
4.49	(a) SEM and (b) TEM image of the nanocomposites (c) SAED pattern (d) Particle size histogram of the AgO/Ag <sub>2</sub> O@TiO <sub>2</sub> modified with Cu nanocomposite (ATC-75)	121
4.50	(a) EDX analysis and (b) EDS mapping of the Cu-based AgO/Ag <sub>2</sub> O@TiO <sub>2</sub> nanocomposite	122
4.51	FTIR spectra of the nanocomposites	123
4.52	XPS spectra of the AgO/Ag <sub>2</sub> O@TiO <sub>2</sub> modified with Cu (ATC-75) nanocomposite	124
4.53	Possible dye degradation mechanism by AgO/Ag <sub>2</sub> O@TiO <sub>2</sub> modified with Cu nanocomposite under solar light	125
4.54	Absorption spectra of AY 17 and RB 220 dye and the mixture of AY 17 and RB 220	127
4.55	Percentage dye degradation in mixture (RB 220 + AY 17) with initial AY17 concentration of 100 ppm being constant	127
4.56	Percentage dye degradation in mixture (RB 220 + AY 17) with initial RB 220 concentration of 100 ppm being constant	128

4.57	Influence of one dye over the other at the end of 5 <sup>th</sup> h	128
4.58	Reusability studies in RB 220 degradation using AgO/Ag <sub>2</sub> O@TiO <sub>2</sub> modified with Cu (ATC-75) nanocomposites	129

## NOMENCLATURE

AOT – Advanced oxidation technologies

Ag – Silver

AgO – Silver oxide

ATC – AgO/Ag<sub>2</sub>O@TiO<sub>2</sub>

AY-17 – Acid yellow - 17

CB – Conduction band

CFS – Cell free supernatant

CuO – Copper oxide

EDS – Energy-dispersive X-ray spectroscopy

H<sub>2</sub>SO<sub>4</sub> – Sulphuric acid

FESEM – Field emission scanning electron microscopy

FTIR – Fourier Transform Infrared Spectroscopy

KBr – Potassium bromide

LCMS – Liquid chromatography mass spectrometry

NaOH – Sodium hydroxide

RB 220 – Reactive blue 220

ROS – Reactive oxygen species

TEM – Transmission electron microscopy

TiO<sub>2</sub> – Titanium dioxide

UV – Ultraviolet

VB – Valence band

XPS – X-ray photoelectron spectroscopy

XRD – X-ray diffraction

$\text{Å}$  – Angstrom

$e^-$  – electrons

$E_g$  – Energy band-gap

eV – Electron volt

g/l – gram per litre

$h^+$  -- holes

h – hour

k – rate constant

LPM – litres per minute

mg/L – milligram per litre

min – minutes

mL – millilitre

mM – millimolar

rpm – rotations per minute

$\cdot\text{OH}$  – hydroxyl radical

$\text{O}_2^-$  – superoxide radical

$\text{H}_2\text{O}_2$  – hydrogen peroxide

ppm – parts per million

nm – nanometre

W – Watt

$\theta$  – theta

% – percentage

# CHAPTER 1

## INTRODUCTION

### 1.1. Background and Need for the study

A large quantity of dyes released into the water reservoirs with textile industry effluents has raised a lot of concern due to their harmful and toxic effect on the ecosystem (Bhakya et al. 2015). Due to the complex structure and presence of azo bond (-N=N-), azo dyes which are largely used in the textile industry are not easily degradable and are carcinogenic (Mirkhani et al. 2009; Pinheiro et al. 2022). Therefore mineralization of these dyes is of utmost importance to avoid any potential risks caused by the dyes and their intermediates. The concentration of azo dyes in the textile effluent vary in the range of 5 – 1500 mg/L (Khan et al. 2013). Conventional methods of effluent treatment are not effective as they do not facilitate the mineralization of the dyes. Among the various methods employed, advanced oxidation technologies (AOT) like heterogeneous photocatalysis have gained increased interest as a promising strategy to decontaminate wastewater (Mishra et al. 2015) by mineralization of organic pollutants. The discovery of photolytic water splitting effect using titania by Fujishima and Honda in 1972, has led to the extensive research on semiconductor photocatalysis especially titanium dioxide in different fields of science. Photocatalysis is based on generation of electron-hole pairs caused by the excitation of photocatalyst on irradiation with light with energy equal to or greater than the band gap of the semiconductor which produces electron-hole ( $e^-/h^+$ ) pairs when valence band electrons are excited to the conduction band, initiating a series of redox reactions ultimately leading to degradation of organic substances (Silva et al. 2002). On the semiconductor surface, the excited electron and the hole can participate in redox reactions to produce reactive oxygen species (ROS) such as hydroxyl radical ( $\cdot\text{OH}$ ), superoxide radical anion ( $\text{O}_2^-$ ), singlet oxygen ( $^1\text{O}_2$ ), and hydrogen peroxide ( $\text{H}_2\text{O}_2$ ) (Cruz-Ortiz et al. 2017), which can further participate in the mineralization of the pollutant (Ibhadon et al. 2013). The electron and hole can

recombine, releasing the absorbed light energy as heat, with no chemical reaction taking place.

Due to its high stability, low-cost and non-toxic nature, TiO<sub>2</sub> has been used in photocatalysis for many applications. But the higher band-gap (3.2 eV) of TiO<sub>2</sub> limits its utilization under visible light irradiation, thus restricting the use of solar light as a source of irradiation for photocatalytic water treatment. These problems, however, can be resolved by doping of TiO<sub>2</sub> or coupling with other semiconductors or metal oxides. Doping with transition metal ions for example, Cu (Ikram et al. 2020, Mingmongkol et al. 2022), Mn, Ni (Prasad et al. 2009), Fe (Vijayan et al. 2009) as well as with noble metals such as Ag (Younas et al. 2014; Nguyen et al. 2023), Au (Pal et al. 2015) and Ru (Akhtar et al. 2023), have been found to red-shift the TiO<sub>2</sub> absorption band from the UV into the visible region, resulting in a great increase in the efficiency of solar-light photocatalysis (Ibhadon and Fitzpatrick 2013).

Several Titania based composite nanomaterials such as TiO<sub>2</sub>- graphene, TiO<sub>2</sub>-graphene oxide (GO) and TiO<sub>2</sub>-reduced graphene (rGO)(Morales-Torres et al. 2012), TiO<sub>2</sub>-CNTs (carbon nanotubes) composite nanostructures (Nguyen et al. 2015), TiO<sub>2</sub>(B)/Ag<sub>2</sub>O (Paul et al. 2016), Au/TiO<sub>2</sub> nanocomposite (Biswas et al. 2015), r-GO/Pd-TiO<sub>2</sub>/r-GO (Dao et al. 2105), TiO<sub>2</sub>@Fe<sub>2</sub>O<sub>3</sub> heterostructures (Trenczek-Zajac et al. 2022), Cu-Cu<sub>2</sub>O@TiO<sub>2</sub> heterojunction (Zhao and Liu 2020) and Cu<sub>2</sub>O/TiO<sub>2</sub> heterostructures (Wei et al. 2019) have emerged as promising materials for photocatalysis. In recent years core-shell structures have been well developed where a noble metal acts as a core and a semiconductor acts like a shell. Ag@TiO<sub>2</sub> is widely studied for its photocatalytic activity (Hirakawa and Kamat 2004; Yang et al. 2014; Khanna and Shetty 2014). Hirakawa and Kamat (2004) reported the separation of electron-hole pair in Ag@TiO<sub>2</sub>, thereby enhancing its photocatalytic efficiency. These core-shell structures have the ability to convert light energy by storing electrons during photoirradiation and then delivering it when required. Khanna and Shetty (2013) have synthesized Ag@TiO<sub>2</sub> using one-pot synthesis method by chemical route with calcination and used it for the degradation of azo dyes under solar light.

Coupling of TiO<sub>2</sub> with other semiconductors such as CdS (Kim et al. 2015), Ag<sub>2</sub>O (Zhou et al. 2010), WO<sub>3</sub> (Arai et al. 2009) and Bi<sub>2</sub>O<sub>3</sub> (Huo et al. 2014) have shown good promise in visible light mediated photocatalysis and high photocatalytic activity. Silver based oxides have been found to be promising because of high efficiency. Silver oxides are low band gap semiconductors and are considered as the potential candidates due to their stability. AgO and Ag<sub>2</sub>O have been effectively used in the degradation of pollutant under visible light ( Liu et al. 2019; Wei et al. 2014; Sobhani-Nasan and Behpour 2016). Mogal et al. (2014) have reported that the silver oxide species when dispersed on the surface of TiO<sub>2</sub> nanoparticles not only increased the surface area but also reduced the band-gap of TiO<sub>2</sub> favouring higher photocatalytic activity. Ag<sub>2</sub>O/TiO<sub>2</sub> composite nanofibers fabricated by Liu et al. (2019) showed better performance than pure Ag<sub>2</sub>O or TiO<sub>2</sub> in photocatalytic degradation of Rhodamine B (RhB).

Ag<sub>2</sub>O nanoparticles having a narrow band gap of 1.3 eV, are efficient in absorbing electrons and can act as photosensitizers in the visible region (Wang et al. 2012; Xu et al. 2013; Liu et al. 2012). Ag<sub>2</sub>O nanoparticles are known to show high absorption in the visible range exciting more photogenerated electron-hole pairs to participate in photocatalytic degradation. Ag<sub>2</sub>O/TiO<sub>2</sub> composite improve the photocatalytic activity of TiO<sub>2</sub> by suppressing the recombination of charge carriers and displaying high absorption in the visible range (Liu et al. 2018). Sarkar et al. (2012) reported superior photocatalytic activity of Ag<sub>2</sub>O/TiO<sub>2</sub> with faster degradation of methyl orange dye than pure TiO<sub>2</sub> under UV light. Ag<sub>2</sub>O and TiO<sub>2</sub> form p-n-type heterojunctions at the interface and electron transfer is reported to occur from TiO<sub>2</sub> to Ag<sub>2</sub>O when their Fermi levels align (Zhao et al. 2017).

Ag<sub>2</sub>O/TiO<sub>2</sub> composites has been proved to exhibit photocatalytic activity and have been employed efficiently for photocatalytic water splitting (Gannoruwa et al. 2016) the degradation of pharmaceuticals (Kerkez and Boz 2015; Gou et al. 2017; Ren and Yang 2017), inactivation of pathogens in water (Liu et al. 2017; Hua et al. 2013) and in the removal of recalcitrant pollutants (Wang et al. 2020; Duran-Alvarez et al. 2020; Ren and Yang 2017; Sarkar et al. 2013) and other photocatalytic applications (Endo-Kimura et al. 2019) under UV and visible light irradiation.

Many researchers have used different transition metals like Zn, Zr, Cu (Karuppasamy et al. 2021), Mn, Ni, Co (Kaur et al. 2017) and investigated their effect in influencing the TiO<sub>2</sub> nanoparticles in photocatalytic degradation studies where they found transition metal doping reduced the band-gap energy of TiO<sub>2</sub> (Kaur et al. 2017). Cu doping modified the properties of TiO<sub>2</sub> thereby enhancing its photocatalytic activity (Ahmadiasl et al. 2022). Presence of copper oxides in TiO<sub>2</sub> nanocomposites have been found to improve the photocatalytic activity in degradation of pollutants under visible light (Cosma et al. 2022). The low band-gap of CuO (1.2 eV) also finds its application in degradation studies when used in combination with the TiO<sub>2</sub> (Bopape et al. 2023).

Recent studies report the evaluation of ternary composite structures where TiO<sub>2</sub> is modified with bimetals or bimetallic oxide nanoparticles and studied for their photocatalytic applications (Pino-Sandoval et al. 2020, Mendez-Medrano et al. 2016). Pino-Sandoval et al. (2020) reported the reduction in the band-gap energy and superior photocatalytic activity of Ag-Cu/TiO<sub>2</sub> photocatalyst under solar light. Mendez-Medrano et al. (2016) have reported the visible activity of the Ag@CuO/TiO<sub>2</sub> catalyst and attributed it to the surface plasmon resonance of Ag nanoparticles and reduced band-gap of CuO. These surface modified TiO<sub>2</sub> nanostructures with Ag and Cu or their oxides have been found to be efficient photocatalyst in water treatment process.

The composite nanomaterials mentioned earlier have been reported to be synthesized by physical and chemical methods. These processes involve the use of toxic reagents or solvents which may be carcinogens and has cytotoxic effect (Ai et al. 2011) and produce hazardous toxic wastes that are harmful, not only to the environment but also to human health. These methods also involve high temperature and pressure conditions and are often energy intensive. Therefore, biological method of nanoparticle synthesis is usually preferred with the use of biological agents such as microbes. The use of expensive and hazardous chemicals is eliminated, and the more acceptable “green” route is not as energy intensive as the chemical method and is also environment friendly. The “biogenic” approach is further supported by the fact that they can be carried out under ambient conditions of temperature and pressure. The particles

generated by these processes have shown greater specific surface area (Bhattacharya et al. 2008).

Microbial mediated synthesis of nanoparticles can be through intracellular (Bai et al. 2009) and extracellular (Jha et al. 2009) routes, latter being beneficial in terms of separation of nanoparticles after the synthesis. The intracellular synthesis of nanoparticles has been most widely reported (Omajali et al. 2015). However, intracellular synthesis faces challenges in terms of downstream processing to remove the nanoparticles from the cell biomass by cell disruption followed by separation of nanoparticles from the cell biomass. Extracellular synthesis may be again classified as (i) cell associated synthesis and (ii) synthesis in the cell free environment. In the cell associated extracellular synthesis, the cell growth may be inhibited by metal ions used as precursors. Though cell disruption step is not required, the separation of nanoparticles from the cell biomass is still a challenge. However, the synthesis in the cell free environment involves the use of cell free culture broth for the synthesis of nanoparticles. This involves initial growth of cells, cell separation from the culture broth and use of cell free culture broth containing the enzymes and metabolites for the nanoparticle synthesis.

Microbial enzymes convert the metal ions into the element metal resulting in the formation of nanoparticles. Exploiting these features of microbes, several metal or metal oxide nanoparticles such as Ag using *Pseudomonas stutzeri* (Desai et al. 2020), *Leuconostoc lactis* (Saravanan et al. 2017), *Bacillus siamensis* C1 (Ibrahim et al. 2019), *Streptomyces* sp (Gupta et al. 2017), *Pseudomonas aeruginosa* (Ali et al. 2017), Au nanoparticles by *Bacillus cereus* (Pourali et al. 2017), *Deinococcus radiodurans* (Li et al. 2016) and oxide nanoparticles like BaTiO<sub>3</sub> by *Fusarium oxysporum* (Bansal et al. 2006), TiO<sub>2</sub> by *Staphylococcus aureus* (Landage et al. 2020), *Bacillus subtilis* (Dhandapani et al. 2012), CuO by *Lactobacillus casei subsp. Casei* (Kouhkan et al. 2020), *Streptomyces* sp. MHM38 (Bukhari et al. 2021), ZnO by *Lactobacillus plantarum* TA4 (Yusof et al. 2020), etc. have been synthesized by microbial route. Recently the cell free culture broth of *Alcaligenes aquatilis* have been used to synthesize Ag and TiO<sub>2</sub> independently (Devadiga, 2016). The nitrate reductase and

hydrolytic enzymes are found to be responsible for the synthesis of silver and TiO<sub>2</sub> nanoparticles respectively. Yusuf et al. (2020) have reported that various functional groups such as hydroxyl, amine and carboxyls from proteins in the cell free supernatant are involved in the reduction and synthesis of nanoparticles. Jayaseelan et al. (2013) found glycyl-L-proline, a secondary metabolite from the bacteria, *Aeromonas hydrophila* might be responsible for reducing, capping and stabilization of TiO<sub>2</sub> nanoparticles. Thus, the biomolecules present in the bacterial cell free supernatant act as reducing and stabilizing agent in synthesis of nanoparticles.

This report presents the studies on selection of the best synthesis strategy for the synthesis of silver based titania such as AgO/Ag<sub>2</sub>O@TiO<sub>2</sub> nanocomposites and AgO/Ag<sub>2</sub>O@TiO<sub>2</sub> nanocomposites modified with Cu using the bacteria *Alcaligenes aquatilis* in the cell free culture broth. The photocatalytic activity of these nanocomposite structures is assessed in terms of degradation of widely used textile azo dyes, Reactive Blue 220 and Acid Yellow 17 dye under artificial visible light and natural sun light. Reactive Blue 220, is an azo dye with vinyl sulfone reactive group and widely used for coloration of cellulosic textiles (Smigiel-Kaminska et al. 2020) Acid yellow-17 is an azo dye mainly used for dyeing wool, silk, polyamide fiber and leather apart from being used in the food, , paper, cosmetics and cleaning materials (Jedynak et al. 2019).

## **CHAPTER 2**

### **LITERATURE REVIEW**

Water pollution has become a major concern due to the discharge of untreated water from various industries among which textile industry contributes majorly (Teli and Nadathur 2018) as they release large quantities of dyes. Dyes are carcinogenic and toxic in nature which affect the human and aquatic life. Due to their complexity, dyes are sufficiently stable compounds and are not easily degradable (Naz et al. 2022). Among various other dyes, azo dyes form the major part in textile industries. Azo dyes are synthetic dyes consisting of azo bond (-N=N-) with aromatic ring structure which poses a great challenge for its elimination (Kgatle et al. 2021). Conventional approaches used in the removal of these dyes has its own limitations and might require further treatment to remove secondary pollutants (Ammari et al. 2020). Homogeneous and heterogeneous photocatalysis are the AOPs aided by light which are employed in the degradation of various pollutants in wastewater. In homogeneous photocatalysis both the photocatalyst and the reactants exist in the same phase. These soluble homogeneous molecules have photosensitizers and catalytic sites to perform the oxidation and reduction reactions. Homogeneous photocatalysis include  $\text{H}_2\text{O}_2/\text{sunlight}$ , solar photo-Fenton ( $\text{Fe}^{+2}/\text{H}_2\text{O}_2/\text{sunlight}$ ),  $\text{light}/\text{O}_3/\text{H}_2\text{O}_2$  etc. However they have temperature limitations and also solubility of the catalyst molecules makes it difficult to separate from the solution and therefore it is less preferred over heterogeneous photocatalysis (Devi et al. 2022; Lakhera and Neppolian 2021) where solid phase photocatalysts are employed and these catalysts can be easily separated from the treated water.

#### **2.1 HETEROGENEOUS PHOTOCATALYSIS**

Heterogeneous photocatalysis has been extensively used in degradation of the harmful compounds into simpler and non-toxic products with the generation of reactive species (Silva et al. 2002). Heterogeneous photocatalysis is a process where photo-activated chemical reactions are caused by the interaction of photons of a proper energy level with the solid catalyst through the generation of free radicals. According to Fujishima

et al. (2008), when a photocatalyst absorbs a photon with energy equal to or greater than its band-gap, an electron-hole pair is generated which is then separated into a free electron and hole that moves to the surface of the photocatalyst and get trapped. These trapped electron and hole could either react with acceptor or donor molecules respectively, or recombine. The recombination is not favourable, as photocatalysis only occurs when there are at least two reactions occurring simultaneously, the first involving oxidation from photogenerated holes, and the second involving reduction, from photogenerated electrons. Both processes must be balanced precisely in order for the photocatalyst itself not to undergo change, which is one of the basic requirements for a catalyst (Fujishima et al. 2008). Fig. 2.1 shows the schematic representation of photocatalytic process (Silva et al. 2002).

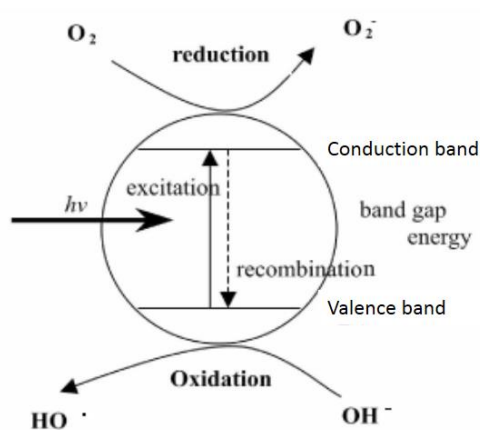


Fig.2.1. Schematic representation of photocatalytic process (Silva et al. 2002).

A semiconductor or a photocatalyst absorbs light energy equal to its band gap energy, leading to the generation of electron ( $e^-$ ) – hole ( $h^+$ ) pairs on the surface of semiconductor particles by excitation of an electron from its valence band to conduction band. The hole splits the water molecule into  $H^+$  and  $\cdot OH$  consequently, the oxygen molecule is transformed to superoxide radical anion ( $O_2^{\cdot-}$ ). By combination of  $H^+$  and  $O_2^{\cdot-}$ , hydroperoxyl radical ( $HO_2^{\cdot}$ ) is produced. Hydrogen peroxide anion ( $HO_2^-$ ) is eventually formed by collision of an electron with  $HO_2^{\cdot}$ . Lastly,  $H_2O_2$  is produced by

a hydrogen ion. All these reactive species like  $\cdot\text{OH}$ ,  $\text{O}_2^{\cdot-}$ ,  $\text{HO}_2^{\cdot-}$ , and  $\text{H}_2\text{O}_2$  play their role in photocatalysis but the  $\cdot\text{OH}$  is the most important. Electrons and holes may also recombine with each other without participating in any chemical reactions (Younas et al. 2014). Titanium dioxide is the first ever used semiconductor photocatalyst and has been widely used for various applications.

### **2.1.1 TiO<sub>2</sub> as a photocatalyst**

Fujishima & Honda in 1972 discovered for the first time the photocatalytic process of water splitting using titania. Since then, titania heterogeneous photocatalysis is gaining importance in the field of environmental remediation. The first experiment was conducted by Matsunaga and his co-workers in 1985, where platinum-loaded titanium oxide powder was used to bring about the photoelectrochemical sterilization of microbial cells (Matsunaga et al. 1985). Titanium dioxide is the most commonly used photocatalyst due to its high stability, inexpensive and non-toxic nature (Gupta and Tripathi 2011). However, the photocatalytic efficiency of TiO<sub>2</sub> nanomaterials is limited to the UV light because of its large intrinsic band gap (>3.2 eV) which severely restricts its utilization in the visible light and also its fast electron–hole recombination resulting in a low quantum yield and poor photocatalytic activity. Therefore different strategies have been applied to enhance the photocatalytic efficiency of TiO<sub>2</sub> under visible light including dye sensitization, doping, coupling and capping of TiO<sub>2</sub> (Gupta et al. 2011).

### **2.1.2 Modified TiO<sub>2</sub> photocatalysts**

Doping of TiO<sub>2</sub> can inhibit charge recombination and increase its photocatalytic activity to the visible region through the formation of impurity energy levels. Vijayan et al (2009) reported doping of TiO<sub>2</sub> with iron caused significant absorption shift towards visible region and enhanced the photocatalytic activity. Dye sensitization and coupling of semiconductors can also expand the light response of TiO<sub>2</sub> to the visible region. Excited dyes and small band gap semiconductors can inject electrons into the conduction of large band gap semiconductors, creating efficient charge separation and enhancing photocatalytic efficiency (Gupta et al. 2011). However, dyes themselves can undergo photodegradation or form intermediates that need to be disposed (Gratzel et al. 2003) and also very few dyes are stable towards photodegradation (Wu et al 1999).

A composite structure of metal nanoparticle core and oxide shell is considered a better design because the oxide shell can protect the metal core and stabilize it against chemical attack. Core-shell structures have the ability to store photogenerated electrons which make them suitable for light energy conversion and storage. Hirakawa and Kamat (2005) reported the importance of core shell structures like Ag@TiO<sub>2</sub> that are useful to promote light induced electron-transfer reactions. Khanna and Shetty (2014) optimized the synthesis of Ag@TiO<sub>2</sub> using one pot synthesis method as described by Hirakawa and Kamat (2005) with the addition of calcination step for the dye degradation. Ag@TiO<sub>2</sub> showed higher photocatalytic activity when compared to commercial and synthesized TiO<sub>2</sub> and Ag doped TiO<sub>2</sub> under both UV and solar light with solar light being more efficient in azo dye degradation (Khanna and Shetty 2014).

Mirkhani et al. (2009) found that Ag-TiO<sub>2</sub> nanoparticles are capable of decolourising and degrading few azo dyes under UV light at an optimum pH range of 8-9 and in acidic solutions and also found decrease in TOC for Coperoxon navy blue RL and C.I. Direct red 80. Incorporation of Ag<sup>+</sup> in TiO<sub>2</sub> samples creates oxygen vacancies which act as electron traps thereby reducing the recombination rate of electron-hole pairs and improving the photocatalyst performance under visible and solar light (Nguyen et al. 2023). The superior photocatalytic activity of Ag@Ru/TiO<sub>2</sub> core shell nanoparticles in the degradation of 4-nitrophenol, 2,4-dinitrophenol and 2,4,6-trinitrophenol under visible light was reported by Akhtar et al. (2023) and was mainly attributed to the prevention of electron and hole recombination by the silver core and the extended absorption in the visible region which is due to the doping of Ru. Paul et al. (2016) reported the use of Ag<sub>2</sub>O-nanoparticle decorated monoclinic TiO<sub>2</sub> porous nanorods on the degradation of methylene blue and methyl orange under visible light and found the dyes to be degraded upto 88% within 30 min of irradiation. Ag<sub>2</sub>O nanoparticles was found to act as a visible light sensitizer thereby enhancing the activity of pure B-phase TiO<sub>2</sub> and enabling it to be used in visible range (Paul et al. 2016). Another study by Wei et al. (2016) also reported improved visible and NIR light responses when Ag<sub>2</sub>O is assembled on the surface of TiO<sub>2</sub> exhibiting increased photocatalytic activity in degradation of methyl orange dye. The formation of heterojunction interfaces in the

Ag<sub>2</sub>O/TiO<sub>2</sub> composite nanofibers promotes the separation of charge carriers thereby significantly improving the photocatalytic activity in degradation of Rh B dye under visible light (Liu et al. 2018). Bian et al. (2020) reported 99.3 % degradation efficiency of rhodamine B dye using Ag/ZnO/AgO/TiO<sub>2</sub> composite under UV–Vis light irradiation at 100 min. Mogal et al (2014) reported that doping of 0.75 at % silver which is present as silver oxides on the surface of TiO<sub>2</sub> was found to improve the particle size, surface area, band-gap and photocatalytic activity. Higher concentration of silver can act as recombination centers and hence reduces the photocatalytic activity (Mogal et al 2014). Addition of dopant in optimum concentration hinders the growth of the crystallites leading to smaller particle size. (Ali et al. 2018). Further the incorporation of transition metals helps in improving the photocatalytic activity of TiO<sub>2</sub> by reducing the band-gap and crystallite size and increasing the surface area (Kaur et al. 2018). Doping of Cu at an optimal loading of 0.1 wt% into TiO<sub>2</sub> reduced the band gap and also showed better photocatalytic activity in degradation of methylene blue dye compared to undoped TiO<sub>2</sub> (Mingmongkol et al. 2022). Ikram et al. (2020) reported the shift in the absorption maxima towards the visible region in Cu-doped TiO<sub>2</sub> nanoparticles indicating the reduction in the band-gap and enhancement in the photocatalytic activity of the nanoparticle on increasing the concentration of the dopant. Mukul et al. (2020) reported enhancement in the absorption of TiO<sub>2</sub> on increasing the concentration of Cu present as CuO in TiO<sub>2</sub>/CuO core shell nanoparticles. Similar results were reported by Liao et al. (2018) where the increase in Cu<sub>2</sub>O concentration increased the absorption value of the Cu<sub>2</sub>O-TiO<sub>2</sub> heterojunction films in the visible range and displayed higher photocatalytic activity in degradation of methyl orange dye. Cu<sub>2</sub>O suppresses the electron – hole pair recombination by the transfer of photogenerated electrons to TiO<sub>2</sub>, thereby promoting the photocatalytic activity (Liao et al. 2018). Heterojunction formation of Cu<sub>2</sub>O/TiO<sub>2</sub> nanotubes greatly affected the photocatalytic activity due to the type II band structure between the n-type TiO<sub>2</sub> and p-type Cu<sub>2</sub>O producing internal electric field across the interface and preventing electron-hole recombination (Pham et al 2018). The increased absorption in 600 -700 nm range in Cu<sub>2</sub>O/TiO<sub>2</sub> nanotubes is due to d-d transition of copper ions which enhances the photogenerated carrier life-time (Pham et al. 2018). Zhao and Liu (2020) studied the photocatalytic activity of a Cu–Cu<sub>2</sub>O@TiO<sub>2</sub> heterojunction photocatalyst in dye degradation which showed 95 %

decolourisation of methylene blue in 3 h under visible light.  $\text{Cu}_2\text{O}/\text{CuO}-\text{TiO}_2$  nanocomposite with reduced graphene oxide was studied by Cosma et al. (2022) for their photocatalytic performance in degradation of ciprofloxacin and amoxicillin. Their results showed that the nanocomposites display higher degradation of the antibiotics due to the  $\text{Cu}_2\text{O}/\text{CuO}$  heterojunction which accelerates the interface charge transfer enhancing the photocatalytic activity irrespective of the presence of graphene oxide (Cosma et al. 2022). Few studies have reported that binary and ternary nanocomposites exhibit high quantum yields and lower recombination rate when compared to the individual nanoparticles (Jo et al 2017, Pino-Sandoval et al. 2020). Cobalt oxide in  $\text{Co}_3\text{O}_4/\text{TiO}_2$  showed superior photocatalytic activity which on addition of graphene oxide further enhanced the photocatalytic degradation of oxytetracycline and congo red under visible light (Jo et al. 2017). The ternary composite  $\text{Ti}_3\text{C}_2/\text{TiO}_2/\text{CuO}$  showed good photocatalytic activity in degradation of methyl orange dye under UV light which is attributed to the effective charge separation by  $\text{Ti}_3\text{C}_2$  and  $\text{CuO}$  (Lu et al 2017). It has been reported that surface modification of  $\text{TiO}_2$  with silver and copper leads to higher photocatalytic activity under UV light (Mendez-Medrano et al. 2016).

Table 2.1 presents various  $\text{TiO}_2$  based nanocomposites and their photocatalytic applications. It shows that all the  $\text{TiO}_2$  based nanocomposites used as photocatalyst are synthesized by physical and chemical methods. The physical methods include mechanical milling, etching, laser ablation, sputtering etc (Baig et al 2021) and the chemical methods include chemical vapour deposition (CVD), solvothermal and hydrothermal synthesis, sol-gel, reverse micelle method etc. (Mekuye and Abera 2023; Nam and Luong 2019). The chemical methods available for synthesis are expensive, utilize toxic chemicals, and the processes are comparatively complex (Keat et al. 2015) with processes requiring high temperature and pressure conditions. Physical methods of synthesis are energy intensive.

In recent years, eco-friendly and green synthesis methods for the synthesis of nanoparticles has received attention (Khan and Bano 2016). The biological methods of synthesis utilizing microorganisms such as bacteria and fungi are advantageous due to low energy consumption, no use of toxic or harmful chemicals and involve ambient

conditions with simpler method of synthesis (Khan and Rizvi 2014; Mohammadlou et al. 2016).

**Table 2.1** Modified TiO<sub>2</sub> photocatalysts and their photocatalytic application

Photocatalyst	Synthesis Method	Light source	Application	References
Fe <sup>3+</sup> - doped Ag@TiO <sub>2</sub>	Chemical method (One pot synthesis)	Visible light	Methyl orange degradation; Efficiency - 56.7 % in 3 h	Wang et al. 2008
Ag@TiO <sub>2</sub>	Chemical method (One pot synthesis)	Solar light	Degradation of Acid Yellow dye; almost complete reduction in 60 min	Khanna and Shetty 2013
TiO <sub>2</sub> /SiO <sub>2</sub> /Fe <sub>3</sub> O <sub>4</sub>	Chemical method	UV light	Crude oily wastewater degradation; Efficiency – 100 % in 40 min	Peng et al. 2014
Au@TiO <sub>2</sub>	Chemical method (Sol-gel process)	UV light	Reforming of ethanol (H <sub>2</sub> production),	Goebel et al. 2014
Ag-TiO <sub>2</sub>	Chemical method	UV light	Azo dyes degradation; Efficiency – 98 –	Mirkhani et al. 2009

			100 % in 30 - 150 min	
TiO <sub>2</sub> -polyaniline (RTP) composite	Chemical method (One-pot method)	Sunlight	Direct Blue (Efficiency – 89.34 %) and Methylene Blue (Efficiency - 69.29 %) degradation	Yazhini et al. 2014
Ag-TiO <sub>2</sub>	Liquid Impregnation Method	UV light	<i>p</i> -nitrophenol (98 %), 2,4-dichlorophenol (99 %), 2,5-dichlorophenol (98 %), and 2,4,6-trichlorophenol (96 %) degradation in 1 h	Ilyas et al. 2010
Fe <sub>2</sub> O <sub>3</sub> /TiO <sub>2</sub>	Chemical method (Sol-gel method)	UV light	Methylene blue degradation	Ahmed et al. 2012
Ag <sub>2</sub> O-nanoparticle-decorated porous pure TiO <sub>2</sub> nanorods	Chemical Method (Solvothermal technique)	Visible light	Methylene blue and methyl orange degradation (88.2 % in 30 min)	Paul et al. 2016

Pani-TiO <sub>2</sub>	Chemical Method	UV & Visible light	Methyl orange (efficiency – almost complete reduction in 6 h) and 4-chlorophenol (efficiency – 30 %) degradation under visible light	Lin et al. 2012
Iron doped TiO <sub>2</sub>	Chemical Method (Sol-gel)	UV light	2,4,6-trichlorophenol degradation; Efficiency – 98 % in 180 min	Vijayan et al. 2008
Cu <sub>2</sub> O/TiO <sub>2</sub>	Physical method	Simulated solar light	Photocatalytic water splitting	Wei et al. 2019
Cu-doped TiO <sub>2</sub>	Chemical method	Visible light	Antibacterial activity and methylene blue dye degradation (efficiency – 99 % in 120 min)	Ikram et al. 2020
Cu-doped TiO <sub>2</sub>	Chemical method	UV-A	Methylene blue dye degradation (efficiency – 95.83 % in 60 min) and antimicrobial activity	Mingmongkol et al. 2022

Ag/TiO <sub>2</sub> composites	Chemical Method (Sol-gel)	UV and solar light	Oxytetracycline degradation; Efficiency – 94.1 % in 180 min	Nguyen et al. 2023
Cu–Cu <sub>2</sub> O@TiO <sub>2</sub>	Chemical method	Visible light	Methylene blue (efficiency – 95.5 % in 3 h), methyl orange and 4-nitrophenol degradation	Zhao and Liu 2020
Ag-Cu/TiO <sub>2</sub>	Chemical method	Simulated solar radiation	photocatalytic inactivation of <i>E. coli</i> and <i>S. typhimurium</i> ; Efficiency – 100 % in 10 min	Pino-Sandoval et al. 2020
Cu <sub>2</sub> O-TiO <sub>2</sub>	Chemical method	UV and visible light	Ethanol dehydrogenation	Xing et al. 2021
Ag@CuO/TiO <sub>2</sub>	Chemical method	UV and visible light	Phenol (efficiency - 100 % in 15 min under UV light) and acetic acid degradation	Mendez-Medrano et al. 2016
Cu <sub>2</sub> O/CuO-TiO <sub>2</sub>	Chemical method	Visible light	Antibiotic and dye degradation	Cosma et al. 2022

Cu-TiO <sub>2</sub>	Chemical method	UVA-LED irradiation	Gabapentin degradation; Efficiency – 100 % in 20 min	Ahmadiasl et al. 2022
Ag <sub>2</sub> O nanoparticle/TiO <sub>2</sub> nanobelt heterostructure	Chemical method	UV, visible and NIR irradiation	Methyl orange degradation; Efficiency – 87%	Wei et al. 2016
Ag/ZnO/AgO/TiO <sub>2</sub> composite	Chemical method	UV–Vis irradiation	Rhodamine B degradation; Efficiency – 99.3 % in 100 min	Bian et al. 2020
Ag <sub>2</sub> O/TiO <sub>2</sub>	Chemical method	Visible light	Methylene blue degradation; Efficiency – 48.9 %	Kerkez and Boz 2015
Ag-TiO <sub>2</sub>	Chemical method	UV light	Phthalic acid degradation	Mogal et al. 2014
Ag-doped TiO <sub>2</sub>	Chemical method (Sol-gel)	Visible light	Methylene blue degradation (efficiency – 96 % in 60 min) and antibacterial activity	Ali et al. 2018
Cu <sub>2</sub> O-TiO <sub>2</sub> nanotube arrays	Chemical method	Visible light	Methyl orange degradation;	Liao et al. 2018

			Efficiency – 91 % in 3 h	
Co <sub>3</sub> O <sub>4</sub> /TiO <sub>2</sub> /graphene oxide	Chemical method	Visible light	Oxytetracycline and Congo Red degradation; Efficiency – 91 % in 90 min	Jo et al. 2017

Although these nanocomposites show higher photocatalytic efficiency in degradation of organic chemicals, their synthesis using physical and chemical methods often are not only energy intensive, but also result in the use of solvents and release toxic chemicals that are hazardous to environment and mankind (Ai et al. 2011). Hence, there is a need to develop clean, reliable and eco-friendly process to synthesize nanoparticles and biosynthesis is one of it.

## 2.2 BIOSYNTHESIS OF NANOPARTICLES

Biosynthesis involves using an environment-friendly green chemistry-based approach that employs unicellular and multicellular biological entities (Shah et al. 2015). These entities consist of various combinations of biomolecules such as amino acids, vitamins, proteins, enzymes, and polysaccharides which have the reducing potential that are environmentally benign (Moghaddam et al. 2010). The size and geometry of nanoparticles are dependent on the synthetic route adopted for its synthesis. Using conventional methods for the synthesis requires reducing agent, and stabilizer/capping agent (for avoiding agglomeration of the newly synthesized nanoparticles. However in biological techniques, biomolecules replaced the conventional reducing and stabilizing agents (Sintubin et al. 2012).

Microbial based synthesis of nanoparticles can be classified as intracellular or extracellular biosynthesis. In intracellular synthesis, the ions and molecules are transported into the bacterial cells in the presence of enzymes (Alamri et al. 2018; Yang

et al. 2022). Due to this, the intracellular process takes a longer time for the formation of nanoparticles than the extracellular mechanism (Gemeel Abd et al. 2018) . The intracellular synthesis requires several downstream processing involving the biomass separation, disruption to break the cells and then separation of the released nanoparticles from the liquid making it more challenging (Alfryyan et al. 2022). The Extracellular synthesis is easier as the synthesis happens outside the cells and the nanoparticles produced may be easily separated and purified. The extracellular processes are cheap and involve simpler downstream processing (Das et al. 2014).The extracellular process may be carried out in the presence of cells or in the absence of cells. The extracellular synthesis in the presence of cells also involves challenges as it needs the separation of cell biomass from the nanoparticles. Several studies have been reported on the use of cell-free synthesis using either culture supernatant or cell-free extracts. In the cell free synthesis with the culture supernatant, the microorganisms are first cultured in liquid culture medium, the biomass is separated by centrifugation and the supernatant is used to synthesize the nanoparticles. In this method, the some of the enzymes and other secretory components produced by the microorganism which are present in the culture supernatant are used to synthesize the nanoparticles and they act as reducing and capping agents. In approaches using cell-free extracts, the microorganisms are resuspended in sterile distilled water after removing them from the culture medium for a required period of time. The resulting cell free extract is collected after centrifugation and is incubated with the precursor salt solution for the synthesis (Kato and Suzuki 2020). In this method, the microorganisms are subjected to repeated washings and only biomolecules released by cells due to autolysis or starvation conditions mediate synthesis of the of nanoparticles (Ali et al. 2020). The cell free synthesis processes are much simpler and do not need downstream processes for cell biomass disruption as in intracellular synthesis or separation of cell biomass from the nanoparticles as in extracellular synthesis in the presence of cells. The culture supernatants of some bacteria belonging to *Bacillus*, *Shewanella* sp., *Arthrobacter*, *Pseudomonas* and *Escherichia*, have been used for the synthesis of nanoparticles (Kumar and Mamidyala 2011; Kalishwaralal et al. 2008; Mondal et al. 2020; Shivaji et al. 2011).

In the extracellular process, microbial enzymes and proteins, other cell wall components or organic molecules present in the culture medium play a major role in the synthesis of nanoparticles. In the intracellular process, there is initial electrostatic attraction of precursor metal ions by carboxyl groups of the cell wall, which allows the passage of metal ions through the cells and the synthesis occurs inside the cells by intracellular proteins and cofactors (Siddiqi et al. 2018).

As a natural defence mechanism, microbes are able to tolerate high concentration of metal ions and convert them into metals. Nanoparticles are biosynthesized when the microorganisms grab target ions from their environment and then turn the metal ions into the element metal through enzymes generated by the cell activities (Li et al. 2011). Nanoparticles like gold (Li et al. 2018), silver (Ibrahim et al. 2019, Prema et al. 2022), titanium dioxide (Fulekar et al. 2018), platinum (Gupta and Chundawat 2019), copper oxide (Kouhkan et al. 2020, Bukhari et al. 2021), palladium (Sriramulu and Sumathi 2018), zinc oxide (Taran et al. 2018) etc synthesized by microbes are used in various applications including antibacterial, photocatalytic, cytotoxic activity, cancer therapy etc. Nanoparticles synthesis by microorganisms depends on various parameters like microbial biochemical activity, growth media, metal salt concentration, medium pH and temperature which are known to be responsible in regulating the size and morphology of the nanoparticles (Natarajan et al. 2010, Honary et al. 2012, Domany et al. 2018).

Bacteria is one of the widely used microorganism in the synthesis of nanoparticles because of easy handling, faster growth and lower cost (Hasan et al. 2007; Fulekar and Khan 2016). Ahmed et al (2018) employed electrochemically active biofilms of a single bacteria strain *Shewanella loihica* PV-4 in the synthesis of noble metals gold, platinum and palladium nanoparticles. The bacteria in the biofilms were found to produce extracellular electrons by biologically oxidizing sodium lactate (electron donor) and the electrons further reduce metal salts to produce nanoparticles.). Bunge et al. (2010) synthesized Pd(0) nanoparticles using *Cupriavidus necator*, *Pseudomonas putida*, and *Paracoccus denitrificans* and they found that the microbial surface acts as a scaffold to bind Pd (II) before reducing to Pd (0), with the surface of cell playing the

role of biological stabilizer thus preventing the agglomeration. Sinha and Khare (2011) investigated the role of *Enterobacter* sp. in bioaccumulating mercury and its ability to simultaneously synthesize intracellular mercury nanoparticles. They have found that the remediated mercury which is trapped in the form of nanoparticles is unable to vaporize back into the environment and thus possible to recover it in its nanoparticle form. Synthesis of manganese oxide nanoparticles using *Shewanella* strains were reported by Wright et al. (2016). Their studies have found that *Shewanella loihica* strain PV-4 being the strongest oxidizer was able to produce finely grained nanosized particles. Yusof et al. (2020) used both cell biomass and supernatant of *Lactobacillus plantarum* TA4 in synthesis of ZnO nanoparticles. The nanoparticles showed different morphology with cell supernatant synthesized nanoparticles showing flower like pattern and cell biomass showing an irregular shape (Yusof et al. 2020).

Due to the widespread application of Ag nanoparticles, many research groups used different bacteria in synthesis of silver nanoparticles by microbial route. Natarajan et al. (2010) reported the extracellular and intracellular synthesis of silver nanoparticles using *E. coli* culture. Maximum activity of enzymes that are involved in reduction of silver ions to produce silver nanoparticles occurs during the stationary phase of incubation. The extracellular formation of silver nanoparticles would be more expressed than intracellular formation and also it would make the process easier for downstream processing (Natarajan et al. 2010). Apart from its biocidal activity, silver nanoparticles stabilized by exopolysaccharide showed good photocatalytic activity in degradation of textile dyes (Saravanan et al. 2017). *Shewanella oneidensis* (a metal reducing agent) was used for the biosynthesis of Ag-NPs using AgNO<sub>3</sub> solution as precursor. The synthesized Ag-NPs size was less than 15 nm, with uniform dispersion, spherical shape, enhanced stability, and large surface area. Such methods used for the synthesis of Ag-NPs are highly economical and reproducible and consume lesser energy compared to the conventional methods (Suresh et al. 2010). Elbeshehy and co-workers (2015) synthesized silver nanoparticles using newly isolated strains of *Bacillus pumilus*, *B. persicus* and *Bacillus licheniformis*. Oxidation of the hydroxyl groups of extracellular peptides could be involved in the silver ion reduction and its conversion to nanoparticles formation (Elbeshehy et al. 2015). Silver nanoparticles synthesized by

a *Xanthomonas* sp. in a fermentation process was found to be effective against gram positive and gram negative bacteria due to the smaller size (Santos et al. 2016). Desai et al. (2020) synthesized Ag nanoparticles using *Pseudomonas stutzeri* and optimized the various parameters like precursor concentration, pH, reaction incubation time and temperature. Increased temperature leads to increased kinetic energy of the reaction resulting in the faster synthesis rate of nanoparticles (Desai et al. 2020). Wei et al. (2012) studied the influence of cell-free extracts of *Bacillus amyloliquefaciens*, light intensity and NaCl concentration on silver nanoparticles synthesis. The capping of negatively charged proteins present in silver nanoparticles could be responsible for its stability and high negative zeta potential (Wei et al. 2012). Ibrahim et al. (2019) demonstrated strong antibacterial activity of silver nanoparticles synthesized by an endophytic bacterium *Bacillus siamensis* strain C1 isolated from medicinal plant against rice pathogen. Rahimirad et al. (2019) synthesized Ag nanoparticles using four food pathogenic bacteria namely, *Bacillus cereus*, *E. coli*, *Staphylococcus aureus* and *Salmonella enterica subsp. enterica*. Minimum particle size of 25.62 nm and maximum zeta potential of -29.5 mV was obtained for nanoparticles synthesized using *S. e. subsp. enterica* extract. Silver nanoparticles produced using cell free supernatant of *Lactobacillus plantarum* had an average size of 40-50 nm and was effective against bacterial pathogens (Prema et al. 2022).

Extracellular oxide synthesis of TiO<sub>2</sub> and BaTiO<sub>3</sub> nanoparticles by *Lactobacillus* sp. and *Fusarium oxysporum* has also been reported in the literature (Jha et al. 2009; 2010; Bansal et al. 2005; 2006). Ordenes-Aenishanslins et al. (2014) reported the extracellular synthesis of TiO<sub>2</sub> nanoparticles using *Bacillus mycoides* and studied its application in Quantum Dot Sensitized Solar Cells. Fulekar et al. (2018) demonstrated the role of microbial consortium as well as individual rhizospheric microorganisms (*Micrococcus lylae*, *Micrococcus aloeverae* and *Cellulosimicrobium* sp.) associated with sorghum plant roots in the synthesis of TiO<sub>2</sub> nanoparticles. Presence of glucosidase enzyme in these bacterial strains acted as a bioreducing agent resulting in the formation of TiO<sub>2</sub> nanoparticles. The nanoparticles produced were pure anatase phase with particle size ~ 14 to 17 nm (Fulekar et al. 2018). Landage et al (2020) used a reproducible bacteria

*Staphylococcus aureus* for synthesizing TiO<sub>2</sub> nanoparticles with titanium tetraisopropoxide as the TiO<sub>2</sub> precursor could also facilitate the synthesis of TiO<sub>2</sub> NPs.

Two silver resistant *Morganella* species namely *M. psychrotolerans* and *M. morganii* RP42 was reported for the first time by Bansal et al. (2011) in the synthesis of Cu nanoparticles using Cu<sup>+2</sup> ions which was dark green colour and had the absorbance peak at 610 nm indicating the formation of copper nanoparticles. Kouhkan et al. (2020) reported eco-friendly approach to synthesize copper oxide nanoparticles using *Lactobacillus casei subsp. Casei*. Their study showed the interaction of carbonyl group of amino acids and peptides with the metals forms a capping leading to the stabilization of nanoparticles. Bukhari et al. (2021) reported the extracellular synthesis of copper oxide nanoparticles using *Streptomyces* sp. MHM38 after 60 min of exposure of cell free supernatant to the precursor solution with size ranging between 1.72–13.49 nm. These small sized spherical nanoparticles displayed prominent antibacterial activity against pathogenic microorganisms. CuO nanoparticles produced using bacterial strains newly isolated from an Antarctic consortium were monodispersed and well segregated with an average size of 30 nm (John et al. 2021).

Devadiga, (2016 ) synthesized silver nanoparticles using the cell free supernatant of the bacteria *Alcaligenes aquatilis* isolated by Devadiga (2016) from silver rich soil using cell free supernatant and found that the presence of NADH dependant nitrate reductase enzyme present in the bacterial supernatant were involved in the synthesis of AgNPs by reducing the Ag<sup>+</sup> ions. TiO<sub>2</sub> nanoparticles using the cell free supernatant of the bacteria *Alcaligenes aquatilis* were also synthesized by them using the cell free culture supernatant of *Alcaligenes aquatilis* and they found that hydrolytic enzymes present in the cell free supernatants were found responsible for the synthesis of TiO<sub>2</sub>-NPs.

From Table 2.2, it can be seen that microbes can be well utilized to efficiently synthesize nanoparticles. Both intracellular (John et al. 2021) and extracellular (Prema et al. 2022) synthesis of nanoparticles are reported (Natarajan et al. 2010) using different microbial source with extracellular synthesis being more predominant. In culture supernatant, protein molecules released outside the bacterial cell helps in the formation and stabilization of nanoparticles (Alsamhary, K. I. 2020). These

biosynthesized nanoparticles are found to have anti-cancerous (Mishra et al. 2011, Kouhkan et al. 2020) and antibacterial effect (Dhandapani et al. 2012, Ibrahim et al. 2019) and also include its application in degradation of dyes (Devadiga, A. 2016; Kilpady, A. 2016) and nitroaromatic compounds (Tuo et al. 2015). However the literature reports on microbial based biosynthesis of nanocomposite structures are scarce.

**Table 2.2** Nanoparticles synthesized using microbial based synthesis method

Nanoparticles	Microorganism	Location	Synthesis condition	Applications	References
SiO <sub>2</sub> , TiO <sub>2</sub>	<i>Fusarium oxysporum</i>	Intracellular	K <sub>2</sub> TiF <sub>6</sub> & K <sub>2</sub> SiF <sub>6</sub> : 10 <sup>-3</sup> M; Temp.: 27° C; duration: 24 h	—	Bansal et al. 2005
BaTiO <sub>3</sub>	<i>Fusarium oxysporum</i>	Extracellular	—	—	Bansal et al. 2006
TiO <sub>2</sub>	<i>Lactobacillus</i> sp., <i>Sachharomyces cerevisiae</i>	Intracellular	TiO(OH) <sub>2</sub> : 0.025 M	—	Jha et al. 2009
Ag	<i>Bacillus</i> sp.	Intracellular	AgNO <sub>3</sub> : 3.5 mM; temp.: 30 ° C	—	Pugazhenthiran et al. 2009

CdS	<i>Rhodopseudomonas palustris</i>	Intracellular	CdSO <sub>4</sub> : 1 mM; temp.: 30° C; duration: 72 h	—	Bai et al. 2009
Ag	<i>E. coli</i>	Intracellular & Extracellular	AgNO <sub>3</sub> : 10 <sup>-3</sup> ; duration: 24 h	—	Natarajan et al. 2010
Ag	<i>E. coli</i>	Extracellular	AgNO <sub>3</sub> : 5 mM; pH: 10; duration: 60° C	—	Gurunathan et al. 2009
TiO <sub>2</sub>	<i>Bacillus subtilis</i>	Intracellular	Ti(OH) <sub>2</sub> : 0.025M	—	Kirithi et al. 2011
Au	<i>Penicillium brevicompactum</i>	Extracellular	HAuCl <sub>4</sub> : 1 mM pH: 5-8	Cytotoxicity against cancer cells	Mishra et al. 2011
TiO <sub>2</sub>	<i>Bacillus subtilis</i>	Extracellular	Duration: 48 h	Effective against aquatic biofilm	Dhandapani et al. 2012
Pd/Fe <sub>3</sub> O <sub>4</sub> , Au/Fe <sub>3</sub> O <sub>4</sub> and	<i>Shewanella oneidensis</i> MR-1	Extracellular synthesis		Reduction of nitroaromatic compounds	

PdAu/Fe <sub>3</sub> O <sub>4</sub>		of Fe <sub>3</sub> O <sub>4</sub> followed by chemical method to load Pd or Au	Temp. : 30 ° C		Tuo et al. 2015
TiO <sub>2</sub>	<i>Alcaligenes aquatilis</i>	Extracellular	K <sub>2</sub> TiF <sub>6</sub> :10 g/L; pH: 11	Dye degradation	Devadiga, A. 2016
TiO <sub>2</sub>	<i>Staphylococcus aureus</i>	Extracellular	Ti(OH) <sub>2</sub> : 0.0025 M; duration: 12-48 h	Antibacterial & antibiofilm activity	Landage et al. 2020
TiO <sub>2</sub>	<i>Halomonas elongata</i> IBRC-M 10214	Extracellular	TiO(OH) <sub>2</sub> : 0.1 M; temp.: 37° C; duration: 96 h	Antimicrobial activity	Taran et al. 2018
Ag	<i>Bacillus cereus</i> , <i>E. coli</i> , <i>Staphylococcus aureus</i> and <i>Salmonella entericasubsp. enterica</i>	Extracellular	AgNO <sub>3</sub> : 1 mM	—	Rahimirad et al. 2019

Ag	<i>Bacillus siamensis</i> C1	Extracellular	AgNO <sub>3</sub> : 3 mM; temp.: 30° C; duration: 24 h	Antibacterial activity	Ibrahim et al. 2019
Cu/CuO	<i>Serratia</i>	Intracellular	CuSO <sub>4</sub> : 5 mM; temp.: 37° C	—	Hasan et al. 2007
CuO	<i>Lactobacillus casei subsp. Casei</i>	Intracellular	CuSO <sub>4</sub> : 1 mM; temp.: 48 h; duration: 37°C.	Anticancer and antibacterial activity	Kouhkan et al. 2020
Ag	<i>Bacillus cereus</i>	Intracellular	AgNO <sub>3</sub> : 1 mM; inoculum size: 8.7 mL; temp.: 48.5 °C; duration: 69 h; pH: 9	Methyl orange degradation	Ibrahim et al. 2021
Ag	<i>Lactobacillus plantarum</i>	Extracellular	AgNO <sub>3</sub> : 1 mM;	Antibacterial and	Prema et al. 2022

			temp.: 75° C	antioxidant activity	
Ag	<i>Bacillus</i> ROM6	Extracellu lar	pH: neutral; temp.: 30 °C; duration: 48 h.	Antibacterial activity	Esmail et al. 2022
Ag	<i>Bacillus</i> <i>subtilis</i>	Extracellu lar	AgNO <sub>3</sub> : 1 mM; temp.: 30° C, duration: 24 h	Antibacterial activity	Alsamhary (2020)
TiO <sub>2</sub>	<i>Aspergillus</i> <i>tubingensis</i> TFR-5	Extracellu lar	TiO <sub>2</sub> salt: 0.1 M; temp.: 28° C; duration: 48 h	Photosynthes is	Tarafdar et al. 2013
Copper/co pper oxide	<i>Stereum</i> <i>hirsutum</i>	Extracellu lar	CuCl, Cu(NO <sub>3</sub> ) <sub>2</sub> , and CuSO <sub>4</sub> : 5 mM; pH: 9	—	Cuevas et al. 2015
CdTe	<i>Fusarium</i> <i>oxysporum</i>	Extracellu lar	CdCl <sub>2</sub> and TeCl <sub>4</sub> :	Antibacterial activity	Syed and Ahmad 2013

			1 mM; temp.: 25– 27° C; duration: 96 h		
AgO	<i>Bacillus thuringiensis</i> SSV1	Extracellular	AgNO <sub>3</sub> : 1 mM; duration: 72 h	Antimicrobial activity	Vithiya et al. 2014
Silica-silver nanocomposite	<i>R. oryzae</i>	Extracellular	AgNO <sub>3</sub> : 5 mM; temp.: 30° C	Antimicrobial activity	Parandhama n et al. 2015
Ag <sub>2</sub> O	<i>Aspergillus terreus</i> VIT 2013.	Extracellular	AgNO <sub>3</sub> : 0.1 mM	Antibacterial activity	Sangappa and Thiagarajan 2015
Ag <sub>2</sub> O	<i>Bacillus paramycooides</i>	Extracellular	AgNO <sub>3</sub> : 1 mM; temp: 35° C	Antibacterial activity	Dharmaraj et al. 2021
CuO	<i>Marinomonas Rhodococcus Pseudomonas Brevundimonas Bacillus</i>	Intracellular	CuSO <sub>4</sub> . 5H <sub>2</sub> O: 1 mM: temp.: 22° C; duration: 24 to 48 h	Antimicrobial activity	John et al. 2021

CuO	<i>Streptomyces</i> sp. MHM38	Extracellular	CuSO <sub>4</sub> : 5 mM; pH: 8; temp.: 30° C–32° C; duration: 60 min	Antimicrobial activity	Bukhari et al. 2021
ZnO	<i>Lactococcus lactis</i> NCDO1281 (T) and <i>Bacillus</i> sp PTCC 153	Intracellular	Zn(NO <sub>3</sub> ) <sub>2</sub> . 6H <sub>2</sub> O: 0.1 M; temp.: 37° C; duration: 24 h	electrochemical determination of bisphenol A	Mahdi et al. 2021
ZnO	<i>Lactobacillus plantarum</i> TA4	Extracellular	Zn(NO <sub>3</sub> ) <sub>2</sub> . 6H <sub>2</sub> O: 500 and 100 mM; temp.: 37° C	Antibacterial activity	Yusof et al. 2020
CuO	<i>Stenotrophomonas</i> sp. BS95	Extracellular	CuSO <sub>4</sub> . 5H <sub>2</sub> O: 0.01 M	Antibacterial, antioxidant and anticancer activity	Talebian et al. 2023

Based on review of literature on biosynthesis of nanoparticles, it was found that there are very few papers on the application of microbially synthesized nanoparticles in photocatalytic degradation of dyes. Very few researchers have studied on the synthesis of TiO<sub>2</sub> by bacterial based synthesis. The reports on completely microbial based

synthesis of heterostructured nanocomposites consisting of semiconductors and metal oxides, are scarce.

### **2.2.1 Factors affecting biosynthesis of nanoparticles**

Like physical and chemical methods the size of nanoparticles in biological methods can be controlled using parameters like microorganism type, growth stage (phase) of microbial cells, growth medium, synthesis conditions, pH, substrate concentrations, source compound of target nanoparticle, temperature, reaction time etc. (Li et al. 2011).

Bai et al. (2009) investigated the role of *Rhodospseudomonas palustris*, a photosynthetic bacteria in the synthesis of cadmium sulphide nanoparticles. Their studies showed that an intracellular enzyme, cysteine desulfhydrase producing  $S^{2-}$  located in the cytoplasm was involved in the formation of CdS nanoparticles, which was later transported out of the cell by *R. palustris*. The formation and stabilization of the CdS nanoparticles in aqueous medium could be due to the biological molecules (Bai et al. 2009). According to Gurunathan et al. (2009) who synthesized silver nanoparticles, the growth phase of the culture influences the nanoparticle synthesis. They have observed maximum synthesis in stationary phase of microbial growth. Bai et al (2009) reported an increase of about 3-fold in CdS nanoparticles formation by *Rhodospseudomonas palustris* in the stationary phase compared to the late logarithmic phase. Composition of nutrient media is also important in biosynthesis of metallic and/or oxide nanoparticles (Kirthi et al. 2011). Stress sensitive membrane bound oxido-reductases and carbon source dependent oxidation–reduction potential (rH<sub>2</sub>) in the culture solution were found responsible for the synthesis of BaTiO<sub>3</sub> nanoparticles by Jha et al. (2010). Gurunathan et al. (2009) observed that nitrate medium induces the synthesis of nitrate reductase enzyme resulting in the synthesis of silver nanoparticles at a faster rate. Bansal et al. (2006) observed increase in size of BaTiO<sub>3</sub> nanoparticles from  $4 \pm 1$  nm to 4-8 nm after calcination. pH 6 was used for the synthesis of BaTiO<sub>3</sub> nanoparticles as a lower value delayed the process of transformation (Jha et al. 2010). The noble metal nanoparticles (gold, platinum and palladium) produced at pH 7 of the metal precursor solution were uniform and ultrafine with size dimension 2 - 7 nm and exhibited good catalytic activity in degradation of methyl orange dye (Ahmed et al 2018). One pot synthesis of TiO<sub>2</sub>

nanoparticles reported by Selvakumar and Suriyaraj (2014) using an extremophilic *Bacillus licheniformis* at room temperature exhibited high crystallinity with anatase phase. Formation of TiO<sub>2</sub> nanoparticles on the cell wall surface was due to the extracellular oxidase enzyme from bacteria (Selvakumar and Suriyaraj 2014). Fulekar and Khan synthesized TiO<sub>2</sub> nanoparticles using *Bacillus amyloliquefaciens* and studied its photocatalytic activity on degradation of Reactive Red 31 dye. The study revealed the presence of alpha amylase which was responsible for the synthesis of nanoparticles and its stabilization (Fulekar and Khan 2016). Glycyl-L-proline was found to be the major secondary metabolite involved in the reduction and stabilization of TiO<sub>2</sub> nanoparticles using *Aeromonas hydrophila* (Jayaseelan et al. 2013). Dhandapani et al. (2012) reported that the maximum production of TiO<sub>2</sub> nanoparticles occurred at 12 h of incubation time after the addition of potassium hexafluorotitanate to the bacterial biomass of *Bacillus subtilis* which was isolated from a rare earth element soil (Dhandapani et al. 2012). TiO<sub>2</sub> nanoparticles synthesis was maximum under optimum condition of 0.1 M TiO(OH)<sub>2</sub> concentration, incubation temperature of 37 °C and culturing time of 96 h using *Halomonas elongata* IBRC-M 10214 strain (Taran et al. 2018). Cuevas et al. (2015) reported that alkaline pH and of CuCl<sub>2</sub> concentration of 5 mM favoured the formation of copper/copper oxide nanoparticles using white rot fungus *Stereum hirsutum*. Mishra et al. (2011) found that the nanoparticles synthesized using live biomass solution of *Penicillium brevicompactum* was slower when compared to those synthesized by live cell filtrate and supernatant latter showing the better morphology. Nanoparticle formation was favoured at pH 5 -8 with different shapes like spherical, triangular and hexagonal (Mishra et al. 2011). An equal volume ratio of cell filtrate to the substrate (CuSO<sub>4</sub> solution) and 60 min of incubation time led to the formation of well-defined CuO nanoparticles synthesized using *Streptomyces* sp. MHM38 strain (Bukhari et al. 2021). Devadiga, A. (2016) has found that the precursor salt concentration, volume ratio of the cell free culture broth to the precursor salt solution and pH of the synthesis mixture play an important role in the formation of Ag and TiO<sub>2</sub> nanoparticles in extracellular cell free synthesis and these parameters influence the crystallinity, morphology, crystalline phase formed and photocatalytic antibacterial properties of the nanoparticles.

Based on the literature review, it is concluded that composition, size, shape, morphology, crystallinity characteristics, properties, activity and application potential of the nanoparticles depend on the microorganism used, method of synthesis, synthesis conditions such as precursor salts used, their concentration, synthesis mixture pH, volume ratio of cell free supernatant and precursor solution, calcination temperature and time.

### **2.3 REACTION PARAMETERS AFFECTING DEGRADATION PROCESS**

Various reaction parameters like pH of the solution, catalyst dosage, initial concentration of the pollutant greatly influences the photocatalytic degradation process. Shi et al. (2022) observed high photocatalytic activity of Magnetic graphene oxide(MGO)/peroxymonosulfate (PMS) in degradation of Coomassie brilliant blue G250 at pH 9.4 and on further increase in the pH to 11, resulted in decrease in dye degradation due to repulsive forces between MGO and (PMS) at pH > 9.4. Kumar et al (2016) studied the effect of pH on degradation of methylene blue using Ag/TiO<sub>2</sub>@polypyrrole under UV and visible light where the degradation increased from pH 3 to 9 with maximum degradation at pH 9 which is attributed to the electrostatic interaction of negative surface charge of the catalyst and the positive MB ions. Acidic pH tends to decrease the degradation due to the positive charge of the catalyst acquired through protonation in acidic medium and the positive MB ions. Therefore pH plays a major role in the interaction of the catalyst surface and the dye molecules further affecting the degradation rate.

Initial dye concentration is also an important parameter influencing the adsorption process in degradation studies as it can increase or reduce the availability of binding sites on the surface of adsorbent (Rapo and Tonk 2021). Saruchi et al. (2019) have found the increase in adsorption capacity of CuO nanoparticles from 21.56 to 98.1 mg/g with the increase in methylene blue dye concentration from 100 - 500 mg/L which also implies that dye uptake increases with concentration until equilibrium is attained beyond which there is lack of space for the absorption to occur. Kumar et al. (2016) have reported that the degradation of methylene blue dye decreased from 99.62 % to 83.9 % on increasing the concentration of dye from 4 – 20 mg/L due to the surface

coverage of the Ag/TiO<sub>2</sub>@polypyrrole catalyst with the dye molecules suppressing the production of hydroxyl radicals and also due to the decrease in light penetration with the increase in the dye concentration (Kumar et al. 2016). Catalyst dosage also influence the degradation efficiency, as reported by Kgatle et al. (2021) where the increase in Fe/Cu/Ag catalyst dosage favoured the degradation rate of methyl orange dye with higher degradation obtained at 10 mg of catalyst dosage for 10 mg/L of initial concentration of dye. According to Narasaiah et al. (2022) as the catalyst dose increases more free radicals are generated leading to higher degradation rate. They varied the TiO<sub>2</sub> dosage of 10, 20 and 30 mg with the initial concentration of 10 ppm of rhodamine B and methylene blue and found that the degradation of both the dyes increased with increased catalyst dosage. The enhancement in degradation could be due to the more number of active sites available for adsorption which results in higher degradation (Kgatle et al. 2021), however higher than optimum amount leads to turbidity of the solution preventing the absorption of light ultimately reducing the degradation rate (Sheydaei et al. 2019).

Several of these studies has focused on the application of these efficient photocatalysts on degradation of dyes with single dye component, however textile industry releases mixture of dyes into the aquatic body, therefore studying the effect of one dye on the other in mixed condition is highly necessary. Ammari et al. (2020) investigated the photocatalytic activity of the TiO<sub>2</sub> in the degradation of the binary dyes (methyl orange and methylene blue) in the mixture as well as individually under UV light and studied the influence of reaction conditions such as initial concentration, pH etc. and found that the degradation of methylene blue is greatly affected by the presence of methyl orange than vice-versa. Another study conducted by Sanni and group (2020) found that the titania dispersed on dealuminated clinoptilolite exhibited excellent photocatalytic activity in degradation of methylene blue and methyl orange in mixed condition in the presence of UV light. ZnS quantum dots was used in the photocatalytic degradation of brilliant green, rhodamine B and binary mixture of the same with optimal catalyst loading of 1 mg/ and showed significant reduction of dyes in individual and in mixtures (Ajibade and Oluwalana 2021). Zinc oxide nanoparticles synthesized using purple tea leaf extract had the ability to degrade Malachite green and Rhodamine B under visible

light with higher reduction obtained for their mixture than single dye solutions (Das et al. 2021). Chemically synthesized Ag@ TiO<sub>2</sub> nanoparticles were found to effectively degrade dyes such as Acid Yellow -17 and RB 220 dye under both UV and solar light with highest degradation seen under sunlight (Khanna and Shetty 2014).

## **2.4 RESEARCH GAPS, SCOPE AND OBJECTIVES OF THE RESEARCH WORK**

The review of literature suggested that the conventional methods of treatment of dye contaminated effluents from industries are not adequate as they do not lead to mineralization of the dyes. Heterogeneous photocatalysis using  $\text{TiO}_2$  is gaining interest as it leads to mineralization of dyes. But its wide band-gap restricts its utilization under visible light, which can however be resolved by applying strategies like doping, coupling or capping of  $\text{TiO}_2$ . (Gupta et al. 2011). Core-shell and composite structures are found to enhance the photocatalytic activity of  $\text{TiO}_2$  in visible light.  $\text{TiO}_2$  modified with other semiconductors or metal/metal oxides exhibit visible light activity and prevent electron-hole recombination effectively, thus enhancing the photocatalytic activity. Such nanostructured materials can harness solar energy making the photocatalytic treatment economical and energy efficient.

Ag based  $\text{TiO}_2$  nanocomposite was found to be effective as a photocatalyst under visible light (Liu et al. 2019). Ag based  $\text{TiO}_2$  nanocomposites therefore shows great promise as a photocatalytic material due to their photoreactivity and visible light response (Wei et al. 2016). Ag based  $\text{TiO}_2$  nanomaterials have been reported to exhibit solar (Nguyen et al. 2023) or visible (Paul et al. 2016) light mediated photocatalytic activity. The presence of copper oxides in  $\text{TiO}_2$  nanocomposites have been found to improve the photocatalytic activity in degradation of pollutants under visible light (Lu et al. 2019; Bopape et al. 2023). Recent studies report the evaluation of ternary composite structures where  $\text{TiO}_2$  is modified with bimetallic nanoparticles exhibiting photocatalytic applications (Pino-Sandoval et al. 2020, Mendez-Medrano et al. 2016). Ag-Cu/ $\text{TiO}_2$  photocatalyst synthesized by Pino-Sandoval et al. (2020) and Ag@CuO/ $\text{TiO}_2$  nanocomposites synthesized by Mendez-Medrano et al. (2016) have been reported to exhibit reduced band-gap energy and superior photocatalytic activity under visible and solar light. These modified  $\text{TiO}_2$  nanostructures with Ag and Cu or their oxides have been found to be efficient photocatalyst in water treatment processes. However, the literature reports restrict to the nanocomposite materials synthesized by chemical or physical routes.

The chemical and physical methods of synthesis of nanoparticles use toxic chemicals and are energy intensive. This creates a need to develop a greener method which is simpler, which can be carried out under ambient conditions, environmental friendly and cost-effective. Therefore researchers have focused on biological synthesis of nanoparticles by exploiting the living organisms (Pugazhenthiran et al. 2009). Many studies have been reported in the literature with the microbial synthesis of Ag, TiO<sub>2</sub> or CuO nanoparticles individually which were majorly used for antibacterial applications. There are very few literature reports on the application of microbially synthesized nanoparticles for photocatalytic applications.

To the best of our knowledge, the microbial synthesis of nanocomposites have been reported very scarcely and there is no study reported on the synthesis of silver based titanium nanocomposites and their modification with Cu using microbial-mediated approach. It was hypothesized that by suitably developing a method of microbial based synthesis, visible light active silver based titanium nanocomposites and their modification with Cu may be synthesized. Further, the synthesis parameters may be optimized in order to obtain the best photocatalytic activity.

*Alcaligenes aquatilis*, a bacteria isolated from Ag laden environment has been found to be able to independently synthesize Ag and TiO<sub>2</sub> nanoparticles extracellularly by using the cell free supernatant (Devadiga, 2016). It was hypothesized that the method for the synthesis of individual nanoparticles may be suitably modified to prepare Ag based TiO<sub>2</sub> composite nanostructures and their modification with Cu, possessing good photocatalytic activity under solar/visible light. Therefore in the present study microbial based extracellular synthesis of Ag based TiO<sub>2</sub> nanocomposite and Ag based TiO<sub>2</sub> nanocomposite modified with Cu using the cell free culture supernatant of *Alcaligenes aquatilis* at room temperature is investigated in terms of degradation of two of the widely used textile azo dyes, viz Reactive blue 220 and Acid yellow 17 under visible and solar irradiation. Based on the extensive review of literature and the gaps identified thereof, the following objectives are proposed for the current research work.

## **OBJECTIVES OF THE RESEARCH WORK**

The main objective is to biologically synthesize Ag based TiO<sub>2</sub> nanocomposite and Ag based TiO<sub>2</sub> modified with Cu nanocomposite structures using *Alcaligenes aquatilis* for their application in photocatalytic degradation of dyes under visible and solar light irradiation.

### **The specific objectives are**

- To biologically synthesize Ag based TiO<sub>2</sub> nanocomposite structures by different methods and to select a method yielding nanocomposite structures with the best photocatalytic activity in terms of RB 220 dye degradation under visible light irradiation.
- To characterize the biosynthesized nanocomposite structures
- To study the effect of synthesis parameters like molar ratio of silver to titanium used in the synthesis process, pH of culture supernatant and synthesis time (time after the addition of precursors) on the photocatalytic degradation efficacy of these nanocomposite structures under visible light irradiation.
- To study the effect of initial dye solution pH, catalyst loading and initial dye concentration on the photocatalytic degradation of dye by these Ag based TiO<sub>2</sub> nanocomposite structures under visible light irradiation.
- To synthesize Ag based TiO<sub>2</sub> nanocomposite modified with Cu and to optimize the Ag:Ti:Cu ratio and calcination temperatures to maximize the degradation of RB 220 dye.
- To study the photocatalytic degradation of AY 17 dye using Ag based TiO<sub>2</sub> nanocomposite and Ag based TiO<sub>2</sub> modified with Cu nanocomposite structures under visible light irradiation and solar light irradiation.
- To study the effect of the presence of other dyes and its influence on the photocatalytic degradation of RB 220 dye using biosynthesized Ag based TiO<sub>2</sub> nanocomposite modified with Cu under visible light irradiation.
- To study the pathway of degradation and to propose a possible mechanism of dye degradation.

## CHAPTER 3

### MATERIALS AND METHODS

This chapter presents the materials used in this study and the methods adopted to fulfil the stated objectives.

#### 3.1 MATERIALS

The bacterial strain used in the present study was *Alcaligenes aquatilis* (GenBank Accession ID KP772325), which was earlier isolated by our Research Group (Aishwarya Devadiga 2016) from the dust on silver smith's work bench. Nutrient Agar and Nutrient broth for culturing of microorganism was purchased from HiMedia, Mumbai, India. Potassium hexafluorotitanate ( $K_2TiF_6$ ) and silver nitrate ( $AgNO_3$ , 99 % purity) was purchased from Sigma Aldrich and cupric sulphate pentahydrate ( $CuSO_4 \cdot 5H_2O$ , 98.5 %), was procured from Loba Chemie Pvt. Ltd. Mumbai, India. Reactive Blue 220 (RB 220) dye was procured from Indian Fine Chemicals Pvt Ltd, Bangalore, India and Acid Yellow 17 (AY-17) dye of 60 % purity was obtained from Sigma Aldrich Chemicals Pvt.Ltd., Bangalore, India. All the chemicals were used as received. Deionized water was used for all the experiments. The chemical structure of RB 220 and AY 17 are presented in Fig.3.1.

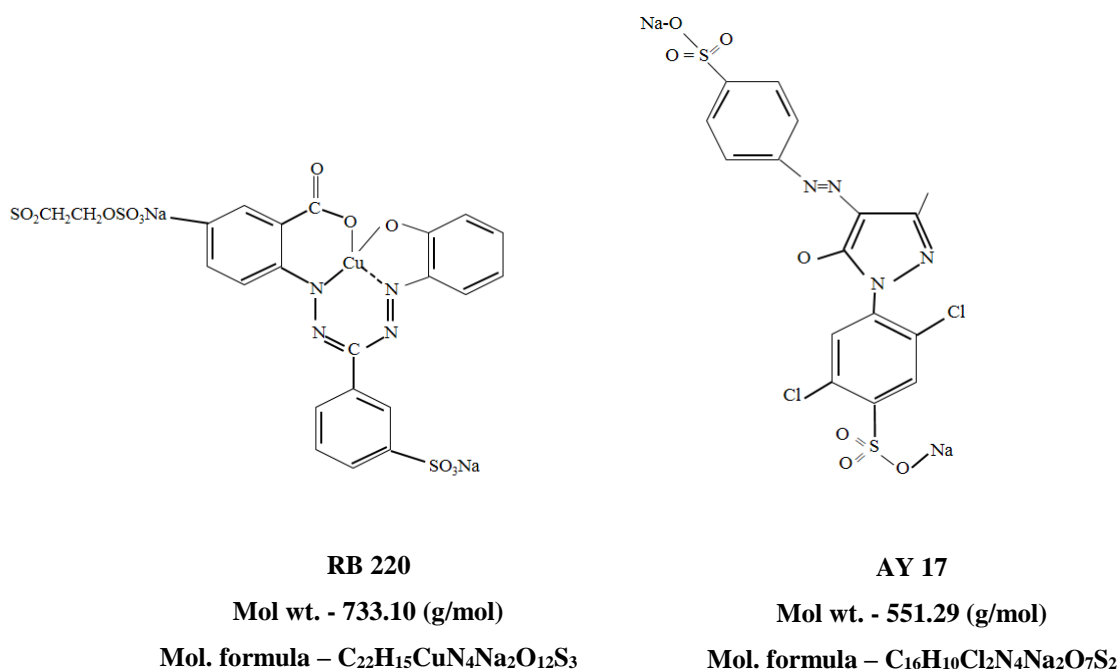


**Fig. 3.1.** Chemical structure of RB 220 (Boduroglu et al. 2014) and AY 17 (<https://pubchem.ncbi.nlm.nih.gov/compound/C.I.-Acid-Yellow-17-disodium-salt>) dye

### 3.2 PREPARATION OF CELL FREE SUPERNATANT (CFS)

A single colony of the bacteria *Alcaligenes aquatilis* was inoculated into a 250 mL conical flask containing 100 mL of sterile nutrient broth. This flask was incubated for 24 h at 28±2°C and 120 rpm in an incubatory shaker. 1 mL from this culture was added to 100 mL sterile nutrient broth and incubated for 24 h at 28±2°C and 120 rpm. The CFS was separated from the biomass by centrifuging the culture at 10000 rpm for 5 min at 4°C and the so obtained supernatant was stored at 4°C until further use. The pH of the CFS was adjusted to a desired value by using 0.1 N NaOH or 0.1 N HCl before the synthesis of nanocomposites.

### 3.3. BIOSYNTHESIS OF Ag BASED TiO<sub>2</sub> NANOCOMPOSITES

Ag-based TiO<sub>2</sub> nanocomposites were synthesized from cell free supernatant of *Alcaligenes aquatilis* bacteria using the following three methods

- Method A – Two-step method
- Method B – One pot synthesis method with consecutive addition of precursors with time gap between the additions
- Method C – One pot synthesis method with simultaneous addition of precursors

### 3.3.1. Method A: (Two step method)

50 mL of 100 mM of silver nitrate solution (precursor for silver oxide) was added to 50 mL of CFS (pH 11) of *Alcaligenes aquatilis* and maintained at 120 rpm for 24 h at  $28\pm 2^\circ\text{C}$  following which the synthesis mixture was centrifuged and the pellet of nanoparticles was washed with distilled water. The pellet of synthesized nanoparticles was added to 50 mL supernatant (CFS pH 11) followed by the addition of 2 g of  $\text{K}_2\text{TiF}_6$  salt as the precursor for  $\text{TiO}_2$ , maintained at room temperature for 24 h at 120 rpm, to obtain Ag to Ti molar ratio of 1:1.6. The synthesis mixture was then centrifuged, washed with distilled water and then dried in hot air oven at  $100^\circ\text{C}$ . The dried nanoparticles were ground in a mortar and pestle and stored in a desiccator till further use. Fig. 3.2 shows the schematic representation of the Method A for the synthesis of nanocomposites.

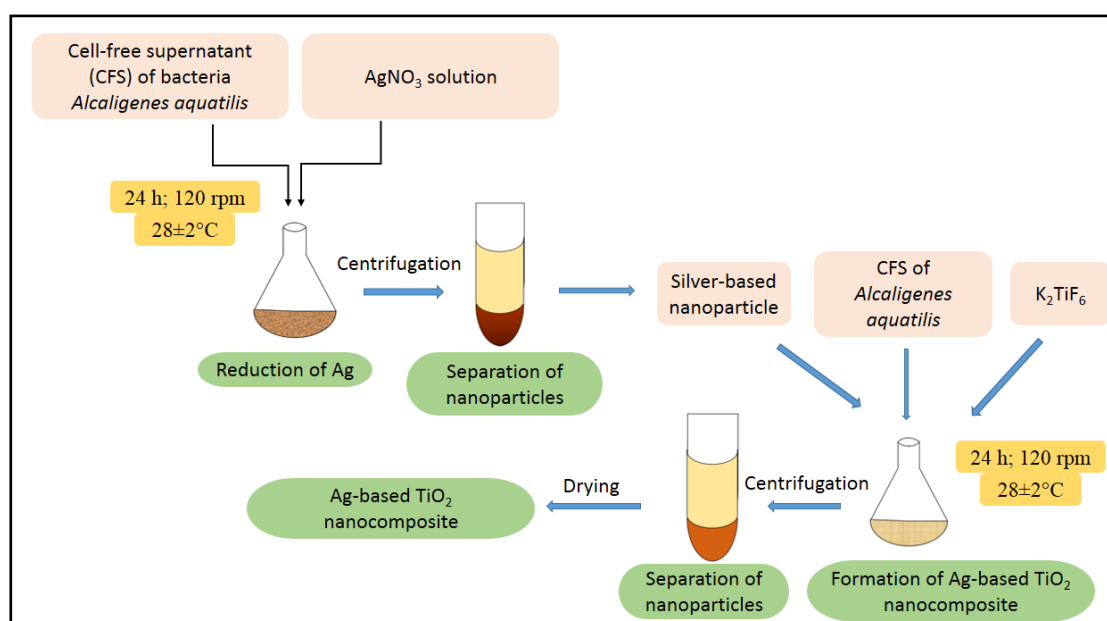


**Fig. 3.2** Schematic representation of Method A for synthesis of the nanocomposites.

### 3.3.2. Method B (One pot synthesis method with consecutive addition of precursors with time gap between the additions):

To 50 mL of 100 mM silver nitrate solution, equal volume of clear CFS (pH 11) was added and kept for reaction at 120 rpm at ambient temperature of  $28\pm 2^\circ\text{C}$ . After 24 h, 2 g of  $\text{K}_2\text{TiF}_6$  salt was added to the same reaction mixture and it was maintained at ambient temperature of  $28\pm 2^\circ\text{C}$  for 24 h at 120 rpm. The resulting mixture was centrifuged, the pellet was washed with distilled water and then dried in hot air oven at  $100^\circ\text{C}$ . The dried nanoparticles were ground in a mortar and pestle and stored in a desiccator till further use. The Ag to Ti molar ratio used in the synthesis process is 1:1.6. Fig. 3.3 shows the schematic representation of Method B for synthesis of the nanocomposites.

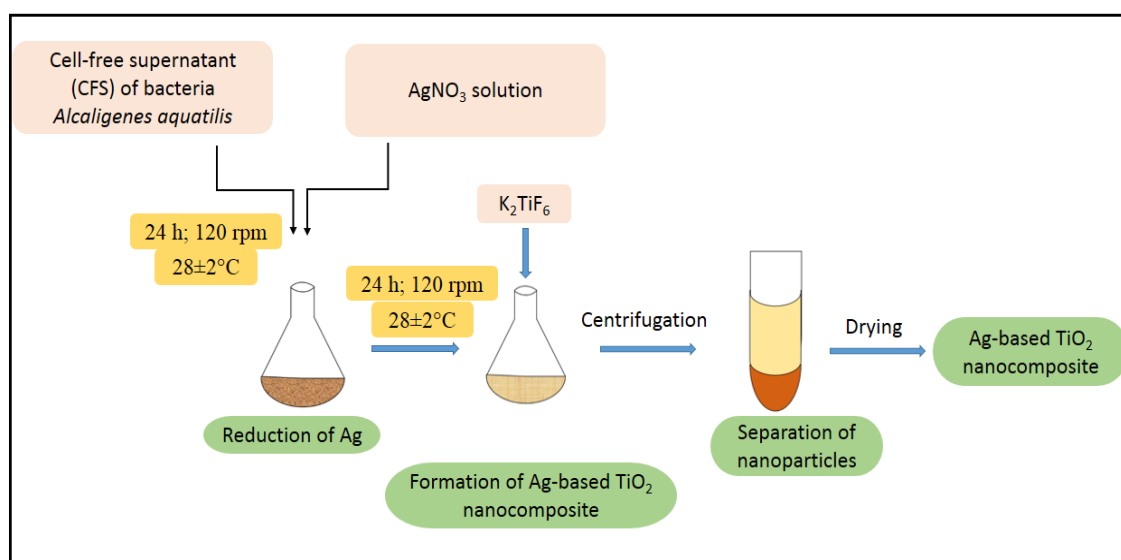


**Fig. 3.3** Schematic representation of Method B for synthesis of the nanocomposites

### 3.3.3. Method C (One pot synthesis method with simultaneous addition of precursors)

To 50 mL of CFS solution (pH 11), 100 mM of 50 mL silver nitrate solution and 2 g of  $\text{K}_2\text{TiF}_6$  salt were added. The reaction mixture was maintained at room temperature of  $28\pm 2^\circ\text{C}$  for 24 h at 120 rpm following which the solution was centrifuged and dried as

explained in Method A. Fig. 3.4 shows the schematic representation of Method C for synthesis of the nanocomposites.

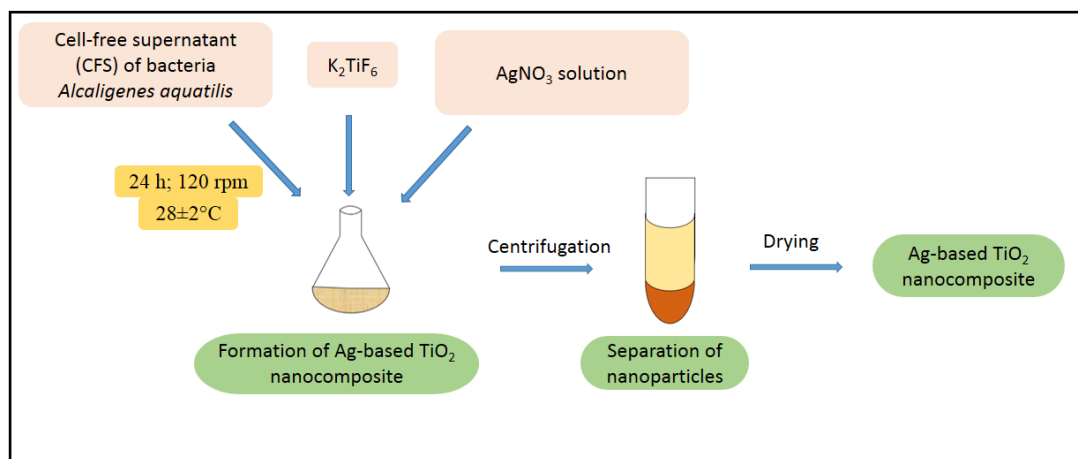


**Fig. 3.4** Schematic representation of Method C for synthesis of the nanocomposites

### 3.4. Choice of method of synthesis

Ag-based TiO<sub>2</sub> nanocomposites synthesized by Method A, Method B and Method C were tested for their photocatalytic activity in the degradation of 100 ppm RB 220 dye by conducting batch experiments as described in Section 3.8 under visible light irradiation. The method of synthesis was chosen based on the maximum photocatalytic activity in terms of degradation of RB 220 dye.

### 3.5. Optimization of synthesis parameters for Ag-based TiO<sub>2</sub> nanocomposites

Further the synthesis parameters in Method A were varied to maximize the degradation of RB 220 dye. The parameters like pH of the CFS used in the synthesis, molar ratio of Ag to Ti used in the synthesis process and the reaction time in the Step 1 (reaction time after the addition of Ag precursor,  $t_{\text{step 1}}$ ) and Step 2 (reaction time after the addition of K<sub>2</sub>TiF<sub>6</sub> salt,  $t_{\text{step 2}}$ ) were varied for the synthesis. The nanocomposites thus synthesized were used as photocatalysts in the degradation of RB 220 under visible light irradiation. The synthesis parameters which yielded the maximum dye degradation were chosen as the optimum.

### **3.5.1 Optimization of molar ratio of Ag to Ti**

The synthesis of Ag-based TiO<sub>2</sub> nanocomposites was carried out by Method A as described in Section 3.3.1, by keeping all the parameters constant (CFS pH 11 and reaction time of 24 h each in both the steps) and by varying the amount of K<sub>2</sub>TiF<sub>6</sub> salt added in Step 2 as 0.5 g, 1.0 g, 1.5 g, 2 g and 2.5 g to obtain the molar ratio of Ag to Ti in the synthesis process as 1:0.4, 1:0.8, 1:1.2, 1:1.6 and 1:2.0 respectively. Dye degradation studies were carried out with 100 ppm RB 220 with the synthesized nanocomposites as the catalyst at loading of 0.1 g/L under visible light irradiation with constant stirring for 90 min. The molar ratio that yielded nanocomposite which resulted in maximum degradation of the dye was selected as the optimum.

### **3.5.2 Optimization of pH of cell free supernatant**

As described in section 3.3.1, nanocomposites were synthesized by Method A by keeping all the parameters constant (optimum Ag to Ti molar ratio of 1:1.6; and reaction time of 24 h each in both the steps) but by varying the CFS pH from 5 to 13. The pH of cell free supernatant was adjusted using 0.1 N H<sub>2</sub>SO<sub>4</sub> or 0.1 N NaOH. Dye degradation studies were carried out with 100 ppm RB 220 with the synthesized nanocomposites as the catalyst at loading of 0.1 g/L under visible light irradiation with constant stirring for 90 min. The pH of the CFS that yielded the nanocomposite which resulted in maximum degradation of the dye was selected as the optimum.

### **3.5.3 Optimization of reaction time after the addition of Ag precursor, $t_{\text{step 1}}$ and after the addition of K<sub>2</sub>TiF<sub>6</sub> salt, $t_{\text{step 2}}$**

Based on the above optimized condition of Ag to Ti molar ratio and pH of CFS, studies were performed to find out the suitable reaction time for the synthesis. The nanocomposites were synthesized by Method A by keeping all the parameters constant (optimum Ag to Ti molar ratio of 1:1.6; optimum pH of CFS 7). The synthesis time after the addition of silver nitrate was varied between 2 - 24 h with 24 h synthesis time kept constant after the addition of K<sub>2</sub>TiF<sub>6</sub>. Dye degradation studies were carried out with 100 ppm RB-220 with the synthesized nanocomposites as the catalyst at loading of 0.1 g/L under visible light irradiation with constant stirring for 90 min. The optimum  $t_{\text{step 1}}$  was selected based on the maximum dye degradation. Further the nanocomposites

were synthesized by Method A by keeping all the parameters constant (optimum Ag to Ti molar ratio of 1:1.6; optimum pH of CFS pH 7 and optimum  $t_{\text{step 1}}$  of 4 h) and varying the synthesis time after the addition of  $\text{K}_2\text{TiF}_6$  ( $t_{\text{step 2}}$ ) as 2, 4, 8, 16 and 24 h. The optimum  $t_{\text{step 2}}$  was selected based on the maximum dye degradation.

### **3.6. BIOSYNTHESIS OF $\text{TiO}_2$ (BIO- $\text{TiO}_2$ ) AND $\text{AgO}/\text{Ag}_2\text{O}$ NANOPARTICLES**

Bio- $\text{TiO}_2$  nanoparticles were biologically synthesized by adding 2 g of  $\text{K}_2\text{TiF}_6$  into 50 mL of CFS (at pH7) and carrying out the synthesis for 4 h at room temperature of  $28\pm 2^\circ\text{C}$  at 120 rpm. The colloidal suspension was then centrifuged, pellets were washed with distilled water and then dried in hot air oven at  $100^\circ\text{C}$ . The dried nanoparticles were ground in a mortar and pestle and stored in a desiccator till further use.

$\text{AgO}/\text{Ag}_2\text{O}$  nanoparticles were biologically synthesized by adding 50 mL of 100 mM silver nitrate solution to 50 mL of CFS (at pH 7) and stirring at 120 rpm for 4 h at room temperature of  $28\pm 2^\circ\text{C}$  for the reduction of silver nitrate to form the nanoparticles.

### **3.7. SYNTHESIS OF Ag BASED $\text{TiO}_2$ MODIFIED WITH Cu NANOCOMPOSITES (ATC) WITH OPTIMIZATION OF SYNTHESIS AND CALCINATION CONDITIONS**

The synthesis of Ag based  $\text{TiO}_2$  modified with Cu nanocomposites (ATC) is a three step method. In this method Ag based  $\text{TiO}_2$  nanocomposite was synthesized by a Two-step method (Method A) under optimized condition of Ag:Ti molar ratio of 1:1.6, synthesis pH of 7 and total time of 8 h with 4 h in each step as follows: 50 mL of 100 mM of silver nitrate solution was added to 50 mL of CFS (pH 7) of *Alcaligenes aquatilis* and maintained at 120 rpm for 4 h at  $28\pm 2^\circ\text{C}$  following which the solution was centrifuged and the pellet of nanoparticles was washed with distilled water. The pellet of synthesized nanoparticles was added to 50 mL CFS followed by the addition of 2 g of  $\text{K}_2\text{TiF}_6$  salt, as the precursor for  $\text{TiO}_2$  maintained at room temperature for 4 h at 120 rpm, to obtain Ag to Ti molar ratio of 1:1.6. The reaction mixture was then centrifuged, pellet was washed with distilled water and further suspended in 50 mL CFS (pH 7) and desired amount of Cu precursor ( $\text{CuSO}_4 \cdot 5\text{H}_2\text{O}$ ) was added to this CFS mixture in the third step and incubated for 4 h at 120 rpm at room temperature of

28±2°C. The amount of CuSO<sub>4</sub>. 5H<sub>2</sub>O was varied as desired. The amount of CuSO<sub>4</sub>. 5H<sub>2</sub>O added was calculated to achieve desired Cu concentration in the synthesis mixture. The amount of CuSO<sub>4</sub>. 5H<sub>2</sub>O added, Cu concentration in the synthesis mixture and the corresponding molar ratio of Ag:Ti:Cu in the synthesis process are presented in Table 3.1. The pellets were separated by centrifugation. The nanoparticles thus obtained were washed with distilled water and dried at 100°C for 3 h. The dried nanoparticles were then calcined for 3 h at 400°C or any other temperature as desired for the experiments and used for further experiments. Fig. 3.5 shows the schematic representation of the synthesis process of Ag based TiO<sub>2</sub> modified with Cu nanocomposites (ATC) using the three step method.

**Table 3.1** Optimization of molar ratio of Ag:Ti:Cu

<b>Designation for Ag based TiO<sub>2</sub> modified with Cu nanocomposites</b>	<b>Amount of Cu precursor (CuSO<sub>4</sub>. 5H<sub>2</sub>O) added per 50 mL of CFS (g)</b>	<b>Concentration of Cu (mM)</b>	<b>Ag:Ti:Cu</b>
ATC-25	0.312	25	1:1.6:0.23
ATC-50	0.625	50	1:1.6:0.46
ATC-75	0.937	75	1:1.6:0.7
ATC-100	1.25	100	1:1.6:0.92

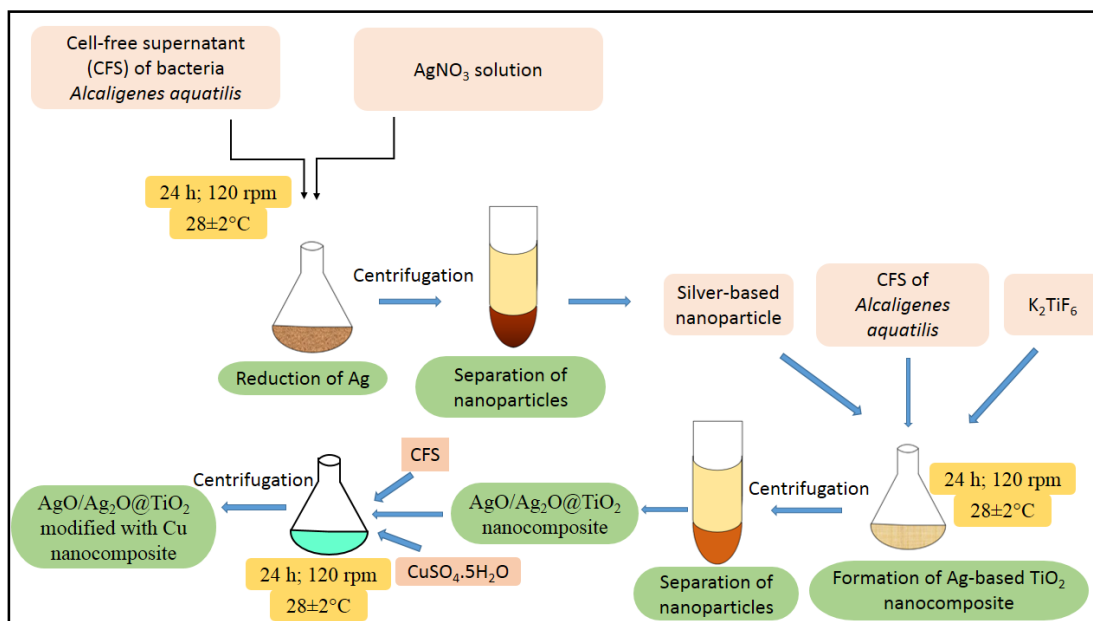


**Fig. 3.5** Schematic representation of the synthesis process for Ag based TiO<sub>2</sub> modified with Cu nanocomposite (ATC)

The synthesis of silver oxide modified with Cu (AC) nanoparticles were performed under similar conditions using Two-step method, by adding 50 mL of 100 mM silver nitrate solution to 50 mL CFS (at pH 7) and followed by incubation at 28±2°C for 4 h at 120 rpm. The pellet (silver oxide nanoparticles) which was obtained after 4 h synthesis was then suspended in 50 mL CFS (pH 7) which is followed by the addition of 0.937 g (optimum) of Cu precursor (CuSO<sub>4</sub>·5H<sub>2</sub>O). The synthesis mixture was then kept under shaking condition at 120 rpm for 4 h at 28±2°C. The synthesis mixture was centrifuged, pellets were washed, dried and calcined at 400°C for 3 h in a muffle furnace.

TiO<sub>2</sub> modified with Cu (TC) nanoparticles were synthesized using Method A, wherein 2 g of K<sub>2</sub>TiF<sub>6</sub> was added to 50 mL of CFS (at pH 7) and incubated at 28±2°C for 4 h at 120 rpm, following which the pellet was separated. The TiO<sub>2</sub> pellets were suspended in 50 mL CFS (at pH 7). To this mixture, of 0.937 g (optimum) of Cu precursor (CuSO<sub>4</sub>·5H<sub>2</sub>O) was added and incubated for 4 h as described in Section 3.7. The synthesis mixture was centrifuged, pellets were washed and dried. The dried nanoparticles were then calcined at 400°C for 3 h and stored in desiccator until further use. Further, the

(silver oxide modified with Cu and TiO<sub>2</sub> modified with Cu) nanocomposites obtained were studied for their photocatalytic activity in the degradation of RB 220 dye with initial concentration of 100 ppm, dye pH 3 and catalyst loading of 1 g/L under visible light.

The dye degradation experiments were conducted with nanocomposites synthesized with various Ag:Ti:Cu ratio and calcined at 400°C. The degradation studies were conducted with initial dye concentration of 100 ppm of RB 220 dye at pH 3 and catalyst loading of 1 g/l for 90 min under visible light irradiation. The optimum ratio of Ag:Ti:Cu was chosen based on the maximum photocatalytic activity in terms of RB 220 degradation. Further, the Ag based TiO<sub>2</sub> modified with Cu nanocomposites synthesized with Ag:Ti:Cu molar ratio of 1:1.6:0.7 (optimum molar ratio) and calcined at temperatures of 350, 400, 450 and 500° C were assessed for their photocatalytic activity and the optimum calcination temperature was chosen based on the maximum photocatalytic activity in terms of RB 220 degradation.

### **3.8 PHOTOCATALYTIC DEGRADATION STUDIES ON RB 220 AND AY 17 USING THE BIOSYNTHESIZED NANOPARTICLES AS CATALYST UNDER VISIBLE LIGHT**

Photocatalytic activity of the biosynthesized nanoparticles was studied in an annular reactor which consisted of a double walled glass immersion well having inlet and outlet tubes for water circulation for cooling. This immersion well was placed inside a borosilicate cylindrical reaction flask containing the dye solution. The reaction flask has provisions for supply of air and for sample withdrawal as shown in the Fig. 3.6. The reaction flask contained 100 mL volume of the dye (RB 220 or AY 17 or the mixture as desired) solution in water at desired concentrations with desired catalyst loading and pH. The pH of the reaction mixture was adjusted to a desired value using 0.1 N NaOH or HCl. The mixture was stirred constantly with magnetic stirrer and an air flow of 1 LPM was provided. 125W White lamp (SAIC, Chennai, India) was placed inside the immersion well and water was continuously circulated through the jacket around the immersion well. The entire reactor set up was placed inside an aluminium chamber. The degradation study was carried out for a desired period of irradiation and

the samples were withdrawn at regular time intervals and centrifuged at 15000 rpm for 15 min to separate the nanoparticles. The absorbance of the clear solution was recorded using UV-Visible spectrophotometer (model: U-2000, Hitachi) at 609 nm for RB 220 and 418 nm for AY 17 dye and the concentration of dyes was determined from the calibration plot. Percentage degradation of dye was calculated using the formula,

$$\% \text{ Degradation} = \left( \frac{C_0 - C}{C_0} \right) \times 100 \quad (1)$$

where  $C_0$  is the initial dye concentration and  $C$  is the dye concentration in the reactor at a particular time.

To study the effect of pH, the degradation studies were conducted by varying the initial pH of the solution from pH 3 to 11 with 0.1 g/L catalyst loading (Ag-based TiO<sub>2</sub> nanocomposites) with 100 ppm RB 220 dye. To study the effect of catalyst loading, experiments were conducted under optimum pH condition and the catalyst loading (Ag-based TiO<sub>2</sub> nanocomposites) was varied 0.005 g/L – 2 g/L with 100 ppm RB 220 dye. The optimum solution pH and catalyst loading were chosen based on maximum degradation of the dye. Effect of initial dye concentration was studied with optimum pH and catalyst loading (Ag-based TiO<sub>2</sub> nanocomposites) for different RB 220 dye concentrations of 100, 200, 300, 400 and 500 ppm for 90 min under visible light.

The studies on degradation of dyes in mixed dye solutions of RB 220 and AY 17 were carried out with different initial concentrations (50-200 ppm) of each of the dyes in mixture using Ag-based TiO<sub>2</sub> modified with Cu nanocomposites (ATC-75) at dye pH 3 and catalyst loading of 1 g/L under visible light irradiation for 5 h.

Reusability studies were conducted upto 3 cycles with 100 ppm of RB 220 dye at pH 3 and catalyst loading of 1 g/L using the optimized Ag-based TiO<sub>2</sub> modified with Cu nanocomposites (ATC-75) under visible light irradiation for 90 min. The nanoparticles used in the first cycle of photocatalytic dye degradation studies were separated by centrifugation and washed with water to remove any dye molecules attached to the surface. The nanoparticles were then dried and used for the subsequent cycles.

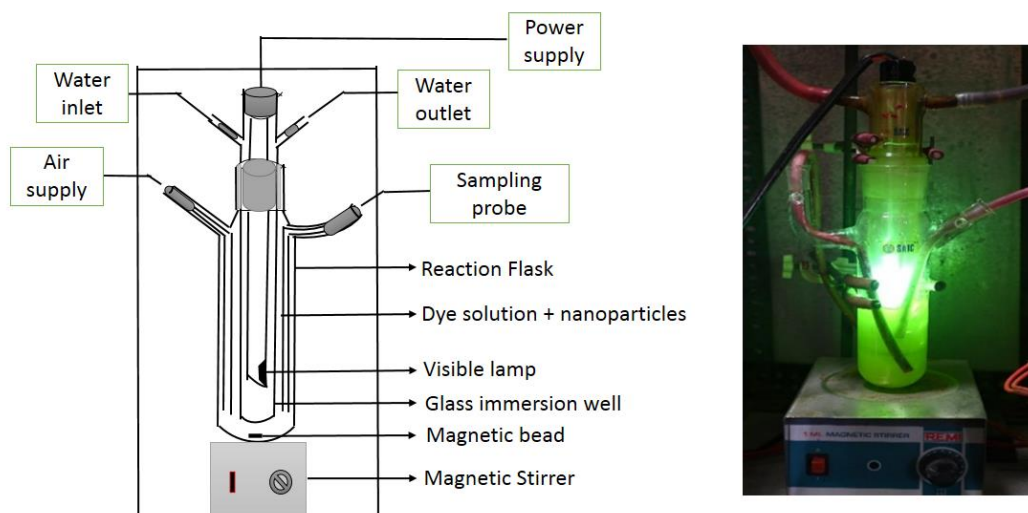


**Fig. 3.6** (Left) Schematic diagram of the annular glass photoreactor and  
(Right) Photographic image of the reactor

### **3.9. PHOTOCATALYTIC DEGRADATION STUDIES OF RB 220 AND AY-17 DYE USING BIOSYNTHESIZED NANOCOMPOSITE UNDER SOLAR LIGHT**

Solar photocatalytic experiments were conducted in an open terrace between 11 AM to 12.30 PM with 100 ppm dye solution (RB 220 or AY 17) at pH 3 and catalyst loading of 1 g/L using the synthesized nanocomposites as a catalyst under constant stirring for 90 min. No additional air supply was provided, as atmospheric air served as a source for supply of oxygen. The schematic representation of the set-up is shown in Fig. 3.7. The light intensity of solar light was measured using LUX meter and it was found to be 900\*100 lux. Samples were withdrawn at regular time intervals and the concentration of dyes was determined by spectrophotometric analysis and the percentage dye degradation was calculated using equation (1).

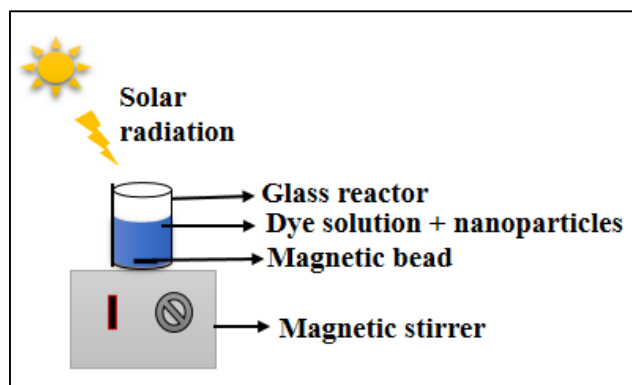


**Fig. 3.7** Schematic diagram of the batch stirred reactor set-up for solar photocatalysis

Liquid Chromatography-Mass Spectrometry (LCMS) analysis of the samples collected at different time intervals during the reaction was performed using Waters ACQUITY UPLC-H Class Plus Bio system having Terra C18 column and acetonitrile-water (70/30) as the mobile phase.

### 3.10 CHARACTERIZATION OF THE BIOSYNTHESIZED NANOPARTICLES

The synthesized Ag based TiO<sub>2</sub> nanocomposite and Ag based TiO<sub>2</sub> modified with Cu nanocomposites (ATC) were characterized for optical absorption by suitably diluting the samples in distilled water using Hitachi UV (model U-2000) spectrophotometer at a scan range of 300-800 nm and band gap (E<sub>g</sub>) was obtained from Tauc plot by plotting (Ahv)<sup>n</sup> vs hv (eV). The topographical features of the synthesized nanocomposites was characterized by Field emission scanning electron microscopy (FESEM) and elemental determination by energy-dispersive X-ray spectroscopy (EDS) using 7610FPLUS, Jeol (Japan) instrument. The shape and morphology of the synthesized nanocomposite was studied using transmission electron microscopy (TEM) by preparing the diluted sample on carbon grid using JEM 2100 instrument. X-ray diffraction (XRD) studies was performed for the synthesized nanocomposites using Rigaku Miniflex 600 under Cu-K<sub>α</sub> radiation (1.5406 Å) operated at a 2θ range of 20° - 80°. The crystallite size was calculated using Debye-Scherrer's formula (2),

$$d = k \lambda / \beta \cos \theta \text{ ----- (2)}$$

where d is the mean diameter of the nanoparticles, k is the constant dependent on crystallite shape (0.89), λ is wavelength of X-ray radiation source, β is the angular

FWHM of the XRD peak at the diffraction angle  $\theta$  (Rahuman et al. 2011). FTIR (Fourier transform infrared spectroscopy) spectrum was recorded to find out the functional groups present in the nanocomposite acting as a capping agent by mixing the dried powder with KBr pellet using Bruker (Alpha) spectrometer. X-ray photoelectron spectroscopy (XPS) analysis was performed to investigate the binding energy and oxidation state of the nanocomposites using PHI 5000 Versa Prob II instrument. The flow rate was maintained at 0.08 mL/min and the injection volume was 20  $\mu$ L. Photoluminescence spectroscopy (PL) of the synthesized nanoparticles was performed to study the recombination of electrons and holes using Horiba FluoroMax-4 spectrofluorometer.

### **3.11 PREPARATION OF RB-220 AND AY-17 DYE SOLUTIONS AND ANALYSIS OF THEIR CONCENTRATION**

0.1 g of RB 220 dye was dissolved in distilled water and diluted to 100 mL in a standard flask to make up 1000 ppm stock solution. To prepare 100 mL of 100 ppm dye solution, 10 mL of 1000 ppm stock solution was added to 100 mL standard flask and the volume was made up to 100 mL using deionized water. AY 17 dye solution was prepared by taking 0.16 g of the dye and dissolving it in water up to 100 mL to make a stock solution of 1000 ppm. To prepare 100 ppm of the dye solution, 10 mL of the stock solution (1000 ppm) was diluted up to 100 mL using deionised water.

Standard solutions of RB 220 dye and AY 17 were prepared at different concentrations of dye and the corresponding absorbance was measured at 609 nm and 418 nm respectively using UV – Visible Spectrophotometer (Hitachi model no. U-2000) to plot the standard calibration. The standard calibration plots for RB-220 (in concentration range of 1 ppm to 10 ppm) and AY-17 (in concentration range of 1 to 10 ppm) are presented in Fig. 3.8 and 3.9 respectively. The dye concentrations in unknown samples were determined corresponding to the measured absorbance values at 609 nm for RB 220 or 418 nm for AY 17 from UV – Visible Spectrophotometer using the corresponding calibration curves.

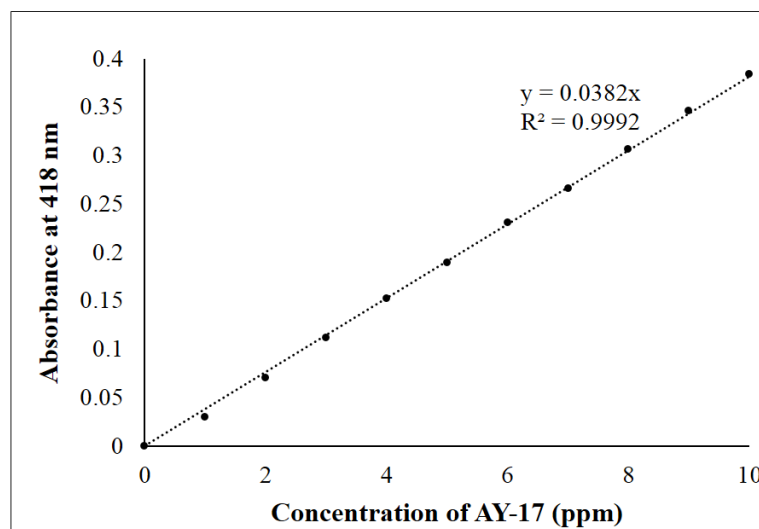


**Fig. 3.8.** Calibration plot for the estimation of Acid Yellow 17 dye

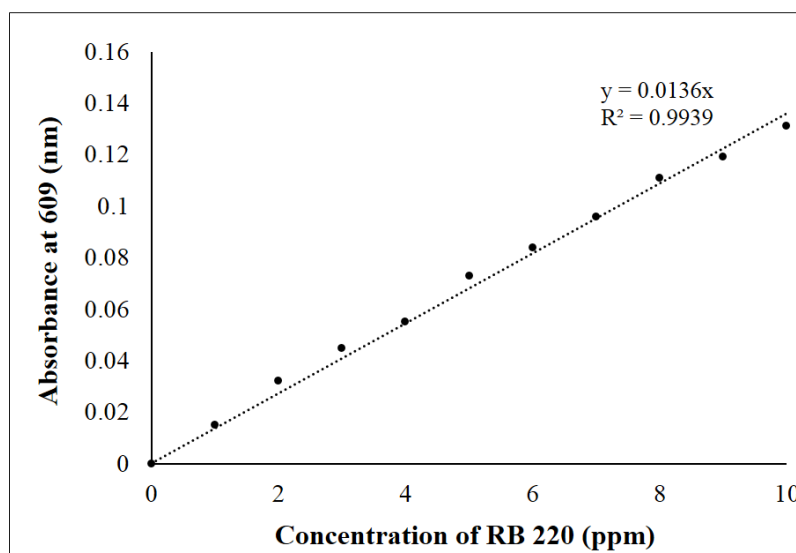


**Fig. 3.9** Calibration plot for the estimation of Reactive Blue 220 dye

## CHAPTER 4

### RESULTS AND DISCUSSION

This chapter presents the results of the experiments conducted to fulfil the objectives along with the discussions. It presents the selection of a suitable method for biosynthesis of Ag based TiO<sub>2</sub> nanocomposite using the bacteria *Alcaligenes aquatilis*, followed by optimization of synthesis parameters to maximize their photocatalytic activity in terms of degradation of RB 220 along with the characterization of the synthesized nanocomposites and studies on the effect of dye degradation parameters to enhance the degradation of RB 220 dye. The biosynthesis of Ag based TiO<sub>2</sub> Modified with Cu nanocomposite, the optimization of its synthesis parameters along with its application in the degradation of RB 220 and AY 17 dyes from single dyes solution and mixed dye solution. The studies on solar light mediated photocatalytic degradation of both the dyes are presented along with kinetics and reusability studies.

#### 4.1 BIOLOGICAL SYNTHESIS OF Ag BASED TiO<sub>2</sub> NANOCOMPOSITES

##### 4.1.1. Selection of method for the synthesis of Ag based TiO<sub>2</sub> nanocomposites

In the present study, the Ag based TiO<sub>2</sub> nanocomposites were synthesized by microbial synthesis method using the cell free culture broth of the bacteria *Alcaligenes aquatilis*. The Ag based TiO<sub>2</sub> nanocomposites were synthesized by three different methods viz. Two step method (Method A), One pot synthesis method with sequential addition of precursors (Method B) and One pot synthesis method with simultaneous addition of precursors (Method C) as explained in Section 3.1. The synthesis was carried out under ambient conditions. The photocatalytic activity of the synthesized nanocomposites was investigated based on their activity in the degradation of Reactive Blue 220 dye under visible light irradiation. Batch experiments were conducted with initial dye concentration of 100 ppm at a catalyst loading of 0.1 g/L under 125W visible light.

As observed in Fig 4.1, the nanocomposites synthesized by all the three methods yielded  $\geq 95\%$  degradation of the dye at the end of 90 min. However, around 49%

degradation of the dye was achieved at the end of 15 min with the nanocomposites synthesized by Method A whereas 46.6 % and 39.8 % degradation was seen with nanocomposites synthesized by Method C and Method B respectively. The initial rate with nanocomposites synthesized by Method A was found to be 3.26 mg/L/min which is comparatively higher than that by Method B (2.63 mg/L/min) and Method C (3.1 mg/L/min) This implies that the rate of degradation is relatively faster with the nanocomposite synthesized by Method A as compared to those synthesized by Method C or Method B. Thus, the Ag based TiO<sub>2</sub> nanocomposites synthesized by Method A exhibits better photocatalytic activity under visible light irradiation.

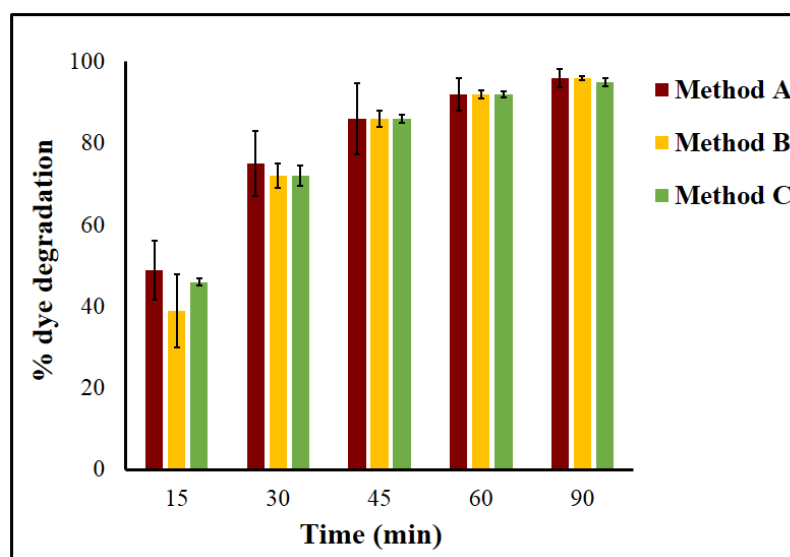


**Fig 4.1** Percentage dye degradation using nanocomposites synthesized by Method A, Method B and Method C

further the photocatalytic activity of Ag based TiO<sub>2</sub> nanocomposites synthesized by Method A, was confirmed by performing the batch experiments for dye removal under the following conditions (i) in the presence of Ag based TiO<sub>2</sub> nanocomposites and light, (ii) only visible light in the absence of nanocomposites and (iii) under dark in the absence of nanocomposites. However when the experiment was conducted under dark in the presence of nanocomposites, there was negligibly small amount of dye removal which indicated that dye removal due to adsorption is very minimal. As observed in Fig. 4.2, on exposure to light for 90 min in the absence of nanocomposites, 71% dye

removal was achieved, while 96% of dye removal was achieved in the presence of nanocomposites and light, which suggested that the Ag based TiO<sub>2</sub> nanocomposite synthesized by method A, enhances the degradation of the dye. The enhancement of rate in the presence of the nanocomposites was observed, which indicates that the Ag based TiO<sub>2</sub> nanocomposites synthesized by Method A are photocatalytically active. Various studies have shown enhanced photocatalytic activity due to the modification of TiO<sub>2</sub> with silver/silver oxides. (Kerkez et al. 2015, Duran-Alvarez et al. 2020, Albiter et al. 2015, Zhao et al. 2017). The initial rate of degradation in the presence of light and the catalyst was found to be 3.26 mg/L/min, which is much higher than 1.57 mg/L/min which was obtained under light, in the absence of the catalyst. These results confirm that Ag based TiO<sub>2</sub> nanocomposites synthesized by Method A can be used as photocatalyst in dye degradation under visible light.

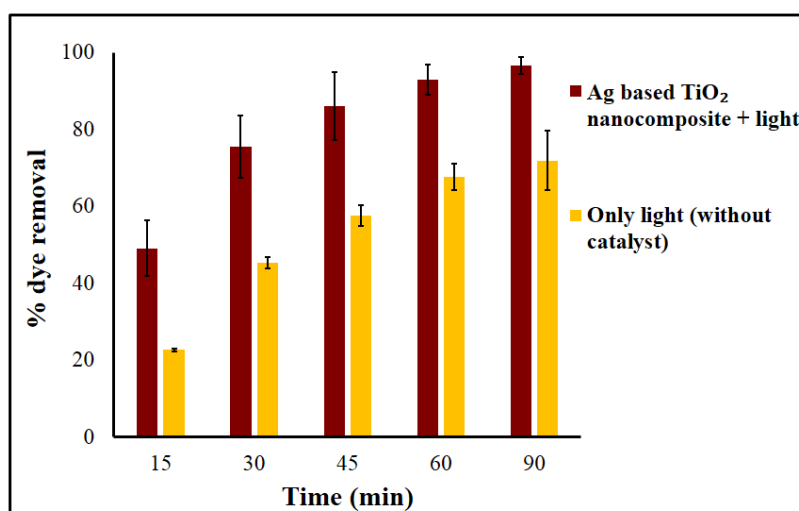


**Fig. 4.2** Percentage dye removal using Ag based TiO<sub>2</sub> nanocomposite (synthesized by Method A) in the presence of (i) nanocomposite and light (ii) only visible light without nanoparticles

The calcination of nanoparticles has been reported to enhance the photocatalytic activity of the nanomaterials (Sienkiewicz et al. 2021; Almeida et al. 2020). In order to assess whether the photocatalytic activity of the synthesized nanoparticles may be improved by calcination, the as synthesized nanocomposites (synthesized by Method A) were calcined at 450°C for 3 h and their activity was compared with that of

uncalcined nanoparticles. As observed in Fig. 4.3, the calcined nanocomposite showed marginally better degradation when compared to uncalcined nanocomposites. However, the marginally better degradation with the calcined particles may be attributed to enhanced crystallinity, phase transformation, changes in crystallite size and alteration in the microstructure of the catalyst by removal of surface residues by calcination (Hu et al. 2014; Narkbuakaew and Sujaridworakun 2019; Kim et al. 2021). As the organic functional groups surrounding the nanoparticles are known to disappear during the heating process (Dhandapani et al. 2012), there may not be any possible role of biomolecules in the photocatalytic activity. However, as the calcination involves higher energy requirement and the resultant enhancement in degradation is only marginal, the application of uncalcined (*as synthesized*) Ag based TiO<sub>2</sub> nanocomposite as photocatalyst is recommended. The biologically synthesized Ag based TiO<sub>2</sub> nanocomposite has been found to be photocatalytically active without calcination as against the chemically synthesized Ag based TiO<sub>2</sub>, which showed good photocatalytic activity only after calcination (Sharma et al. 2018; Narkbuakaew and Sujaridworakun 2019; Khanna and Shetty 2014).

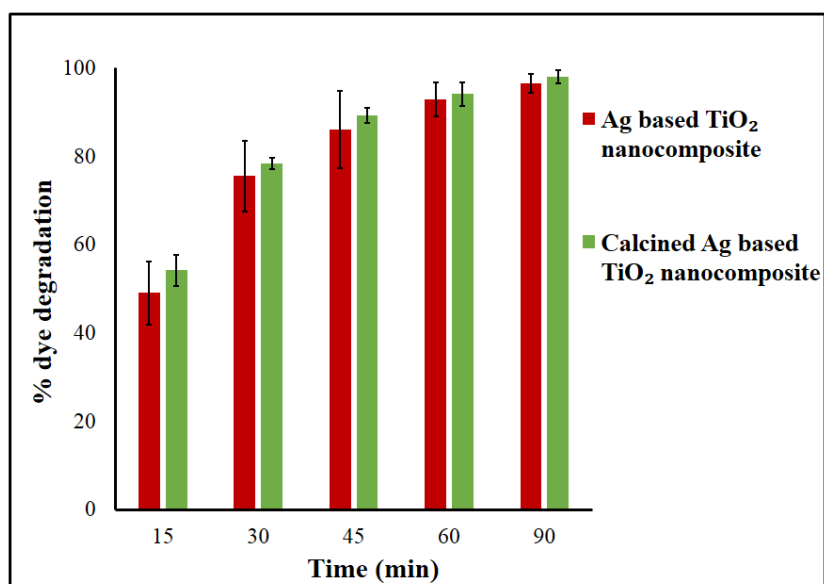


**Fig. 4.3** Effect of calcination on Ag-based TiO<sub>2</sub> nanocomposite synthesized by Method A

#### 4.1.1.1 Characterization of the biosynthesized Ag-based TiO<sub>2</sub> nanocomposite

The nanocomposites synthesized by all the three methods (Method A, B and C) were characterized by XRD and the results are presented in Fig. 4.4. The nanocomposites synthesized by Method A shows the peaks at  $2\theta = 27.85^\circ, 41.26^\circ, 54.89^\circ$ , corresponding to the rutile phase TiO<sub>2</sub> at Miller indices of hkl (110), (111) and (211) respectively (JCPDS 00-088-1173). The presence of both Ag<sub>2</sub>O and AgO crystalline phases were observed in the nanocomposite with the peak of Ag<sub>2</sub>O seen at  $26.24^\circ, 37.63^\circ$  and  $38.69^\circ$  corresponding to crystalline planes (110), (200) and (101) respectively (JCPDS 01-076-1393; 00-019-1155). The peaks at  $30.53^\circ, 32.30^\circ, 43.75^\circ, 46.25^\circ$  and  $57.56^\circ$  can be assigned to (121), (-111), (114), (132) and (402) crystalline planes of AgO (JCPDS 01-084-1108; 01-075-0969). Method B and Method C presents almost similar XRD pattern showing the presence of rutile TiO<sub>2</sub>, Ag<sub>2</sub>O and AgO. Method B shows the presence of TiO<sub>2</sub> peak at  $27.79^\circ$  and which is indexed to (110) rutile planes respectively (JCPDS 00-088-1173). Method C shows the  $2\theta$  peak at  $27.68^\circ$  and  $54.85^\circ$  and corresponding to the (110) and (211) crystalline planes of rutile TiO<sub>2</sub> respectively (JCPDS 00-088-1173). Both Method B and Method C show the significant diffraction peak at  $32.15^\circ$  attributing to the crystalline plane (-111) of cubic AgO. Apart from this, there is also a peak of AgO at  $46.16^\circ$  and  $57.51^\circ$  indexed to the plane (132) and (402) respectively. There are no peaks observed for Ag<sub>2</sub>O in the nanocomposites synthesized by Method B and Method C. Method A shows the presence of additional peaks corresponding to TiO<sub>2</sub> and AgO which is absent in Method B and Method C. These results suggest that higher photocatalytic activity exhibited by Method A could be attributed to the presence of additional peaks of AgO and TiO<sub>2</sub> and also due to the presence of Ag<sub>2</sub>O peaks which is known to render visible light absorption property. These results indicate that the nanocomposites synthesized by Method B and C comprise of rutile TiO<sub>2</sub> and AgO whereas Method A shows the presence of rutile TiO<sub>2</sub>, AgO and Ag<sub>2</sub>O. Thus, the synthesized particles are hereinafter referred as AgO/Ag<sub>2</sub>O-TiO<sub>2</sub> nanocomposite particles. The crystallite size of the nanocomposites calculated using Scherrer's formula for Method A, Method B and Method C was found to be 38 nm, 28.04 nm and 32.37 nm respectively. Although smallest crystallite size is observed for Method B, rapid photocatalysis is exhibited by the nanocomposites synthesized by Method A.

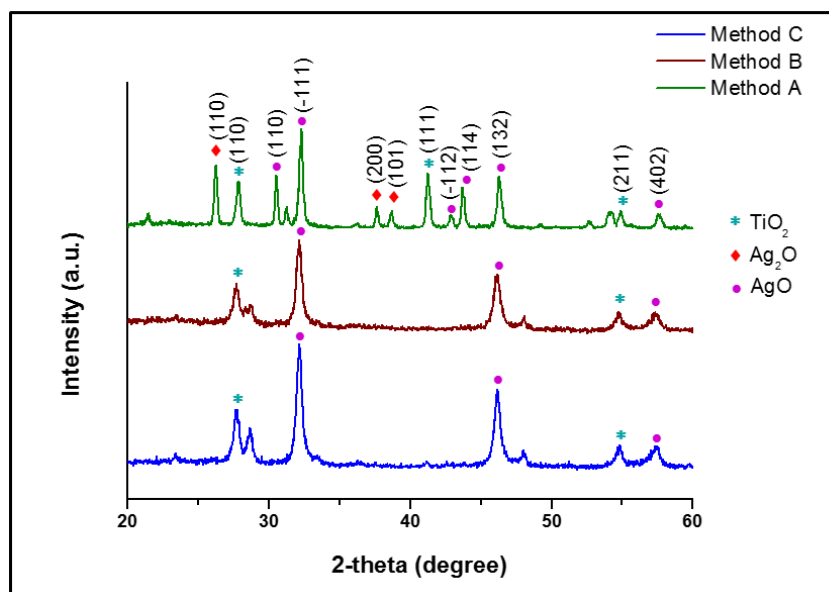


**Fig. 4.4** XRD pattern of the nanocomposites synthesized by Method A, B and C.

The UV-Vis absorption spectra of the nanocomposites synthesized by all the three methods were recorded (Fig. 4.5) in order to understand the reason for higher photocatalytic activity of the nanocomposites synthesized by Method A. The spectra shows that the Ag based TiO<sub>2</sub> nanocomposites synthesized by Methods A, B and C show a narrow peak in the UV range and wide absorption bands in the visible region, with peaks in the visible region lying in the range of 412 nm to 439 nm. It indicates that the synthesized nanocomposites can absorb light in UV range and also in wide wavelength range in the visible region. The absorbance in the visible region is much higher than that found in the UV region. The spectrum for the nanocomposite synthesized by Method A shows two absorption peaks at 326 nm and 439 nm. The nanocomposites synthesized by Method B show the peaks at 324 nm and 412 nm, whereas, those synthesized by Method C show peaks at 330 nm and 421 nm. The absorbance peaks seen at around 324 – 330 nm in all the three nanocomposites, could be attributed to the presence of TiO<sub>2</sub> in the nanocomposites which strongly absorbs light in the UV region. Biswas et al. (2015) have reported the absorption edge for TiO<sub>2</sub> to be  $\approx$  350nm. The threshold edge of absorption band is reported in the range shorter than 400 nm in the area of the ultraviolet spectrum for TiO<sub>2</sub> (Namshah et al. 2016). On the other hand, an intense peak is exhibited by all the three nanocomposites in the

visible region of around 412 – 439 nm, which shows that maximum absorption by the nanocomposites occur in the visible region. This shift in the peak towards higher wavelength could be due to the presence of AgO/Ag<sub>2</sub>O, which absorb the visible light (Wei et al. 2016) by lowering the band gap. Ahmed et al. (2013) have found that with an increase in iron oxide content in titania, the absorption is shifted to longer wavelength toward the visible region. According to Sun et al. (2017), the existence of oxides of silver can introduce impurity level and reduce the band gap of TiO<sub>2</sub> which can lead to the absorption spectrum of the sample shift into the region of visible light. The broad absorption reaching down to ~700 nm may be attributed to the absorption by Ag<sub>2</sub>O (Handoko et al. 2019; Liu et al. 2018; Sun et al. 2014). Silver oxides are considered to be the most potential candidates among the low band gap semiconductors to form heterojunctions with TiO<sub>2</sub> due to their most stable phases (Bian et al. 2020). AgO and Ag<sub>2</sub>O have been reported to effectively degrade organic pollutants by photocatalysis under visible light (Liu et al. 2019; Wei et al. 2014; Sobhani-Nasan and Behpour 2016).

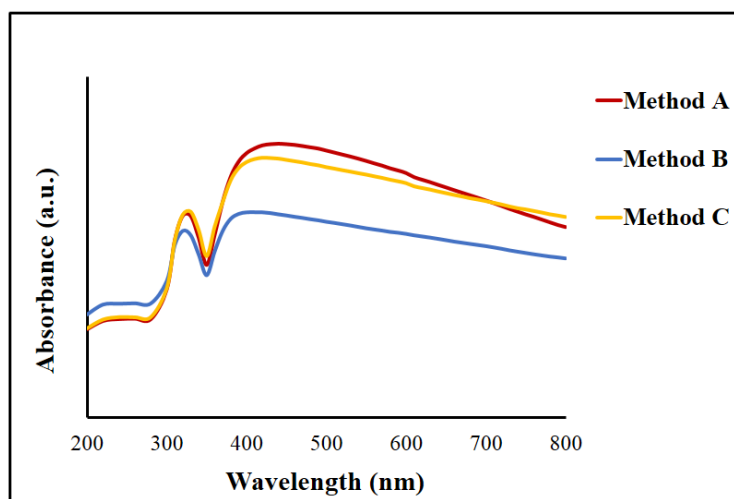


**Fig. 4.5** UV-Vis absorption spectra of Ag based TiO<sub>2</sub> nanocomposites synthesized by Method A, Method B and Method C.

The spectra show that the nanocomposites synthesized by all the three methods display high absorbance in both UV and visible region range with maximum absorbance observed in visible range at 439 nm, 421 nm and 412 nm by Method A, Method C and

Method B respectively. The particles synthesized by Method A and C show almost similar absorption values in UV range but the absorbance under visible light in the range of 400 to 700 nm are higher for nanoparticles synthesized by Method A when compared to Method C. The visible light and UV light absorbance values are the least with the nanocomposites synthesized by Method B. Though the nanocomposites synthesized by both Method A and C show higher visible light absorbance than that at UV, the nanocomposites synthesized by Method A exhibit the maximum absorption of visible light. The presence of  $\text{TiO}_2$  in the composite renders UV light activity and presence of  $\text{Ag}_2\text{O}$  or  $\text{AgO}$  may be responsible for visible light activity and therefore two absorption onsets (AO1 and AO2) are seen in the nanocomposites. Liu et al. (2019) have reported an enhancement of photocatalytic activity of  $\text{TiO}_2$  on incorporation of  $\text{Ag}_2\text{O}$  under visible light. Compositing  $\text{TiO}_2$  with Ag or silver oxides is responsible for the activity of the nanocomposite under visible light irradiation.

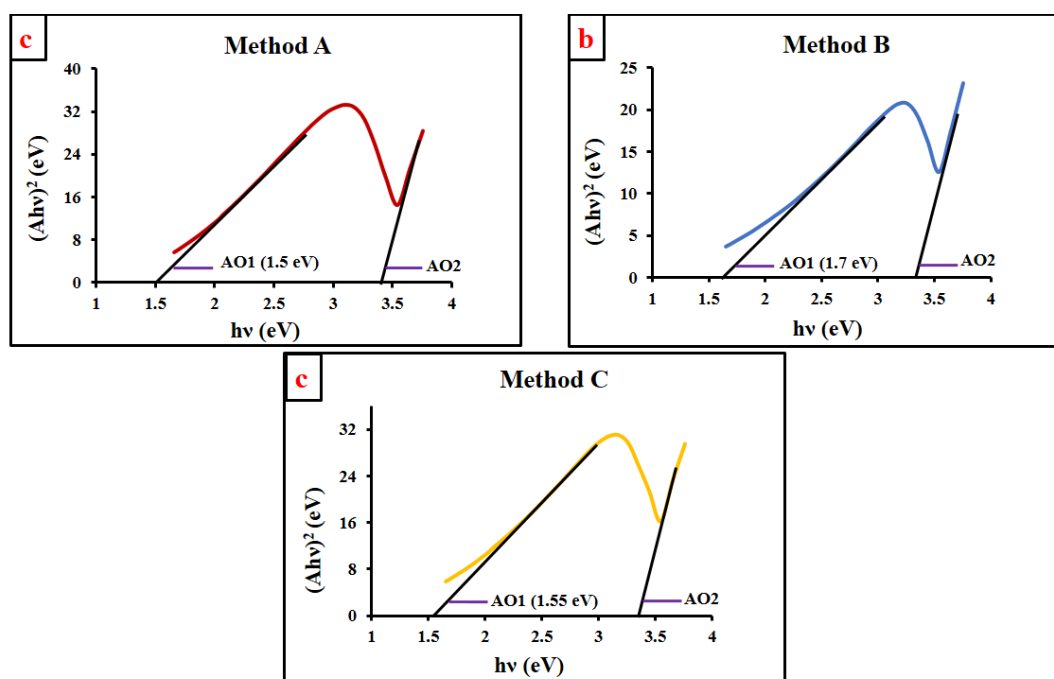


**Fig. 4.6** Tauc plots for the nanocomposites synthesized by Method A, B and C.

The Tauc plot was plotted for all the three nanocomposites to determine the band-gap from the absorption spectra. The linear region of Tauc plot intersecting at  $(h\nu)$  in a graph of  $(A h\nu)^2$  vs  $(h\nu)$  where  $A$  is the absorbance,  $h$  is the Plank's constant, and  $\nu = c/\lambda$  ( $c$  = speed of light and  $\lambda$  is the wavelength) gives the band-gap energy of the nanocomposites. Tauc plot indicates that all the three nanocomposites have two absorption onsets, one in UV range and the other in visible range. The material being a composite, exhibits two absorption onsets. It is also evident from the absorption spectra shown in Fig. 4.6. The band-gap energy of the nanocomposites is the minimum energy required to activate the conduction band electrons. The band-gap energy of the Ag based TiO<sub>2</sub> nanocomposites synthesized by Method A, B and C were found to be 1.5 eV, 1.7 eV and 1.55 eV, respectively. The nanocomposite synthesized by Method A has the minimum band gap energy value (1.5 eV) as compared to those synthesized by Method B and C. Gannoruw et al. (2016) have reported bandgap value of 1.58 eV for chemically synthesized Ag<sub>2</sub>O/TiO<sub>2</sub> catalyst. The highest photocatalytic activity of the nanocomposites synthesized by Method A may be attributed to its lowest band gap energy. However all the three nanocomposites have the band-gap energy value in the range of 1.5 to 1.7 eV much lesser than the bandgap energy value of pure anatase TiO<sub>2</sub> (~3.2eV) or pure Rutile TiO<sub>2</sub> (~3 eV), requiring a wavelength of 388 nm and 414 nm for activation, respectively (Coutts et al. 2016). The synthesized nanocomposites exhibited lower band gap values compared to Degussa P25, which being a mixture of anatase (70-85%) and rutile TiO<sub>2</sub> has a band gap of 3.15 eV due to the high content of the anatase phase (Coutts et al. 2016). The band gap values for TiO<sub>2</sub> nanoparticles synthesized by microbial method has been reported by Suriyaraj and Selvakumar (2014) as 3.76 eV and those synthesized using cell free supernatant of the bacteria *Alcaligenes aquatilis* exhibited band gap value 3.23 eV (Devadiga, 2016) which is much higher than that for the AgO/Ag<sub>2</sub>O-TiO<sub>2</sub> nanocomposites synthesized in the present study. The band gap values of these nanocomposites have also been found to be lower than the other TiO<sub>2</sub> containing nanocomposites reported in literature (Table 4.1).

**Table 4.1** Band gap energy values of different nanocomposites containing TiO<sub>2</sub>

<b>Nanoparticle</b>	<b>Method of synthesis</b>	<b>Band-gap</b>	<b>References</b>
TiO <sub>2</sub> -graphene oxide nanocomposite	Chemical method	2.21 eV	Almeida et al. 2016
Graphene-ZnTiO <sub>3</sub> composite	Chemical method	3.36 eV(calcined at 800 <sup>0</sup> C) 3.25 eV(calcined at 900 <sup>0</sup> C)	Gayathri et al. 2015
Ag doped TiO <sub>2</sub>	Chemical method	2.71 eV	Naraginti et al (2015)
TiO <sub>2</sub> Au/TiO <sub>2</sub>	Biological method (L-tryptophan)	3.86 eV 3.84 eV	Biswas et al. 2015
Ag-TiO <sub>2</sub>	Pulsed cathodic arc technique	2.8 eV	Mosquera et al. 2016
Poly-o-phenylenediamine modified TiO <sub>2</sub> nanocomposites	Chemical method	2.64 eV	Yang et al. 2017
Ag@TiO <sub>2</sub>	Chemical Method	1.85 eV	Khanna, A. 2014
Ag based TiO <sub>2</sub> nanocomposite	Microbial method	Method A – 1.5 eV Method B – 1.7 eV Method C – 1.55 eV	<b>Present study</b>

Therefore, owing to its highest photocatalytic activity as revealed by the maximum initial degradation rate and maximum absorbance in the visible light with lower band-gap, as presented in Table 4.2, nanocomposites synthesized by Method A which is a

Two-step method was selected for the synthesis of AgO/Ag<sub>2</sub>O-TiO<sub>2</sub> nanocomposites. The higher photocatalytic activity of the nanocomposite particles synthesized by Method A, in spite of its highest crystallite size shows that the crystallite size may not be the only governing factor determining the higher catalytic activity, but other factors such as the composition, crystallite phases, the structure and morphology may govern the activity.

**Table 4.2** Initial degradation rate and percentage dye degradation at the end of 15 min, band-gap and crystallite size of nanocomposites synthesized with different methods.

Synthesis Method	Percentage dye degradation after 15 min	Percentage dye degradation at the end of 90 min	Initial degradation rate (mg/L/min)	Band-gap (eV)	Crystallite size (nm)
Method A	49	96.5	3.26	1.5	38
Method B	39.8	96.5	2.63	1.7	28.04
Method C	46.6	95.3	3.10	1.55	32.37

#### 4.1.1.2. Characterization of the AgO/Ag<sub>2</sub>O-TiO<sub>2</sub> nanocomposite synthesized by Method A

As the AgO/Ag<sub>2</sub>O-TiO<sub>2</sub> nanocomposites synthesized using Method A showed better activity, these nanoparticles were further characterized. The formation of AgO/Ag<sub>2</sub>O-TiO<sub>2</sub> nanocomposites synthesized using Method A was evident from a colour change of the synthesis mixture from light yellow to brown after the synthesis duration of 24 h (Fig. 4.7 (a)).

The morphology of the nanocomposites was studied using Transmission Electron Microscopy (TEM). From Fig. 4.7 (b), it is seen that the nanoparticles appear nearly spherical in shape and are distinct. The SAED pattern (Fig. 4.7 (c)) shows the polycrystallinity of the nanocomposite with d-spacing of 2.7, 2.3 and 1.67 Å corresponding to the (-1 1 1), (1 0 1) and (2 1 1) crystalline planes of AgO, Ag<sub>2</sub>O and rutile TiO<sub>2</sub> respectively. The particle size distribution (Fig. 4.7 (d)) shows the size of

the particles ranging between 10 – 90 nm with average size of ~ 39.6 nm which is close to the crystallite size calculated using Scherrer's formula. A small particle size in nanometer range provides higher surface area and more active sites for the adsorption of dye molecules leading to better photocatalytic activity (Kiani et al. 2020).

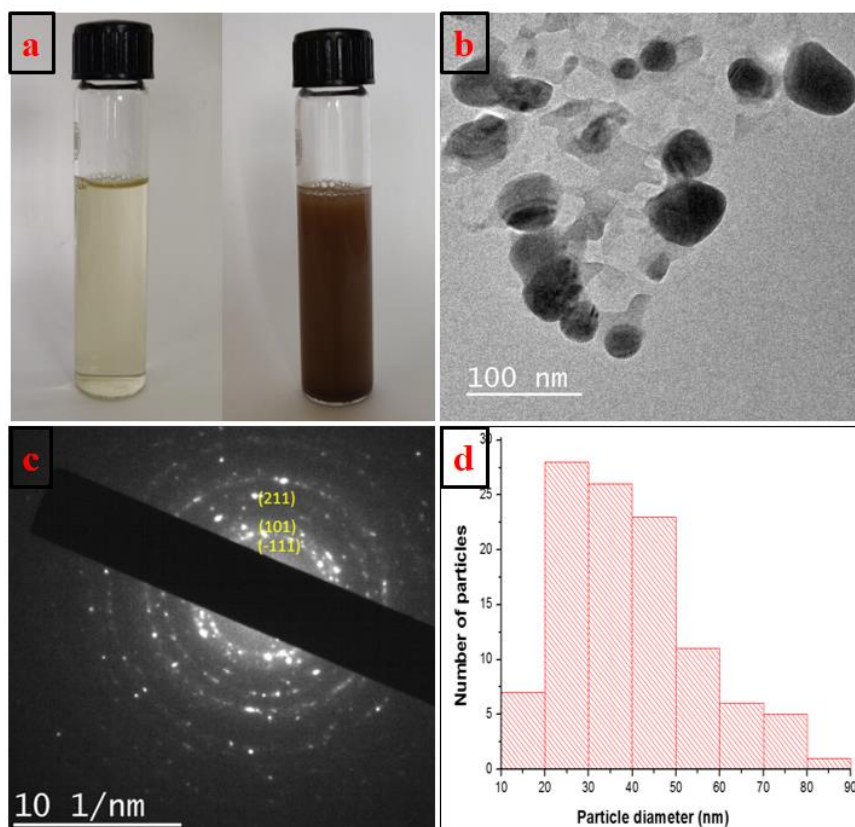


**Fig. 4.7** (a) Colour change of culture supernatant after the addition of the precursor from light yellow (left) to brown (right) indicating the formation of nanocomposite particles (b) TEM image (c) SAED pattern (d) Particle size histogram of the nanocomposites

The X-Ray diffractogram of the nanocomposite particles presented in Fig. 4.8, shows the peaks at  $2\theta = 27.85^\circ$ ,  $41.26^\circ$  and  $54.89^\circ$  and corresponding to the hkl planes (110), (111) and (211) of rutile  $\text{TiO}_2$  respectively (JCPDS No. 088-1173). The presence of both  $\text{Ag}_2\text{O}$  and  $\text{AgO}$  crystalline phases were observed with  $\text{Ag}_2\text{O}$  peak seen at  $26.24^\circ$ ,  $37.63^\circ$  and  $38.69^\circ$  corresponding to cubic crystalline planes (110), (200) and (101) respectively (JCPDS No. 01-076-1393; 00-019-1155).  $\text{AgO}$  peaks at  $30.53^\circ$ ,  $32.30^\circ$ ,

43.75° and 46.25° and 57.56° corresponds to the (121), (-111), (114), (132) and (402) crystalline planes (JCPDS No 01-084-1108; 01-075-0969). The crystallite size of the AgO/Ag<sub>2</sub>O-TiO<sub>2</sub> nanocomposite was found to be 38 nm.

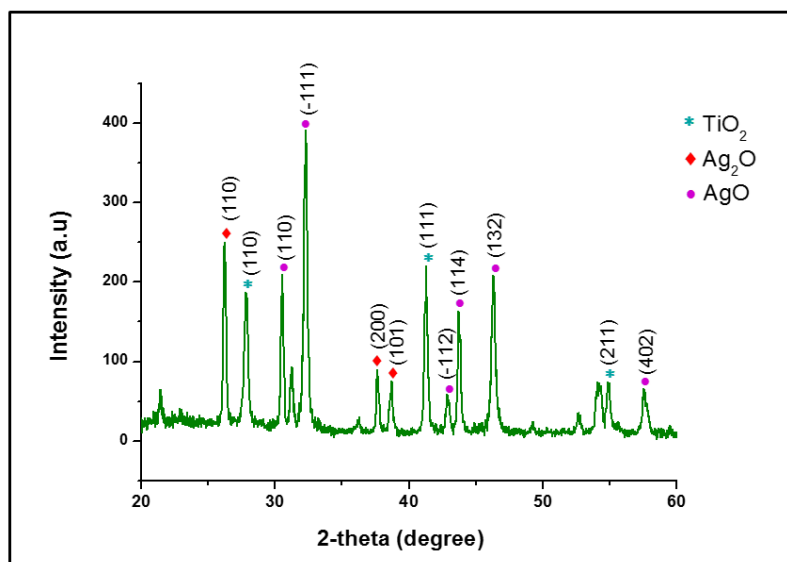


**Fig. 4.8** XRD pattern of the nanocomposites synthesized by Method A.

FTIR analysis was performed for the nanocomposites synthesized by Method A to know the functional groups involved with the nanocomposite particles (Fig. 4.9). FTIR band at 2335.37 cm<sup>-1</sup> corresponds to carboxylate anion (Silverstein et al. 2005). The peak at 1535.05 cm<sup>-1</sup> could be attributed to the bending vibration of secondary amines of proteins (Staden et al. 2013). A strong signal at 1640.16 cm<sup>-1</sup> arises from the stretching vibration of carbonyl group of proteins (Silverstein et al. 2005). Similar results were seen for FTIR bands at 1640 cm<sup>-1</sup> attributing to carbonyl stretching of amides in microbial synthesized silver nanoparticles (Yuan et al. 2019). The spectrum shows bands at 3523.30 cm<sup>-1</sup> corresponding to the hydroxyl stretching vibration and 2879.20 cm<sup>-1</sup> attributing to the C-H stretching vibration of aldehyde group (Silverstein et al. 2005). The presence of such OH stretching and CH stretching vibration groups are observed by Esmail et al. (2022) on the silver nanoparticles synthesized using *Bacillus sp.* N-H stretching vibration of amides could be responsible for the band present at 3296.71 cm<sup>-1</sup> (Barth et al. 2007). Strong N-H stretching vibration band were also observed by Yuan et al. (2019) in the

microbial synthesized silver nanoparticles. The bands at 1040 and 1230.36  $\text{cm}^{-1}$  result from strong C-F stretching vibrations (Silverstein 1981) which may be due to bonding between the biomolecules and the fluorine atoms present in the titanium precursor salt. Taran et al. (2018) have also found the presence of alkyl halides (C-F) on the  $\text{TiO}_2$  nanoparticles synthesized using *Halomonas elongata* bacteria. Ti–O and Ti–O–Ti bands appear between 450 and 1000  $\text{cm}^{-1}$ , which is characteristic of  $\text{TiO}_2$  (Bharati et al. 2017). Ti-O-Ti bond was also seen by Ordenes-aenishanslins et al. (2014) in the region of 450 – 700  $\text{cm}^{-1}$  in microbial synthesis of  $\text{TiO}_2$  nanoparticles. The presence of various groups on the nanocomposite as evidenced by FTIR results, suggests that some biomolecules present in the bacterial cell free supernatant serve as capping agents and they may have been responsible for the formation of the distinct particles and stabilization of the nanoparticles.

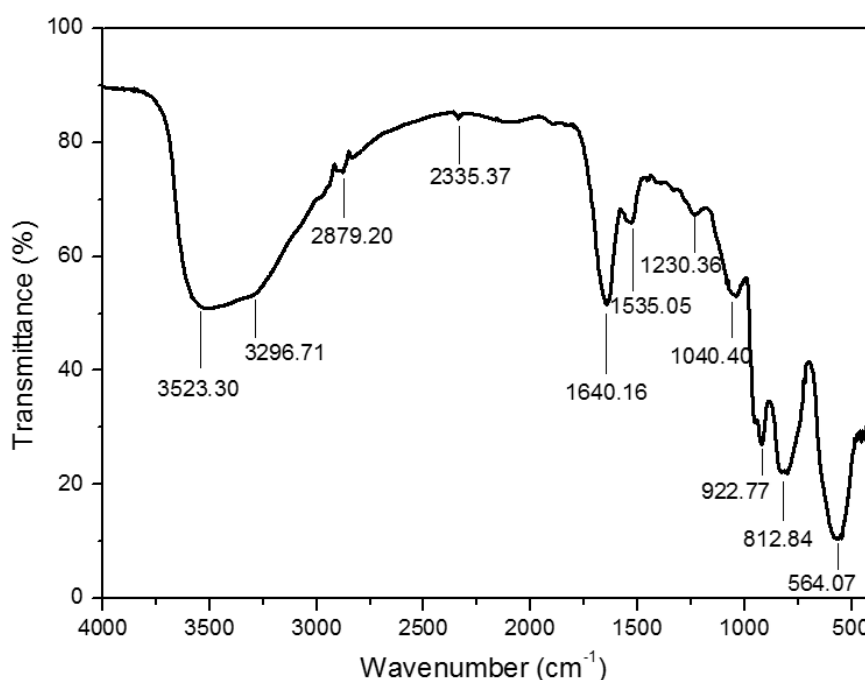


**Fig. 4.9** FTIR spectra of the  $\text{AgO}/\text{Ag}_2\text{O}-\text{TiO}_2$  nanocomposite

The  $\text{AgO}/\text{Ag}_2\text{O}-\text{TiO}_2$  nanocomposite synthesized by Method A were subjected to XPS analysis (Fig. 4.10). XPS analysis reveals the presence of oxygen, carbon, titanium and silver.

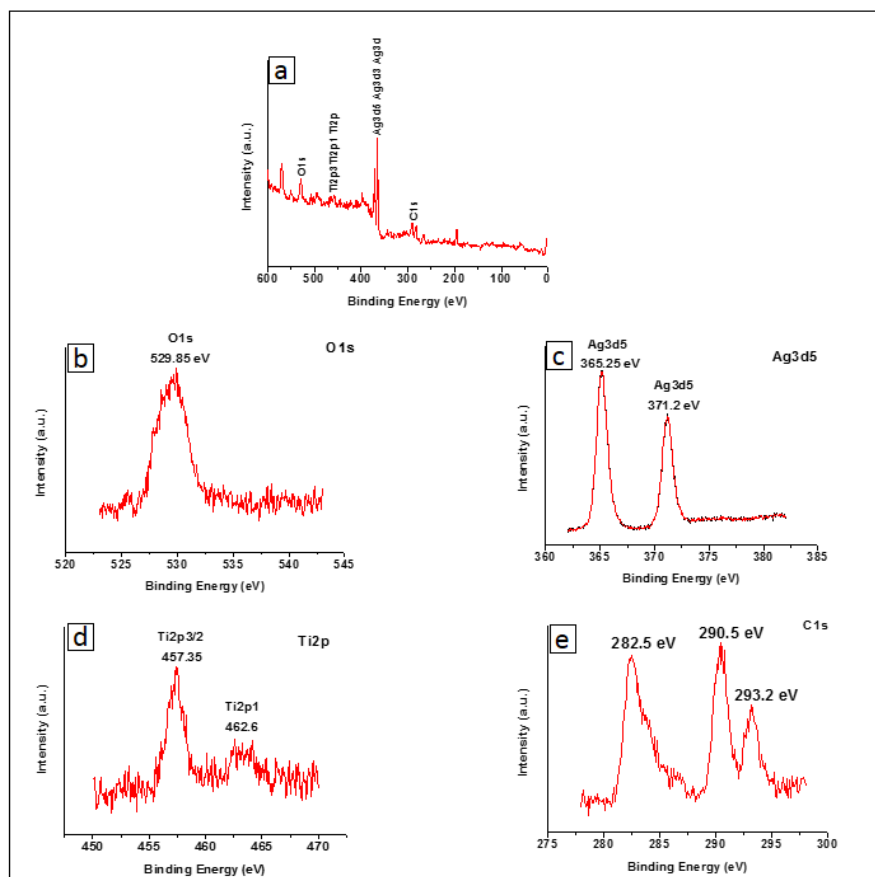


**Fig. 4.10** XPS spectra of (a) AgO/Ag<sub>2</sub>O-TiO<sub>2</sub> nanocomposite (b) O1s (c) Ag3d (d) Ti2p (e) C1s

The binding energy of O1s is shown in Fig. 4.10 b. The peak for O1s located at 529.85 eV could be attributed to the O in TiO<sub>2</sub> which is in agreement with the results obtained by Yang et al. (2017). Ag3d peaks were observed at 365.25 and 371.2 eV corresponding to Ag3d<sub>5/2</sub> and Ag3d<sub>3/2</sub> (Fig. 4.10 c). The binding energies for Ag 3d<sub>5/2</sub> of 367.1 (Handbooks of Monochromatic XPS Spectra) or 367.3 (Hoflund et al. 1995; Hoflund and Hazos 2000) have been assigned to AgO. The binding energy for Ag 3d<sub>5/2</sub> of 367.7 (Hoflund and Hazos 2000; Hoflund et al. 1995) has been assigned to Ag<sub>2</sub>O. Liu et al (2018) reported the peaks of the pristine Ag<sub>2</sub>O at 367.9 and 374 eV, attributing to the Ag 3d<sub>5/2</sub> and Ag3d<sub>3/2</sub> of Ag<sup>+</sup>. However, in the present study a shift in Ag 3d<sub>5/2</sub> binding energy to 365.2 has been observed. Rtimi et al. (2013) have also reported the binding energy ranging from 364.7 to 365.4 eV for Ag3d in their sample of ZrNo-Ag co-sputtered surface attributing to the presence of silver in AgO and Ag<sub>2</sub>O form. Such a

shift was observed by them when they exposed zerovalent silver in ZrNo-Ag co-sputtered surface to bacteria and they attributed the shift to  $\text{Ag}^1/\text{Ag}^{2+}$  redox reactions occurring on the sample surface during the interaction of sample with bacteria. Cho et al. (2019) have observed a shift in the Ag peaks to lower binding energies when Ag nanoparticles were used in Ag-TiO<sub>2</sub> heterostructures. As reported by them, the shift of the Ag peaks to lower binding energy compared to the standard Ag peak may be attributed to the interaction between AgO and Ag<sub>2</sub>O with TiO<sub>2</sub>. Ag3d<sub>3/2</sub> peak also has been found to shift from a standard value of 373.4 eV (Gannoruwa et al. 2016) to 371.2 eV due to similar reasons. The binding energy of Ti2p is seen at 457.35 and 462.6 eV (Fig. 4.10 d) corresponding to Ti<sup>3+</sup> which is slightly shifted towards lower binding energy compared to the result obtained by Zhang et al. (2007), Wagstaffe et al. (2017) and Xiong et al. (2012) where the binding energy values were 457.9 eV, 457.7 eV and 457.8 eV respectively. XPS results confirmed the presence of Ti<sup>3+</sup> on the surface of TiO<sub>2</sub>. Upon exposure to Ag, charge transfer from the Ag to the TiO<sub>2</sub> surface takes place resulting in the reduction of Ti<sup>4+</sup> to Ti<sup>3+</sup> (Wagstaffe et al. 2017). The reduction of Ti<sup>4+</sup> to Ti<sup>3+</sup> may also occur by the reducing agents present in the cell supernatant. No peak for Ti<sup>4+</sup> appeared in XPS, even though XRD showed the presence of TiO<sub>2</sub>. Ti<sup>3+</sup> accumulation on TiO<sub>2</sub> surface results in the appearance of Ti<sup>3+</sup> peak, but the presence of Ti<sup>4+</sup> is not revealed, as XPS can penetrate only a few nanometers at the surface. This may be a result of dense coverage of the surface with Ti<sup>3+</sup>. The carbon peaks at 282.5 and 290.5 eV (Fig. 4.10 (e)) could be attributed to carbides and carbonates respectively and 293.2 eV peak can be ascribed to CF<sub>3</sub> (Shutthanandan et al. 2019) which might have been formed by the bonding between the fluorine atoms of potassium hexafluorotitanate (Ti precursor) used in the synthesis of the AgO/Ag<sub>2</sub>O-TiO<sub>2</sub> nanocomposite with the carbon of the biomolecules present in the supernatant. The carbon peak at 282.5 eV may be ascribed to carbides (Beamson et al. 1992) which is due to carbon-metal binding (Post et al. 2018). The high binding energy peak at 290.5 eV is ascribed to carboxylate functionality peak (O=C-OH) and amide carbon (N-C=O) of protein molecules (Das et al. 2012). Many researchers have reported the shifting of carboxylate and amine groups on binding with metal nanoparticles (Ramanathan et al. 2005, Lim et al. 2010, Tseng et al. 2006). The peak at 293.2 eV is due to CF<sub>3</sub> or CF<sub>2</sub>-O covalent bonding (Shutthanandan et al. 2019, Vandencastele et al. 2010) which is

attributed to the presence of fluorine bound biomolecules on the nanoparticles surface. The presence of fluorine is attributed to  $K_2TiF_6$  used as the precursor salt for the synthesis of  $TiO_2$ . These results prove that organic groups on the surface of nanocomposites are responsible for the presence of carbon peaks. Thus, XRD along with FTIR and XPS analysis reveal that the nanocomposite particles consist of  $AgO/Ag_2O$  and  $TiO_2$  with surface coverage by  $TiO$  and several biomolecules. These biomolecules tend to serve as capping and stabilizing agents.

#### **4.1.2. Optimization of synthesis parameters for $AgO/Ag_2O-TiO_2$ nanocomposites synthesized by Method A**

Further in this study, Method A was chosen for the synthesis and the synthesis parameters were optimized in order to maximize the photocatalytic activity. Optimizing the parameters like molar ratio of Ag to Ti in the synthesis mixture, pH of synthesis mixture, synthesis time etc. during the synthesis process of the nanocomposites is necessary to enhance its photocatalytic activity and also to improve its stability.

##### **4.1.2.1. Optimization of molar ratio of Ag:Ti in the synthesis mixture**

The nanocomposites were synthesized by Method A with five different Ag to Ti molar ratios in the synthesis mixture i.e., 1:0.4, 1:0.8, 1:1.2, 1:1.6 and 1:2.0. The synthesized nanocomposites were tested for their photocatalytic activity in terms of degradation of Reactive Blue 220 dye to find the optimum molar ratio for maximum dye degradation.

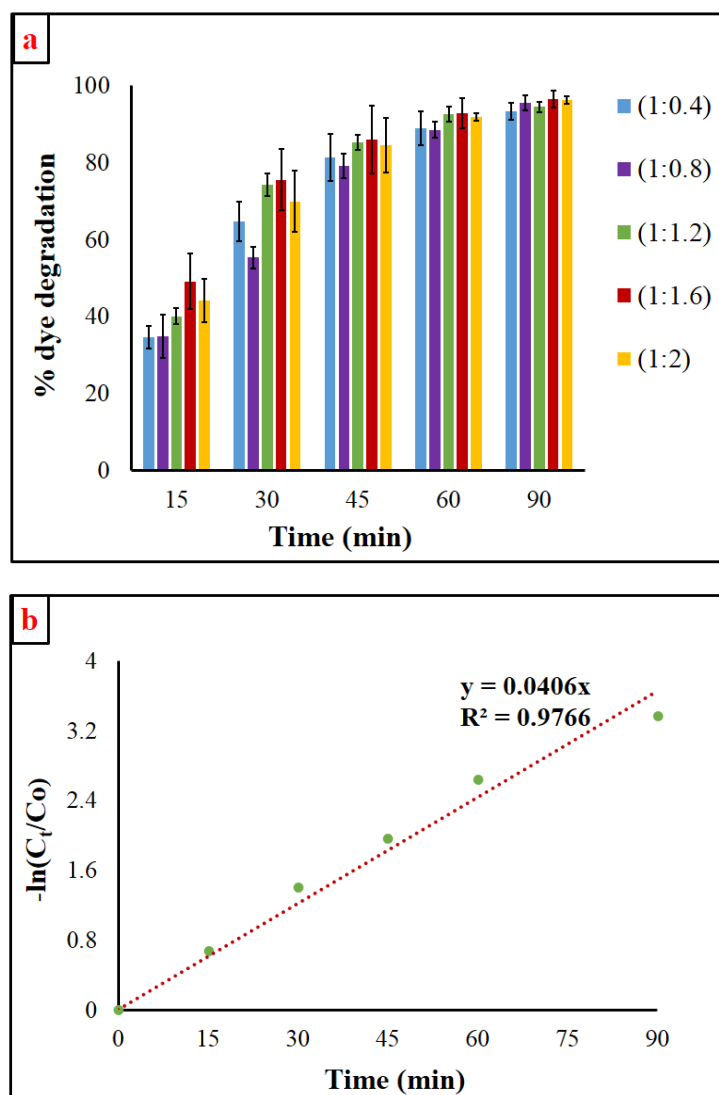


**Fig. 4.11** (a) Time course of variation of percentage dye degradation obtained with AgO/Ag<sub>2</sub>O-TiO<sub>2</sub> nanocomposite synthesized with different molar ratio of Ag to Ti.

(b) Pseudo-first order kinetics plot for 1:1.6 ratio

It is observed from Fig. 4.11, rapid degradation occurred with AgO/Ag<sub>2</sub>O-TiO<sub>2</sub> nanocomposites having molar ratio of 1:1.6 as compared to those by nanocomposites synthesized with other ratios. The rate of degradation was faster with nanocomposites synthesized with molar ratio of 1:1.6 and 1:1.2 as compared to others. All the nanocomposites could yield around 90 – 96 % degradation at the end of 90 min. From the results presented in Table 4.3, when percentage degradation at the end of 15 min was compared, the nanocomposite with Ag to Ti ratio of 1:1.6 yielded almost 49 %

degradation which is the maximum and other nanocomposites yielded less than 45% degradation at the end of 15 min. The initial rates of degradation presented in Table 4.3 show that the initial rate of degradation is 3.26 mg/L/min with the nanocomposites synthesized with Ag to Ti ratio of 1:1.6 and is the maximum in comparison to the nanocomposites synthesized with the other molar ratios. Khanna and Shetty (2014) had optimized the Ag : Ti ratio in the chemical synthesis of Ag@TiO<sub>2</sub> nanoparticles and have found almost similar Ag : Ti molar ratio of 1:1.7 as the optimum ratio for the effective degradation of Reactive Blue 220 dye under UV and solar light. As the moles of Ti was increased in the synthesis mixture up to 1:1.6 ratio, nanoparticles formed were found to catalyse the reaction faster as evidenced from the values of initial degradation rates shown in Table 4.3, however slight reduction was obtained with 1:2 ratio. The first order degradation kinetics of RB 220 dye with initial concentration of 100 ppm dye and 0.1 g/L catalyst loading using nanocomposites synthesized with optimum Ag:Ti molar ratio of 1:1.6 under visible light was tested by plotting  $-\ln(C_t/C_0)$  versus time (Fig. 4.11 b). The linear nature of the plot implies that the photocatalytic reaction follows pseudo first-order kinetics. The photocatalytic rate constant of the reaction was calculated using Equation (2),

$$\ln (C_t/C_0) = -kt, \text{-----(2)}$$

where  $C_0$  is the initial concentration of the dye,  $C_t$  is the concentration of dye at particular time  $t$  and  $k$  is the rate constant ( $\text{min}^{-1}$ ) and the  $k$  value was found to be of  $0.0406 \text{ min}^{-1}$  with  $R^2$  value of 0.9766.

Fig. 4.12 shows the XRD pattern of the nanocomposites synthesized at different Ag:Ti ratios by Method A. As observed from Fig. 4.12 (a), XRD pattern of the nanocomposites synthesized at 1:0.4 Ag to Ti ratio shows  $2\theta$  at  $27.93^\circ$  corresponding to the (110) crystalline plane of rutile TiO<sub>2</sub> (JCPDS 00-088-1173). The peaks at  $30.69^\circ$ ,  $32.36^\circ$ ,  $43.85^\circ$ ,  $46.38^\circ$  and  $57.57^\circ$  can be attributed to the (121), (-111), (114), (132) and (402) crystallographic planes of AgO (JCPDS 01-084-1108; 00-022-0472). Cubic Ag<sub>2</sub>O peaks were seen at  $37.77^\circ$  corresponding to crystalline planes (200) (JCPDS 01-076-1393).

XRD pattern of the nanocomposites synthesized at 1:0.8 is presented in Fig 4.12, which is almost similar to the nanocomposites synthesized at 1:0.4 molar ratio. 1:0.8 ratio shows the diffraction peak at  $27.72^\circ$  ascribing to the crystalline plane of (110) rutile  $\text{TiO}_2$  respectively (JCPDS 00-088-1173). The peaks at  $30.49^\circ$ ,  $32.15^\circ$ ,  $43.68^\circ$ ,  $46.10^\circ$  and  $57.39^\circ$  is attributed to the AgO peaks (121), (-111), (114), (132) and (402) respectively (JCPDS No 01-084-1108; 01-075-0969). The peak at  $37.60^\circ$  is attributed to cubic crystalline plane (200) of  $\text{Ag}_2\text{O}$  (JCPDS 01-076-1393).

The XRD pattern of the nanocomposites synthesized at 1:1.2 ratio shows the rutile  $\text{TiO}_2$  peak at  $27.89^\circ$  corresponding to the crystalline plane (110) (JCPDS 00-088-1173). AgO peaks were observed at  $30.63^\circ$ ,  $32.40^\circ$ ,  $43.83^\circ$  and  $57.62^\circ$  with the crystalline planes (121), (-111), (114) and (402) respectively (01-084-1108; 01-074-1750) with one  $\text{Ag}_2\text{O}$  peak at  $37.78^\circ$  corresponding to the cubic plane (200) of silver (JCPDS 01-076-1393).

Fig. 4.12 (d) presents the XRD pattern of the nanocomposites synthesized at 1:1.6 ratio. The peaks and the crystallographic planes is described in section 4.1.1.1, which shows rutile  $\text{TiO}_2$ ,  $\text{Ag}_2\text{O}$  and AgO. The additional peak of  $\text{Ag}_2\text{O}$  at  $26.24^\circ$  and  $\text{TiO}_2$  at  $41.26^\circ$  is observed in 1:1.6 ratio which is not observed previously for other ratios. This additional peak of  $\text{TiO}_2$  could be attributed to the larger quantity of Ti being used in the synthesis of these nanocomposites as compared to those synthesized with other ratios (1:0.4 and 1:0.8), where Ag is present in higher amount when compared to Ti in the synthesis mixture.

The nanocomposites synthesized at Ag to Ti ratio of 1:2.0 (Fig. 4.12) shows the  $2\theta$  at  $27.98^\circ$ ,  $41.32^\circ$  and  $54.12^\circ$  corresponding to the crystalline plane (110), (111) and (211) of rutile  $\text{TiO}_2$  (JCPDS 00-088-1173), with one peak at  $54.08^\circ$  (122) corresponding to the orthorhombic  $\text{TiO}_2$  (JCPDS No. 00-023-1446). The peaks present at  $30.61^\circ$ ,  $32.35^\circ$ ,  $43.89^\circ$  and  $57.72^\circ$  corresponds to the (121), (-111), (114) and (402) planes of monoclinic AgO respectively (JCPDS 01-084-1108; 00-022-0472).  $\text{Ag}_2\text{O}$  peaks are observed at  $26.33^\circ$ ,  $37.78^\circ$  and  $38.71^\circ$  with the crystalline planes (110), (200) and (101) respectively (JCPDS 01-076-1393; 00-019-1155). The additional peak at  $26.33^\circ$  and  $41.32^\circ$  corresponding to  $\text{Ag}_2\text{O}$  and  $\text{TiO}_2$  is also seen to be present for 1:2.0 ratio similar to those seen in 1:1.6 ratio.

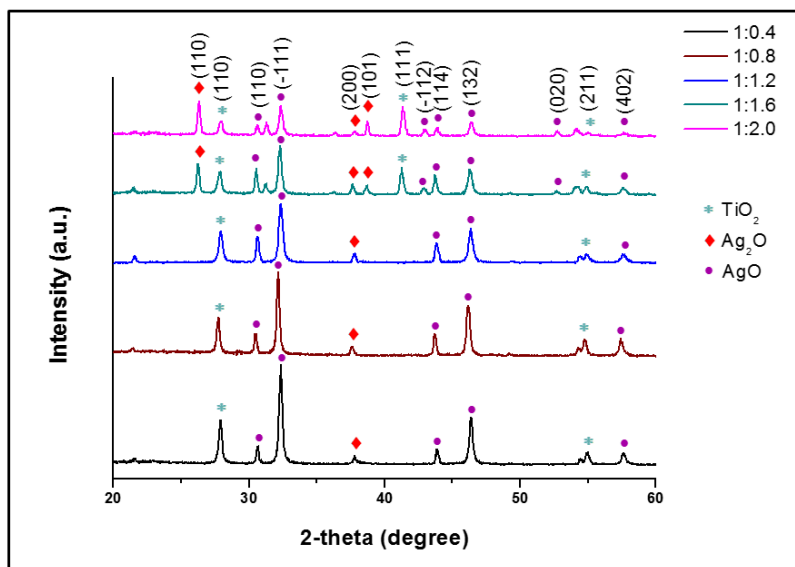


**Fig. 4.12** XRD pattern of the nanoparticles synthesized at different ratios  
 (a) 1:0.4 (b) 1:0.8 (c) 1:1.2 (d) 1:1.6 (e) 1:2.0

These results indicate that the nanocomposite particles formed by Method A with all the ratios of Ag to Ti, comprise of AgO, Ag<sub>2</sub>O and rutile TiO<sub>2</sub>. The average crystallite size calculated using Scherrer's formula is presented in Table 4.3. The crystallite size decreased as the Ti amount was increased when the ratio of Ag to Ti varied from 1:0.4 to 1:1.6 and the ratio of 1:1.6 yielded the particles with the smallest crystallite size of 38 nm. But further increase in the amount of Ti as in the ratio of 1:2, led to further increase in crystallite size, which may be owing to agglomeration of the particles. The presence of additional peaks for TiO<sub>2</sub> and Ag<sub>2</sub>O could also be attributed to the higher degradation rate with 1:1.6 molar ratio.

Tauc plot for the nanocomposites synthesized at different molar ratios of Ag to Ti is presented in Fig. 4.13 and the band gap energy values are presented in Table 4.3. As observed from Fig. 4.13 and Table 4.3, the lowest band-gap was found to be 1.5 eV for the nanocomposite synthesized with Ag to Ti molar ratio of 1:1.6.

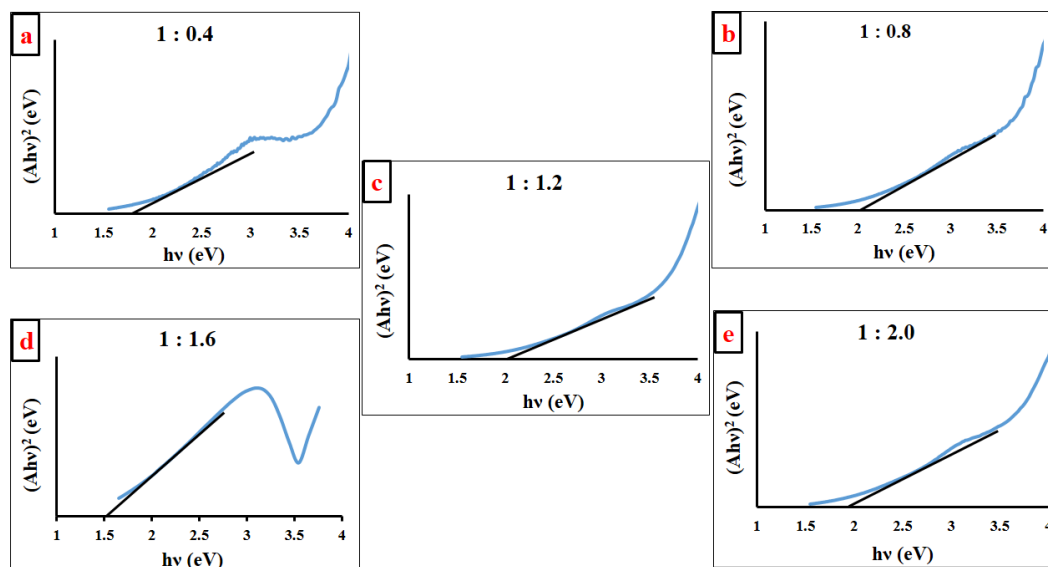


**Fig. 4.13** Tauc plot of the nanocomposites synthesized at different molar ratio

As seen from the degradation experiments, XRD results and the Tauc plot, the degradation rate is the highest with the nanocomposites synthesized using Ag to Ti molar ratio of 1:1.6 with smallest crystallite size and least band-gap compared to those synthesized using the other ratios as presented in Table 4.3. Therefore Ag to Ti molar ratio of 1:1.6, is considered as the optimum for the synthesis of the nanoparticles and used for further experiments.

**Table 4.3** Effect of Ag to Ti molar ratio on percentage dye degradation, initial degradation rate band gap and crystallite size.

Ag:Ti Molar ratio	% dye degradation after 15 min	Initial degradation rate (mg/L/min)	Band-gap (eV)	Crystallite size (nm)
1:0.4	34.6	2.32	1.8	45.9
1:0.8	34.8	2.27	2.0	43.1
1:1.2	40	2.67	2.0	39.7
1:1.6	49	3.26	1.5	38
1:2	44.1	2.94	1.95	44.02

#### 4.1.2.2 Optimization of pH of the supernatant used for the synthesis

The studies on optimization of molar ratio was carried out with cell free supernatant (CFS) pH of 11 as followed by Devadiga, A. (2016) and the optimum molar ratio of Ag to Ti was found to be 1:1.6. Further the CFS pH used for the synthesis was optimized by conducting the synthesis by varying the CFS pH from 5 to 13 with the optimized molar ratio of 1:1.6 and total synthesis time of 48 h (24 h after the addition of Ag precursor and 24 h after the addition of Ti precursor).

As seen from Fig. 4.14, all the nanocomposites synthesized at varied CFS pH of 5 to 11 showed more than 95 % degradation at the end of 90 min whereas 85 % degradation is observed with the nanocomposites synthesized at pH of 13. Although similar percentage degradation is exhibited by all the nanocomposites synthesized at pH 5 to 11, pH 7 showed faster and better degradation with 97 % dye removal in 90 min. The nanocomposite synthesized at pH 5, pH 9 and pH 11 showed around 73 % degradation of the dye and those synthesized at pH 7 showing a maximum of 76 % degradation in 30 min, whereas less than 45 % degradation is observed with the nanocomposite synthesized at pH 13. The initial rates of degradation with the nanoparticles synthesized at various pH are presented in Table 4.4.

It is well evident from the Fig. 4.12 and Table 4.4, that pH 13 displays comparatively lesser dye degradation and lower initial rate than all the other pH and hence slightly acidic to alkaline pH can be acceptable for nanoparticle synthesis so as to get high photocatalytic activity, whereas highly alkaline pH like pH 13 is not favourable for efficient synthesis of AgO/Ag<sub>2</sub>O-TiO<sub>2</sub> nanocomposite. Varying the CFS pH from pH of 5 to 11 showed no significant effect on of the synthesized nanocomposites in terms of their photocatalytic activity. However, pH 13 has negatively influenced the photocatalytic activity. It may be due to inappropriate composition of the formed composite. pH 13 may not have favoured the formation of TiO<sub>2</sub> to form AgO/Ag<sub>2</sub>O-TiO<sub>2</sub> nanocomposite. As the nanoparticles synthesized with CFS pH 7 showed the maximum initial rate of degradation of 3.48 mg/L/min, pH 7 was chosen as the optimum. The degradation kinetics plotted against  $-\ln(C_t/C_o)$  vs time for pH 7 shows the pseudo first-order kinetics (Fig. 4.14 b) with rate constant (k) of 0.0451 min<sup>-1</sup>.

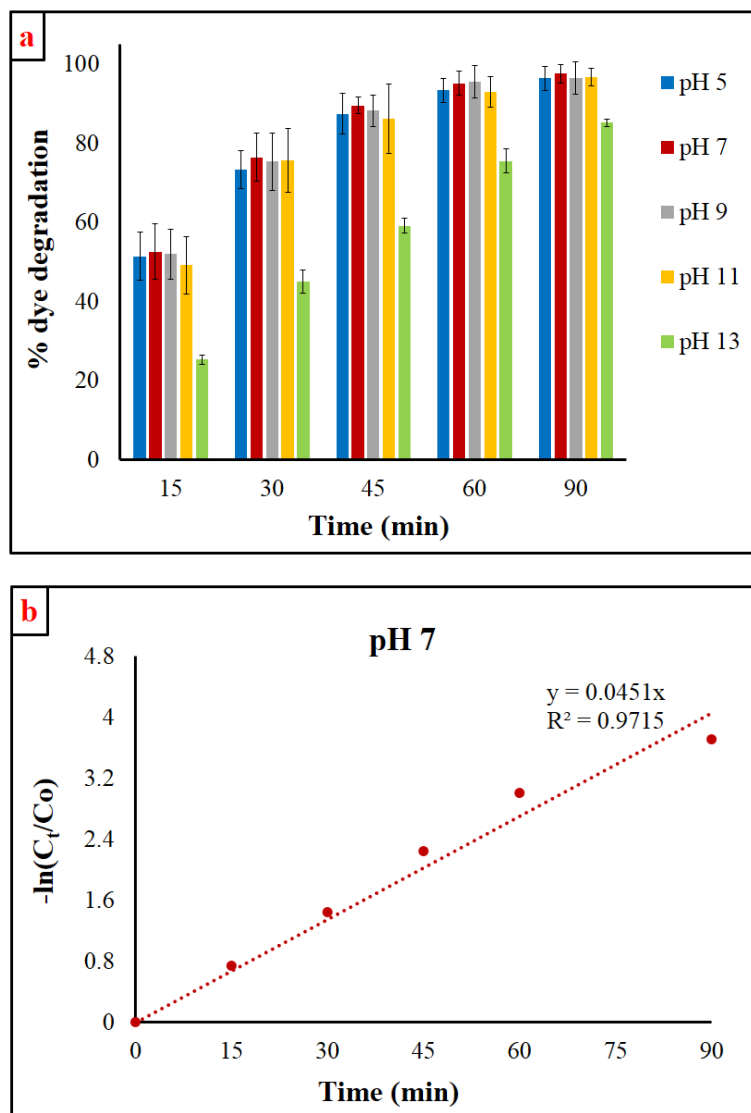


**Fig. 4.14** (a) Time course of variation of percentage dye degradation obtained with nanocomposites synthesized at different pH (b) Pseudo first-order kinetics plot for nanocomposite synthesized at pH 7

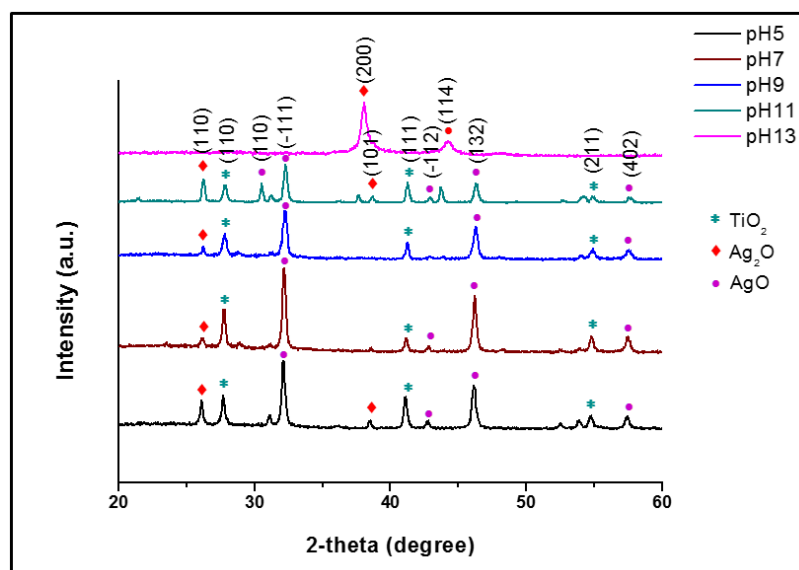
As observed from Fig. 4.15, the XRD of the particles synthesized at pH 5 corresponds to the crystalline plane (110), (111) and (211) of rutile  $\text{TiO}_2$  respectively (JCPDS 01-088-1173). AgO peaks were observed at  $32.11^\circ$ ,  $46.11^\circ$  and  $57.42^\circ$  with planes (-111), (132) and (402) respectively (JCPDS 01-084-1108; 01-075-0969). Ag<sub>2</sub>O peaks are seen at  $26.11^\circ$  and  $38.45^\circ$  corresponding to the crystalline plane (110) and (101) respectively (JCPDS 01-076-1393; 01-07-2108). The average crystallite size calculated from Scherrer's formula was found to be 34.15 nm.

Fig. 4.15 represents the XRD pattern for the nanocomposites synthesized at pH 7. The peaks at  $27.77^\circ$ ,  $41.23^\circ$  and  $54.80^\circ$  corresponds to the rutile crystalline plane (110), (111) and (211) of  $\text{TiO}_2$  respectively (JCPDS 01-088-1173). The peak at  $32.17^\circ$ ,  $46.18^\circ$  and  $57.43^\circ$  is attributed to the (-111), (132) and (402) crystalline plane of cubic AgO (JCPDS 01-076-1489; 01-076-1489). One peak of  $\text{Ag}_2\text{O}$  (JCPDS 01-076-1393) is observed at  $26.20^\circ$  with the crystalline plane (110). The presence of more  $\text{TiO}_2$  peaks might also attribute to the higher photocatalytic activity by the nanocomposites synthesized at pH 7. The average crystallite size was found to be 35.9 nm.

pH 9 shows the  $\text{TiO}_2$  peaks (Fig. 4.15) at  $27.84^\circ$ ,  $41.27^\circ$  and  $54.85^\circ$  corresponding to the crystalline plane (110), (111) and (211) respectively (JCPDS 01-088-1173-74, 03-065-1118). The peak at  $32.26^\circ$  and  $57.53^\circ$  is ascribed to the crystalline plane (-111) and (402) of monoclinic AgO (JCPDS 01-084-1547). Two peaks of  $\text{Ag}_2\text{O}$  (JCPDS 01-076-1393; 00-042-0874) are observed at  $26.24^\circ$  (110) and  $46.24^\circ$  (132) confirming its presence. The average crystallite size of the nanocomposites synthesized at pH 9 was found to be 34.08 nm.

XRD pattern for the nanocomposites synthesized at pH 11 is presented in Fig. 4.15 which shows the following peaks attributing to the crystalline planes (110), (111) and (211) of rutile  $\text{TiO}_2$  respectively (JCPDS 00-088-1173). The peaks at  $30.53^\circ$ ,  $32.30^\circ$ ,  $43.75^\circ$ ,  $46.25^\circ$  and  $57.56^\circ$  can be assigned to (121), (-111), (114), (132) and (402) crystalline planes of AgO (JCPDS 01-084-1108; 01-074-1743). Further the peak at  $26.24^\circ$ ,  $37.63^\circ$  and  $38.69^\circ$  corresponds to  $\text{Ag}_2\text{O}$  with crystalline planes (110), (200) and (101) respectively (JCPDS 01-076-1393; 00-019-1155). The average crystallite size of the nanocomposite was found to be 38 nm.

pH 13 shows very few peaks (Fig. 4.15) with crystalline plane (200) at  $38.06^\circ$  corresponding to  $\text{Ag}_2\text{O}$  (01-072-2108) and one AgO peak at  $44.24^\circ$  with crystalline plane (114). The average crystallite size was found to be 15.7 nm.



**Fig. 4.15** XRD pattern of Ag-TiO<sub>2</sub> nanocomposites synthesized at different pH (a) pH 5, (b) pH 7, (c) pH 9, (d) pH 11 and (e) pH 13

The nanocomposites synthesized at CFS pH 5, pH 7, pH 9 and pH 11 exhibit crystalline peaks for TiO<sub>2</sub>, Ag<sub>2</sub>O and AgO indicating the formation of the nanocomposite whereas only few peaks are seen at pH 13, representing AgO and Ag<sub>2</sub>O. The absence of TiO<sub>2</sub> peak at pH 13 suggests that the synthesis of TiO<sub>2</sub> is not favoured when synthesis was carried out with CFS pH of 13. The nanocomposite is not formed effectively and absence of TiO<sub>2</sub> could be a reason for its lower photocatalytic activity. As shown in Table 4.4, the nanocomposite synthesized a with CFS pH 13 has the least crystallite size, which is an indicative of the formation of silver oxides in the first step and no adequate formation of TiO<sub>2</sub> coating in the subsequent step leading to lower size.

Table 4.4 presents the percentage degradation at 15 min, initial degradation rate, band-gap energy and crystallite size. Fig. 4.16 shows that the nanocomposites have the band-gaps in the range of 1.45 – 1.75 eV (Table 4.4) with the least band-gap of 1.45 eV exhibited by the nanocomposites synthesized at pH 13 followed by those synthesized at pH 7 and pH 11 showing band-gap energy of 1.5 eV. Even though the nanocomposite synthesized at pH 11 and 13 exhibit band-gap of 1.5 eV and 1.45 eV respectively, the initial rate of dye degradation is marginally faster and the better photocatalytic activity is exhibited by nanoparticles synthesized at pH 7.

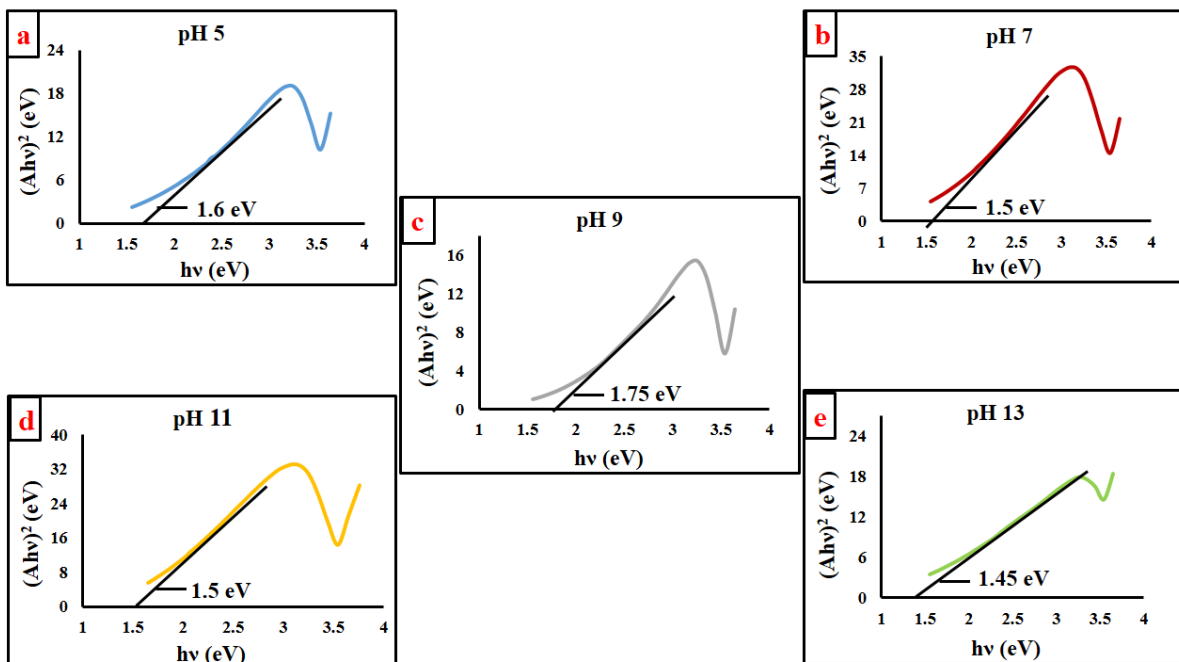


**Fig. 4.16** Tauc plot displaying band-gap energy of the nanocomposites synthesized at different pH

Therefore as seen from the above experiments and as depicted in Table 4.4, nanocomposites synthesized at pH 7 shows marginally better degradation of the dye with better photocatalytic activity with lower band-gap energy when compared to nanocomposites synthesized at other pH values, though the crystallite size is not the smallest. These results indicate that synthesis CFS pH is an important parameter in determining the composition and band gap of nanocomposites, thus governing the photocatalytic activity. Considering the better photocatalytic activity and in order to reduce the challenges involved in controlling the pH, neutral pH of pH 7 was chosen as the optimum pH for further experiments. 97 % of 100 ppm dye could be degraded in 90 min under visible light irradiation with the nanocomposite synthesized at pH 7.

**Table 4.4** Effect of CFS pH used in the synthesis on dye degradation, initial rate, band-gap energy and crystallite size of synthesized nanocomposites

CFS pH for synthesis	% dye degradation after 15 min	Initial degradation rate (mg/L/min)	Band-gap (eV)	Crystallite size (nm)
5	51.34	3.38	1.6	34.15
7	52.52	3.48	1.5	35.9
9	51.87	3.43	1.75	34.08
11	49.07	3.26	1.5	38
13	25.27	1.66	1.45	15.7

#### 4.1.2.3. Optimization of synthesis time after the addition of silver precursor (step 1)

The nanocomposite particles were synthesized by Two step method (Method A), by varying the synthesis time in the first step after the addition of silver precursor solution. The Ag to Ti ratio of 1:1.6 was used in the synthesis process with 50 mL supernatant (at pH 7) in each step and total 100 mL of supernatant in two steps. The synthesis time in the first step, i.e the time for reduction of Ag salt after its addition (before the addition of Ti precursor) was varied as 2, 4, 8, 16 and 24 h ( $t_{\text{step 1}}$ ). However, synthesis time for TiO<sub>2</sub> provided after the addition of Ti precursor ( $t_{\text{step 2}}$ ) was kept constant as 24 h.

As observed in Fig. 4.17 (a), the percentage dye degradation at the end of 90 min of irradiation time was found to be almost equal with the nanocomposites synthesized with varying  $t_{\text{step 1}}$ . Around 96.2, 97.4, 97.4, 97.4 and 97.5 % degradation of dye could be achieved in 90 min with the nanocomposites synthesized with  $t_{\text{step 1}}$  of 2, 4, 8, 16 and 24 h. With the nanocomposite synthesized with  $t_{\text{step 1}}$  of 16 h and 24 h, slightly higher degradation was achieved when compared to that synthesized with 2 h to 8 h of  $t_{\text{step 1}}$ . The initial degradation rates are presented in Table 4.5. The initial rate of degradation of the dye is the maximum (3.85 mg/L/min) with nanocomposites synthesized with  $t_{\text{step 1}}$  of 4 h and  $t_{\text{step 2}}$  of 24 h. The rate constant obtained from the kinetics plot (Fig. 4.17 b) for optimum time interval of 4 h ( $t_{\text{step 1}}$ ) was found to be 0.0427 min<sup>-1</sup>.

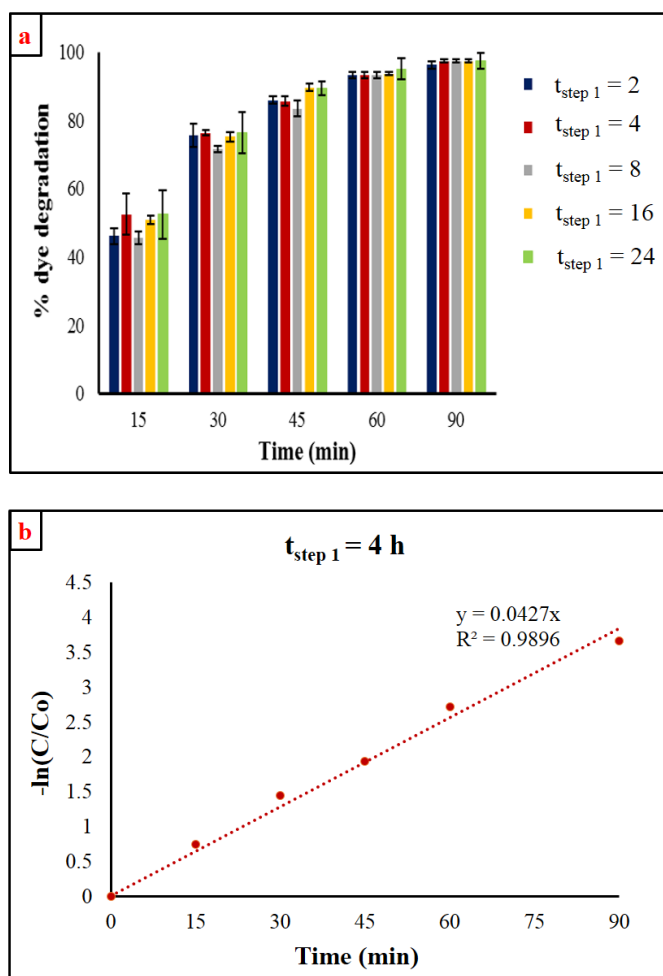


**Fig. 4.17** (a) Time course of variation of percentage dye degradation obtained with nanocomposite synthesized with varying  $t_{\text{step 1}}$  and constant  $t_{\text{step 2}}$  of 24 h (b) Pseudo first-order kinetics plot for  $t_{\text{step 1}} = 4$  h

Fig. 4.18 presents the XRD of the nanocomposites synthesized at varying synthesis time,  $t_{\text{step 1}}$  of 2, 4, 8, 16 and 24 h with  $t_{\text{step 2}}$  being constant at 24 h. The nanocomposites synthesized at  $t_{\text{step 1}}$  of 2 and 4 h, show the same pattern with crystallographic planes (110) and (211) of rutile  $\text{TiO}_2$  (JCPDS 01-088-1173) and AgO peaks corresponding to the crystallographic planes (-111), (132) and (402) (JCPDS 01-076-1489). No peaks were detected for  $\text{Ag}_2\text{O}$  indicating that the synthesis time in step 1 ( $t_{\text{step 1}}$ ) of 2 and 4 h consists of only AgO and  $\text{TiO}_2$ . From the XRD analysis, it can be inferred that formation of  $\text{Ag}_2\text{O}$  occurs after 4 h of  $t_{\text{step 1}}$ . The nanocomposites synthesized at  $t_{\text{step 1}}$  of 8, 16 and 24 h displayed additional peaks corresponding to the (111) of rutile  $\text{TiO}_2$  and

(110) of  $\text{Ag}_2\text{O}$  along with those peaks of  $\text{TiO}_2$  and  $\text{AgO}$  present for 2 and 4 h. The average crystallite size of the nanocomposites synthesized with varying  $t_{\text{step 1}}$  of 2, 4, 8, 16 and 24 h are presented in Table 4.5, which shows that the crystallite size is the maximum for the nanocomposites synthesized with  $t_{\text{step 1}}$  of 4. Although there is absence of few peaks and slight larger crystallite size for the nanocomposites synthesized at 4 h, it exhibited higher photocatalytic activity.

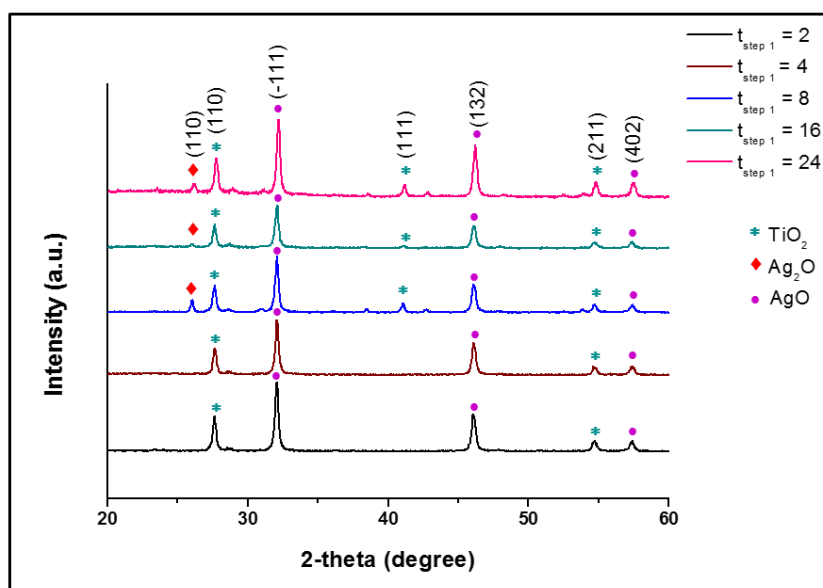


**Fig. 4.18** XRD pattern of the nanocomposites synthesized with varying  $t_{\text{step 1}}$  and constant  $t_{\text{step 2}}$  of 24 h

The nanocomposites synthesized at different time interval for reduction of silver precursor ( $t_{\text{step 1}}$ ), show band-gap in the range of 1.5 eV – 2.0 eV as shown in Fig. 4.19. Nanocomposites synthesized at 8 h shows 2.0 eV, 16 h shows 1.95 eV, 2 h shows 1.8 eV and both 4 h and 24 h show a band-gap of 1.5 eV as presented in Table 4.5. Among all the nanocomposites synthesized at different synthesis time for silver ion reduction, the nanocomposites synthesized with 4 h and 24 h time for synthesis in step 1, show the lowest band-gap of 1.5 eV attributing to its highest photocatalytic activity in the degradation of dye. Bian et al. (2020) in their studies on photocatalysis using  $\text{Ag}/\text{ZnO}/\text{AgO}/\text{TiO}_2$  nanocomposite in RhB degradation under UV–Vis irradiation have reported that band gap lowering enhances the photocatalytic activity and silver oxides absorb the light in the visible range, owing to their low band gap energy. When the

band-gap energy is lower, the catalysts can be excited by longer wavelength light such as those in visible or NIR range. Hence such materials can absorb light in the wide range of solar spectrum where as those with higher band-gap energy can absorb light only in the narrow range falling under ultraviolet region (Farooq et al. 2019).

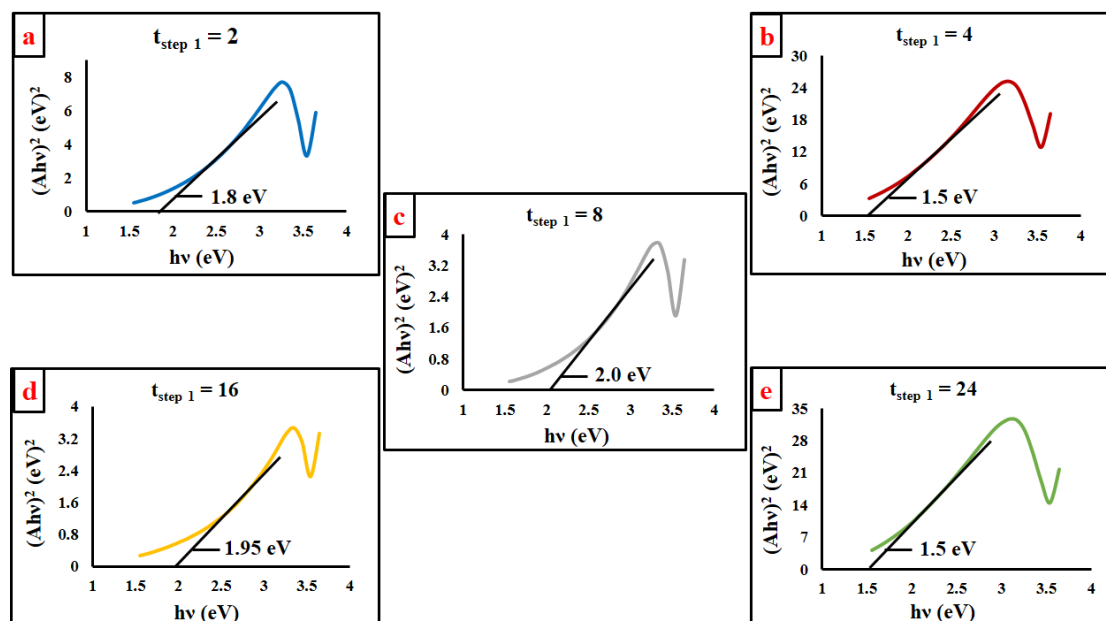


**Fig. 4.19** Tauc plot showing band-gap energy for  $\text{Ag}_2\text{O}/\text{AgO-TiO}_2$  nanocomposite synthesized at varying  $t_{\text{step 1}}$  and constant  $t_{\text{step 2}}$  of 24 h

**Table 4.5** Effect of  $t_{\text{step 1}}$  on dye degradation, initial dye degradation rate, band-gap energy and crystallite size of nanocomposites synthesized at different time periods.

Time period after the addition of Ag precursor ( $t_{\text{step 1}}$ )	% dye degradation after 15 min	Initial degradation rate (mg/L/min)	Band-gap energy (eV)	Crystallite size (nm)
2	46.08	3.08	1.8	41.18
4	52.44	3.85	1.5	46.96
8	45.61	3.13	2.0	43.91
16	50.925	3.62	1.95	38.91
24	52.52	3.48	1.5	37.2

It is known from the above experiments that 4 h duration for the step 1 of reduction of silver precursor in the synthesis process is better in terms of higher initial degradation rate, lowest band-gap and maximum photocatalytic activity. The higher photocatalytic activity of the nanocomposite at  $t_{\text{step 1}}$  of 4 h could be due to the small band-gap and the composition with presence of only AgO and TiO<sub>2</sub> in the nanocomposite formation which could provide better light absorption thereby enhancing its activity in spite of its larger crystallite size. Since lesser time is involved in the synthesis of the nanocomposite with 4 h duration in Step 1 for silver ion reduction, as compared to that synthesized at 16 h or 24 h with nearly similar initial rates, 4 h time for reduction of silver ions in the synthesis of nanocomposites was chosen. The method thus chosen involved 4 h for step 1 of silver ion reduction, followed by addition of Ti precursor and 24 h synthesis time after the addition of Ti precursor for the formation of TiO<sub>2</sub>, thus making total synthesis time as 28 h. Further the synthesis time after the addition of Ti precursor was varied by keeping the time for step 1 of silver ion reduction as 4 h.

#### **4.1.2.4. Optimization of synthesis time after the addition of Ti precursor ( $t_{\text{step 2}}$ )**

Based on the results discussed above, it is found that 4 h synthesis time was the optimum for the reduction of silver ions ( $t_{\text{step 1}}$ ) at CFS pH 7 with Ag to Ti molar ratio of 1:1.6 and hence further the time for the synthesis of nanocomposite after the addition of Ti precursor ( $t_{\text{step 2}}$ ) was varied while keeping the  $t_{\text{step 1}}$  constant at 4 h for reduction of silver ions.

From Fig. 4.20 (a) it is evident that the nanocomposite synthesized with 4 h synthesis time after the addition of Ti precursor ( $t_{\text{step 2}}$ ) showed maximum photocatalytic degradation of the dye when compared to those synthesized with other synthesis times. Initial rates of degradation (Table 4.6) is faster in case of  $t_{\text{step 2}}$  of 4 h, however at the end of 90 min, all the nanocomposites showed almost similar percentage of degradation with 97.4, 98, 96.6, 97 and 97.4 % for  $t_{\text{step 2}}$  of 2, 4, 8, 16 and 24 h respectively. Maximum dye degradation at the end of 15 min was 57 % with nanocomposites synthesized with 4 h time ( $t_{\text{step 2}}$ ) for TiO<sub>2</sub> formation, followed by 54%, 52%, 47% and 46 % for 16 h, 24 h, 8 h and 2 h respectively (Table 4.6). Therefore 4 h synthesis time

after the addition of Ti precursor ( $t_{\text{step } 2}$ ) was found to be better in terms of degradation rate. The degradation kinetics for the optimum  $t_{\text{step } 1}$  of 4 h and  $t_{\text{step } 2}$  of 4 h with total time of 8 h followed pseudo first-order kinetics with  $k$  value of  $0.0492 \text{ min}^{-1}$  (Fig. 4.20 b) which is higher than  $0.0406 \text{ min}^{-1}$  which is for the unoptimized condition (Section 4.2.1).

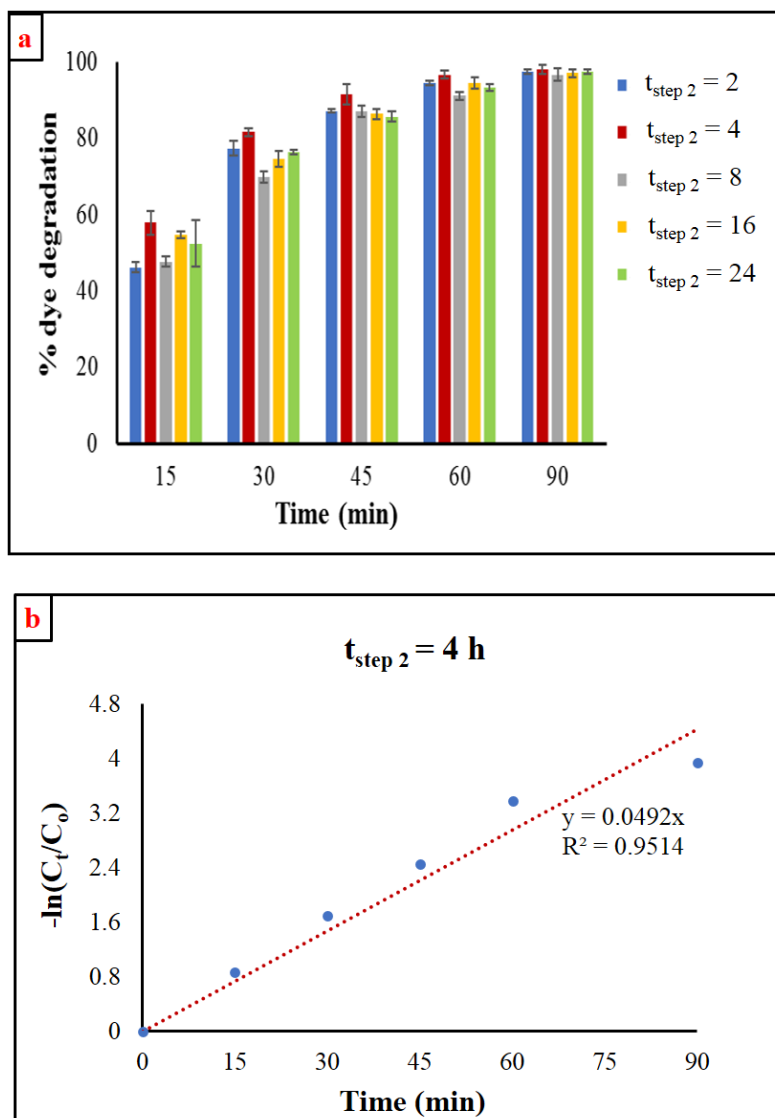


**Fig. 4.20** (a) Time course of variation of percentage dye degradation obtained with nanocomposite synthesized with varying  $t_{\text{step } 2}$  and constant  $t_{\text{step } 1}$  of 4 h (b) Pseudo first-order kinetics plot for  $t_{\text{step } 2} = 4$

XRD characterization of the nanocomposites synthesized at varied  $t_{\text{step } 2}$  of 2, 4, 8, 16 and 24 h are presented in Fig. 4.21. As observed from Fig. 4.19, nanocomposites

synthesized at  $t_{\text{step } 2}$  of 2, 4, 8 and 16 h displayed similar pattern showing the presence of  $\text{TiO}_2$ ,  $\text{Ag}_2\text{O}$  and  $\text{AgO}$  with (110), (111) and (211) crystallographic planes corresponding to rutile  $\text{TiO}_2$  (JCPDS 01-088-1173) and  $\text{AgO}$  peaks corresponding to (-111), (132) and (402) planes (JCPDS 01-076-1489). Additional peak attributing for the (110) crystallographic plane of  $\text{Ag}_2\text{O}$  is observed in the XRD of the nanocomposites synthesized with all the  $t_{\text{step } 2}$ , which is absent in  $t_{\text{step } 2}$  of 24 h. The presence of additional peak of  $\text{TiO}_2$  at (111) plane indicates that higher amount of Ti precursor being utilized in the formation of the nanocomposites for all the  $t_{\text{step } 2}$  except for 24 h. The absence of additional  $\text{TiO}_2$  peak when 24 h synthesis time was used after the addition of Ti precursor ( $t_{\text{step } 2}$ ) may be attributed to phase transformation of  $\text{TiO}_2$  after 16 h. The presence of the additional peaks could lead to higher degradation rate as observed in Fig. 4.18 in nanocomposites synthesized at  $t_{\text{step } 2}$  of 4 h. The average crystallite size calculated from Scherrer's formula was found to be 41.7, 28.8, 29.2, 36.5 and 46.9 nm for  $t_{\text{step } 2}$  of 2, 4, 8, 16 and 24 h (Table 4.6). The smallest crystallite size was found to be 28.8 nm for  $t_{\text{step } 2}$  of 4 h beyond which the size increases with increase in time upto 24 h.

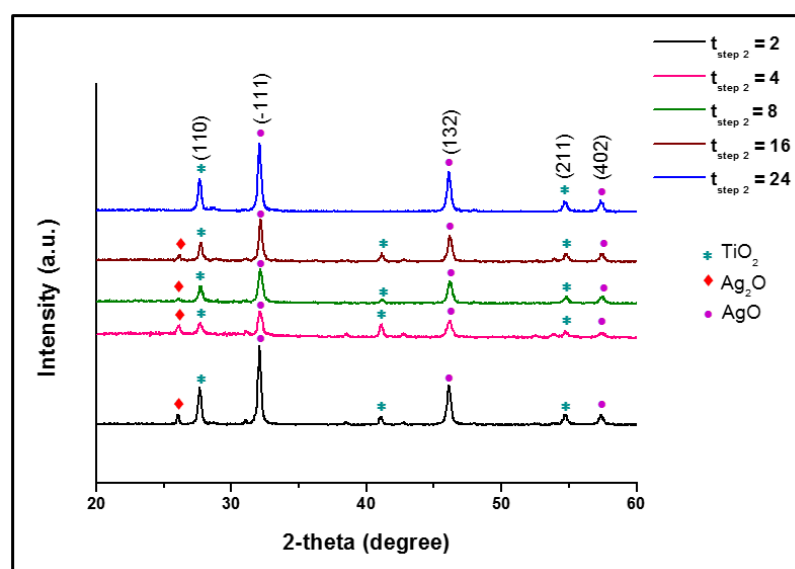


**Fig 4.21** XRD pattern of the nanocomposites synthesized with varying  $t_{\text{step } 2}$  and constant  $t_{\text{step } 1}$  of 4 h

Fig. 4.22 shows the band-gap energy for the nanocomposites synthesized at different time period after the addition of Ti precursor ( $t_{\text{step 2}}$ ). As it is seen, the lowest band-gap is displayed for nanoparticles synthesized with  $t_{\text{step 2}}$  of 24 h with 1.5 eV (Fig. 4.22) followed by 16 h and 4 h showing 1.65 and 1.7 eV respectively. Table 4.6 shows the band-gap energies for nanocomposites synthesized by varying  $t_{\text{step 2}}$  keeping  $t_{\text{step 1}}$  constant at 4 h.

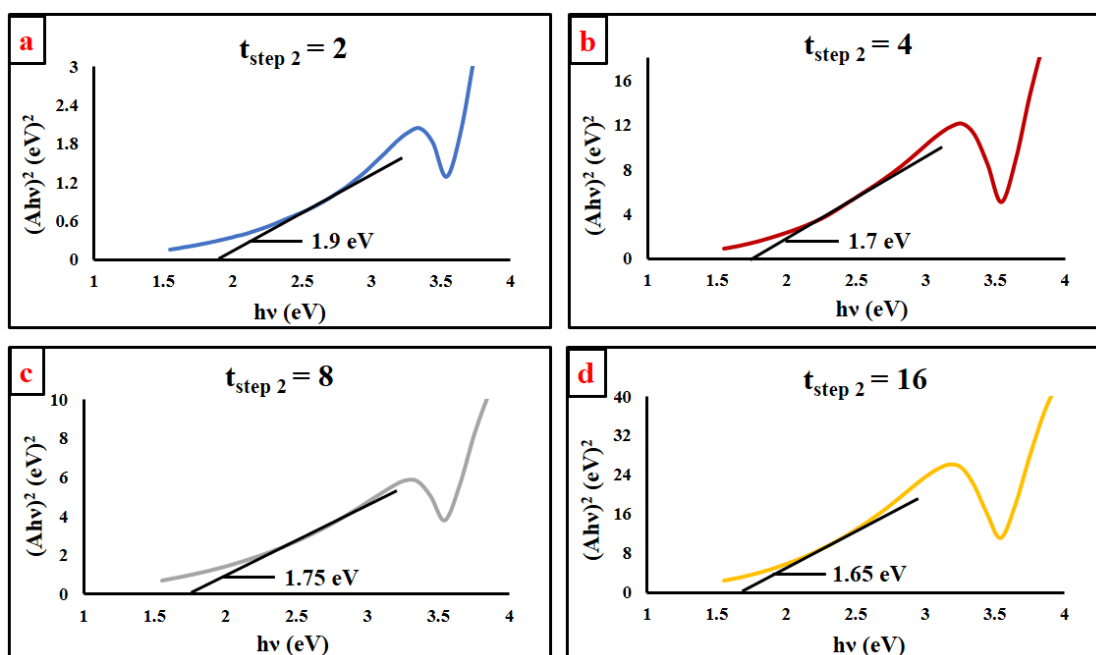


**Fig. 4.22** Tauc plot for the nanocomposites synthesized at varying  $t_{\text{step 2}}$  with  $t_{\text{step 1}}$  of 4 h.

**Table 4.6** Effect of  $t_{\text{step 2}}$  on dye degradation, initial rate of dye degradation, band-gap energy and crystallite of the synthesized nanocomposites

Time period after the addition of Ti precursor ( $t_{\text{step 2}}$ )	% dye degradation after 15 min	Initial degradation rate (mg/L/min)	Band-gap energy (eV)	Crystallite size (nm)
2 h	46.15	3.08	1.9	41.7
4 h	57.88	3.85	1.7	28.8
8 h	47.48	3.13	1.75	29.2
16 h	54.61	3.62	1.65	36.5
24 h	52.44	3.48	1.5	46.9

The nanocomposite synthesized at  $t_{\text{step 2}}$  of 4 h showed band-gap of 1.7 eV with maximum and faster dye degradation at the end of 15 min. Although the least band-gap is exhibited by the nanocomposites synthesized at 24 h time ( $t_{\text{step 2}}$ ), considering lesser process time involved in the synthesis of nanocomposites, smaller crystallite size of 28.8 nm and maximum initial rate of dye degradation and percentage degradation after 15 min of irradiation, 4 h synthesis time for  $\text{TiO}_2$  formation ( $t_{\text{step 2}}$ ), was selected for the synthesis of the nanocomposite. The method thus chosen involved 4 h for step 1 of silver ion reduction ( $t_{\text{step 1}}$ ), followed by addition of Ti precursor and 4 h synthesis time after the addition of Ti precursor ( $t_{\text{step 2}}$ ) for the formation of  $\text{TiO}_2$ , thus making total synthesis time as 8 h. On optimization, the total synthesis time could be reduced from 48 h to 8 h.

After optimization, the optimum synthesis conditions were found to be molar ratio of Ag to Ti of 1:1.6, CFS pH of 7,  $t_{\text{step 1}}$  and  $t_{\text{step 2}}$  of 4 h each. On optimization of the synthesis parameters for the nanocomposite, the initial degradation rate of dyes could be increased from 3.26 to 3.85 (mg/L/min) with percentage reduction being changed from 96 % to 98 % at the end of 90 min in comparison to the unoptimized nanocomposite.

Further, LCMS analysis was performed in order to study the intermediates and products formed during photocatalysis by the nanocomposites synthesized under optimum conditions based on the mass to charge ratio and to further confirm the degradation and mineralization of the dye molecules by photocatalysis. The samples before and during the reaction were subjected to LCMS. Electrospray ionization (ESI) in positive ion mode was used to ionize the compounds. The MS spectra of the reaction mixture before the photocatalysis experiment and degraded samples after 30 min and 60 min of irradiation are shown in Fig. 4.23 (a) to (c) respectively. The peak at 733.54 in Fig. 9 (a) corresponds to the dye. Several other peaks present in Fig. 9 (a) correspond to the impurities present in the dye, as the dye used was a commercial dye. The peak for  $m/z$  733.54 disappeared as the reaction proceeded (Fig. 4.23 (b) and (c)), indicating the degradation of the dye molecules. All the other peaks which were initially present have disappeared and the intensity of the peak at  $m/z$  of 301.14 reduced indicating that

several compounds which were present as impurities along with the dye have been degraded as the reaction proceeded. However, new peaks for  $m/z$  of 705.53, 689.56, 494.81, 425.21, 385.28 and 229.13 were observed after 30 min which correspond to the reaction intermediates. Further, after 60 min of irradiation, a few more new peaks have been formed with  $m/z$  value of 663.45, 587.49 and 359.23 indicating the formation of other intermediates. The peaks for  $m/z$  of 705.53, 689.56 and 229.13 have increased showing the formation of more amount of these intermediates.

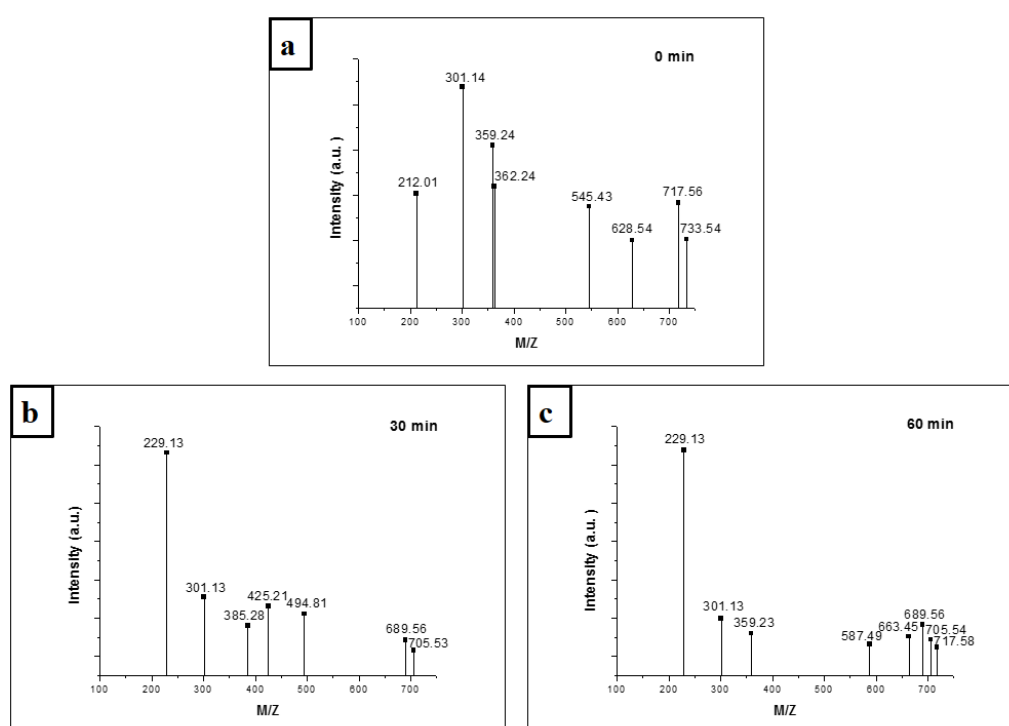


**Fig. 4.23** Mass spectrum of the reactor samples (a) before the start of photocatalysis experiment (b) after 30 min of photocatalytic reaction under visible light irradiation (c) after 60 min of photocatalytic reaction under visible light irradiation.

Based on the  $m/z$  values of the intermediates observed, two schemes for the pathway of the degradation of the dye are proposed and shown in Fig. 4.24 (a) and (b). The proposed pathway shows the degradation of the dye and the intermediate with  $m/z$  of 229.13 may get further mineralized into organic acids and other inorganic compounds.



1 and  $t_{\text{step } 2}$  of 4 h each, were further characterized. XRD pattern for the nanocomposites is presented in Fig. 4.25. XRD study shows major peaks at  $27.65^\circ$  and  $32.10^\circ$  attributing to the formation of rutile  $\text{TiO}_2$  (JCPDS No.01-088-1173) and  $\text{AgO}$  (JCPDS No 01-076-1489) with crystalline planes (110) and (111) respectively. The peaks at  $41.07^\circ$  and  $54.74^\circ$  is attributed to the (111) and (211) crystalline plane of  $\text{TiO}_2$  (JCPDS No, 01-088-1173). The peak at  $26.11^\circ$  and  $38.49^\circ$  can be indexed to the crystalline plane (110) and (101) of  $\text{Ag}_2\text{O}$  (JCPDS 01-072-2108). Apart from the peak at  $32.10^\circ$ ,  $\text{AgO}$  peaks is also seen at  $46.21^\circ$  and  $57.47^\circ$  with crystalline plane (132) and (402) respectively (JCPDS 01-076-1489). The nanocomposite synthesized under optimum conditions comprise of  $\text{Ag}_2\text{O}$ ,  $\text{AgO}$  and  $\text{TiO}_2$ . Thus, these nanocomposite particles are represented as  $\text{AgO}/\text{Ag}_2\text{O}@\text{TiO}_2$  nanocomposites. The average crystallite size calculated using Scherrer's formula was found to be 28.8 nm.

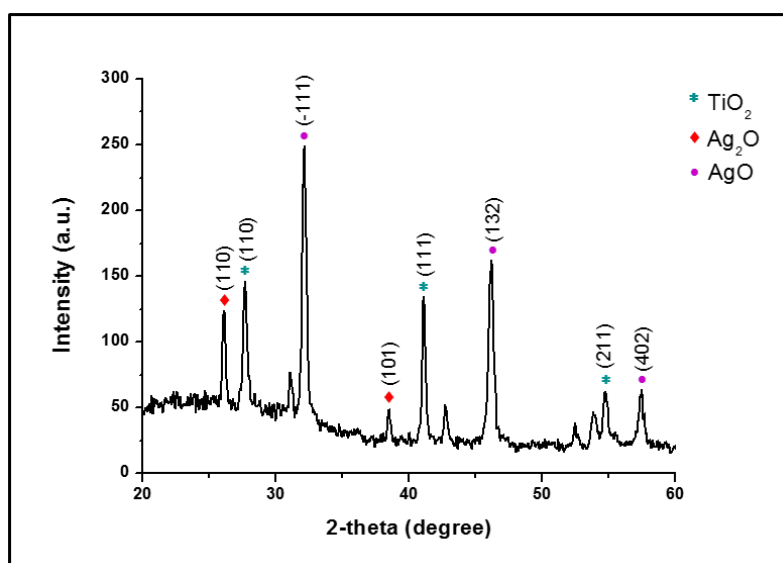


**Fig. 4.25** XRD pattern of the  $\text{AgO}/\text{Ag}_2\text{O}@\text{TiO}_2$  nanocomposite synthesized at optimum condition of total 8 h synthesis time

Fig. 4.26 (a) shows the SEM images of the  $\text{AgO}/\text{Ag}_2\text{O}@\text{TiO}_2$  nanocomposite synthesized by cell-free supernatant of *Alcaligenes aquatilis* under optimum conditions. Nanoparticles produced were found to be spherical in shape. EDX analysis (Fig. 4.26 b) of the nanocomposites show strong signal for Ag, Ti and O atoms with few weak signals which might be due to the elements in the macromolecules present in the cell

free supernatant of the bacteria. The atomic and weight percentage of Ag, O and Ti elements are shown in the inset of Fig. 4.26 (b).

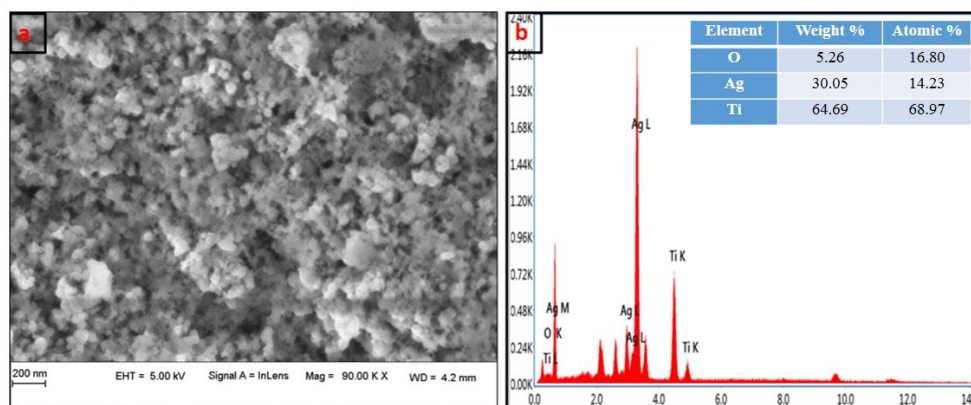


**Fig. 4.26** (a) SEM and (b) EDX of the nanocomposites synthesized under optimized condition (inset – weight and atomic and percentage of Ag, O and Ti)

TEM image in the Fig. 4.27 (a) and (b) show different sized nanoparticles with dark coloured AgO/Ag<sub>2</sub>O particles embedded inside TiO<sub>2</sub> (grey) film. The AgO/Ag<sub>2</sub>O@TiO<sub>2</sub> nanocomposite particles are small and spherical with average particle size of 29.8 nm as observed from particle size distribution graph (Fig. 4.27 c). The SAED pattern (Fig. 4.27 (d)) shows the polycrystalline nature of the nanocomposite with d-spacing value of 1.96 Å and 2.78 Å corresponding to the (132) and (-111) plane of AgO, 2.33 Å corresponding to (101) plane of Ag<sub>2</sub>O and 1.67 Å corresponding to the (211) planes of rutile TiO<sub>2</sub> respectively.

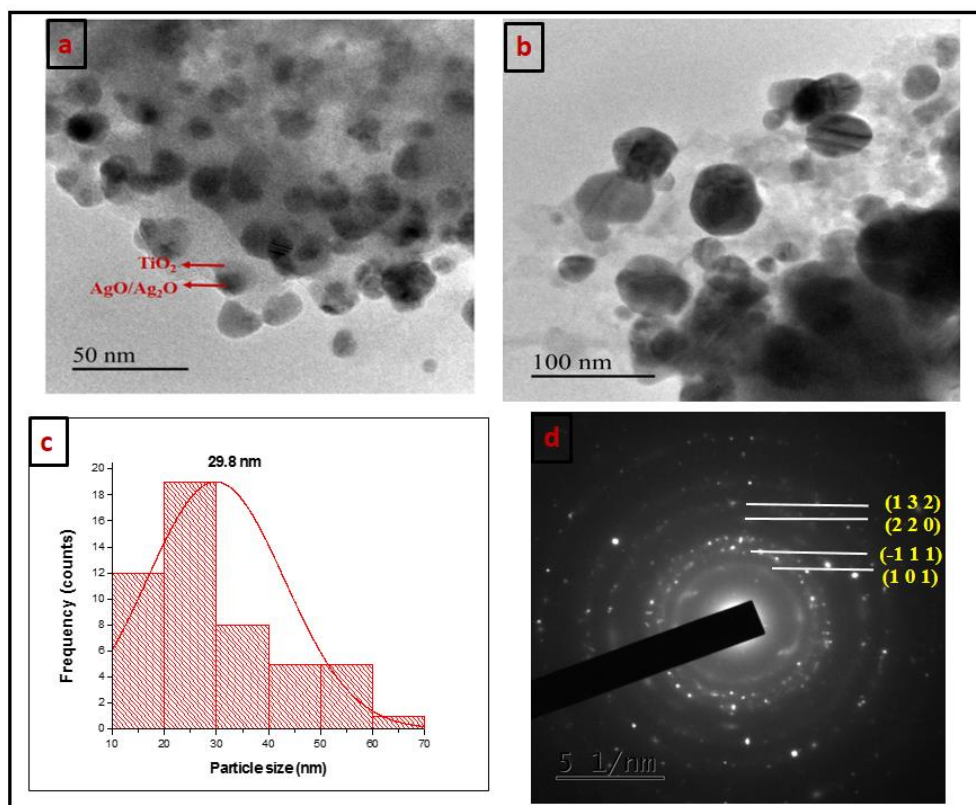


**Fig. 4.27** TEM image (a) and (b) of the nanocomposites at different magnification (c) Particle size distribution (d) SAED image of the nanocomposites synthesized under optimized condition.

FTIR spectra of the nanocomposite is shown in Fig. 4.28. The peak at  $3432\text{ cm}^{-1}$  and  $3501\text{ cm}^{-1}$  indicates the presence of alcoholic group seen as O-H stretching (Ordenes-Aenishanslins et al. 2014, Zhang et al. 2012). The bands in the  $3200\text{--}3600\text{ cm}^{-1}$  regions are associated with OH stretching mode. The band at  $1771\text{ cm}^{-1}$  is most likely associated with C=O bonds due to carboxylic group vibrations (Petit et al. 2017). The peak obtained at  $1627\text{ cm}^{-1}$  with N-H bending showed the presence of primary amines and the peak located at  $1026\text{ cm}^{-1}$  is due to the C-N stretching of aliphatic amines (Janakiraman et al. 2015). The region between  $1800$  and  $1500\text{ cm}^{-1}$  could be ascribed to the amide I and amide II bands (Nauman, D. 2000). The peaks from  $900$  to  $500\text{ cm}^{-1}$  are due to the presence of Ti-O bond (Hamrouni et al. 2020). The presence of various groups on the nanocomposite as evidenced by FTIR results, suggests that some biomolecules present in the bacterial cell free supernatant serve as capping agents and they may have been responsible for the formation and stabilization of nanoparticles.

The extracellular polymeric substances (EPS) present in the cell free supernatant containing the proteins, amino acids, lipids etc are known to play a key role in the synthesis of these nanoparticles and in stabilization of the nanoparticles due to capping proteins (Wei et al. 2012; Fouad et al. 2016).

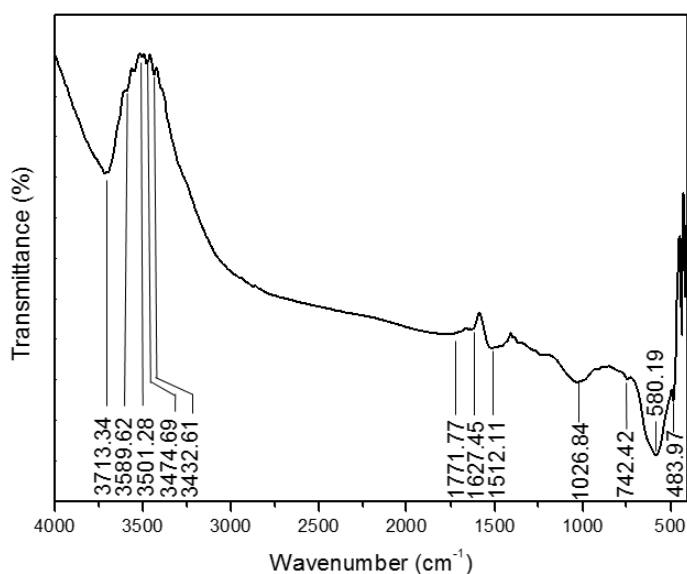


**Fig. 4.28** FTIR spectra of the nanocomposites

XPS (Fig. 4.29 a) of the nanocomposite shows the presence of O1s, Ag3d, Ti2p and C1s with respective binding energies. The XPS spectra of Ti2p (Fig. 4.29 b) shows two peaks at 465.5 and 459.5 eV which is ascribed to Ti2p<sub>1/2</sub> and Ti2p<sub>3/2</sub> respectively in TiO<sub>2</sub>. However, they have reported Ti2p peaks found at slightly lower binding energies (459.4 and 464.9 eV) which is corresponding to Ti<sup>4+</sup> state (Gannoruwa et al. 2016). Ag3d consists of two main peaks positioned at 365.2 and 371.2 eV corresponding to Ag3d<sub>5/2</sub> and Ag3d<sub>3/2</sub> along with another small peak at 375.65 eV (Fig. 4.29 c). The binding energies for Ag 3d<sub>5/2</sub> of 367.3 and 367.7 have been assigned to AgO and Ag<sub>2</sub>O respectively (Hoflund and Hazos, 2000, Hoflund and Weaver 1995). Liu et al. (2019) reported the peaks of the pristine Ag<sub>2</sub>O at 367.9 and 374 eV, attributing to the Ag 3d<sub>5/2</sub> and Ag3d<sub>3/2</sub> of Ag<sup>+</sup>. However, in the present study a shift in Ag 3d<sub>5/2</sub> binding energy to 365.2 has been observed. Rtimi et al. (2013) have also reported the binding energy ranging from 364.7 to 365.4 eV for Ag3d attributing to the presence of silver in AgO and Ag<sub>2</sub>O respectively. Such a shift was attributed to a shift to Ag<sup>1+</sup>/Ag<sup>2+</sup> redox

reactions on interaction of sample with bacterial metabolic constituents (Rtimi et al. 2013). Su et al. (2012) have reported that the shift of the peaks to lower binding energy compared to the standard may be attributed to the interaction between AgO and Ag<sub>2</sub>O with TiO<sub>2</sub>. Ag3d<sub>3/2</sub> peak also has been found to shift from a standard value of 373.4 eV (Su et al. 2012) to 371.2 due to similar reasons. The appearance of additional Ag3d<sub>3/2</sub> peaks at 374, 375 and 378 eV have also been reported by Gannoruwa et al. (2016), attributing to the presence of both Ag<sup>+</sup> and Ag<sup>0</sup> states in the Ag<sub>2</sub>O / TiO<sub>2</sub> photocatalyst. The O1s peak (Fig. 4.29 d) located at 528.85 can be ascribed to the O<sup>2-</sup> in Ag<sub>2</sub>O as reported in the literature (Akel et al. 2018). The peaks for C at 282.5, and 290.7 eV (Fig. 4.29 e) are assigned to carbides, carbonates respectively and the peak at 293.5 eV is ascribed to CF<sub>3</sub> which can be due to the K<sub>2</sub>TiF<sub>6</sub> (used as Ti precursor) used in the synthesis of TiO<sub>2</sub> embedded AgO/Ag<sub>2</sub>O nanocomposite. The peaks for carbon could be attributed to the presence of organic groups of biological origin on the surface of nanocomposite particles which act as capping agents.

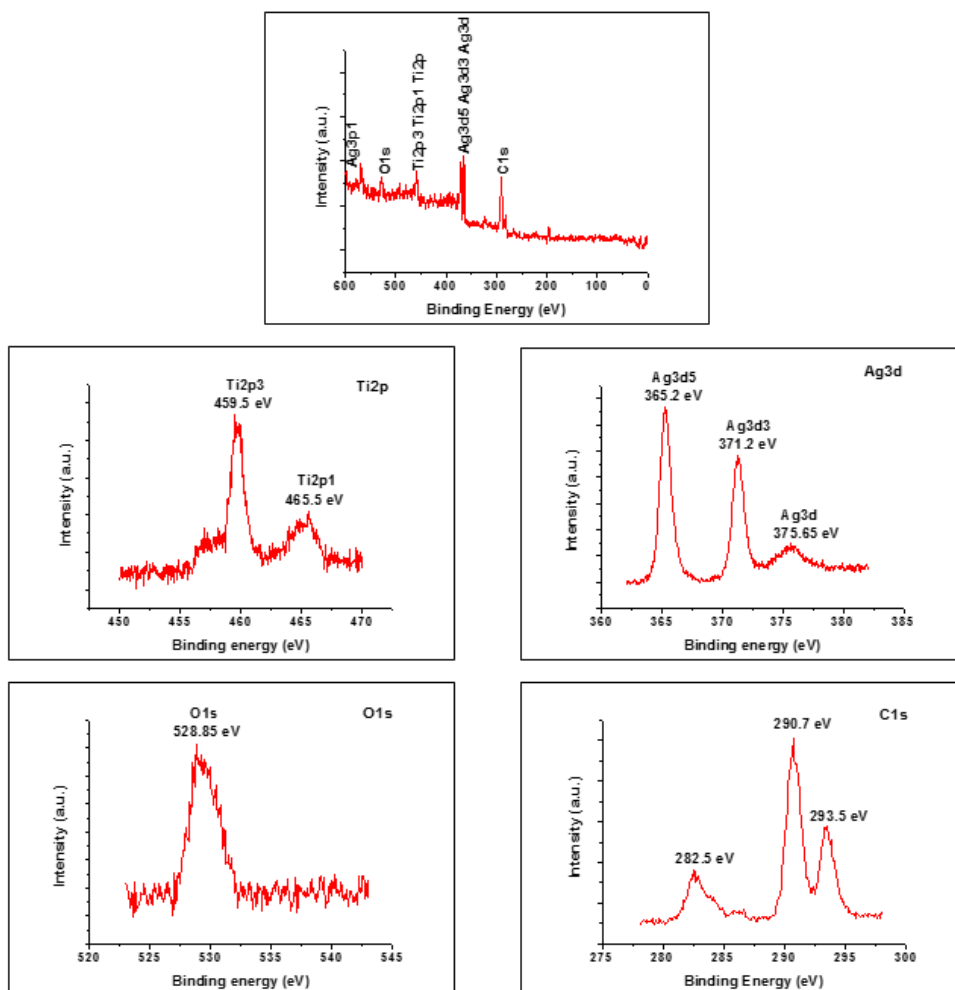


**Fig. 4.29** (a) XPS spectra of the nanocomposite, (b) O1s, (c) C1s, (d) Ag3d, (e) Ti2p.

In order to find the influence of the silver oxides and  $\text{TiO}_2$  present in the nanocomposite on the photocatalysis, XRD analysis and dye degradation experiments were carried out at similar conditions with the biosynthesized  $\text{TiO}_2$  (Bio- $\text{TiO}_2$ ) and  $\text{AgO}/\text{Ag}_2\text{O}$  (obtained after the first step) and the results were compared with that of the  $\text{AgO}/\text{Ag}_2\text{O}@/\text{TiO}_2$  nanocomposite. XRD analysis (Fig. 4.30) of the Bio- $\text{TiO}_2$  nanoparticles shows the presence of rutile  $\text{TiO}_2$  with crystallographic planes (110), (111) and (211) (JCPDS No 01-088-1173). The planes (-111), (132) and (402) in the  $\text{AgO}/\text{Ag}_2\text{O}$  nanoparticles corresponds to  $\text{AgO}$  and (110) and (220) planes are assigned to  $\text{Ag}_2\text{O}$ . XRD of  $\text{AgO}/\text{Ag}_2\text{O}@/\text{TiO}_2$  nanocomposite shows the peaks for  $\text{TiO}_2$ ,  $\text{AgO}$  and  $\text{Ag}_2\text{O}$  that are found in Bio- $\text{TiO}_2$  and  $\text{AgO}/\text{Ag}_2\text{O}$  nanoparticles.

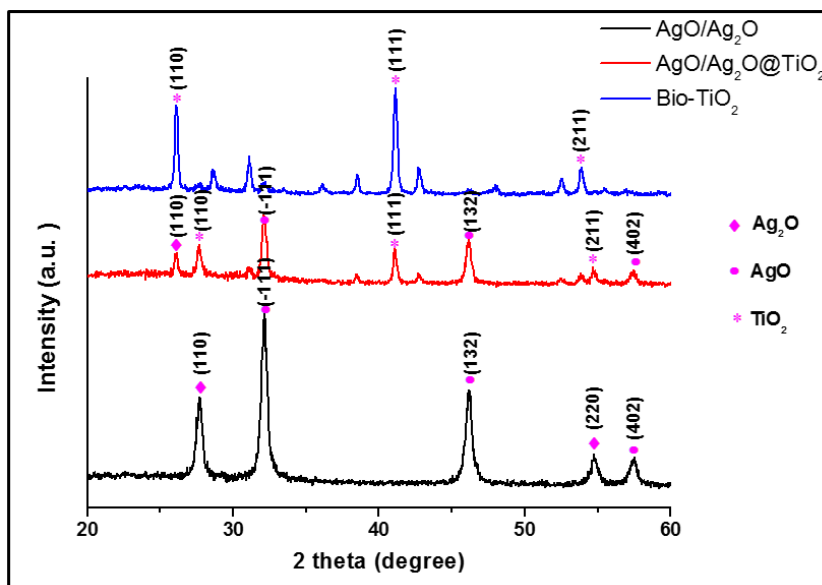


**Fig. 4.30** XRD analysis of Bio-TiO<sub>2</sub>, AgO/Ag<sub>2</sub>O and AgO/Ag<sub>2</sub>O@TiO<sub>2</sub> nanocomposite

#### 4.1.3. Comparison of photocatalytic activity of biosynthesized AgO/Ag<sub>2</sub>O@TiO<sub>2</sub> nanocomposites with biosynthesized AgO/Ag<sub>2</sub>O and Bio-TiO<sub>2</sub>

The photocatalytic activity of the AgO/Ag<sub>2</sub>O@TiO<sub>2</sub> nanocomposites were compared with AgO/Ag<sub>2</sub>O (obtained after the first step) and Bio-TiO<sub>2</sub> in terms of RB 220 degradation under visible light irradiation with dye solution pH of  $6 \pm 0.2$ , catalyst loading of 0.1 g/L and with 100 ppm RB 220. Fig. 4.31 (a) shows the colour change of RB 220 dye solution from initial time to 90 min using AgO/Ag<sub>2</sub>O@TiO<sub>2</sub> nanocomposite under light. As observed from Fig. 4.31b, maximum degradation is observed with AgO/Ag<sub>2</sub>O@TiO<sub>2</sub> nanocomposite, followed by Bio-TiO<sub>2</sub> and the least is seen with AgO/Ag<sub>2</sub>O. The AgO/Ag<sub>2</sub>O@TiO<sub>2</sub> nanocomposite showed maximum degradation of 98 % followed by Bio-TiO<sub>2</sub> with 93.7 % and AgO/Ag<sub>2</sub>O showing 89.8 % at the end of 90 min. At the end of 30 min, AgO/Ag<sub>2</sub>O shows 50 % degradation and Bio-TiO<sub>2</sub> shows 63 % degradation whereas 81 % degradation is obtained with AgO/Ag<sub>2</sub>O@TiO<sub>2</sub> nanocomposite under light. It is seen that the rate of degradation is much faster in AgO/Ag<sub>2</sub>O@TiO<sub>2</sub> nanocomposite compared to Bio-TiO<sub>2</sub> and AgO/Ag<sub>2</sub>O. Fig. 4.31 (c) shows the pseudo first-order kinetics plot for the nanocomposites. The rate constants of RB 220 degradation were found to be 0.0326,

0.0251 and 0.0492  $\text{min}^{-1}$  for Bio-TiO<sub>2</sub>, AgO/Ag<sub>2</sub>O and AgO/Ag<sub>2</sub>O@TiO<sub>2</sub> nanocomposite respectively (Fig. 4.31 d) indicating the higher degradation rate achieved with AgO/Ag<sub>2</sub>O@TiO<sub>2</sub> nanocomposite. This shows that incorporation of oxides of silver could play a positive role in enhancing the photocatalytic activity of TiO<sub>2</sub> as evident from XRD in Fig. 4.30. The enhancement in the photocatalytic activity of the nanocomposite in comparison to Bio-TiO<sub>2</sub> could be due to the presence of silver oxides which are having absorption peak in the visible region and low band gap energy (Kerkez and Boz 2015). The combination of silver oxides (p-type semiconductor) and TiO<sub>2</sub> (n-type) forms a *p-n* hetero-junction, which then results in very effective separation of photogenerated electrons and holes (Ren and Yang 2017).

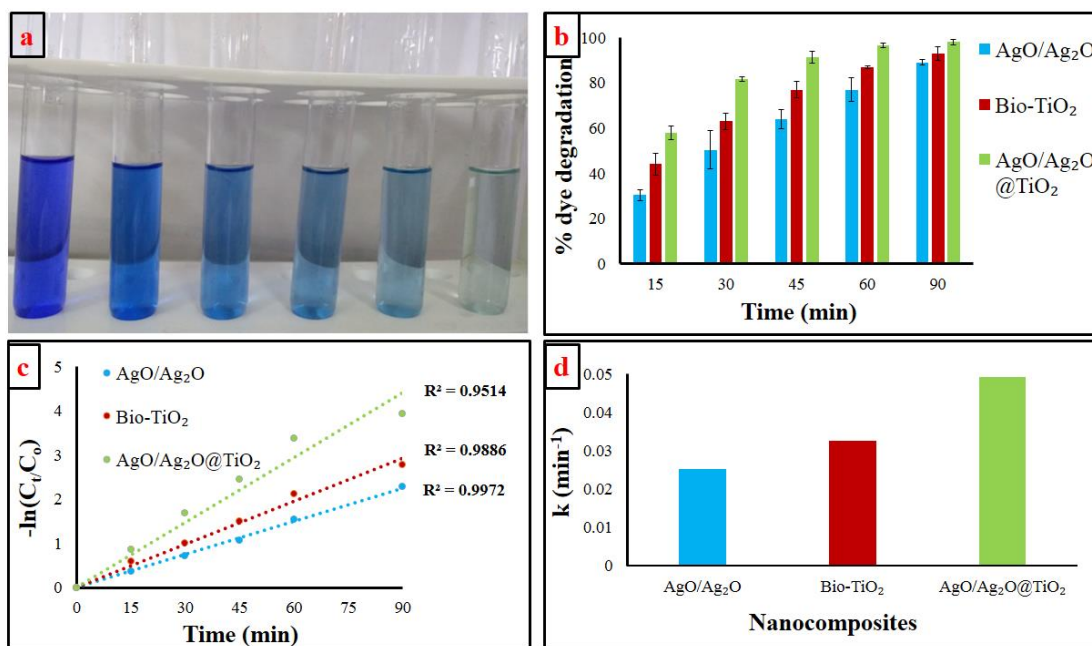


**Fig. 4.31** (a) Colour change of RB 220 dye solution from initial till the end of 90 min using AgO/Ag<sub>2</sub>O@TiO<sub>2</sub> nanocomposite under light (b) Percentage dye (RB 220) degradation using AgO/Ag<sub>2</sub>O, Bio-TiO<sub>2</sub> and AgO/Ag<sub>2</sub>O@TiO<sub>2</sub> nanocomposite (c) Pseudo first-order kinetics plot for AgO/Ag<sub>2</sub>O, Bio-TiO<sub>2</sub> and AgO/Ag<sub>2</sub>O@TiO<sub>2</sub> nanocomposite (d) Rate constants (*k*) for the nanocomposites

Further Photoluminescence (PL) spectroscopy was performed to understand the electronic structure and loss of photogenerated electron-holes by recombination process in semiconductors. Fig. 4.32 shows the PL spectra of Bio-TiO<sub>2</sub>, AgO/Ag<sub>2</sub>O and

AgO/Ag<sub>2</sub>O@TiO<sub>2</sub> nanocomposite at an excitation wavelength of 320 nm. Bio-TiO<sub>2</sub> and AgO/Ag<sub>2</sub>O@TiO<sub>2</sub> nanocomposite showed luminescent peaks at the same wavelength of 410 nm, but the AgO/Ag<sub>2</sub>O@TiO<sub>2</sub> nanocomposite exhibited lowered PL intensity than the Bio-TiO<sub>2</sub>. Higher PL emission intensity of TiO<sub>2</sub> implies higher recombination of the charge carriers. Lowering of PL intensity in AgO/Ag<sub>2</sub>O@TiO<sub>2</sub> nanocomposites on compositing Bio-TiO<sub>2</sub> with AgO/Ag<sub>2</sub>O implies reduced recombination of the electron-hole pairs. As the separated charge carriers are responsible for the photocatalytic performance, AgO/Ag<sub>2</sub>O@TiO<sub>2</sub> nanocomposites exhibit higher photocatalytic activity. The lowering of PL intensity after the incorporation of AgO/Ag<sub>2</sub>O nanoparticles may be due to band bending at the interface, causing very efficient charge transfer process in the case of AgO/Ag<sub>2</sub>O@TiO<sub>2</sub> nanocomposites (Paul et al. 2016). Due to the efficient charge transfer process the electrons and holes are sufficiently separated to reduce the probability of recombination and hence the PL intensity lowered. The lowering of PL intensity may have also caused due to partial passivation of luminescent centers in Bio-TiO<sub>2</sub> by AgO/Ag<sub>2</sub>O nanoparticles (Paul et al. 2016). Under visible light illumination, plenty of excitons are available at the interface of TiO<sub>2</sub> and AgO/Ag<sub>2</sub>O, which may help in achieving high photocatalytic activity. Thus, the lower intensity of AgO/Ag<sub>2</sub>O@TiO<sub>2</sub> nanocomposite as compared to Bio-TiO<sub>2</sub> suggests inhibition of electron and hole recombination and their participation in photochemical transformation leading to enhanced photocatalytic activity of the nanocomposites (Ali et al. 2018, Wei et al. 2016). The low PL intensity of AgO/Ag<sub>2</sub>O could be due to formation of lesser number of excited electrons in AgO/Ag<sub>2</sub>O and availability of low luminescent centers. These results are in agreement with that reported by Paul et al. (2016) in their study of Ag<sub>2</sub>O-nanoparticles decorated monoclinic TiO<sub>2</sub> nanorods, wherein they have observed a reduction of PL intensity on decorating TiO<sub>2</sub> with Ag<sub>2</sub>O nanoparticle and a lowest intensity for Ag<sub>2</sub>O nanoparticles.

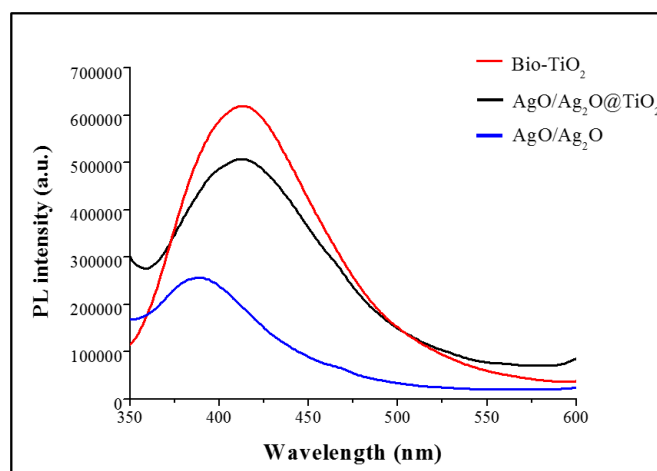


**Fig. 4.32** Photoluminescence spectroscopy of Bio-TiO<sub>2</sub>, AgO/Ag<sub>2</sub>O and AgO/Ag<sub>2</sub>O@TiO<sub>2</sub> nanocomposite

## 4.2 OPTIMIZATION OF PHOTOCATALYTIC PROCESS PARAMETERS

The photocatalytic degradation of RB 220 dyes was conducted in the presence of the AgO/Ag<sub>2</sub>O@TiO<sub>2</sub> nanocomposites synthesized by Method A under optimum conditions of CFS pH 7, Ag to Ti molar ratio of 1:1.6 and 4 h of reaction time in each step with total reaction time of 8 h. The effect of various photocatalytic process parameters such as dye solution pH, catalyst loading and initial dye concentration was investigated.

### 4.2.1 Optimization of dye solution pH

pH of the dye solution is one of the important parameters affecting the photocatalytic degradation rate as it influences the surface charge of the photocatalyst. Under acidic condition, photocatalyst surface is found to be positively charged and it is negatively charged in alkaline condition (Mirkhani et al. 2007). The effect of dye pH on the degradation of RB 220 by the nanocomposites synthesized by Method A under optimum conditions was studied. The dye pH was varied from 3 to 11 and the photocatalytic degradation experiment was carried out with 0.1 g/L catalyst load for 100 ppm dye concentration under visible light for 90 min.

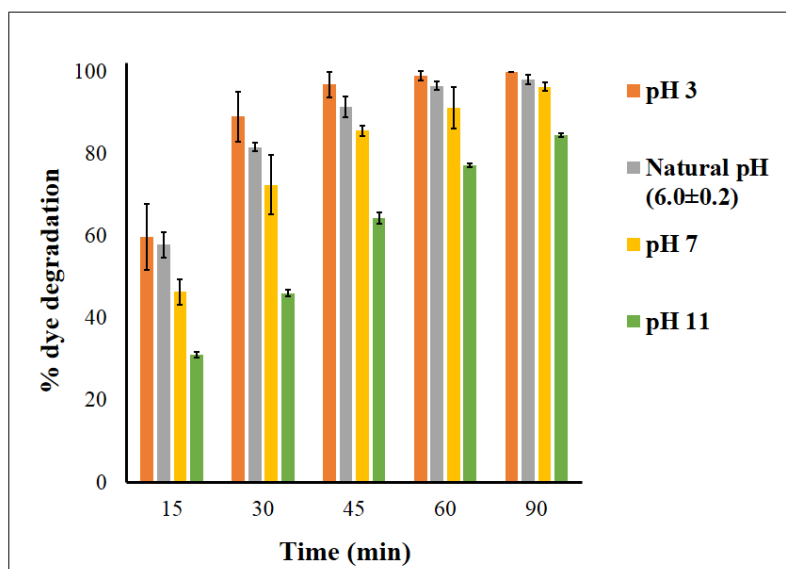


**Fig. 4.33** Percentage dye degradation at different dye pH with initial dye concentration of 100 ppm and catalyst loading of 0.1 g/l.

As observed in Fig. 4.33 as the pH increases, the percentage dye degradation decreases. Acidic pH shows better degradation when compared to neutral or alkaline pH. Maximum dye removal is seen at pH 3 with almost 90% degradation in 30 min. whereas less than 50% degradation is observed at pH 11. The dye was degraded completely at pH 3 in 90 min, whereas the degradation achieved with the natural pH (pH  $6 \pm 0.2$ ), pH 7 and pH 11 were found to be 98, 96.3 and 84.6 % at the end of 90 min. Neutral pH and alkaline pH of 11 showed lower degradation, with pH 11 showing the least degradation than all the other pH. As the AgO/Ag<sub>2</sub>O particles are embedded inside a TiO<sub>2</sub> film, TiO<sub>2</sub> surface of the nanocomposite is exposed to the aqueous reaction media. The surface of TiO<sub>2</sub> may attain positive or negative charge depending on the pH due to its amphoteric behaviour. The point of zero charge of TiO<sub>2</sub> is 6.8, below which the TiO<sub>2</sub> surface is positively charged and above it is negatively charged. Due to the amphoteric character, the point of zero charge of TiO<sub>2</sub> is 6.8, below which the TiO<sub>2</sub> surface is positively charged and above it is negatively charged (Chiou et al. 2008). RB-220 is an anionic dye. Under acidic condition, electrostatic interaction occurs between negatively charged dye molecule and positively charged TiO<sub>2</sub> leading to adsorption of the dye molecules onto the surface of TiO<sub>2</sub> and thus leading to maximum dye degradation. On the other hand, repulsive forces between negatively charged photocatalyst and

negatively charged dye molecule occurs at neutral pH or highly alkaline pH, hence degradation is lesser at neutral pH and at pH 11. Similar results were reported by Villanueva et al. (2018). Thu et al. (2016) reported increased adsorption capacity of methyl orange dye on Cu-doped TiO<sub>2</sub> catalyst at pH 3 and low or no adsorption at pH 6 and 9 respectively under UV light. In the studies by Khanna and Shetty (2014), the degradation of RB 220 in the presence of chemically synthesized Ag based TiO<sub>2</sub> catalyst (Ag@TiO<sub>2</sub> core shell particles) was found to be higher under acidic pH. The other reason for better photocatalytic activity at pH 3 may be due to the acidic media facilitating the production of hydroxyl radicals in the presence of light whereas under alkaline conditions the radical species get scavenged and hence reducing the photocatalyst activity (Muthirulan et al. 2013).

#### **4.2.2 Effect of Catalyst loading**

Catalyst loading is also an important parameter influencing the percentage of dye degradation. As the catalyst loading increases, availability of active sites also increases thereby enhancing the degradation rate (Naraginti et al. 2015). The catalyst loading was varied from 0.05 g/L – 20 g/L and the photocatalytic degradation experiments were carried out with 100 ppm dye concentration with solution pH of 3 under visible light for 90 min.

As observed in Fig.4.34, at the end of 30 min,  $\approx$  95 % degradation is observed for all the catalyst loading from 1 g/L to 20 g/L. It is very obvious from the Fig. 4.34 that initial degradation percentage is increasing with the increase in the catalyst loading from 0.05 g/L – 20 g/L with 0.05 g/L showing the least degradation. It is observed that almost complete degradation is obtained at the end of 90 min for the catalyst loading of 0.1 g/L, 0.5 g/L and 1 g/L. Further increase in catalyst loading to 5, 10 and 20 g/L, led to a marginal decrease in percentage degradation. At high photocatalyst dose there can be agglomeration of particles and number of active sites on the photocatalyst surface may almost become constant (Gulce et al. 2013) in spite of increase in the catalyst loading. It is observed that catalyst loading of 1 g/L shows marginally better photocatalytic activity throughout the 90 min irradiation time with dye to catalyst ratio of 1:10. Therefore it is necessary to maintain the optimum dye to catalyst ratio of 1:10

when AgO/Ag<sub>2</sub>O@TiO<sub>2</sub> nanocomposite is used to achieve maximum removal of RB 220 in wastewater treatment. It is also seen that hindering effect at higher catalyst loading is not predominant. Yang et al. (2017) have reported the optimum dosage of 1.5 g/L of poly-o-phenylenediamine (PoPD)/TiO<sub>2</sub> nanocomposites in photocatalytic degradation of methylene blue dye beyond which the absorption of visible light decreased by hindrance effect leading to reduction in the formation of reactive oxygen species. Khanna, (2014) have also found the dye to catalyst ratio of 1:10 as the optimum for the degradation of RB 220 dye with chemically synthesized Ag@TiO<sub>2</sub> cores shell structured nanoparticles as the photocatalyst under solar light irradiation.

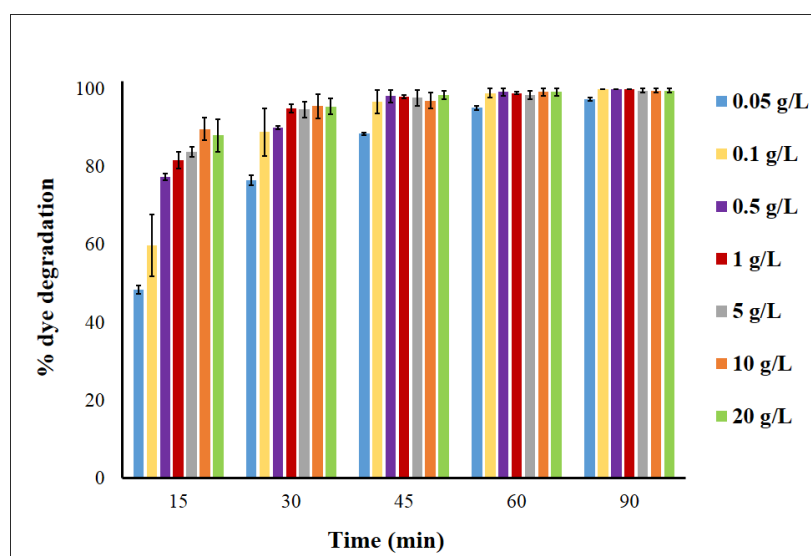


**Fig. 4.34** Percentage dye degradation at different catalyst loading with initial dye concentration – 100 ppm and pH 3.

#### 4.2.3 Effect of initial dye concentration

Further the effect of different concentrations of dye on the photocatalytic activity of AgO/Ag<sub>2</sub>O@TiO<sub>2</sub> nanoparticles were studied at a catalyst loading of 1 g/L with initial dye pH of 3 under visible light. From Fig. 4.35 (a), it is seen that as concentration of dye increased from 100 to 500 ppm with the same catalyst loading, rate of photocatalytic degradation decreased. The degradation of the dye at the end of 90 min, decreased from 99 % to 31 % as the initial concentration of dye was increased from 100 to 500 ppm (Fig. 4.35 b). As the initial dye concentration increases, the number of dye

molecules in the solution increases. The AgO/Ag<sub>2</sub>O@TiO<sub>2</sub> loading being constant, the number of available active sites for adsorption and surface area available for light absorption remain the same, this results in lowering the rate of photocatalytic degradation with increase in initial dye concentration. Further, the increased concentration of the dye reduces the passage of light through the solution and thus hinders the light from reaching the catalyst surface thereby decreasing the efficiency of degradation (Alkaykh et al. 2020; Fouad et al. 2022). The degradation rate was found to be the maximum when the initial dyes concentration was 100 ppm with initial degradation rate of 5.49 mg/L/min. The dye to catalyst ratio for 100 ppm initial concentration of dye was 1:10, whereas for initial dye concentration of 500 ppm, the ratio changed to 1:2 and therefore it can be said that the concentration of dye greatly influences the dye degradation rate. Fig. 4.36 (a) shows the pseudo first-order kinetics for the varying initial dye concentrations. As observed from Fig. 4.36 (b), the pseudo first order rate constant decreased with increasing dye concentration from 100 to 500 ppm with highest rate constant of 0.0846 min<sup>-1</sup> obtained for 100 ppm initial dye concentration at 1 g/L catalyst dosage.

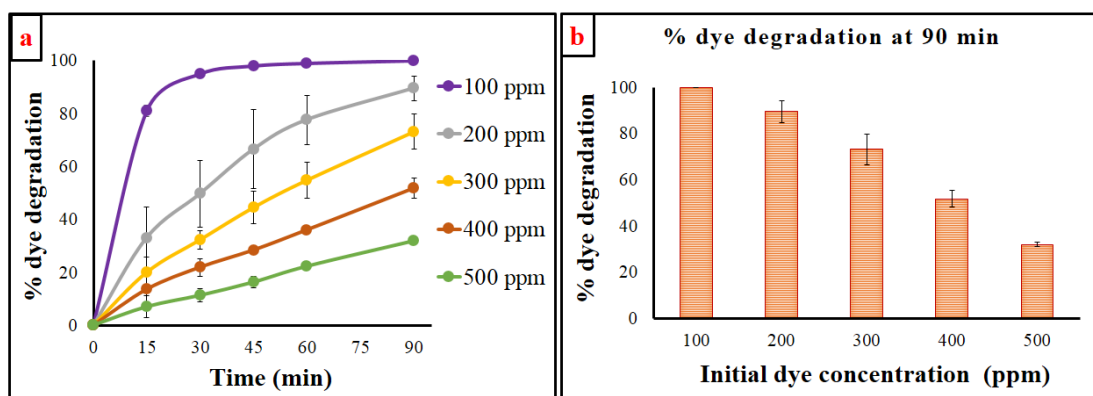


**Fig. 4.35 (a)** Percentage dye degradation at different initial concentration at different time intervals **(b)** Percentage dye degradation at 90 min

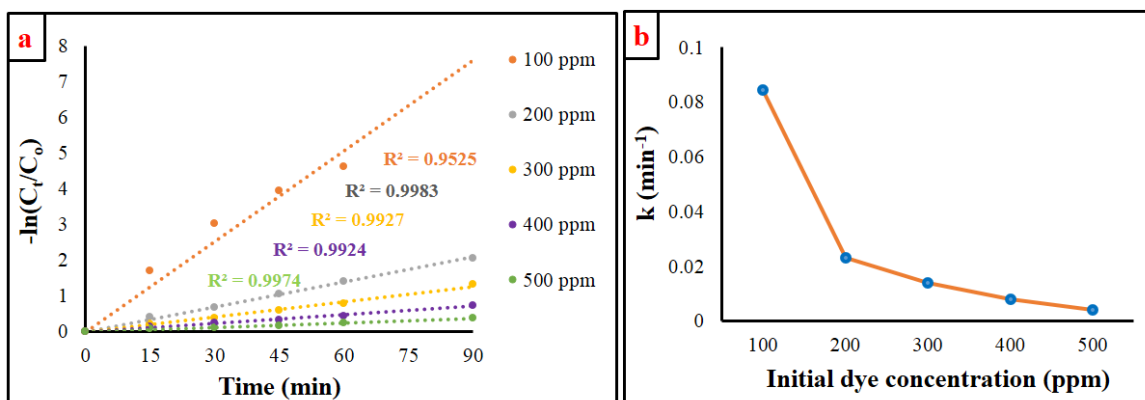


**Fig. 4.36** (a) Pseudo first-order kinetics plot for dye degradation at different initial dye concentration (b) rate constants for different initial concentrations of dye

### 4.3 PHOTOCATALYTIC ACTIVITY OF THE AgO/Ag<sub>2</sub>O@TiO<sub>2</sub> NANOCOMPOSITE ON RB 220 DYE DEGRADATION UNDER SOLAR LIGHT

Sunlight is abundantly available natural source of energy, which can be utilized in photocatalytic treatment of dye in the presence of a suitable photocatalyst making the process more economically viable (Ahmed et al. 2020; Ayodhya et al. 2016). Based on the studies presented in earlier sections, it is evident that the biosynthesized AgO/Ag<sub>2</sub>O@TiO<sub>2</sub> nanocomposite possess good visible light activity and thus it was hypothesized that it would be photocatalytically active under solar light. Thus, the photocatalytic efficiency of the prepared AgO/Ag<sub>2</sub>O@TiO<sub>2</sub> nanocomposite in the degradation of RB-220 was studied under solar light irradiation with 1 g/L catalyst and 100 ppm of dye solution. The absorption spectra displaying the reduction of RB 220 dye from 0<sup>th</sup> min till 90 min of irradiation time under solar light is shown in Fig. 4.37 (a) showing reduction in absorbance by the dye. As observed from Fig. 4.37 (b) almost 50% degradation occurred within 30 min of exposure of dye molecules to the nanocomposite under solar irradiation and 96.6 % degradation was achieved in 90 min. It is evident from Fig. 4.37 (a), that there is very little or no dye removal under only light (without nanocomposite) indicating that dye degradation does not occur solely by photolysis by sun light. These results indicate the AgO/Ag<sub>2</sub>O@TiO<sub>2</sub> nanocomposites are photocatalytically active under solar light and catalyzes the degradation of the dye on irradiation with solar light. The superior photocatalytic activity of AgO/Ag<sub>2</sub>O@

TiO<sub>2</sub> nanocomposite may be attributed to photosensitization by AgO/Ag<sub>2</sub>O as reported by Paul et al. (2016). The incorporation of silver oxides on titania enhances visible light sensitization of the catalyst and suppresses the electron-hole pairs recombination leading to the improved activity in dye decolorization under sunlight irradiation on modification of TiO<sub>2</sub> with silver oxides (Paul et al. 2016). Ren and Yang (2017) in their studies with Ag<sub>2</sub>O/TiO<sub>2</sub> synthesized using chemical precipitation method, have also reported an enhancement in the photocatalytic activity of TiO<sub>2</sub> modified with Ag<sub>2</sub>O in comparison to that of TiO<sub>2</sub> both under UV and visible light irradiation. The nanocomposites which exhibit light absorption in the entire UV and visible region of the spectrum show good photocatalytic activity under sunlight (Gayathri et al. 2015). The modification of TiO<sub>2</sub> with silver oxides, facilitate interfacial charge transfer between the semiconductors and restraining the electron-hole recombination by charge separation thereby enhancing the photocatalytic performance of the nanocomposite (Bian et al. 2020).

The degradation kinetics of RB 220 dye with initial concentration of 100 ppm dye and 1 g/L catalyst loading under solar light was studied and the linear fit of the plot of  $-\ln(C_t/C_0)$  versus time (Fig. 4.37 c) implied that the photocatalytic reaction follows pseudo first-order kinetics with  $k$  value of 0.0367 min<sup>-1</sup>.

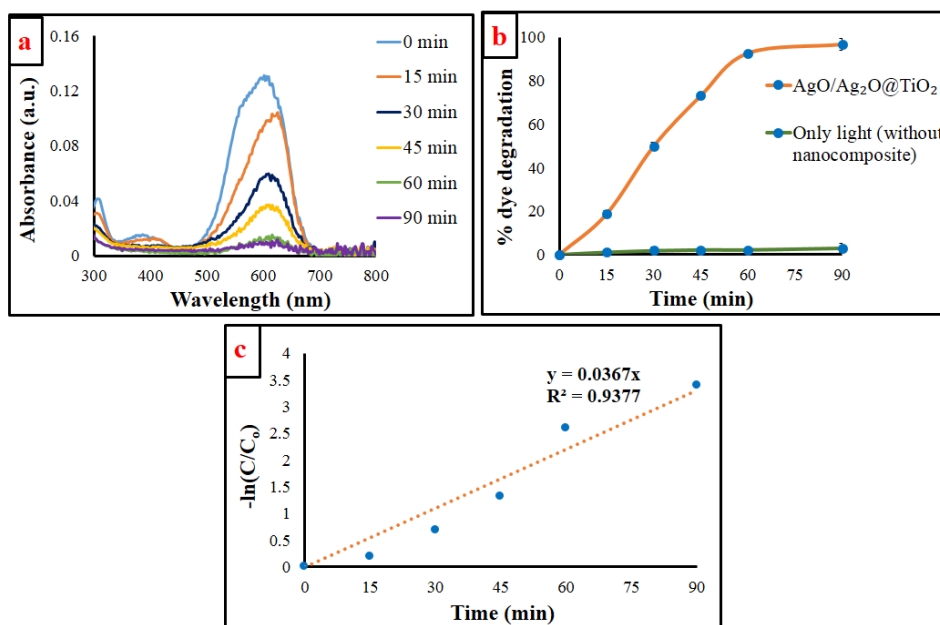


**Fig. 4.37** (a) Absorption spectra of RB 220 dye from 0<sup>th</sup> min till 90 min under solar light (b) Dye removal using (i) AgO/Ag<sub>2</sub>O@TiO<sub>2</sub> nanocomposite under solar light (ii) under light (without nanocomposite) (c) Pseudo-first-order kinetic plot for dye degradation

The proposed mechanism of dye degradation by the AgO/Ag<sub>2</sub>O@TiO<sub>2</sub> nanocomposite under sunlight is presented in Fig. 4.38. As TiO<sub>2</sub> is UV light active, electrons from the valence band of TiO<sub>2</sub> gets excited to the conduction band on absorption of UV rays from solar spectrum whereas Ag<sub>2</sub>O and AgO absorb visible part of the solar radiation. As reported by Sun et al. (2018), the CB of silver oxide is more negative than that of TiO<sub>2</sub>. Therefore, the excited electrons are transferred from CB of silver oxide to the CB of TiO<sub>2</sub>. The CB of TiO<sub>2</sub> acts as an electron centre. The electrons present in conduction band of TiO<sub>2</sub> reacts with oxygen molecules to produce highly reactive species which further leads to the breakdown of dye. The holes in the valence band of TiO<sub>2</sub> migrate to Ag<sub>2</sub>O and AgO which interacts with water molecules to produce hydroxyl radicals leading to the decomposition of the dye forming simpler products like CO<sub>2</sub> and H<sub>2</sub>O (Sun et al. 2018). The electron-hole reaction in AgO/Ag<sub>2</sub>O@TiO<sub>2</sub> nanocomposite leads to breakdown the organic molecules such as dyes (Sadollahkhani et al. 2014, Ramki et al. 2020).

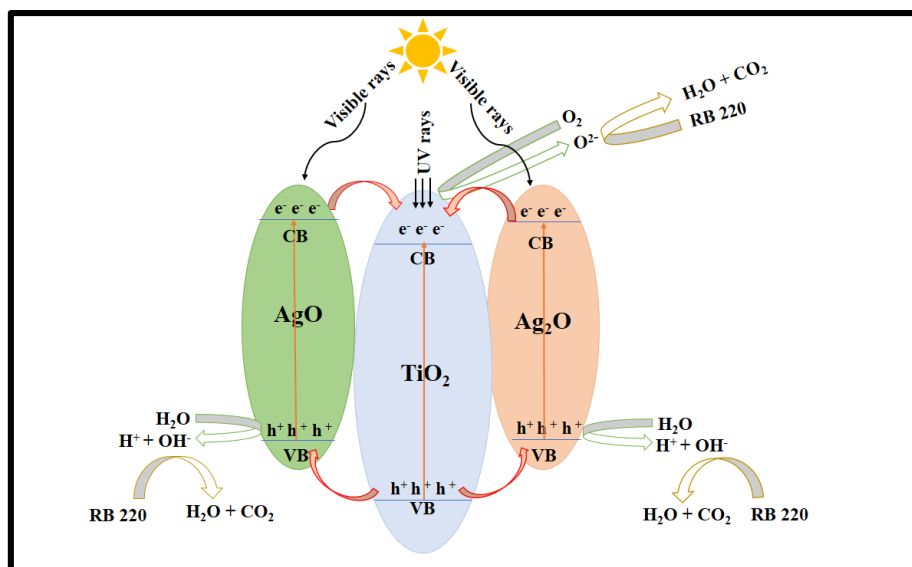


**Fig. 4.38** Possible RB 220 degradation mechanism by AgO/Ag<sub>2</sub>O@TiO<sub>2</sub> nanocomposite under solar light

#### 4.4 PHOTOCATALYTIC DEGRADATION OF ACID YELLOW 17 (AY 17) DYE USING AgO/Ag<sub>2</sub>O@TiO<sub>2</sub> UNDER VISIBLE AND SOLAR LIGHT

Further to confirm the visible light mediated photocatalytic activity of the biosynthesized AgO/Ag<sub>2</sub>O@TiO<sub>2</sub> in terms of its ability to degrade other complex azo dyes, the degradation studies were conducted on another anionic azo dye, Acid Yellow 17 (AY 17) under both visible (125 W) and solar light. As observed from Fig. 4.39, under visible light source, there is more than 50 % degradation whereas under solar irradiation less than 10 % degradation is seen at the end of 90 min with initial dye concentration of 100 ppm, pH 3 and catalyst loading of 1 g/l. Compared to RB 220 dye, the degradation rate of AY 17 was much lower under both visible and solar light using AgO/Ag<sub>2</sub>O@TiO<sub>2</sub> nanoparticles. AgO/Ag<sub>2</sub>O@TiO<sub>2</sub> nanoparticles were found to be not effective in the degradation of AY 17 probably owing to the thermodynamically feasible but kinetically unfavourable degradation reaction of AY 17. Though, the biosynthesized AgO/Ag<sub>2</sub>O@TiO<sub>2</sub> has lower charge recombination rate, it may not be sufficient enough to provide the electrons and holes at a rate required for the degradation of AY 17 to sufficient extent, leading to lower degradation rate of AY 17. So, further modification in the catalyst may be required to reduce the charge recombination rate.

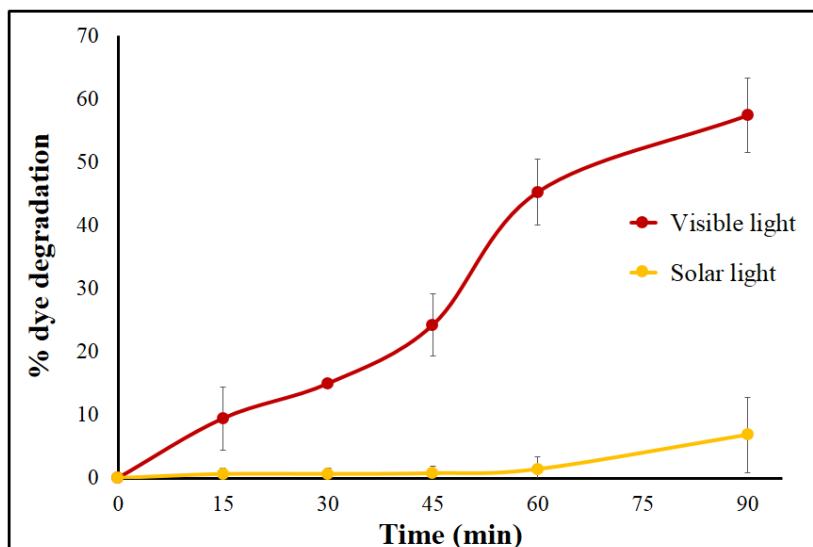


**Fig. 4.39** Photocatalytic degradation of AY-17 dye using AgO/Ag<sub>2</sub>O@TiO<sub>2</sub> nanocomposite under visible and solar light

Incorporation of certain metals like Cu (Raguram and Rajni 2022), Fe (Shymanovska et al. 2022), Zn (Jiang et al. 2021) etc are known to improve and enhance the photocatalytic activity of the nanocomposites. Modification of TiO<sub>2</sub> with Cu or CuO can enhance the photocatalytic activity of TiO<sub>2</sub> by reducing the recombination rate of electron-hole pair (Ikram et al. 2020). Therefore in order to improve the efficiency of AgO/Ag<sub>2</sub>O@TiO<sub>2</sub> nanocomposite for other class of dyes, AgO/Ag<sub>2</sub>O@TiO<sub>2</sub> nanocomposite was further modified with Cu and its photocatalytic activity was studied in terms of degradation of dyes under visible and solar irradiation

#### **4.5 PHOTOCATALYTIC DEGRADATION STUDIES USING AgO/Ag<sub>2</sub>O@TiO<sub>2</sub> MODIFIED WITH Cu (ATC) NANOCOMPOSITE**

##### **4.5.1. Effect of Cu loading in AgO/Ag<sub>2</sub>O@TiO<sub>2</sub> modified with Cu (ATC) nanocomposite on its photocatalytic activity under visible light**

Incorporation of Cu is known to enhance the photocatalytic activity of TiO<sub>2</sub> by activating it in a wider range of wavelength under visible light (Mendez-Medrano et al. 2016). AgO/Ag<sub>2</sub>O@TiO<sub>2</sub> modified with Cu (ATC) nanocomposite was prepared by three step method as described in Section 3.7, with the first two steps similar to the synthesis of AgO/Ag<sub>2</sub>O@TiO<sub>2</sub> followed by a third step of modification with Cu. The

AgO/Ag<sub>2</sub>O@TiO<sub>2</sub> obtained after the second step was added to cell free supernatant containing different concentrations of Cu (25, 50, 75 and 100 mM) in the synthesis mixture of step 3 so as to obtain varying molar ratio of Ag:Ti:Cu of 1:1.6:0.23; 1:1.6:0.46; 1:1.6:0.7 and 1:1.6:0.92 for the synthesis process. The corresponding AgO/Ag<sub>2</sub>O@TiO<sub>2</sub> modified with Cu (ATC) nanocomposites thus synthesized were labelled as ATC-25, ATC-50, ATC-75 and ATC-100 respectively as described in section 3.7. The studies on the degradation of RB 220 dye using the as synthesized AgO/Ag<sub>2</sub>O@TiO<sub>2</sub> modified with Cu nanocomposites was studied under visible light with 100 ppm RB 220 dye, catalyst loading of 1 g/L and solution pH 3. Fig. 4.40 shows faster degradation using ATC-75 nanocomposites when compared to other ATC. As the Cu loading increased, degradation efficiency also increased upto ATC-75 nanocomposites with slight reduction in the case of degradation with ATC-100 sample. Although ATC-25 and ATC-50 did not show better degradation when compared to AgO/Ag<sub>2</sub>O@TiO<sub>2</sub>, ATC-75 nanocomposites exhibited marginally greater degradation with 88 % degradation at the end of 15 min. ATC-75 nanocomposites could degrade RB 220 almost completely in 45 minutes, whereas complete degradation could be achieved with AgO/Ag<sub>2</sub>O@TiO<sub>2</sub> at the end of 90 min. The initial rates of degradation with AgO/Ag<sub>2</sub>O@TiO<sub>2</sub> and ATC nanocomposites are presented in Table 4.7, which show the maximum initial rate of degradation of 5.94 mg/L/min with ATC-75. The enhancement in the dye degradation using ATC-75 nanocomposites could be due to modification of AgO/Ag<sub>2</sub>O@TiO<sub>2</sub> with Cu which is known to influence the activity of AgO/Ag<sub>2</sub>O@TiO<sub>2</sub> nanocomposite. Studies have reported that modification with Cu reduces the charge carrier recombination thereby improving its photocatalytic efficiency (Mingmongkol et al. 2022). Complete degradation of RB 220 dye was observed with ATC-75 nanocomposites within 45 min of irradiation. Therefore ATC-75 nanocomposite was found to be the optimum and further experiments were carried out using ATC-75 nanocomposite.

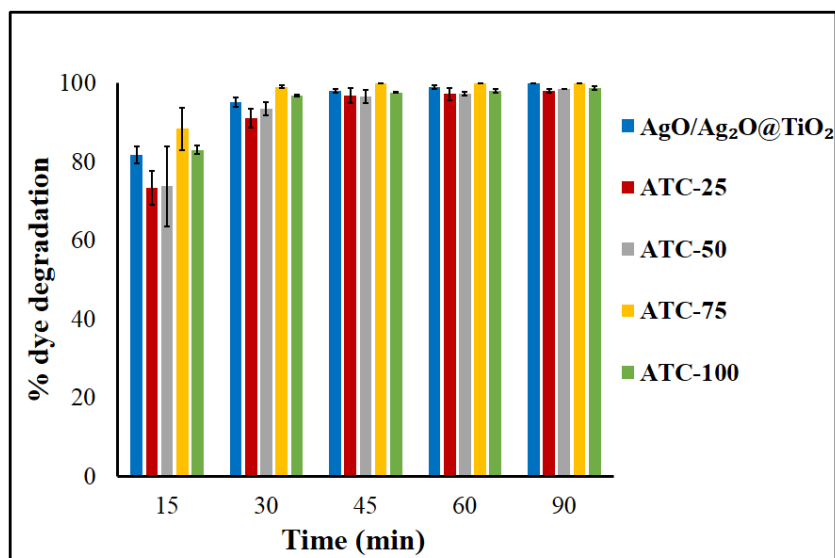


**Fig. 4.40** Percentage dye degradation using AgO/Ag<sub>2</sub>O@TiO<sub>2</sub> and AgO/Ag<sub>2</sub>O@TiO<sub>2</sub> modified with Cu (ATC) with varying Cu loading

#### 4.5.2. Effect of calcination temperature on the photocatalytic activity of AgO/Ag<sub>2</sub>O@TiO<sub>2</sub> modified with Cu (ATC) nanocomposite under visible light

Calcination temperature also plays an important role in the crystallinity, crystalline phase composition and crystallite size of the nanoparticles thereby influencing the activity of the nanocomposites. The as synthesized ATC-75 nanoparticles were calcined at 350, 400, 450 and 500° C for 3 h to study the change in the activity of the nanocomposites. The nanocomposites calcined at 400° showed maximum degradation followed by that calcined at 350°, with the least degradation observed for ATC-75 calcined at 500° C temperature (Fig. 4.41). Although nanocomposites calcined at 350 and 400° C show almost complete degradation at the end of 90 min, initial degradation is faster with the nanoparticles calcined at 400°C. The initial rate of degradation is the maximum (5.94 mg/L/min) with ATC-75 nanoparticles calcined at 400°C as presented in Table 4.7. It could result in complete degradation of the dye in 45 minutes. However, the calcination at higher temperature resulted in lowering of the rates. Lal et al. (2021) found that calcination temperature of 400° C was better in terms of band-gap, morphology and crystallite size as higher temperature would lead to agglomeration of nanoparticles. Several researchers (Yu et al. 2003, Yu et al. 2001, Yu et al. 2002, Wang et al. 2019, Kim et al. 2021, Yuan et al. 2018, Yuan et al. 2016) have reported that the

photocatalytic activity of nanomaterials is affected by their phase structure, crystallite size, pore structure and size and the specific surface area. Calcination temperature is known to influence the particle and crystallite sizes, phase transformations and thereby affecting the photocatalytic performance (Kim et al. 2021). In the present case, the calcination temperature may have changed the phase composition, crystallite size and oxidation states of the components in the catalyst and the phase composition and oxidation states of Cu in the nanocomposite formed after calcination at 400° C appears to offer favourable in terms of photocatalytic activity. Therefore 400° C was chosen as optimum calcination temperature for ATC-75 and the further experiments were carried out using ATC-75 nanocomposites calcined at 400° C.

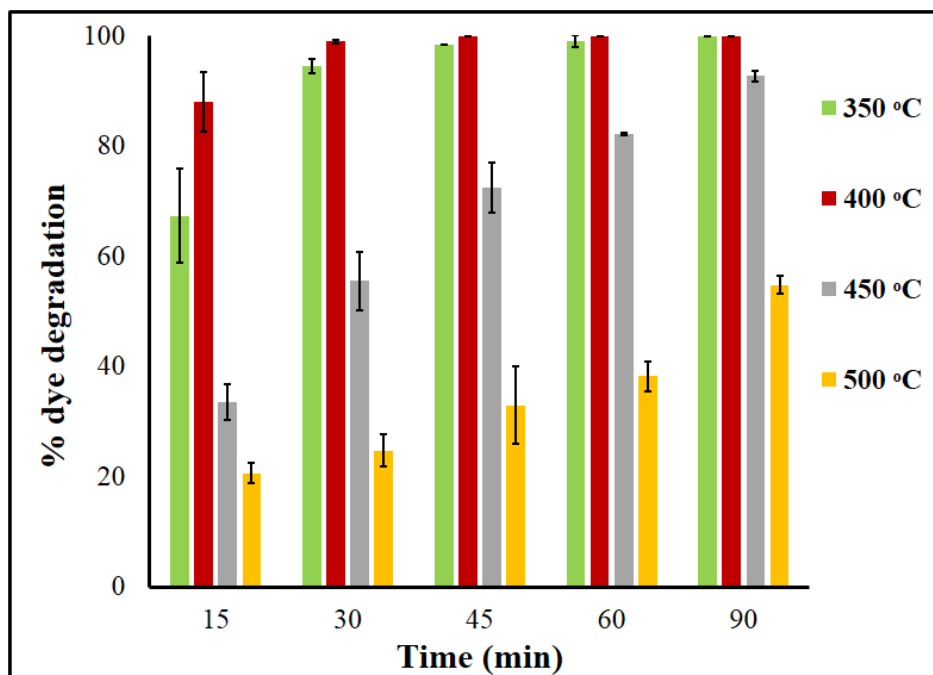


**Fig. 4.41** Percentage dye degradation using ATC-75 nanocomposite calcined at varied temperature

**Table 4.7** The initial rates of degradation with AgO/Ag<sub>2</sub>O@TiO<sub>2</sub> (AAT), ATC nanocomposites and calcination temperatures of ATC-75

Initial degradation rate (mg/L/min)	Nanocomposites					Calcination temperature (°C) (ATC-75)			
	AAT	ATC-25	ATC-50	ATC-75	ATC-100	350	400	450	500
	5.49	4.7	4.7	5.94	5.26	4.33	5.94	2.18	1.34

Control experiments were carried out using silver oxide modified with Cu (AC) and Bio-TiO<sub>2</sub> modified with Cu (TC) nanocomposites to find out the effect of Cu on silver oxide and titanium dioxide nanoparticles. From Fig. 4.42, it is observed that TiO<sub>2</sub> modified with Cu shows the least degradation of RB 220 dye when compared to AgO/Ag<sub>2</sub>O@TiO<sub>2</sub>, ATC-75, and silver oxide modified with Cu nanoparticles with only 36 % degradation at the end of 90 min. Silver oxide modified with Cu shows less than 50 % degradation whereas ATC-75 exhibits faster degradation with more than 85 % degradation at the end of 15 min. The presence of both Cu and silver oxides in TiO<sub>2</sub> is necessary to achieve better degradation rate. Therefore ATC-75 appears to be a better photocatalyst when compared to AgO/Ag<sub>2</sub>O@TiO<sub>2</sub>, silver oxide modified with Cu and TiO<sub>2</sub> modified with Cu nanoparticles.

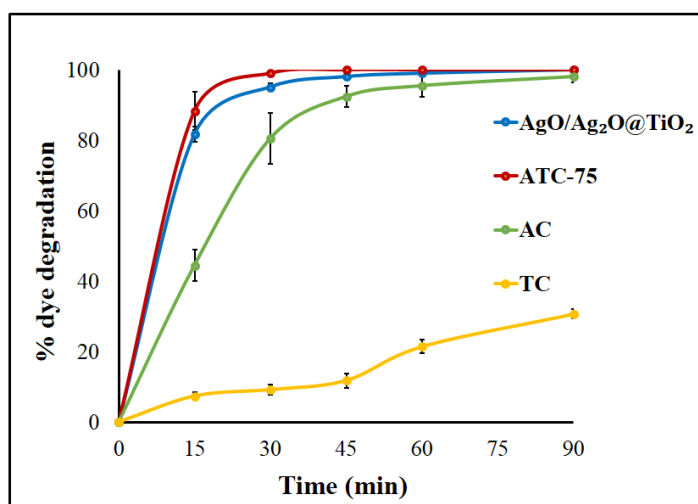


**Fig. 4.42** Percentage dye degradation using AgO/Ag<sub>2</sub>O@TiO<sub>2</sub>, ATC-75, AC and TC nanocomposites under visible light

#### 4.5.3 Photocatalytic degradation studies of RB-220 using AgO/Ag<sub>2</sub>O@TiO<sub>2</sub> modified with Cu nanocomposite under solar light

The photocatalytic activity of AgO/Ag<sub>2</sub>O@TiO<sub>2</sub> modified with Cu (ATC-75) nanocomposite was studied in the degradation of RB 220 dye under solar irradiation with initial dye concentration of 100 ppm, dye pH 3 and catalyst loading of 1 g/l. Fig. 4.43 shows that almost >95 % degradation of RB 220 could be achieved in 90 min with both ATC-75 nanocomposites and AgO/Ag<sub>2</sub>O@TiO<sub>2</sub> nanocomposite. However, the degradation with ATC-75 is faster than that with AgO/Ag<sub>2</sub>O@TiO<sub>2</sub> nanocomposite. Greater than 50 % degradation of RB 220 could be achieved at the end of 15 min with ATC-75 which is much higher than that obtained with AgO/Ag<sub>2</sub>O@TiO<sub>2</sub> nanocomposite which showed less than 20 % degradation. Cu incorporated nanocomposites greatly improved the activity of the AgO/Ag<sub>2</sub>O@TiO<sub>2</sub> nanocomposite exhibiting higher degradation rate. Mendez-Medrano et al. (2016) have reported that modification of TiO<sub>2</sub> with oxides copper and silver combined together induces efficient charge separation and reduces band-gap making it efficient under visible light.

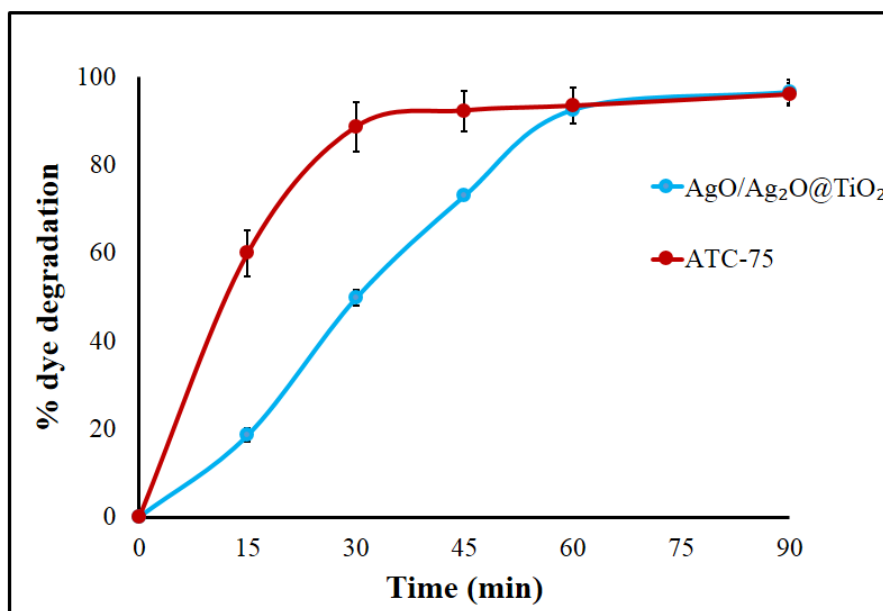


**Fig. 4.43** Comparison of RB 220 dye degradation with ATC-75 and AgO/Ag<sub>2</sub>O@TiO<sub>2</sub> nanocomposite under solar light

#### 4.5.4 Photocatalytic degradation studies of AY 17 dye using AgO/Ag<sub>2</sub>O@TiO<sub>2</sub> modified with Cu nanocomposite under visible and solar light

The photocatalytic efficacy of AgO/Ag<sub>2</sub>O@TiO<sub>2</sub> modified with Cu nanocomposites for the degradation of AY 17 was further studied under both visible and solar light and it was also compared with that of AgO/Ag<sub>2</sub>O@TiO<sub>2</sub> nanocomposites. Fig. 4.44 shows the decrease in absorbance of AY 17 in the presence of AgO/Ag<sub>2</sub>O@TiO<sub>2</sub> modified with Cu nanocomposite (ATC-75) from initial to 90 min under visible light which is also evident from the colour change of the dye (Fig. 4.44 Inset). Under visible light, around 90 % degradation was achieved with AgO/Ag<sub>2</sub>O@TiO<sub>2</sub> modified with Cu nanocomposite (ATC-75) whereas around 57 % degradation was observed using AgO/Ag<sub>2</sub>O@TiO<sub>2</sub> nanocomposite at the end of 90 min (Fig. 4.45 a) with a k value of 0.035 min<sup>-1</sup> (Fig. 4.45 b). Although both the nanocomposites showed no significant difference in degradation of RB 220 dye, large difference was observed in degradation of AY 17 dye using AgO/Ag<sub>2</sub>O@TiO<sub>2</sub> nanocomposite modified with Cu. It is well evident from the graph that Cu addition plays a major role in improving the photocatalytic activity resulting in higher degradation rate and such an incorporation of Cu plays a major role in the degradation of complex dyes.

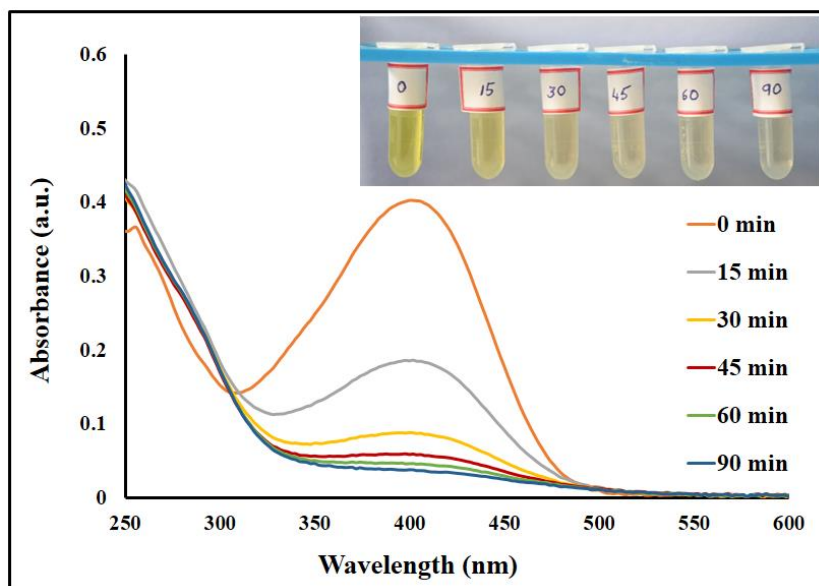


**Fig. 4.44** Absorption spectra of AY 17 dye displaying reduction in the dye concentration from initial to 90 min irradiation time under visible light (Inset) Colour change of AY 17 dye from initial to 90 min

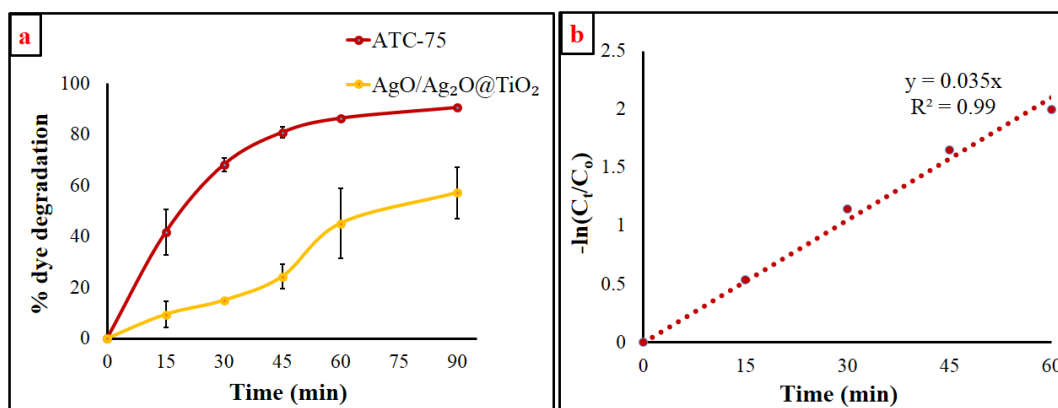


**Fig. 4.45 (a)** Time course variation of percentage dye degradation using AgO/Ag<sub>2</sub>O@TiO<sub>2</sub> and AgO/Ag<sub>2</sub>O@TiO<sub>2</sub> modified with Cu (ATC-75) nanocomposite  
**(b)** Pseudo first-order kinetics plot for AY-17 degradation using ATC-75 nanocomposite

From the above experiments, it is known that AgO/Ag<sub>2</sub>O@TiO<sub>2</sub> modified with Cu nanocomposite (ATC-75) shows superior photocatalytic activity when compared to AgO/Ag<sub>2</sub>O@TiO<sub>2</sub> nanocomposite under visible light. Further the degradation efficiency of AY 17 was studied using AgO/Ag<sub>2</sub>O@TiO<sub>2</sub> nanocomposite and AgO/Ag<sub>2</sub>O@TiO<sub>2</sub> modified with Cu nanocomposite under solar light. Similar trend was observed under solar light where around 90 % degradation is seen (Fig. 4.46 a) using ATC-75 nanocomposite within 90 min of irradiation time whereas only around 7% degradation is observed for AgO/Ag<sub>2</sub>O@TiO<sub>2</sub> nanocomposite even after 90 min. The rate of degradation is faster in case of AgO/Ag<sub>2</sub>O@TiO<sub>2</sub> modified with Cu than AgO/Ag<sub>2</sub>O@TiO<sub>2</sub> for AY 17 under both visible and solar light. This shows that AgO/Ag<sub>2</sub>O@TiO<sub>2</sub> modified with Cu nanocomposite acts as a better photocatalyst than AgO/Ag<sub>2</sub>O@TiO<sub>2</sub> in degradation of both the dyes under visible and solar light. Degradation reaction of AY 17 using AgO/Ag<sub>2</sub>O@TiO<sub>2</sub> modified with Cu nanocomposite followed the pseudo first-order kinetics with k value of 0.0263 min<sup>-1</sup> (Fig. 4.46 b).

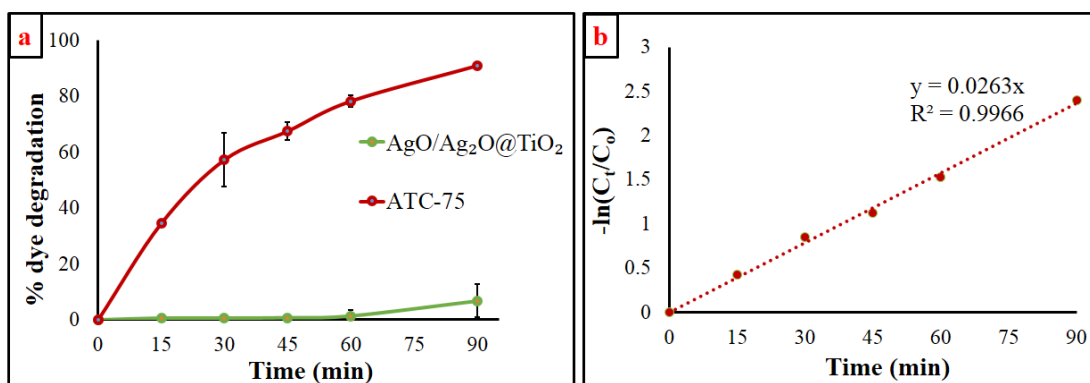


**Fig. 4.46** (a) Time course of variation of percentage dye degradation using AgO/Ag<sub>2</sub>O@TiO<sub>2</sub> and Cu-based AgO/Ag<sub>2</sub>O@TiO<sub>2</sub> nanocomposite under solar light (b) Pseudo first-order kinetics plot for AgO/Ag<sub>2</sub>O@TiO<sub>2</sub> modified with Cu (ATC-75) nanocomposites

XRD analysis of the AgO/Ag<sub>2</sub>O@TiO<sub>2</sub>, ATC-25, ATC-50, ATC-75 and ATC-100 nanocomposites are presented in Fig. 4.47. As observed, ATC composites showed similar pattern with rutile TiO<sub>2</sub> peaks corresponding to (110) and (211) planes (JCPDS No 01-088-1173) and AgO peaks corresponding to the (-111), (132) and (402) crystallographic planes respectively (JCPDS 01-076-1489). There was no Cu, CuO or Cu<sub>2</sub>O peaks detected in any of the Cu loaded samples. The reason could be that the surface doping of Cu or CuO with saturation would have taken place wherein the capping species on the surface of nanostructures is replaced by the doping species during mixing condition (Sahu et al. 2016) or the weight percentage of Cu or CuO in the composite may be very minute with reference to silver oxides and TiO<sub>2</sub>. The additional peaks present in AgO/Ag<sub>2</sub>O@TiO<sub>2</sub> nanocomposite ascribing to the crystallographic plane (111) of TiO<sub>2</sub> and (110), (101) of Ag<sub>2</sub>O respectively disappeared in Cu loaded (ATC) samples. Therefore all the Cu loaded samples comprised of only rutile TiO<sub>2</sub> and AgO peaks.

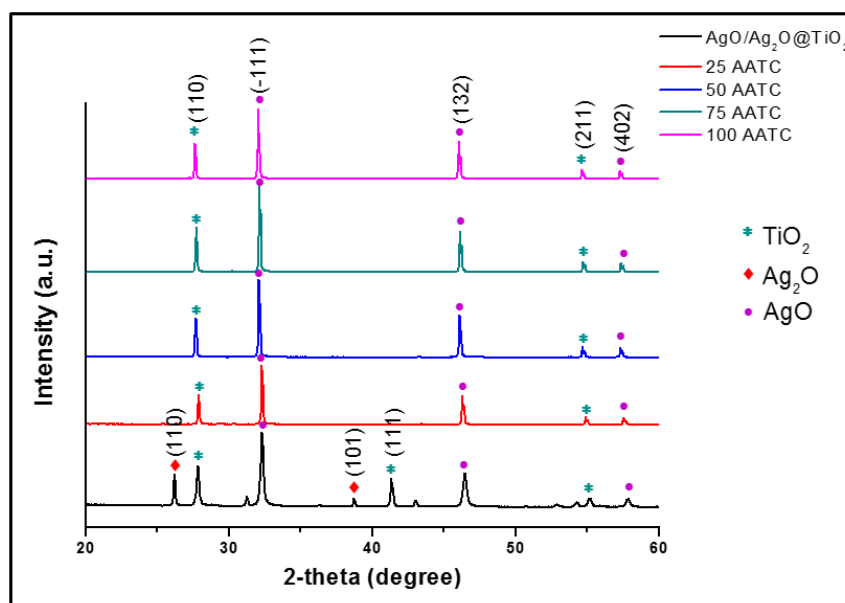


**Fig. 4.47** XRD pattern of the AgO/Ag<sub>2</sub>O@TiO<sub>2</sub> nanocomposite with different Cu loaded samples

Fig. 4.48 presents the Tauc plot showing band-gap energy of varied Cu loaded AgO/Ag<sub>2</sub>O@TiO<sub>2</sub> samples. All the Cu loaded samples viz, ATC-25, ATC-50, ATC-75 and ATC-100 displayed the band-gap energy of 2.75, 2.9, 2.7 and 2.8 eV, with higher band-gap obtained for ATC-50 sample. Zhao and Liu (2020) have reported the band-gap of Cu–Cu<sub>2</sub>O@TiO<sub>2</sub> nanocomposite to be 2.25 eV which is slight lower than the band-gap obtained for ATC-75 nanocomposites (2.7 eV) reported in this study. The band gap energy of ATC samples are higher than that of AgO/Ag<sub>2</sub>O@TiO<sub>2</sub> nanocomposite. This may be due to the presence of Cu and/or CuO. Although the band-gap energy increased in Cu loaded samples when compared to AgO/Ag<sub>2</sub>O@TiO<sub>2</sub> nanocomposite, higher degradation efficiency was observed with Cu loaded samples. (Gao et al. 2021) have observed increase in the energy band gap of  $\beta$ -Ga<sub>2</sub>O<sub>3</sub> after doping with Cu, which means that on doping the energy required for the transition of electrons from the valence band to the conduction band has not reduced. Even though they have found the energy band gap to increase slightly after Cu doping, but the absorption in the visible light range increased significantly. They attributed it to the impurity energy level that appears in the middle of the band gap, which acts as a springboard to promote the electronic transition. The impurity level generated in the band gap reduces the

energy required for the transition of electrons in the Valence band maximum (VBM) to conduction band minimum (CBM), so the energy of visible light may excite electrons to the CB. Singh et al. (2018) explained that as the particle size becomes smaller in the nanoscale, the number of overlapping of orbitals or energy level bands decreases and bands becomes thinner, causing an increase in energy band gap between the valence band and the conduction band (Singh et al. 2018). This shows that band gap is not the only criteria that governs the visible light activity.

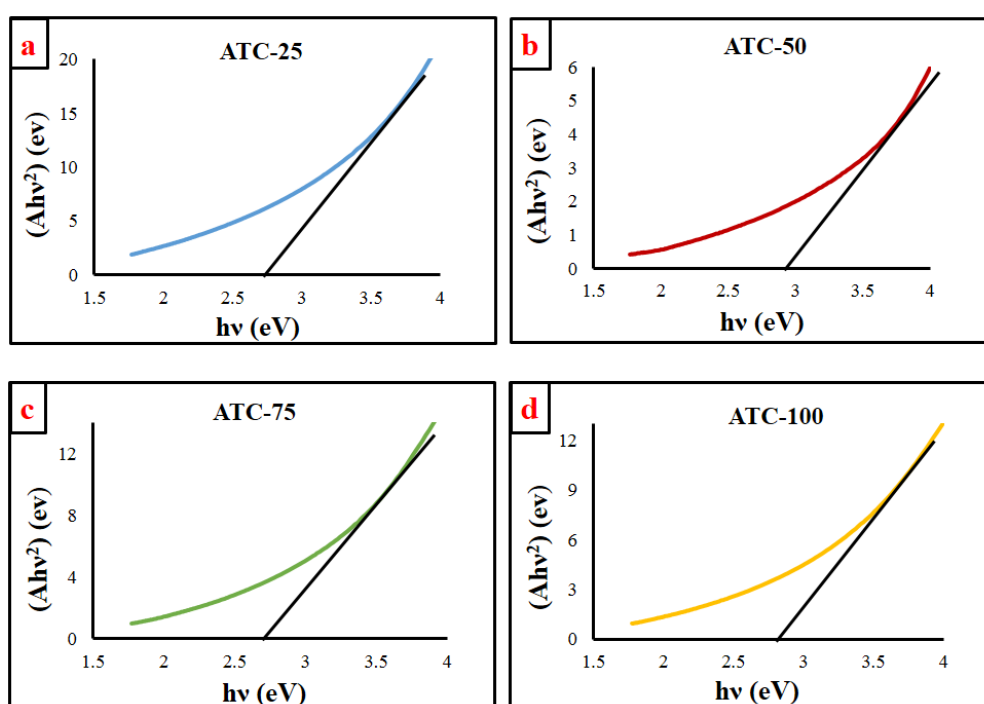
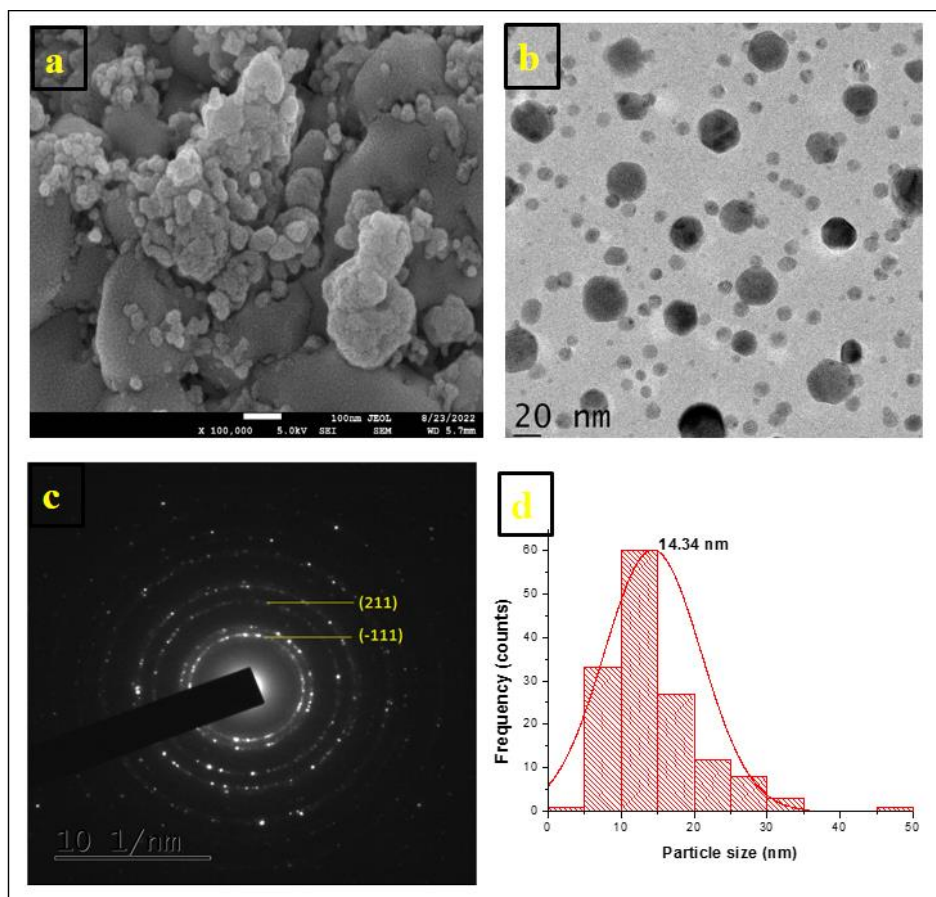


**Fig. 4.48** Tauc plot displaying the band-gap energy of varied Cu loaded AgO/Ag<sub>2</sub>O@TiO<sub>2</sub> samples

#### 4.5.5 Characterization of AgO/Ag<sub>2</sub>O@TiO<sub>2</sub> modified with Cu nanocomposite

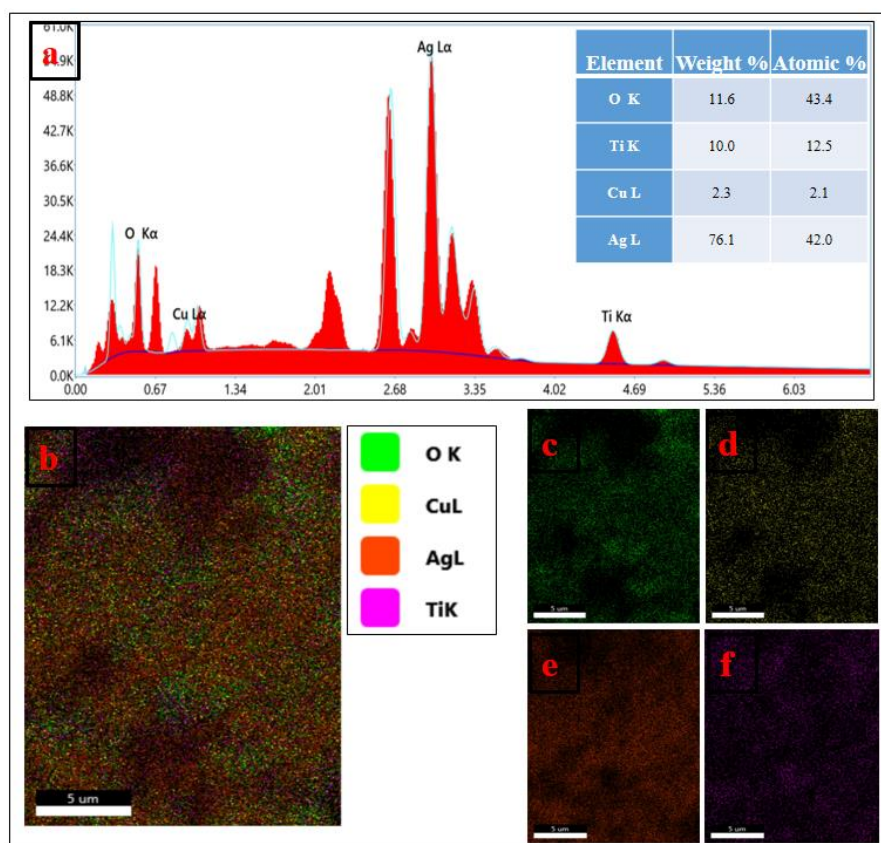
In Fig. 4.49 (a), SEM images of AgO/Ag<sub>2</sub>O@TiO<sub>2</sub> modified with Cu nanocomposite shows the particles synthesized were roughly spherical in shape with varied particle size. TEM analysis (Fig. 4.49 b) shows spherical shaped nanoparticles which are distinct with no agglomeration. As seen in the Fig. 4.49 (b), the particles formed are found to be of varied sizes in the range of 1-35 nm. SAED pattern in Fig. 4.49 (c) shows the polycrystalline nature of the nanocomposite with d-spacing value of 2.78 Å and 1.67 Å corresponding to the crystalline planes (-111) and (211) of AgO and TiO<sub>2</sub>

respectively which is in agreement with the XRD results. Histogram representation shows the nanoparticles obtained were of different size with average particle size of 14.3 nm (Fig. 4.49 (d)).



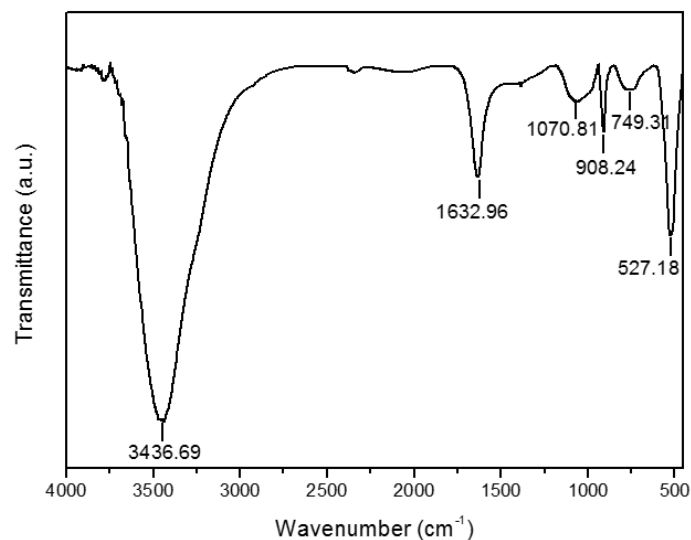
**Fig. 4.49** (a) SEM and (b) TEM image of the nanocomposites (c) SAED pattern (d) Particle size histogram of the AgO/Ag<sub>2</sub>O@TiO<sub>2</sub> modified with Cu nanocomposite (ATC-75)

Fig. 4.50 (a) shows the EDX spectra of the AgO/Ag<sub>2</sub>O@TiO<sub>2</sub> modified with Cu (ATC-75) nanocomposite showing strong signal for Ag along with small peaks for Ti, Cu and O. Further EDS mapping also indicates the presence of Ag, Ti, Cu and O with different colours distributed within the nanocomposite (Fig. 4.50 (b)).



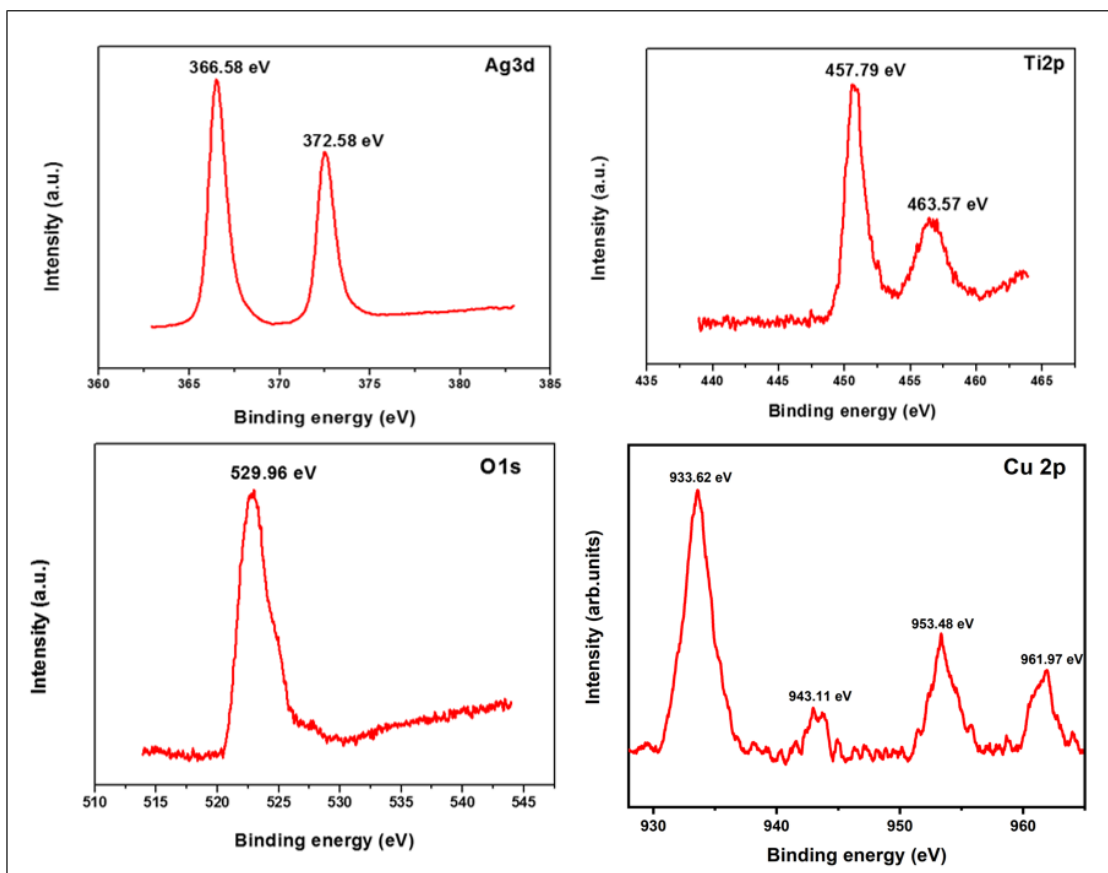
**Fig. 4.50** (a) EDX analysis and (b) EDS mapping of the Cu-based AgO/Ag<sub>2</sub>O@TiO<sub>2</sub> nanocomposite (c) EDS mapping for O, (d) EDX mapping for Cu, (e) EDX mapping for Ag and (f) EDX mapping for Ti

Fig. 4.51 shows FTIR spectra displaying different characteristic bands in AgO/Ag<sub>2</sub>O@TiO<sub>2</sub> modified with Cu nanocomposite. The band at 749.31 cm<sup>-1</sup> represents the stretching vibration of Cu-O bond (Truong et al. 2022). The Cu-O vibration is also observed at 527.18 cm<sup>-1</sup> (Sahu et al 2021). The band at 908 cm<sup>-1</sup> represents C-N stretching vibration (Metuku et al. 2014). The 1070 cm<sup>-1</sup> band corresponds to the stretching vibration of -C-O (Meng et al. 2015). The band at 1632.96 cm<sup>-1</sup> is ascribed to the C=O stretching of amides (Sinha and Ahmaruzzaman 2015). The band at 3436.69 cm<sup>-1</sup> corresponds to the O-H stretching vibrations (Arif et al. 2015). The presence of these functional groups indicate the role of biomolecules in stabilization of the nanoparticles.



**Fig. 4.51** FTIR spectra of the nanocomposites

Fig. 4.52 shows the XPS spectra of the nanocomposites with peaks for O1s, Ti2p, Ag3d and Cu2p. Ag3d spectra shows shift in the 3d<sub>5/2</sub> and 3d<sub>3/2</sub> peaks of AgO to lower binding energy of 366.5 and 372.5 eV (Fig. 4.52 (a)) respectively than the values of 367.1 eV and 373.2 eV for AgO as reported in Handbooks of Monochromatic XPS spectra and Hoflund et al (1995) respectively. The shift in the peaks may be attributed to interaction between AgO and TiO<sub>2</sub> at the heterojunction (Cho et al 2019). Ti2p spectra shows binding energies of Ti2p<sub>1/2</sub> and Ti2p<sub>3/2</sub> at slightly lower values at 457.7 and 463.5 eV (Fig. 4.52 (b)) respectively compared to the standards (458.6 and 464.4 eV) with the difference between the two of 5.8 eV indicating the state of Ti as Ti<sup>4+</sup> (Pino-Sandoval et al. 2020). The O1s spectra (Fig. 4.52 (c)) shows the peak at 529.5 which can be attributed to Ti-O bond. Cu2p peaks were located at 933.6 and 953.4 eV (Fig. 4.52 (d)) corresponding to Cu2p<sub>3/2</sub> and Cu2p<sub>1/2</sub> respectively indicating the presence of CuO in the nanocomposite which is in agreement with the Imyen and co-authors (2019). In addition to these peaks, satellite peaks were observed at 943.1 and 961.9 eV associated to Cu2p<sub>3/2</sub> and Cu2p<sub>1/2</sub> respectively with slight shift to lower binding energy of 944.7 and 963.03 eV as reported by Arasu et al. (2020). Therefore it can be inferred that Cu is present in the form of CuO and Ag as AgO in the AgO/Ag<sub>2</sub>O@TiO<sub>2</sub> nanocomposite modified with Cu (ATC-75). So, the nanocomposite modified with Cu (ATC-75) may be referred as AgO@TiO<sub>2</sub> nanocomposite modified with Cu



**Fig. 4.52** XPS spectra of the AgO/Ag<sub>2</sub>O@TiO<sub>2</sub> modified with Cu (ATC-75) nanocomposites

#### 4.6. MECHANISM OF PHOTOCATALYTIC DEGRADATION OF RB 220 AND AY 17 DYES BY AgO@TiO<sub>2</sub> MODIFIED WITH Cu NANOCOMPOSITE (ATC 75)

The dye degradation mechanism by AgO @TiO<sub>2</sub> modified with Cu nanocomposite (ATC-75) under sunlight is presented in Fig. 4.53. It consists of AgO, TiO<sub>2</sub> and CuO. These may form heterojunctions at the interface. AgO in the composite absorbs visible light and upon excitation, electrons are transferred from the conduction band (CB) of AgO to the CB of TiO<sub>2</sub>. The UV rays of the sunlight excites the TiO<sub>2</sub> where the electrons are generated in the conduction band leaving behind the holes in the valence band (VB). The electrons are further transferred to CuO, which acts as electron centre. The electrons from the CuO migrate to the catalyst surface when the electron acceptor such as O<sub>2</sub>, reaches to the surface, facilitate the reduction of oxygen molecules to free

radicals on the catalyst surface leading to the dye degradation. The electrons in the  $\text{TiO}_2$  can also directly react with the surface adsorbed oxygen resulting in the degradation of dye molecules into simpler products through reactive species. The holes formed in the VB of  $\text{TiO}_2$  gets transferred to VB of AgO which acts as the hole centre. The holes in the AgO will react with water molecules to form hydroxyl radicals resulting in the degradation of dye to carbon dioxide and water (Perovic et al. 2020). The ternary composite comprises of AgO as the photosensitizer for visible light,  $\text{TiO}_2$  which can absorb UV radiation in the solar light for charge generation along the CuO which can efficiently act as electron centre. This ternary composite heterostructure with efficient electron-hole separation mechanism, exhibits high photocatalytic activity even under solar light by utilizing UV and visible radiation which forms its major portion.

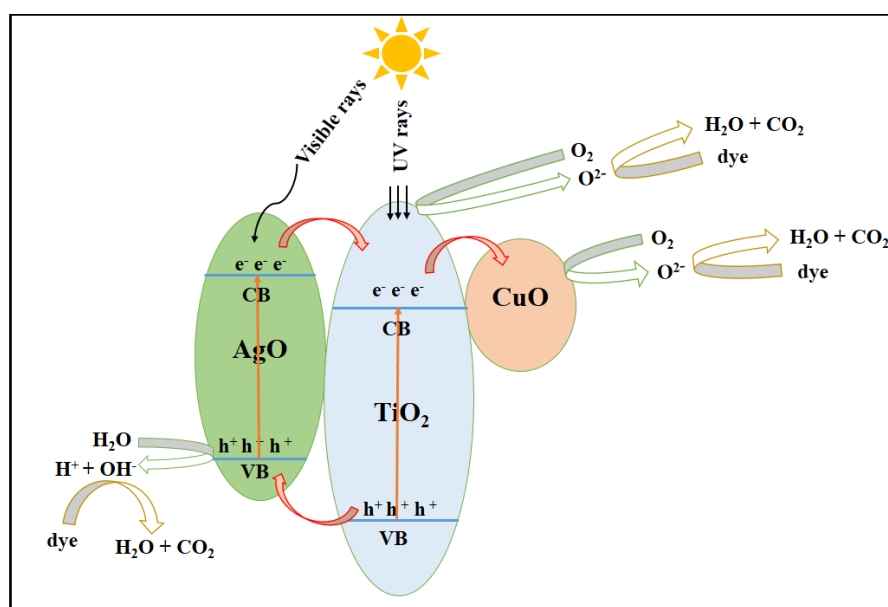


**Fig. 4.53** Possible dye degradation mechanism by AgO/Ag<sub>2</sub>O@TiO<sub>2</sub> modified with Cu nanocomposite under solar light

#### 4.7 STUDIES ON DEGRADATION OF DYES IN A MIXED DYE SYSTEM OF RB-220 AND AY 17 WITH AgO@TiO<sub>2</sub> modified with Cu NANOCOMPOSITE (ATC-75)

The effluents from industry is usually composed of a complex system containing mixture of dyes. But during the degradation process, these dyes can interfere in the degradation process of one another, therefore studying the influence of one dye on the

other is very much important in practical application. From Fig. 4.54, it can be seen that absorption maxima of both the dyes do not change even in mixed condition and is known to have its maximum absorption at its respective wavelength of 418 and 609 nm for AY 17 and RB 220 respectively, implying that the two dyes do not interfere with one another in analysis. Hence in this study mixture of two dyes namely, RB 220 and AY 17 with different concentration were measured at their respective wavelengths using the AgO @TiO<sub>2</sub> modified with Cu (ATC-75) nanocomposites. Fig. 4.55 shows the degradation of RB 220 dye with initial concentration of 50, 150 and 200 ppm with AY 17 concentration being constant at 100 ppm. As observed, the degradation rate is high for both RB 220 and AY 17 dye with initial RB 220 concentration of 50 ppm further which the degradation rate decreases for both the dyes when the concentration of RB 220 is increased to 150 and 200 ppm. Fig. 4.56 shows that the degradation rate of AY 17 dye greatly reduced when the concentration of AY 17 dye increased from 50 to 200 ppm with no much reduction in the degradation of RB 220 dye which is maintained at 100 ppm. It is well evident from the Fig. 4.57 (top) that only 50 % and 9% degradation of RB 220 and AY 17 respectively occurred at the 60 min of irradiation when used in combination of 100 ppm of both the dyes whereas almost complete degradation for RB 220 and more than 85% degradation for AY 17 was seen when used individually. The degradation rate has reduced significantly in case of mixture of dyes as compared to their individual degradation rate at all combinations of concentrations. This shows that the presence of one dye greatly affects the degradation of the other. The decrease in the degradation might be due to the competition in occupying the active centres on the surface of the catalyst (Gunture et al. 2019). As the concentration of one dye increases, degradation rate of other decreases. However there was no much reduction in degradation of RB 220 dye was seen at the end of 5<sup>th</sup> h, whereas the case is not the same with AY 17, the degradation was significantly affected by the presence of RB 220 dye as observed in Fig. 4.57 (a) and (b).

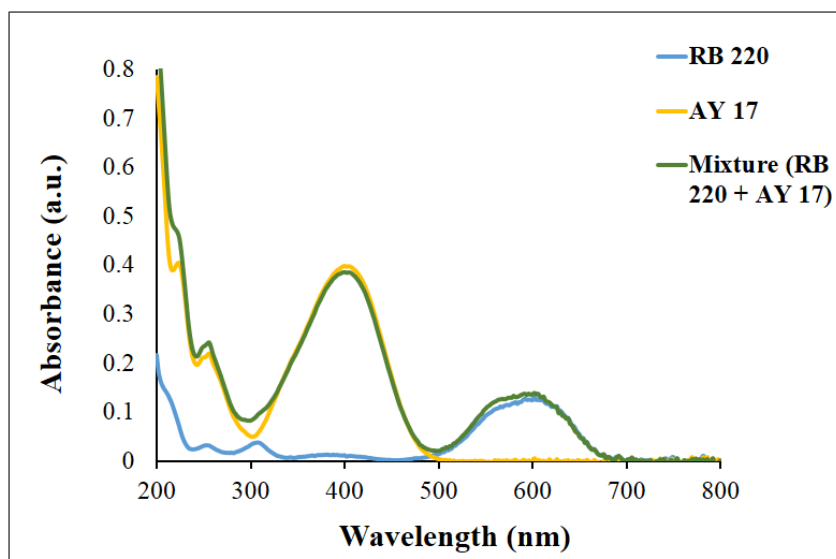


**Fig. 4.54** Absorption spectra of AY 17 and RB 220 dye and the mixture of AY 17 and RB 220

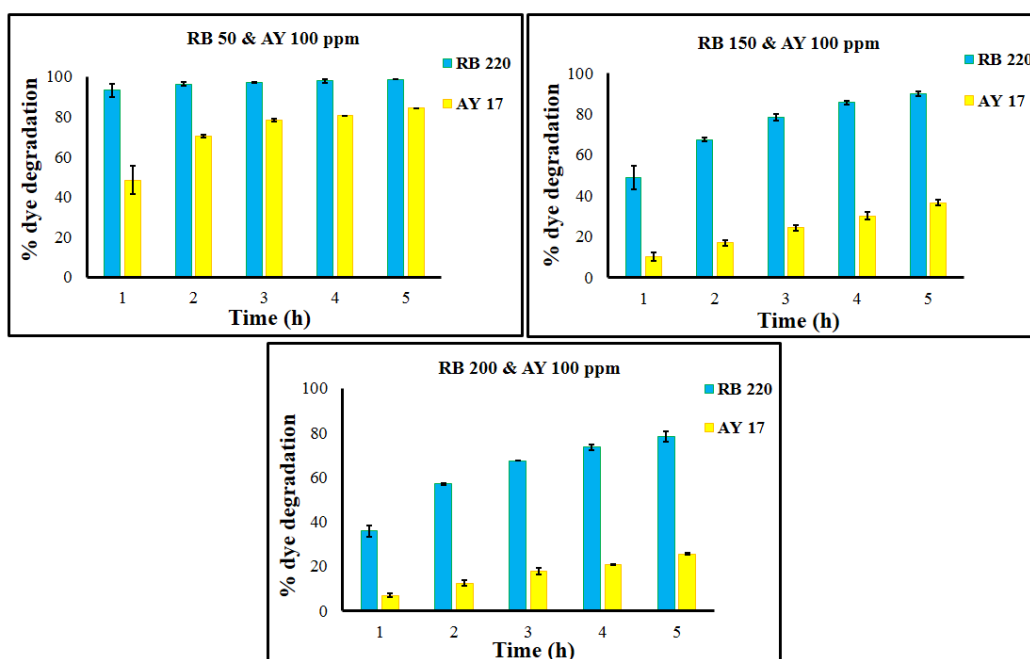


**Fig. 4.55** Percentage dye degradation in mixture (RB 220 + AY 17) with initial AY17 concentration of 100 ppm being constant

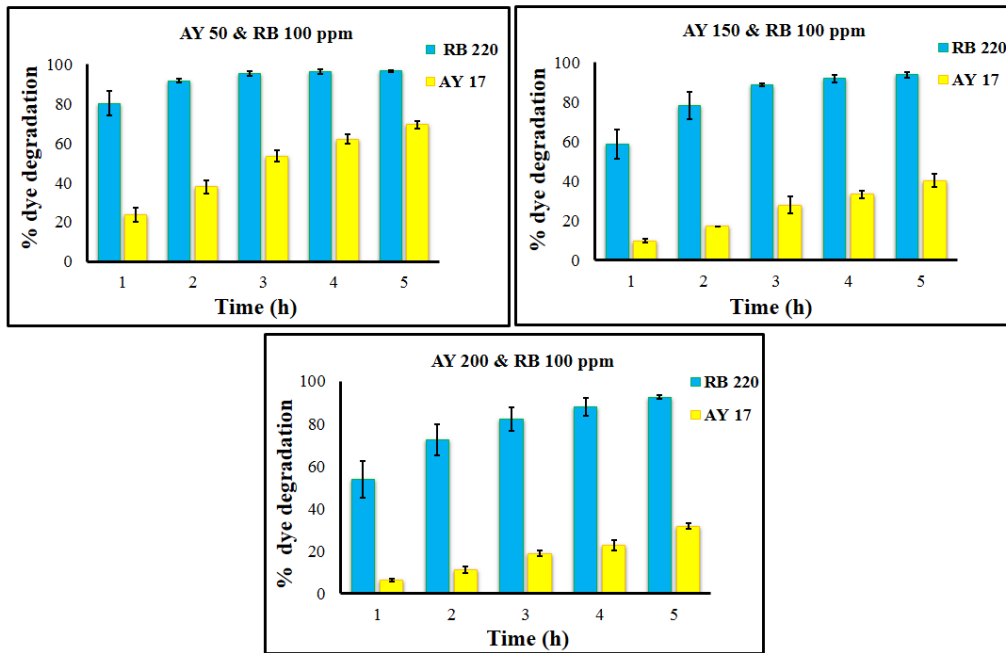


**Fig. 4.56** Percentage dye degradation in mixture (RB 220 + AY 17) with initial RB 220 concentration of 100 ppm being constant

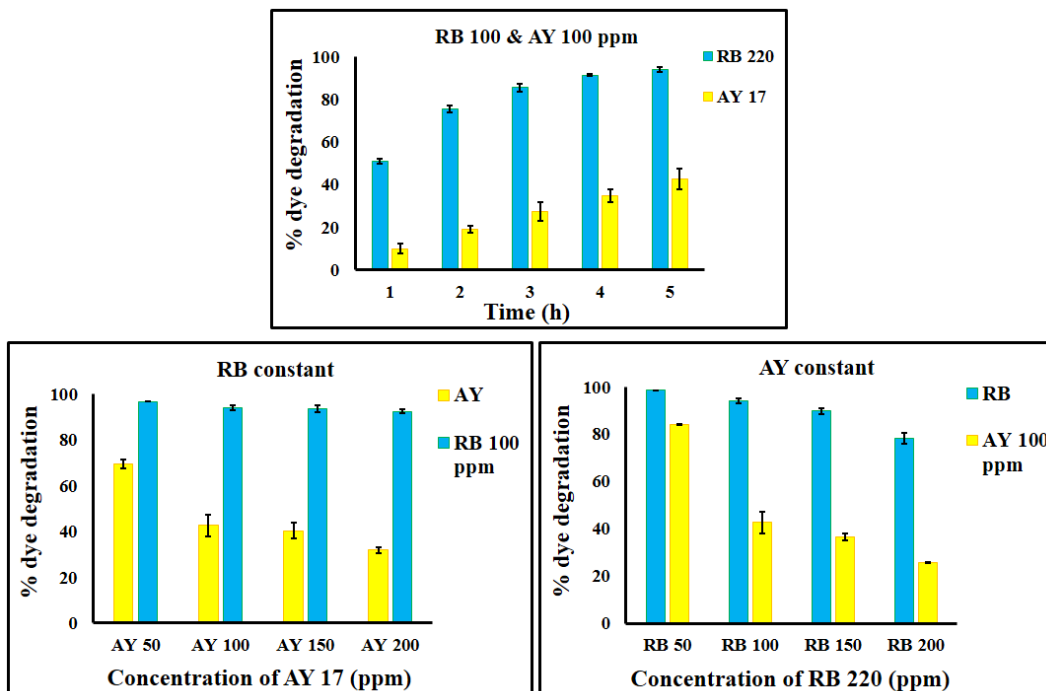


**Fig. 4.57** Influence of one dye over the other at the end of 5<sup>th</sup> h

#### 4.8 REUSABILITY STUDIES OF AgO@TiO<sub>2</sub> modified with Cu nanocomposite (ATC 75) IN RB 220 DYE DEGRADATION

The reusability studies conducted for AgO/Ag<sub>2</sub>O@TiO<sub>2</sub> modified with Cu (ATC 75) nanocomposites in RB 220 dye degradation with initial dye concentration of 100 ppm and catalyst loading of 1 g/L under visible light showed that the catalyst can be reused upto three cycles. Almost complete degradation was obtained in first cycle which slightly decreased to 90% in the second cycle followed by a reduction upto 71 % in the third cycle at the end of 90 min (Fig. 4.58). Though there was no much loss in catalytic activity upto third cycle, further reusability might decrease its activity to a greater extent, therefore it can be concluded that the AgO/Ag<sub>2</sub>O@TiO<sub>2</sub> modified with Cu catalyst exhibits good photocatalytic activity upto three cycles and hence can be reused for three cycles.

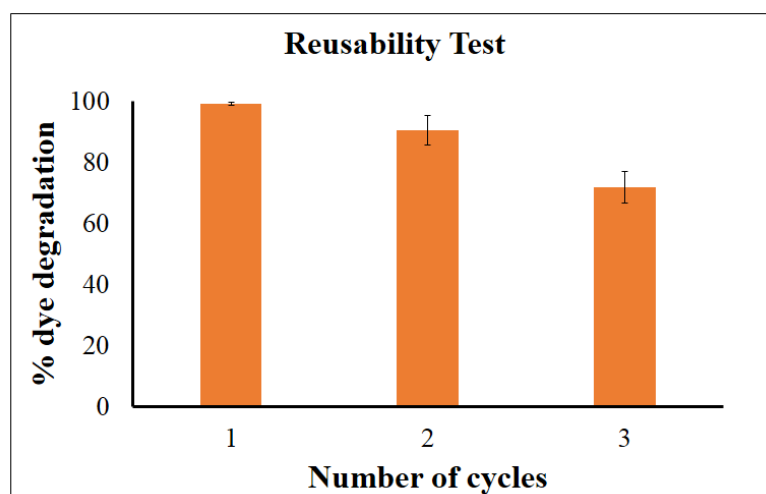


**Fig. 4.58** Reusability studies in RB 220 degradation using AgO @TiO<sub>2</sub> modified with Cu (ATC-75) nanocomposites



## CHAPTER 5

### SUMMARY AND CONCLUSION

The silver-based TiO<sub>2</sub> and silver-based TiO<sub>2</sub> modified with Cu nanocomposites were extracellularly synthesized using culture supernatant of *Alcaligenes aquatilis* at room temperature and evaluated for their application in the degradation of RB 220 and AY 17 dyes under visible and solar light. Three different methods of synthesis were tested and the best method was chosen based on the photocatalytic activity of the synthesized nanocomposite particles. Various synthesis parameters and dye degradation process parameters were optimized based on one factor at a time approach in order to maximize the photocatalytic activity and the degradation of the dyes.

The findings of this study are summarized as below:

- The Ag-based TiO<sub>2</sub> nanocomposite was synthesized by three different methods, namely Two step method (Method A), One pot synthesis method with sequential addition of precursors (Method B) and One pot synthesis method with simultaneous addition of precursors (Method C).
- Two-step method (Method A) was chosen as the best method as the synthesized Ag based TiO<sub>2</sub> nanocomposites exhibited better photocatalytic activity in terms of degradation of RB 220 under visible light irradiation
- The optimum synthesis conditions were found to be molar ratio of Ag to Ti of 1:1.6, CFS pH of 7, synthesis time of 4 h for silver ion reduction ( $t_{\text{step 1}}$ ), and 4 h synthesis time after the addition of Ti precursor ( $t_{\text{step 2}}$ ) for the formation of TiO<sub>2</sub>, thus making total synthesis time as 8 h, based on the photocatalytic activity.
- The nanocomposite synthesized under optimum conditions consisted AgO, Ag<sub>2</sub>O and rutile TiO<sub>2</sub> where AgO/Ag<sub>2</sub>O particles were embedded in TiO<sub>2</sub> and referred as AgO/Ag<sub>2</sub>O@TiO<sub>2</sub>. The particles were spherical in shape with

average particle size of 29.8 nm and capped with molecules of biological origin acting like capping agents and exhibited band gap energy of 1.7 eV.

- AgO/Ag<sub>2</sub>O@TiO<sub>2</sub> nanocomposite synthesized under optimum conditions resulted in the initial degradation rate of 3.85 mg/L/min with 98 % degradation of RB 220 at the end of 90 min and pseudo first-order kinetic constant of 0.0492 min<sup>-1</sup> and showed better photocatalytic activity than the Bio-TiO<sub>2</sub>, AgO/Ag<sub>2</sub>O and AgO/Ag<sub>2</sub>O@TiO<sub>2</sub> nanocomposite synthesized under unoptimized conditions.
- LCMS results revealed the disappearance of certain peaks after the photocatalytic reaction which were present in the initial samples indicating the breakdown of dyes into simpler compounds with two possible pathways based on the m/z values.
- Further, the photocatalytic process parameters were optimized to maximize the degradation of RB 220 based on which dye solution pH of pH 3 and dye to catalyst ratio of 1:10 were found to be the optimum. Acidic pH favoured the degradation process
- Under optimum dye degradation process conditions, almost complete degradation of 100 ppm RB 220 dye could be achieved in 90 min in the presence of 1 g/L of AgO/Ag<sub>2</sub>O@TiO<sub>2</sub> nanocomposite synthesized under optimized conditions, with initial degradation rate of 5.49 mg/L/min.
- As the concentration of dye increased from 100 to 500 ppm with the same catalyst loading, rate of photocatalytic degradation decreased and the dye degradation at the end of 90 min, decreased from 99 % to 31 %.
- AgO/Ag<sub>2</sub>O@TiO<sub>2</sub> nanocomposite synthesized under optimum conditions was found to be photocatalytically active under solar light exhibiting 96.6 % degradation of 100 ppm RB 220 in 90 min and first order rate constant of 0.0367 min<sup>-1</sup>.
- A mechanism of photocatalytic degradation under solar light by AgO/Ag<sub>2</sub>O@TiO<sub>2</sub> nanocomposite is proposed wherein TiO<sub>2</sub> gets excited by UV light and AgO as well as Ag<sub>2</sub>O get excited by visible light following charge

separation, with CB of TiO<sub>2</sub> acting as electron centre and VB of AgO and Ag<sub>2</sub>O acting as hole centres.

- Though AgO/Ag<sub>2</sub>O@TiO<sub>2</sub> nanocomposite was very effective in the degradation of RB-220 both under visible and solar light, it did not exhibit appreciable activity in the degradation of AY 17.
- AgO/Ag<sub>2</sub>O@TiO<sub>2</sub> modified with Cu (ATC) nanocomposite was prepared by three step method and the optimum molar ratio of Ag:Ti:Cu used in the synthesis process and the calcination temperature were 1:1.6:0.7 and 400°C respectively. It consisted AgO, TiO<sub>2</sub> and Cu as CuO and referred as AgO@TiO<sub>2</sub> modified with Cu nanocomposite (ATC-75).
- AgO@TiO<sub>2</sub> modified with Cu nanocomposite particles were distinct and spherical in shape of average size of 14.3 nm and possessing band gap energy of 2.7 eV.
- ATC-75 nanocomposites could degrade 100 ppm RB 220 almost completely in 45 minutes, whereas complete degradation could be achieved with AgO/Ag<sub>2</sub>O@TiO<sub>2</sub> at the end of 90 min with 1 g/L catalyst under visible light irradiation.
- ATC-75 nanocomposite was also found to be highly active under solar light in degradation of AY 17 dyes as compared to AgO/Ag<sub>2</sub>O@TiO<sub>2</sub> nanocomposite.
- Degradation reaction of AY 17 using ATC-75 nanocomposite followed the pseudo first-order kinetics with k value of 0.0263 min<sup>-1</sup>.
- The degradation rate of AY 17 with ATC-75 greatly reduced on increasing its own concentration or on increasing the concentration of the other dye in the solution of binary dye mixtures of RB 220 and AY 17, whereas the degradation rate of RB 220 was not much affected by the presence of AY 17 dye.
- ATC -75 nanocomposite showed good reusability potential upto three cycles of reuse with only 30% reduction in the percentage degradation of the RB-220 dye.

It may be concluded that AgO/Ag<sub>2</sub>O@TiO<sub>2</sub> nanocomposite and AgO/Ag<sub>2</sub>O@TiO<sub>2</sub> modified with Cu nanocomposites synthesized by extracellular microbial based method using *Alcaligenes aquatilis* are visible light active and show potential in their application as solar light active photocatalyst in the degradation of dyes. These photocatalysts can be used in the treatment of wastewater containing dyes by harnessing solar energy. The synthesis was carried out under ambient conditions in aqueous solution without the use of any toxic solvents and thus proves to be a green, environmental friendly and energy efficient method. The developed method involved the extracellular synthesis being carried out under cell free environment, circumventing the challenges involved in the separation of nanoparticles and cell biomass, thus proving to be technologically attractive and potentially economical.

### **Scope for future studies**

- To assess the effectiveness of the biosynthesized silver based titania nanocomposites for other class of pollutants.
- To study the application of the biosynthesized silver based titania nanocomposites in continuous photocatalytic reactors in immobilized form
- To scale up the biosynthesis process.

## REFERENCES

- Ahmadiasl, R., Moussavi, G., Shekoohiyan, S., and Razavian, F. (2022). "Synthesis of Cu-Doped TiO<sub>2</sub> Nanocatalyst for the Enhanced Photocatalytic Degradation and Mineralization of Gabapentin under UVA/LED Irradiation: Characterization and Photocatalytic Activity." *Catalysts.*, 12, 1310.
- Ahmed, A., Usman, M., Yu, B., Ding, X., Peng, Q., Shen, Y., and Cong, H. (2020). "Efficient photocatalytic degradation of toxic Alizarin yellow R dye from industrial wastewater using biosynthesized Fe nanoparticle and study of factors affecting the degradation rate." *J. Photochem. Photobiol. B Biol.* 202, 111682
- Ahmed, E., Kalathil, S., Shi, L., Alharbi, O., and Wang, P. (2018). "Synthesis of ultra-small platinum, palladium and gold nanoparticles by *Shewanella loihica* PV-4 electrochemically active biofilms and their enhanced catalytic activities." *Journal of Saudi Chemical Society.*, 22 (8), 919-929.
- Ahmed, M. A., El-katori, E. E., and Gharni, Z. H. (2013). "Photocatalytic degradation of methylene blue dye using Fe<sub>2</sub>O<sub>3</sub>/TiO<sub>2</sub> nanoparticles prepared by sol – gel method." *J. Alloys Compd.*, 553, 19–29.
- Ai, J., Biazar, E., Jafarpour, M., Montazeri, M., Majdi, A., Aminifard, S., Rad, H. G. (2011). "Nanotoxicology and nanoparticle safety in biomedical designs." *Int J Nanomedicine*, 6, 1117-1127
- Ajibade, P.A.; Oluwalana, A.E. (2021). "Photocatalytic Degradation of Single and Binary Mixture of Brilliant Green and Rhodamine B Dyes by Zinc Sulfide Quantum Dots." *Molecules.*, 26, 7686.
- Akel, S., Dillert, R., Balayeva, N.O., Boughaled, R., Koch, M. El Azzouzi, J., and Bahnemann, D. W. (2018). "Ag/Ag<sub>2</sub>O as a Co-catalyst in TiO<sub>2</sub> photocatalysis: effect of the Co-catalyst/photocatalyst mass ratio." *Catalysts.*, 8 (2018) 647
- Akhtar, T., Hill, A. J., Bhat, A., Schwank, J. W., Nasir, H., Aqsa, S., Bukhari, B., and Sitara, E. (2023). "Fabrication of ruthenium doped Ag@TiO<sub>2</sub> core-shell

nanophotocatalyst for the efficient reduction of nitrophenols.” *Appl. Surf. Sci.*, 630, 157491.

Akram, N., Guo, J., Guo, Y., Kou, Y., Suleman, H., and Wang, J. (2021). “Enhanced synergistic catalysis of novel Ag<sub>2</sub>O/CuO nanosheets under visible light illumination for the photodecomposition of three dyes.” *Journal of Environmental Chemical Engineering*, 9(2), 104824.

Alamri, S. A. M. (2018). “Controllable biogenic synthesis of intracellular silver/silver chloride nanoparticles by *Meyerozyma guilliermondii* KX008616.” *J. Microbiol. Biotechnol.* 28(6), 917–930

Alfryyan, N., Kordy, M. G. M., Abdel-Gabbar, M., Soliman, H. A., and Shaban, M. (2022). “Characterization of the biosynthesized intracellular and extracellular plasmonic silver nanoparticles using *Bacillus cereus* and their catalytic reduction of methylene blue.” *Sci. Rep.*, 12(1), 1–14

Ali, J., Ali, N., Jamil, S. U. U., Waseem, H., Khan, K., & Pan, G. (2017). Insight into eco-friendly fabrication of silver nanoparticles by *Pseudomonas aeruginosa* and its potential impacts. *Journal of environmental chemical engineering*, 5(4), 3266-3272.

Ali, M. A., Ahmed, T., Wu, W., Hossain, A., Hafeez, R., Masum, M. M. I., Wang, Y., An, Q., Sun, G., and Li, B. (2020). “Advancements in plant and microbe-based synthesis of metallic nanoparticles and their antimicrobial activity against plant pathogens.” *Nanomaterials*, 10(6), 1–24

Ali, T., Ahmed, A., Alam, U., Uddin, I., Tripathi, P., Muneer, M. (2018). “Enhanced photocatalytic and antibacterial activities of Ag-doped TiO<sub>2</sub> nanoparticles under visible light.” *Materials Chemistry and Physics.*, 212, 325e335

Alkaykh, S., Mbarek, A., and Ali-Shattle, E. E. (2020). “Photocatalytic degradation of methylene blue dye in aqueous solution by MnTiO<sub>3</sub> nanoparticles under sunlight irradiation.” *Heliyon.*, 6 (4) e03663.

Almeida, N. A., Martins, P.M., Teixeira, S., Silva, J.A., Sencadas, V., Kuhn, K., Cuniberti, G., Lanceros-Mendez, S., and Marques, P.A.A.P. (2016). "TiO<sub>2</sub>/graphene oxide immobilized in P(VDF-TrFE) electrospun membranes with enhanced visible-light induced photocatalytic performance." *J Mater Sci*, 51, 6974–6986.

Al-namshah, K. S., Baeissa, E. S., and Mohamed, R. M. (2016). "Effect of weight percent of tetrapropyl ammonium hydroxide solution on chemical and photocatalytic properties of titanium dioxide nanoparticles." *Front Nanosci Nanotech*, 2(4), 169–172.

Alsamhary, K. I. (2020). "Eco-friendly synthesis of silver nanoparticles by *Bacillus subtilis* and their antibacterial activity." *Saudi J. Biol. Sci.*, 27(8), 2185–2191.

Ammari, Y., Atmani, K. El, Bay, L., Bakas, I., Qourzal, S., and Ichou, I. A. (2020). "Elimination of a mixture of two dyes by photocatalytic degradation based on TiO<sub>2</sub> P-25 Degussa." *Mater. Today Proc.*, 22, 126–129.

Ankita Khanna, (2014). "Batch and Continuous Photocatalytic Degradation of Azodyes using Ag core-TiO<sub>2</sub> Shell Structured Nanoparticles in Free and Immobilized form (thesis)." National Institute of Technology, Karnataka

Arai, T., Horiguchi, M., Yanagida, M., Gunji, T., Sugihara, H., and Sayama, K. (2009). "Reaction mechanism and activity of WO<sub>3</sub>-catalyzed photodegradation of organic substances promoted by a CuO cocatalyst." *J. Phys. Chem. C*, 113(16), 6602–6609

Arasu, K. A. S., Raja, A.G., Rajaram, R. (2020). "Photocatalytic Degradation of Effluent water by CuO@Ag Core-shell Nanoparticles as Effective Catalyst under Irradiation of UV-light." *Materials Today: Proceedings.*, 68, 556–563

Arif, D., Niazi, M. B. L., Ul-Haq, N., Anwar, M. B., and Hashmi, E. (2015). "Preparation of Antibacterial Cotton Fabric Using Chitosan-silver Nanoparticles." *Fibers and Polymers.*, 16 (7) 1519-1526.

Ayodhya, D., Venkatesham, M., Santoshi, A., Bhagavanth, G., Ramakrishna, D., and Veerabhadram, G. (2016). "Photocatalytic degradation of dye pollutants under solar ,

visible and UV lights using green synthesised CuS nanoparticles.” *Journal of Experimental Nanoscience*, 11 (6) 418 - 432.

Bai, H. J., Zhang, Z. M., Guo, Y., and Yang, G. E. (2009). “Biosynthesis of cadmium sulfide nanoparticles by photosynthetic bacteria *Rhodospseudomonas palustris*.” *Colloids and Surfaces B: Biointerfaces*, 70, 142–146.

Baig, N., Kammakakam, I., Falath, W., and Kammakakam, I. (2021). “Nanomaterials: A review of synthesis methods, properties, recent progress, and challenges.” *Mater. Adv.*, 2(6), 1821–1871.

Bansal, V., Poddar, P., Ahmad, A., and Sastry, M. (2006). “Room-Temperature Biosynthesis of Ferroelectric Barium Titanate Nanoparticles.” *J. AM. CHEM. SOC* (10), 11958–11963.

Bansal, V., Rautaray, D., Bharde, A., Ahire, K., and Sanyal, A. (2005). “Fungus-mediated biosynthesis of silica and titania particles.” *J. Mater. Chem*, 15, 2583–2589.

Barth, A. (2007). “Infrared spectroscopy of proteins.” *Biochim. Biophys. Acta.*, 1767, 1073–1101

Beamson, G., Briggs, D. (1992). High Resolution XPS of Organic Polymers – The Scienta ESCA 300 Database, *John Wiley & Sons*, Chichester, 280.

Bhakya, S., Muthukrishnan, S., Sukumaran, M., Muthukumar, M., Kumar, S. T., & Rao, M. V. (2015). Catalytic degradation of organic dyes using synthesized silver nanoparticles: a green approach. *Journal of Bioremediation & Biodegradation*, 6(5), 1.

Bharati, B., Sonkar, A. K., Singh, N., Dash, D., and Rath, C. (2017). “Enhanced photocatalytic degradation of dyes under sunlight using biocompatible TiO<sub>2</sub> nanoparticles nanoparticles.” *Mater. Res. Express*, 4, 085503.

Bhattacharya, R., and Mukherjee, P. (2008). “Biological properties of ‘naked’ metal nanoparticles.” *Adv. Drug Deliv. Rev.*, 60(11), 1289–1306

Bian, H., Zhang, Z., Xu, X., Gao, Y., Wang, T., (2020). “Photocatalytic activity of Ag/ZnO /AgO/TiO<sub>2</sub> composite.” *Physica E: Low-dimensional Systems and Nanostructures.*, 124, 14236

Biswas, A., Mandal, R. P., Dutta, S., Nandi, N., and De, S. (2015). “Catalytic and photocatalytic behavior of TiO<sub>2</sub> based nanoparticles—their use in the synthesis of a novel TICT probe.” *Mater. Res. Express*, 2(6), 065011.

Boduroglu, G., Kilic, N.K., and Donmez, G. (2014). “Bioremoval of Reactive Blue 220 by *Gonium* sp. Biomass.” *Environmental Technology.*, 35 (19) 2410-2415

Bopape, D. A., Mathobela, S., Matinise, N., Motaung, D. E., and Hintsho-mbita, N. C. (2023). “Green Synthesis of CuO-TiO<sub>2</sub> Nanoparticles for the Degradation of Organic Pollutants : Physical , Optical and Electrochemical Properties.” *Catalysts.*, 13, 163

Bukhari, S. I., Hamed, M. M., Al-agamy, M. H., Gazwi, H. S. S., Radwan, H. H., and Youssif, A. M. (2021). “Biosynthesis of Copper Oxide Nanoparticles Using *Streptomyces* MHM38 and Its Biological Applications.” *Journal of Nanomaterials.*, 6693302,

Bunge, M., Søbjerger, L. S., Rotaru, A., Gauthier, D., Lindhardt, A. T., Hause, G., Finster, K., Kingshott, P., Skrydstrup, T., and Meyer, R. L. (2010). “Formation of Palladium (0) Nanoparticles at Microbial Surfaces Formation of Palladium (0) Nanoparticles at Microbial Surfaces.” *Biotechnology and Bioengineering.*,

Chiou, C.-H., Wu, C.-Y., and Juang, R.-S. (2008). “Influence of operating parameters on photocatalytic degradation of phenol in UV/TiO<sub>2</sub> process.” *Chem. Eng. J.*, 139, 322–329.

Cosma, D., Urda, A., Radu, T., Rosu, M. C., Mihet, M., and Socaci, C. (2022). “Evaluation of the Photocatalytic Properties of Copper Oxides/Graphene/TiO<sub>2</sub> Nanoparticles *Composites.*, 27, 5803

Coutts, J., Hintze, P., Meier, A., Devor, R., Surma, J., Maloney, P., and Mazyck, D. (2016). "Visible-light-responsive photocatalysis: ag-doped TiO<sub>2</sub> catalyst development and reactor design testing." *46th International Conference on Environmental Systems*.

Cruz-Ortiz, B. R., Hamilton, J. W. J., Pablos, C., Díaz-Jiménez, L., Cortés-Hernández, D. A., Sharma, P. K., Castro-Alfárez, M., Fernández-Ibañez, P., Dunlop, P. S. M., and Byrne, J. A. (2017). "Mechanism of photocatalytic disinfection using titania-graphene composites under UV and visible irradiation." *Chem. Eng. J.*, 316, 179–186.

Cuevas, R., Durán, N., Diez, M. C., Tortella, G. R., and Rubilar, O. (2015). "Extracellular Biosynthesis of Copper and Copper Oxide Nanoparticles by *Stereum hirsutum*, a Native White-Rot Fungus from Chilean Forests." *Journal of Nanomaterials.*, 789089

Dao, A.Q., Thi, T.T.L., Asif, M., Dong, S., Fu, C., and Liu, H. (2015). "Facile fabrication of stable r-GO/Pd–TiO<sub>2</sub>/r-GO thin film and its photoactivity under visible light." *Semicond. Sci. Technol*, 30.

Das, J., Das, K. C., Thakurata, D. G., and Dhar, S. S. (2021). "Visible light-assisted degradation of binary mixture of dyes using purple tea-mediated zinc oxide nanoparticles." *Environ QualManage.*,

Das, S.K., Dickinson, C., Lafir, F., Brougham, D.M., and Marsili, E. (2012). "Synthesis, characterization and catalytic activity of gold nanoparticles biosynthesized with *Rhizopus oryzae* protein extract." *Green Chem.*, 14, 1322–1334.

Das, V. L., Thomas, R., Varghese, R. T., Soniya, E. V., Mathew, J., and Radhakrishnan, E. K. (2014). "Extracellular synthesis of silver nanoparticles by the *Bacillus* strain CS 11 isolated from industrialized area." *3 Biotech*, 4(2), 121–126.

Desai, M. P., Patil, R. V, and Pawar, K. D. (2020). "Selective and sensitive colorimetric detection of platinum using *Pseudomonas stutzeri* mediated optimally synthesized antibacterial silver nanoparticles." *Biotechnol. Reports*, 25, e00404

Devadiga, A. (2016) "Biobased synthesis of Silver and Titanium dioxide nanoparticles for anti-bacterial sensor and photocatalytic applications." PhD thesis, National Institute of Technology Karnataka.

Devi, M., Praharaj, S., and Rout, D. (2022). "20 - Industrial problems and solution towards visible light photocatalysis." *Micro and Nano Technologies.*, 535-567.

Dhandapani, P., Maruthamuthu, S., and Rajagopal, G. (2012). "Bio-mediated synthesis of TiO<sub>2</sub> nanoparticles and its photocatalytic effect on aquatic biofilm." *J. Photochem. Photobiol. B Biol.*, 110, 43–49.

Dharmaraj, D., Krishnamoorthy, M., Rajendran, K., Karupiah, K., Annamalai, J., Durairaj, K. R., Santhiyagu, P., and Ethiraj, K. (2021). Antibacterial and cytotoxicity activities of biosynthesized silver oxide (Ag<sub>2</sub>O) nanoparticles using *Bacillus paramycoides*. *J. Drug Deliv. Sci. Technol.*, Elsevier B.V

Domany, E. B. El, Essam, T. M., Ahmed, A. E., and Farghali, A. A. (2018). "Biosynthesis Physico-Chemical Optimization of Gold Nanoparticles as Anti-Cancer and Synergetic Antimicrobial Activity Using *Pleurotus ostreatus* Fungus." *Journal of Applied Pharmaceutical Science.*, 8(05), 119-128.

Duran-Alvarez , J.C., Hernandez-Morales, V.A., Rodriguez-Varela, M., Guerrero-Araque, D., Ramirez-Ortega, D., Castillon, F., Acevedo-Pena, P., Zanella, R. (2020). "Ag<sub>2</sub>O/TiO<sub>2</sub> nanostructures for the photocatalytic mineralization of the highly recalcitrant pollutant iopromide in pure and tap water." *Catalysis Today.*, 341, 71–81

Elbeshehy, E. K. F., Elazzazy, A. M., and Aggelis, G. (2015). "Silver nanoparticles synthesis mediated by new isolates of *Bacillus* spp ., nanoparticle characterization and their activity against Bean Yellow Mosaic Virus and human pathogens." *Front. Microbiol.*, 6, 453.

Endo-Kimura, M., Janczarek, M., Bielan, Z., Zhang, D., Wang, K., Markowska-Szczupak, A., and Kowalska, E. (2019). "Photocatalytic and antimicrobial properties of ag<sub>2</sub>o/tio<sub>2</sub> heterojunction." *ChemEngineering*, 3(1), 1–18.

Esmail, R., Afshar, A., Morteza, M., Abolfazl, A., and Akhondi, E. (2022). "Synthesis of silver nanoparticles with high efficiency and stability by culture supernatant of *Bacillus* ROM6 isolated from Zarshouran gold mine and evaluating its antibacterial effects." *BMC Microbiology.*, 22, 97.

Farooq, M. H., Aslam, I., Shuaib, A., Anam, H. S., Rizwan, M., and Kanwal, Q. (2019). "Band gap engineering for improved photocatalytic performance of CuS/TiO<sub>2</sub> composites under solar light irradiation." *Bull. Chem. Soc. Ethiop.*, 33(3), 561–571.

Fouad, H., Li, H., Ding, Y., Yu, B., Ahmed, E., Ghulam, and A., Mo, J. (2016). "Synthesis and characterization of silver nanoparticles using *Bacillus amyloliquefaciens* and *Bacillus subtilis* to control filarial vector *Culex pipiens pallens* and its antimicrobial activity." *Artif. Cells, Nanomedicine, Biotechnol.*, 45 (7) 1369–1378.

Fujishima, A., & Honda, K. (1972). Electrochemical photolysis of water at a semiconductor electrode. *nature*, 238(5358), 37-38.

Fulekar, J., Dutta, D. P., Pathak, B., and Fulekar, M. H. (2018). "Novel microbial and root mediated green synthesis of TiO<sub>2</sub> nanoparticles and its application in wastewater remediation." *Journal of Chemical Technology and Biotechnology*, 93(3), 736-743.

Gao, S., Li, W., Dai, J., Wang, Q., and Suo, Z. (2021). "Effect of transition metals doping on electronic structure and optical properties of  $\beta$ -Ga<sub>2</sub>O<sub>3</sub>." *Materials Research Express.*, 8(2), 025904.

Gannoruwa, A., Ariyasinghe, B., & Bandara, J. (2016). The mechanism and material aspects of a novel Ag<sub>2</sub>O/TiO<sub>2</sub> photocatalyst active in infrared radiation for water splitting. *Catalysis Science & Technology*, 6(2), 479-487.

Gayathri, S., Jayabal, P., and Kottaisamy, M. (2015). "Synthesis of the graphene-ZnTiO<sub>3</sub> nanocomposite for solar light assisted photodegradation of methylene blue." *J. Phys. D. Appl. Phys.*, 415305, 415305.

Gemeel Abd, F., Mohsen, L. Y., Al-Shalah, L. A. M., and Alkaim, A. F. (2018). "Silver nanoparticles synthesized by using *Pseudomonas Aeruginosa* synergistically act with antibiotic." *Asian J. Microbiol. Biotechnol. Environ. Sci.*, S50–S52.

Goebel, J., Joo, J.B., Dahl, M., and Yin, Y. (2014). "Synthesis of tailored Au@TiO<sub>2</sub> core–shell nanoparticles for photocatalytic reforming of ethanol." *Catalysis Today* 225, 90– 95.

Gou, J., Ma, Q., Deng, X., Cui, Y., Zhang, H., Cheng, X., and Cheng, Q. (2017). "Fabrication of Ag<sub>2</sub>O/TiO<sub>2</sub>-Zeolite composite and its enhanced solar light photocatalytic performance and mechanism for degradation of norfloxacin." *Chemical Engineering Journal*, 308, 818-826.

Gratzel, M. (2003). "Dye-sensitized solar cells." *Journal of photochemistry and photobiology C: Photochemistry Reviews.*, 4(2), 145-153.

Gulce, H., Eskizeybek, V., Haspulat, B., Sar, F., Gu, A., and Avc, A. (2013). "Preparation of a New Polyaniline/CdO Nanocomposite and Investigation of Its Photocatalytic Activity : Comparative Study under UV Light and Natural Sunlight Irradiation." *Ind. Eng. Chem. Res.*, 52, (32), 10924-10934.

Gunture., Singh, A., Bhati, A., Khare, P., Tripathi, K. M., and Sonkar, S. K. (2019). "Soluble Graphene Nanosheets for the Sunlight-Induced Photodegradation of the Mixture of Dyes and its Environmental Assessment." *Scientific Reports.*, 9, 2522

Gupta, K., and Chundawat, T. S. (2019). "Bio-inspired synthesis of platinum nanoparticles from fungus *Fusarium oxysporum*: its characteristics , potential antimicrobial , antioxidant and photocatalytic activities." *Mater. Res. Express.*, 6, 1050d6

Gupta, R. K., Kumar, V., Gundampati, R. K., Malviya, M., Hasan, S. H., & Jagannadham, M. V. (2017). Biosynthesis of silver nanoparticles from the novel strain of *Streptomyces* Sp. BHUMBU-80 with highly efficient electroanalytical detection of hydrogen peroxide and antibacterial activity. *Journal of environmental chemical engineering*, 5(6), 5624-5635.

Gupta, S. M., and Tripathi, M. (2011). "A review of TiO<sub>2</sub> nanoparticles." *Chinese Sci. Bull.*, 56(16), 1639–1657.

Gurunathan, S., Kalishwaralal, K., Vaidyanathan, R., Venkataraman, D., Pandian, S. R. K., Muniyandi, J., Hariharan, N., and Eom, S. H. (2009). "Biosynthesis, purification and characterization of silver nanoparticles using *Escherichia coli*." *Colloids Surfaces B Biointerfaces*, 74(1), 328–335.

Hamrouni, A., Azzouzi, H., Rayes, A., Palmisano, L., Ceccato, R., and Parrino, F. (2020). "Enhanced solar light photocatalytic activity of Ag doped TiO<sub>2</sub>-Ag<sub>3</sub>PO<sub>4</sub> composites." *Nanomaterials.*, 10, 795.

Handbooks of Monochromatic XPS Spectra, Volume two, Commercially Pure Binary Oxides, 37-42.

Handoko, C. T., Moustakas, N. G., Peppel, T., Springer, A., Oropeza, F. E., Huda, A., Bustan, M. D., Yudono, B., Gulo, F., and Strunk, J. (2014). "Characterization and Effect of Ag(0) vs. Ag(I) Species and Their Localized Plasmon Resonance on Photochemically Inactive TiO<sub>2</sub>." *Catalysts*, 9, 323;

Hasan, S. S., Singh, S., Parikh, R. Y., and Dharne, M. S. (2008). "Bacterial Synthesis of Copper / Copper Oxide Nanoparticles Bacterial Synthesis of Copper / Copper Oxide Nanoparticles." *J. Nanosci. Nanotechnol.*, 8, 5.

Hirakawa, T., and Kamat, P. V. (2004). "Charge Separation and Catalytic Activity of Ag @ TiO<sub>2</sub> Core - Shell Composite Clusters under UV - Irradiation." *JACS*, (39), 0–6.

Hoflund, G. B., and Hazos, Z. F. (2000). "Surface characterization study of Ag, AgO, and Ag<sub>2</sub>O using x-ray photoelectron spectroscopy and electron energy-loss spectroscopy." *Physical Review B*, 62(16), 126–133.

Hoflund, G. B., Weaver, J. F., and Epling, W. S. (1995). "AgO XPS Spectra Host Material : AgO." *Surface Science Spectra*, 3(2).

Honary, S., Barabadi, H., Gharaei-, E., and Naghibi, F. (2012). "Green synthesis of copper oxide nanoparticles using *Penicillium aurantiogriseum*, *Penicillium citrinum*

and *Penicillium waksmanii*.” *Digest Journal of Nanomaterials and Biostructures.*, 7(3), 999–1005.

Hua, H., Xi, Y., Zhao, Z., Xie, X., Hu, C., and Liu, H. (2013). “Gram-scale wet chemical synthesis of Ag<sub>2</sub>O/TiO<sub>2</sub> aggregated sphere heterostructure with high photocatalytic activity.” *Mater. Lett.*, 91, 81-83.

Huo, Y., Chen, X., Zhang, J., Pan, G., Jia, J., and Li, H. (2014). “Ordered macroporous Bi<sub>2</sub>O<sub>3</sub>/TiO<sub>2</sub> film coated on a rotating disk with enhanced photocatalytic activity under visible irradiation.” *Appl. Catal. B Environ.*, 148–149, 550–556

Ibhadon, A. O., and Fitzpatrick, P. (2013). “Heterogeneous Photocatalysis: Recent Advances and Applications.” 189–218.

Ibrahim, E., Fouad, H., Zhang, M., Zhang, Y., Qiu, W., Yan, C., Li, B., Mo, J., and Chen, J. (2019). “Biosynthesis of silver nanoparticles using endophytic bacteria and their role in inhibition of rice pathogenic bacteria and plant growth promotion.” *RSC Adv.*, 9, 29293

Ibrahim, S., Ahmad, Z., Manzoor, M. Z., Mujahid, M., Faheem, Z., and Adnan, A. (2021). “Optimization for biogenic microbial synthesis of silver nanoparticles through response surface methodology , characterization , their antimicrobial , antioxidant , and catalytic potential.” *Sci. Rep.*, 11, 770

Ikram, M., Umar, E., Raza, A., Haider, A., Naz, S., Haider, J., Shahzadi, I., Hassan, J., and Ali, S. (2020). “Dye degradation performance, bactericidal behavior and molecular docking analysis of Cu-doped TiO<sub>2</sub> nanoparticles.” *RSC Adv.*, 10, 24215–24233.

Ilyas, H., Qazi, I. A., Asgar, W., Awan, M. A., and Khan, Z. (2011). “Photocatalytic Degradation of Nitro and Chlorophenols Using Doped and Undoped Titanium Dioxide Nanoparticles.” *Journal of Nanomaterials*, 589185.

Imyen, T., Limphirat, W., Rupprechter, G., and Kongkachuichay, P. (2019). “Roles of ZnO in Cu / Core – Shell Al – MCM-41 for NO Reduction by Selective Catalytic

Reduction with NH<sub>3</sub> : The Effects of Metal Loading and Cu / ZnO Ratio.” *ACS Omega*, 4, 1077–1085.

Janakiraman, N., and Johnson, M. (2015). “Functional groups of tree ferns ( *Cyathea* ) using FT-IR : chemotaxonomic implications.” *Romanian J. Biophys*, 25(2), 131–140.

Jayaseelan, C., Abdul, A., Mohana, S., Vishnu, A., Venkatesan, J., Kim, S., and Iyappan, M. (2013). “Biological approach to synthesize TiO<sub>2</sub> nanoparticles using *Aeromonas hydrophila* and its antibacterial activity.” *Spectrochim. Acta Part A Mol. Biomol. Spectrosc.*, 107, 82–89.

Jedynak, K., Wideł, D., and Rędzia, N. (2019). “Removal of rhodamine b (A basic dye) and acid yellow 17 (an acidic dye) from aqueous solutions by ordered mesoporous carbon and commercial activated carbon.” *Colloids and Interfaces*, 3(1).

Jha, A. K., and Prasad, K. (2010). “Colloids and Surfaces B : Biointerfaces Ferroelectric BaTiO<sub>3</sub> nanoparticles : Biosynthesis and characterization.” 75, 330–334.

Jha, A. K., and Prasad, K. (2010). “Ferroelectric BaTiO<sub>3</sub> nanoparticles : Biosynthesis and characterization.” *Colloids and Surfaces B : Biointerfaces*, 75, 330–334.

Jha, A. K., Prasad, K., and Kulkarni, A. R. (2009). “Synthesis of TiO<sub>2</sub> nanoparticles using microorganisms.” *Colloids and Surfaces B : Biointerfaces*, 71, 226–229.

Jiang, K., Zhang, J., Luo, R., Wan, Y., Liu, Z., and Chen, J. (2021). “A facile synthesis of Zn-doped TiO<sub>2</sub> nanoparticles with highly exposed (001) facets for enhanced photocatalytic performance.” *RSC advances*, 11(13), 7627-7632.

Jo, W. K., Kumar, S., Isaacs, M. A., Lee, A. F., and Karthikeyan, S. (2017). “Cobalt promoted TiO<sub>2</sub>/GO for the photocatalytic degradation of oxytetracycline and Congo Red.” *Applied Catalysis B: Environmental*, 201, 159-168.

John, M.S., Nagoth, J.A., Zannotti, M., Giovannetti, R., Mancini, A., Ramasamy, K.P., Miceli, C., Pucciarelli, S. (2021). “Biogenic Synthesis of Copper Nanoparticles Using Bacterial Strains Isolated from an Antarctic Consortium Associated to a Psychrophilic

Marine Ciliate: Characterization and Potential Application as Antimicrobial Agents.” *Mar. Drugs.*, 19, 263.

Kalishwaralal, K., Deepak, V., Ramkumarpandian, S., Nellaiah, H., and Sangiliyandi, G. (2008). “Extracellular biosynthesis of silver nanoparticles by the culture supernatant of *Bacillus licheniformis*.” *Mater Lett.*, 62, 4.

Karuppasamy, P., Ramzan, N., Nisha, N., Pugazhendhi, A., Kandasamy, S., and Pitchaimuthu, S. (2021). “An investigation of transition metal doped TiO<sub>2</sub> photocatalysts for the enhanced photocatalytic decoloration of methylene blue dye under visible light irradiation.” *J. Environ. Chem. Eng.*, 9(4), 105254.

Kato, Y., and Suzuki, M. (2020). “Synthesis of Metal Nanoparticles by Microorganisms.” *Crystals.*, 10(7), 589.

Kaur, R., Singla, P., & Singh, K. (2018). Transition metals (Mn, Ni, Co) doping in TiO<sub>2</sub> nanoparticles and their effect on degradation of diethyl phthalate. *International Journal of Environmental Science and Technology*, 15, 2359-2368.

Keat, C. L., Aziz, A., Eid, A. M., & Elmarzugi, N. A. (2015). Biosynthesis of nanoparticles and silver nanoparticles. *Bioresources and Bioprocessing*, 2(1), 1-11.

Kerkez, O., and Boz, I. (2015). “Photodegradation of Methylene Blue with Ag<sub>2</sub>O/TiO<sub>2</sub> under Visible Light: Operational Parameters.” *Chem. Eng. Commun.*, 202(4), 534–541

Kgatle, M., Sikhwivhilu, K., Ndlovu, G., and Moloto, N. (2021). “Degradation Kinetics of Methyl Orange Dye in Water Using Trimetallic Fe/Cu/Ag Nanoparticles.” *Catalysts.*, 11(4), 428 1–23.

Khan, R., Bhawana, P., and Fulekar, M.H. (2013). “Microbial decolorization and degradation of synthetic dyes: a review.” *Rev Environ Sci Biotechnol.*, 12 (1), 75-97.

Khan, M. R., & Rizvi, T. F. (2014). Nanotechnology: scope and application in plant disease management. *Plant Pathol J*, 13(3), 214-231.

Khan, N., and Bano, A. (2016). "Modulation of phytoremediation and plant growth by the treatment with PGPR, Ag nanoparticle and untreated municipal wastewater." *Int. J. Phytoremediation*, 18(12), 1258–1269

Khan, R., and Fulekar, M. H. (2016). "Biosynthesis of titanium dioxide nanoparticles using *Bacillus amyloliquefaciens* culture and enhancement of its photocatalytic activity for the degradation of a sulfonated textile dye Reactive Red 31." *J. Colloid Interface Sci.*, 475, 184–191.

Khanna, A. (2014). "Photocatalytic Degradation of Azo Dyes Using Ag@TiO<sub>2</sub> Core-Shell Structured Nanoparticles." PhD Thesis, National Institute of Technology Karnataka, Surathkal.

Khanna, A., and Shetty K, V. (2013). "Solar photocatalysis for treatment of Acid Yellow-17 (AY-17) dye contaminated water using Ag@TiO<sub>2</sub> core-shell structured nanoparticles." *Environ. Sci. Pollut. Res.*, 20(8), 5692–5707.

Khanna, A., and Shetty, V. K. (2014). "Solar light induced photocatalytic degradation of Reactive Blue 220 (RB-220) dye with highly efficient Ag@TiO<sub>2</sub> core-shell nanoparticles: A comparison with UV photocatalysis." *Sol. Energy*, 99, 67–76.

Kiani, F.A., Shamraiz, U., Badshah, A. (2020). "Enhanced photo catalytic activity of Ag<sub>2</sub>O nanostructures through strontium doping." *Mater. Res. Express.*, 7, 015035

Kilpady, A. (2016). "Development of biologically synthesized Ag/Ag<sub>2</sub>O@TiO<sub>2</sub> photocatalyst." M.tech thesis, National Institute of Technology Karnataka

Kim, M., Kim, Y. K., Lim, S. K., Kim, S., and In, S. I. (2015). "Efficient visible light-induced H<sub>2</sub> production by Au@ CdS/TiO<sub>2</sub> nanofibers: Synergistic effect of core-shell structured Au@ CdS and densely packed TiO<sub>2</sub> nanoparticles." *Applied Catalysis B: Environmental.*, 166, 423-431.

Kim, M. G., Kang, J. M., Lee, J. E., Kim, K. S., Kim, K. W., Cho, M., and Lee, S. G. (2021). "Effects of Calcination Temperature on the Phase Composition, Photocatalytic

Degradation, and Virucidal Activities of TiO<sub>2</sub> Nanoparticles.” *ACS Omega.*, 6, 10668–10678

Kirthi, V. A., Abdul Rahuman, A., Rajakumar, G., Marimuthu, S., Santhoshkumar, T., Jayaseelan, C., Elango, G., Abdul Zahir, A., Kamaraj, C., and Bagavan, A. (2011). “Biosynthesis of titanium dioxide nanoparticles using bacterium *Bacillus subtilis*.” *Mater. Lett.*, 65(17-18), 2745–2747.

Kouhkan, M., Ahangar, P., Babaganjeh, L. A., and Allahyari-devin, M. (2020). “Biosynthesis of Copper Oxide Nanoparticles Using *Lactobacillus casei* Subsp. *Casei* and its Anticancer and Antibacterial Activities.” *Current Nanoscience.*, 16, 101–111

Kumar, C. G., and Mamidyala, S. K. (2011). “Extracellular synthesis of silver nanoparticles using culture supernatant of *Pseudomonas aeruginosa*.” *Colloids Surfaces B Biointerfaces*, 84(2), 462–466.

Kumar, R., El-Shishtawy, R. M., Barakat, M. A. (2016). “Synthesis and Characterization of Ag-Ag<sub>2</sub>O/TiO<sub>2</sub>@polypyrrole Heterojunction for Enhanced Photocatalytic Degradation of Methylene Blue.” *Catalysts.*, 6, 76.

Lakhera, S. K., and Neppolian, B. (2021). “Visible light photocatalysis: Case study (process)”. *Handb. Nanomater. Wastewater Treat. Fundam. Scale up Issues*, 1101-1123.

Landage, K. S., Arbade, G.K., Khanna, P., Bhongale, C.J. (2020). “Biological approach to synthesize TiO<sub>2</sub> nanoparticles using *Staphylococcus aureus* for antibacterial and anti-biofilm applications.” *J Microbiol Exp.*, 8(1), 36–43

Li, J., Li, Q., Ma, X., Tian, B., Li, T., Yu, J., and Hua, Y. (2016). Biosynthesis of gold nanoparticles by the extreme bacterium *Deinococcus radiodurans* and an evaluation of their antibacterial properties. *International journal of nanomedicine*, 5931-5944.

Liao, Y, Deng, P., Wang, X., Zhang, D., Li, F., Yang, Q., Zhang, H., and Zhong, Z. (2018). “A Facile Method for Preparation of Cu<sub>2</sub>O-TiO<sub>2</sub> NTA Heterojunction with Visible-Photocatalytic Activity.” *Nanoscale Research Letters.*, 13, 221

Lim, J.S., Kim, S.M., Lee, S.Y., Stach, E.A., Culver, J.N., and Harris, M.T. (2010). “Biotemplated aqueous-phase palladium crystallization in the absence of external reducing agents.” *Nano Lett.*, 10 (10), 3863–3867.

Lin, Y., Li, D., Hu, J., Xiao, G., Wang, J., Li, W., and Fu, X. (2012). “Highly Efficient Photocatalytic Degradation of Organic Pollutants by PANI-Modified TiO<sub>2</sub> Composite.” *J. Phys. Chem. C*, 116, 5764–5772

Liu, B., Mu, L., Han, B., Zhang, J., and Shi, H. (2017). “Fabrication of TiO<sub>2</sub>/Ag<sub>2</sub>O heterostructure with enhanced photocatalytic and antibacterial activities under visible light irradiation.” *Appl. Surf. Sci.*, 396, 1596–1603

Liu, G., Wang, G., Hu, Z., Su, Y., and Zhao, L. (2019). “Ag<sub>2</sub>O nanoparticles decorated TiO<sub>2</sub> nano fibres as a p-n heterojunction for enhanced photocatalytic decomposition of RhB under visible light irradiation.” *Applied Surface Science* 465, 902–910.

Liu, R., Wang, P., Wang, X., Yu, H., and Yu, J. (2012). “UV- and visiblelight photocatalytic activity of simultaneously deposited and doped Ag/Ag(I)–TiO<sub>2</sub> photocatalyst.” *J. Phys. Chem. C.*, 116, 17721–17728.

Ljubas, D., Smoljani, G., and Jureti, H. (2015). “Degradation of Methyl Orange and Congo Red dyes by using TiO<sub>2</sub> nanoparticles activated by the solar and the solar-like radiation.” *Journal of Environmental Management*, 161, 83–91.

Lu, Y., Yao, M., Zhou, A., Hu, Q., & Wang, L. (2017). Preparation and photocatalytic performance of Ti<sub>3</sub>C<sub>2</sub>/TiO<sub>2</sub>/CuO ternary nanocomposites. *Journal of Nanomaterials*, 1978764

Mahdi, Z. S., Roshan, F. T., Nikzad, M., and Ezoji, H. (2021). “Biosynthesis of zinc oxide nanoparticles using bacteria: a study on the characterization and application for electrochemical determinationof bisphenol A.” *Inorganic and nano-metal chemistry.*, 51( 9), 1249–1257

Matsunaga, T., Tomoda, R., Nakajima, T., & Wake, H. (1985). Photoelectrochemical sterilization of microbial cells by semiconductor powders. *FEMS Microbiology letters*, 29 (1-2), 211-214.

Mekuye, B., and Abera, B. (2023). “Nanomaterials: An overview of synthesis, classification, characterization, and applications.” *Nano Sel.*, 4(8), 486–501.

Méndez-Medrano, M. G., Kowalska, E., Lehoux, A., Herissan, A., Ohtani, B., Bahena, D., Briois, V., Colbeau-Justin, C., Rodríguez-López, J. L., and Remita, H. (2016). “Surface Modification of TiO<sub>2</sub> with Ag Nanoparticles and CuO Nanoclusters for Application in Photocatalysis.” *J. Phys. Chem. C.*, 120, 5143–5154

Meng, Y. (2015). “A Sustainable Approach to Fabricating Ag Nanoparticles/PVA Hybrid Nanofiber and its Catalytic Activity.” *Nanomaterials.*, 5(2) 1124-1135.

Metuku, R. P., Pabba, S., Burra, S., Bindu, S. V. S. S. L. N., Gudikandula, K., and Charya, M.A.S. (2014). “Biosynthesis of silver nanoparticles from *Schizophyllum radiatum* HE 863742.1: their characterization and antimicrobial activity.” *3 Biotech.*, 4, 227-234.

Mingmongkol, Y., Trinh, D. T. T., Phuinthiang, P., Channei, D., Ratananikom, K., Nakaruk, A., & Khanitchaidecha, W. (2022). Enhanced photocatalytic and photokilling activities of Cu-doped TiO<sub>2</sub> nanoparticles. *Nanomaterials*, 12(7), 1198.

Mirkhani, V., Tangestaninejad, S., Moghadam, M., and Habibi, M. H. (2009). Photocatalytic Degradation of Azo Dyes Catalyzed by Ag Doped TiO<sub>2</sub> Photocatalyst.” *Iranian Chemical Society*, 6(3), 578–587.

Mishra, A., Tripathy, S. K., Wahab, R., and Jeong, S. (2011). “Microbial synthesis of gold nanoparticles using the fungus *Penicillium brevicompactum* and their cytotoxic effects against mouse mayo blast cancer C<sub>2</sub> C<sub>12</sub> cells.” *Appl Microbiol Biotechnol*, 92, 617–630.

Mogal, S. I., Gandhi, V. G., Mishra, M., Tripathi, S., Shripathi, T., Joshi, P. A., & Shah, D. O. (2014). Single-step synthesis of silver-doped titanium dioxide: influence of silver

on structural, textural, and photocatalytic properties. *Industrial & Engineering Chemistry Research*, 53(14), 5749-5758.

Moghaddam, K.M. (2010). “An Introduction to microbial metal nanoparticle preparation method.” *J Young Invest*, 19(19), 1–6

Mohammadlou, M., Maghsoudi, H., and Jafarizadeh-Malmiri, H. (2016). “A Review on Green Silver Nanoparticles Based on Plants: Synthesis, Potential Applications and Eco-Friendly Approach.” *International Food Research Journal.*, 232, 446-463.

Mohd Yusof, H., Abdul Rahman, N. A., Mohamad, R., Zaidan, U. H., & Samsudin, A. A. (2020). Biosynthesis of zinc oxide nanoparticles by cell-biomass and supernatant of *Lactobacillus plantarum* TA4 and its antibacterial and biocompatibility properties. *Scientific reports*, 10(1), 19996.

Mondal, A. H., Yadav, D., Mitra, S., and Mukhopadhyay, K. (2020). “Biosynthesis of Silver Nanoparticles Using Culture Supernatant of *Shewanella* sp. ARY1 and Their Antibacterial Activity.” *International Journal of Nanomedicine.*, 15, 8295-8310.

Morales-Torres, S., Pastrana-Martínez, L. M., Figueiredo, J. L., Faria, J. L., & Silva, A. M. (2012). Design of graphene-based TiO<sub>2</sub> photocatalysts—a review. *Environmental Science and Pollution Research*, 19, 3676-3687.

Mosquera, A. A., Albella, J. M., Navarro, V., and Bhattacharyya, D. (2016). “Effect of silver on the phase transition and wettability of titanium oxide films.” *Scientific Reports* 6, 1–14.

Mukul, M., Devi, N., Sharma, S., Tripathi, S. K., and Rani, M. (2020). “Materials Today : Proceedings Synthesis and study of TiO<sub>2</sub>/CuO core shell nanoparticles for photovoltaic applications.” *Mater. Today Proc.*, 28, 1382–1385.

Muthirulan, P., Devi, C. N., and Sundaram, M. M. (2017). “Synchronous role of coupled adsorption and photocatalytic degradation on CAC–TiO<sub>2</sub> composite generating excellent mineralization of alizarin cyanine green dye in aqueous solution.” *Arabian Journal of Chemistry.*, 10 (1) 1477-1483.

- Nam, N. H., and Luong, N. H. (2019). *Nanoparticles: Synthesis and applications. Mater. Biomed. Eng.*, 211–240.
- Naraginti, S., Thejaswini, T.V.L., Prabhakaran, D., Sivakumar, A., Satyanarayana, V.S.V., Arun Prasad, A. S. (2015). “Enhanced Photo-catalytic Activity of Sr and Ag co-doped TiO<sub>2</sub> Nanoparticles for the degradation of Direct Green-6 and Reactive Blue-160 under UV & Visible Light.” *Spectrochimica Acta Part A Molecular and Biomolecular Spectroscopy.*, 149, 571-579
- Narasaiah, B. P., Banoth, P., Guillermo, A., Dominguez, B., Mandal, B. K., Kumar, C. K., Barnes, C. H. W., Valladares, L. D. L. S., and Kollu, P. (2022). “Biogenic Photo-Catalyst TiO<sub>2</sub> Nanoparticles for Remediation of Environment Pollutants.” *ACS Omega.*, 7(30), 26174–26189
- Natarajan, K., Selvaraj, S., and Murty, V. R. (2010). “Microbial production of silver nanoparticles.” *Digest Journal of Nanomaterials and Biostructures*, 5(1), 135–140.
- Naumann, D. (2000). “Infrared Spectroscopy in Microbiology.” *Encyclopedia of Analytical Chemistry*, 102–131.
- Naz, F., Asimullah, G., Nabi, K., Nawaz, A., Ali, S., and Siddique, M. (2022). “A Novel Approach for the Photocatalytic Degradation of Binary Dyes Mixture Using - SnO<sub>2</sub> Nanoparticles as a Catalyst.” *J. Clust. Sci.*, (0123456789).
- Nguyen, C.H., Tuong, T., Tran, V., Tran, L., Juang, R-S. (2023). “Facile synthesis of reusable Ag/TiO<sub>2</sub> composites for efficient removal of antibiotic oxytetracycline under UV and solar light irradiation.” *Journal of the Taiwan Institute of Chemical Engineers.*, 145, 104825
- Nguyen, M. T., Nguyen, C. K., Vu, T. M. P., Van Duong, Q., Pham, T. L., & Nguyen, T. C. (2014). A study on carbon nanotube titanium dioxide hybrids: experiment and calculation. *Advances in Natural Sciences: Nanoscience and Nanotechnology*, 5(4), 045018.

Omajali, J. B., Mikheenko, I. P., Merroun, M. L., Wood, J., and Macaskie, L. E. (2015). “Characterization of intracellular palladium nanoparticles synthesized by *Desulfovibrio desulfuricans* and *Bacillus benzeovorans*.” *J Nanopart Res.*, 17, 264.

Ordenes-aenishanslins, N. A., Saona, L. A., Durán-toro, V. M., Monrás, J. P., Bravo, D. M., and Pérez-donoso, J. M. (2014). “Use of titanium dioxide nanoparticles biosynthesized by *Bacillus mycoides* in quantum dot sensitized solar cells.” *Microbial Cell Factories*, 13 (90) 1–10.

Pal, N.B., and Kryschi, C. (2016). “Improved photocatalytic activity of gold decorated differently doped TiO<sub>2</sub> nanoparticles: A comparative study.” *Chemosphere*, 144, 1655-1664.

Parandhaman, T., Das, A., Ramalingam, B., Samanta, D., Sastry, T. P., Baran, A., and Das, S. K. (2015). “Antimicrobial behavior of biosynthesized silica – silver nanocomposite for water disinfection : A mechanistic perspective.” *J. Hazard. Mater.*, 290, 117–126.

Paul, K. K., Ghosh, R., and Giri, P. K. (2016). “Mechanism of strong visible light photocatalysis by Ag<sub>2</sub>O-nanoparticle- decorated monoclinic TiO<sub>2</sub> (B) porous nanorods.” *Nanotechnology*, 27(31), 1–15.

Peng, Z., Tang, H., Tang, Y., Yao, K. F., and Shao, H. H. (2014). “Synthesis and Photocatalytic Activity of Magnetically Recoverable Core-Shell Nanoparticles.” *International Journal of Photoenergy*, 867565.

Perovic, K., dela Rosa 1, F.M., Kovacic, M., Kusic, H., Stangar, U. L., Fresno, F., Dionysiou, D.D., and Bozic, A. L. (2020). “Recent Achievements in Development of TiO<sub>2</sub>-Based Composite Photocatalytic Materials for Solar Driven Water Purification and Water Splitting.” *Materials.*, 13, 1338.

Petit, T., Puskar, L., Dolenko, T., Choudhury, S., Ritter, E., Burikov, S., Laptinskiy, K., Brzustowski, Q., Schade, U., Yuzawa, H., Nagasaka, M., Kosugi, N., Kurzyp, M., Girard, H., Arnault, J., Osawa, E., Nunn, N., Shenderova, O., and Aziz, E. F. (2017).

“Unusual Water Hydrogen Bond Network around Hydrogenated Nanodiamonds.” *J. Phys. Chem. C*, 121, 5185–5194

Pham, V. V., Bui, D. B., Tran, H. H., Cao, M. T., Nguyen, T.K., Kim, Y. S., and Le, V. H. (2018). “Photoreduction route for Cu<sub>2</sub>O/TiO<sub>2</sub> nanotubes junction for enhanced photocatalytic activity.” *RSC Adv.*, 8, 12420.

Pinheiro, L. R. S., Gradíssimo, D. G., Xavier, L. P., and Santos, A. V. (2022). “Degradation of Azo Dyes: Bacterial Potential for Bioremediation.” *Sustain.*, 14(3), 1–23.

Pino-sandoval, D., Villanueva-rodríguez, M., and Cantú-c, M. E. (2020). “Performance of Ag-Cu /TiO<sub>2</sub> photocatalyst prepared by sol-gel method on the inactivation of Escherichia coli and Salmonella typhimurium.” *Journal of Environmental Chemical Engineering.*, 8, 104539

Post, P., Wurlitzer, L., Maus-Friedrichs, W., Weber, A.P. (2018). “Characterization and applications of nanoparticles modified in-flight with silica or silica-organic coatings.” *Nanomaterials.*, 8, 530.

Pourali, P., Badiee, S. H., Manafi, S., Noorani, T., Rezaei, A., & Yahyaei, B. (2017). Biosynthesis of gold nanoparticles by two bacterial and fungal strains, *Bacillus cereus* and *Fusarium oxysporum*, and assessment and comparison of their nanotoxicity in vitro by direct and indirect assays. *Electronic Journal of Biotechnology*, 29, 86-93..

Prasad, G.K., Agarwal, G.S., Singh, B., Rai, G.P., and Vijayaraghavan, R. (2009). “Photocatalytic inactivation of *Bacillus anthracis* by titania nanomaterials.” *J Hazardous Materials*, 165, 506–510

Prema, P., Ranjani, S.S., Kumar, K.R., Veeramanikandan, V., Mathiyazhagan, N., Nguyen, V-H., Balaji, P. (2022). “Microbial synthesis of silver nanoparticles using *Lactobacillus plantarum* for antioxidant, antibacterial activities.” *Inorganic Chemistry Communications.*, 136, 109139

PubChem [Internet]. Bethesda (MD): National Library of Medicine (US), National Center for Biotechnology Information; 2004-. PubChem Compound Summary for CID 22842, C.I. Acid Yellow 17, disodium salt; [cited 2023 Aug. 1]

[https://pubchem.ncbi.nlm.nih.gov/compound/C.I.-Acid-Yellow-17\\_-disodium-salt](https://pubchem.ncbi.nlm.nih.gov/compound/C.I.-Acid-Yellow-17_-disodium-salt)

Pugazhenthiran, N., Anandan, Æ. S., Crawford, S., Ashokkumar, Æ. M., and Nanobiotechnology, S. Á. (2009). “Microbial synthesis of silver nanoparticles by *Bacillus* sp.” *J Nanopart Res*, 11, 1811–1815.

Raguram, T., and Rajni, K.S. (2022). “Synthesis and characterization of Cu-Doped TiO<sub>2</sub> nanoparticles for DSSC and photocatalytic applications.” *International Journal of Hydrogen Energy.*, 47 (7), 4674-4689

Rahimirad, A., Javadi, A., Mirzaei, H., Anarjan, N., and Jafarizadeh-Malmiri, H. (2019). “Biosynthetic potential assessment of four food pathogenic bacteria in hydrothermally silver nanoparticles fabrication.” *Green Processing and Synthesis.*, 8(1), 629-634.

Ramanathan, T., Fisher, F.T., Ruoff, R.S., and Brinson, L.C. (2005). “Amino-functionalized carbon nanotubes for binding to polymers and biological systems.” *Chem. Mater.*, 17 (6), 1290–1295.

Ramki, K., RajaPriya, A., Sakthivel, P., Murugadoss, G., Thangamuthu, R., Rajesh Kumar, M., (2020). “Rapid degradation of organic dyes under sunlight using tin-doped ZnS nanoparticles.” *Journal of Materials Science: Materials in Electronics.*, 31, 8750–8760.

Rápó, E., and Tonk, S. (2021). “Factors Affecting Synthetic Dye Adsorption; Desorption Studies: A Review of Results from the Last Five Years (2017-2021).” *Molecules.*, (17), [34500848](https://doi.org/10.3390/molecules17083450)

Ravele, M. P., Oyewo, O. A., Ramaila, S., Mavuru, L., and Onwudiwe, D. C. (2022). “Facile synthesis of copper oxide nanoparticles and their applications in the photocatalytic degradation of acyclovir.” *Results Eng.*, 14, 100479.

Ren, H. T., & Yang, Q. (2017). Fabrication of Ag<sub>2</sub>O/TiO<sub>2</sub> with enhanced photocatalytic performances for dye pollutants degradation by a pH-induced method. *Applied Surface Science*, 396, 530-538.

Rtimi, S., Pascu, M., Sanjines, R., Pulgarin, C., Ben-simon, M., and Houas, A. (2013). “ZrNO – Ag co-sputtered surfaces leading to E. coli inactivation under actinic light : Evidence for the oligodynamic effect.” *Applied Catal. B, Environ.*, 138-139, 113–121.

Sadollahkhani, A., Kazeminezhad, I., Lu, J., and Nur, O. (2014). “Synthesis, structural characterization and photocatalytic application of ZnO@ZnS core–shell nanoparticles.” *RSC Adv.*, 4, 36940–36950.

Sahu, K. K., Raj, B., Basu, S., and Mohapatra, M. (2021). “Calcination Strategy for Scalable Synthesis of Pithecellobium-Type Hierarchical Dual-Phase Nanostructured Cu<sub>x</sub>O to Columnar Self- Assembled CuO and Its Electrochemical Performances.” *ACS Omega.*, 6, 1108–1118

Sahu, A., Russ, B., Urban, J.J., Coates, N.E., Segalman, R. A., Forster, J. D., Liu, M., Yang, F., Persson, K. A., Dames, C. “Surface doping of nanostructures.” Pub. No.: US 2017/0069498A1, Pub year 2017.

Sanni, S. O. S., Modise S. J., and Ofomaja, E. L. V. A. E. (2020). “Enhanced degradation of dye mixtures : physicochemical and electrochemical properties of titania dispersed on clinoptilolite , synergistic influence.” *SN Appl. Sci.*, 2(10), 1668

Sangappa, M., and Thiagarajan, P. (2015). “Combating drug resistant pathogenic bacteria isolated from clinical infections, with silver oxide nanoparticles.” *Indian J. Pharm. Sci.*, 77(2), 151–155

Santos, K. S., Barbosa, A. M., da Costa, L. P., Pinheiro, M. S., Oliveira, M. B. P. P., and Padilha, F. F. (2016). “Silver Nanocomposite Biosynthesis: Antibacterial Activity against Multidrug-Resistant Strains of *Pseudomonas aeruginosa* and *Acinetobacter baumannii*.” *Molecules.*, 21, 1255

Saravanan, C., Rajesh, R., Kaviarasan, T., Muthukumar, K., Kavitate, D., & Shetty, P. H. (2017). Synthesis of silver nanoparticles using bacterial exopolysaccharide and its application for degradation of azo-dyes. *Biotechnology Reports*, 15, 33-40.

Sarkar, D., Ghosh, C. K., Mukherjee, S., & Chattopadhyay, K. K. (2013). Three dimensional Ag<sub>2</sub>O/TiO<sub>2</sub> type-II (p–n) nanoheterojunctions for superior photocatalytic activity. *ACS applied materials & interfaces*, 5(2), 331-337.

Saruchi., Thakur, P., and Kumar, V. (2019). “Kinetics and thermodynamic studies for removal of methylene blue dye by biosynthesize copper oxide nanoparticles and its antibacterial activity.” *J Environ Health Sci Eng.*, 17(1), 367–376

Shah, M., Fawcett, D., Sharma, S., Tripathy, S. K., and Poinern, G. E. J. (2015). “Green synthesis of metallic nanoparticles via biological entities.” *Materials*, 8, 7278–7308).

Sharma, M., Pathak, M., and Kapoor, P. (2018). “The sol-gel method: pathway to ultrapure and homogeneous mixed metal oxide nanoparticles.” *Asian J Chem* 30, 1405–1412.

Sheydaei, M., Fattahi, M., Ghalamchi, L., and Vatanpour, V. (2019). “Systematic comparison of sono-synthesized Ce-, La- and Ho-doped ZnO nanoparticles and using the optimum catalyst in a visible light assisted continuous sono-photocatalytic membrane reactor.” *Ultrasonics Sonochemistry.*, 56, 361-371

Shi, Y., Wang, H., Song, G., Zhang, Y., Tong, L., Sun, Y., and Ding, G. (2022). “Efficient degradation of organic dyes using peroxymonosulfate activated by magnetic graphene oxide.” *RSC Adv.*, 12, 21026–21040.

Shivaji, S., Madhu, S., and Singh, S. (2011). “Extracellular synthesise of antibacterial silver nanoparticles using psychrophilic bacteria.” *Process Biochem.*, 49, 830–837.

Shutthanandan, V., Nandasiri, M., Zheng, J., Engelhard, M.H., Xu, W., Thevuthasan, S., and Murugesan, V. (2019). “Applications of XPS in the characterization of battery materials.” *J. Electron Spectrosc. Relat. Phenom.*, 231, 2–10.

- Shymanovska, V. V., Khalyavka, T. A., Manuilov, E. V., Gavrilko, T. A., Aho, A., Naumov, V. V., and Shcherban, N. D. (2022). "Effect of surface doping of TiO<sub>2</sub> powders with Fe ions on the structural, optical and photocatalytic properties of anatase and rutile." *Journal of Physics and Chemistry of Solids.*, 160, 110308
- Siddiqi, K. S., Husen, A., and Rao, R. A. K. (2018). A review on biosynthesis of silver nanoparticles and their biocidal properties." *J. Nanobiotechnology* 16:14
- Silva, M. K., Marques, R. G., Machado, N. R. C. F., and Santos, O. A. A. (2002). "Evaluation of Nb<sub>2</sub>O<sub>5</sub> and Ag/Nb<sub>2</sub>O<sub>5</sub> in the photocatalytic degradation of dyes from textile industries." *Brazilian Journal of Chemical Engineering*, 19(04), 359–363.
- Silverstein, R.M., Webster, F.X., and Kiemle, D.J. (2005). "Spectrometric Identification of Organic Compounds" 7th edition.
- Singh, M., Jampaiah, D., Kandjani, A. E., Sabri, Y. M., Della Gaspera, E., Reineck, P., and Bansal, V. (2018). "Oxygen-deficient photostable Cu<sub>2</sub>O for enhanced visible light photocatalytic activity." *Nanoscale*, 10(13), 6039-6050.
- Sinha, T., and Ahmaruzzaman, M. (2015). "Green synthesis of copper nanoparticles for the efficient removal (degradation) of dye from aqueous phase." *Environmental Science and Pollution Research.*, 22. 20092-20100.
- Sinha, A., and Khare, S. K. (2011). "Mercury bioaccumulation and simultaneous nanoparticle synthesis by." *Bioresour. Technol.*, 102(5), 4281–4284.
- Sintubin, L., Verstraete, W., and Boon, N. A. (2012). "Biologically produced nanosilver: current state and future perspectives," *Biotechnology and Bioengineering*, 109 (10), 2422–2436
- Smigiel-Kaminska, D., Kumirska, J., Wąs-Gubala, J., and Stepnowski, P. (2020). "The Identification of Cotton Fibers Dyed with Reactive Dyes for Forensic Purposes." *Molecules*, 25(22).

Sobhani-Nasab, A., and Behpour, M. (2016). "Synthesis and characterization of AgO nanostructures by precipitation method and its photocatalyst application." *J. Mater. Sci. Mater. Electron.*, 27(2), 1191–1196

Sriram, M. I., Kalishwaralal, K., and Gurunathan, S. (2012). "Biosynthesis of Silver and Gold Nanoparticles Using *Bacillus licheniformis*." 906, 33–43.

Sriramulu, M., and Sumathi, S. (2018). "Biosynthesis of palladium nanoparticles using *Saccharomyces cerevisiae* extract and its photocatalytic degradation behaviour." *Adv. Nat. Sci: Nanosci. Nanotechnol.* 9 025018

Staden, J.V., Kannan, R.R.R., and Stirk, W.A. (2013). "Synthesis of silver nanoparticles using the seaweed *Codium capitatum* P.C. Silva (Chlorophyceae)." *S. Afr. J. Bot.* 86, 1–4.

Su, C., Liu, L., Zhang, M., and Shao, C. (2012). "Fabrication of Ag /TiO<sub>2</sub> nanoheterostructures with visible light photocatalytic function via a solvothermal approach." *CrystEngComm*, 3989–3999.

Sun, C., He, P., Pan, G., Miao, Y., Zhang, T., and Zhang, L. (2018). "Study on preparation and visible-light activity of Ag – TiO<sub>2</sub> supported by artificial zeolite." *Res. Chem. Intermed.* 44 (4), 2607-2620.

Suresh, A. K., Pelletier, D. A., Wang, W., Moon, J. W., Gu, B., Mortensen, N. P., Allison, D.P., Joy, D.C., Phelps, T.J., and Doktycz, M. J. (2010). "Silver nanocrystallites: biofabrication using *Shewanella oneidensis*, and an evaluation of their comparative toxicity on gram-negative and gram-positive bacteria." *Environmental science & technology*, 44(13), 5210-5215.

Suriyaraj, S. P., and Selvakumar, R. (2014). "Room temperature biosynthesis of crystalline TiO<sub>2</sub> nanoparticles using *Bacillus licheniformis* and studies on the effect of calcination on phase structure and optical properties ." *RSC Adv.*, 2014, 4, 39619–39624.

Syed, A., and Ahmad, A. (2013). "Extracellular biosynthesis of CdTe quantum dots by the fungus *Fusarium oxysporum* and their anti-bacterial activity." *Spectrochim. ACTA PART A Mol. Biomol. Spectrosc.*, 106, 41–47.

Talebian, S., Shahnava, B., and Nejabat, M. (2023). "Bacterial-mediated synthesis and characterization of copper oxide nanoparticles with antibacterial, antioxidant, and anticancer potentials." *Front. Bioeng. Biotechnol.* 11:1140010.

Tarafdar, J. C., Tarafdar, A., Wang, W., and Biswas, P. (2013). "Green synthesis of TiO<sub>2</sub> nanoparticle using *Aspergillus tubingensis*." *Adv. Sci. Eng. Med.*, 5

Taran, M., Rad, M., and Alavi, M. (2018). "Biosynthesis of TiO<sub>2</sub> and ZnO nanoparticles by *Halomonas elongata* IBRC-M 10214 in different conditions of medium." *Tabriz Univ. Med. Sci.*, 8(2), 81–89.

Teli, M. D., and Nadathur, G. T. (2018). "Adsorptive removal of acid yellow 17 (an anionic dye) from water by novel ionene chloride modified electrospun silica nanofibres." *J. Environ. Chem. Eng.*, 6(6), 7257–7272.

Thu, T.N.T., Thi, N.N., Quang, V.T., Hong, K.N., Minh, T.N., and Hoai, N.L.T. (2016). "Synthesis, characterisation, and effect of pH on degradation of dyes of copper-doped TiO<sub>2</sub>." *J. Exp. Nanosci.*, 11 (3) (2016) 226–238.

Trenczek-zajac, A., Synowiec, M., Zakrzewska, K., Zazakowny, K., Kowalski, K., Dziedzic, A., and Radecka, M. (2022). "Scavenger-Supported Photocatalytic Evidence of an Extended Type I Electronic Structure of the TiO<sub>2</sub>@Fe<sub>2</sub>O<sub>3</sub> Interface." *ACS Appl. Mater. Interfaces.*, 14, 38255–38269

Truong, T. T., Pham, T. T., Truong, T. T. T., and Duc, T. (2022). "Synthesis, characterization of novel ZnO/CuO nanoparticles, and the applications in photocatalytic performance for rhodamine B dye degradation." *Environ. Sci. Pollut. Res.*, 22576–22588.

Tseng, R. J., Tsai, C., Ma, L., Ouyang, J., Ozkan, C.S., and Yang, Y. (2006). "Digital memory device based on tobacco mosaic virus conjugated with nanoparticles." *Nat. Nanotechnol.*, 1 (1) 72–77.

Tuo, Y., Liu, G., Dong, B., Zhou, J., Wang, A., Wang, J., and Jin, R. (2015). "Microbial synthesis of Pd/Fe<sub>3</sub>O<sub>4</sub>, Au/Fe<sub>3</sub>O<sub>4</sub> and PdAu/Fe<sub>3</sub>O<sub>4</sub> nano - composites for catalytic reduction of nitroaromatic compounds." *Nat. Publ. Gr.*, 1–12.

Vandencastele, N., and Reniers, F. (2010). "Plasma-modified polymer surfaces: characterization using XPS." *J. Electron Spectrosc. Relat. Phenom.*, 178–179, 394–408.

Vijayan, P., Mahendiran, C., Suresh, C., and Shanthi, K. (2009). "Photocatalytic activity of iron doped nanocrystalline titania for the oxidative degradation of 2, 4, 6-trichlorophenol." *Catalysis Today*, 141, 220–224.

Villanueva, M.E., Copello, G.J., and Dall'Orto, V.C. (2018). "Solar light efficient photocatalytic activity degradation of emergent contaminants by coated TiO<sub>2</sub> nanoparticles." *New J. Chem.*, 42, 15405–15412

Vishnu Kirthi, A., Abdul Rahuman, A., Rajakumar, G., Marimuthu, S., Santhoshkumar, T., Jayaseelan, C., Elango, G., Abdur Zahir, A., Kamaraj, C., and Bagavan, A. (2011). "Biosynthesis of titanium dioxide nanoparticles using bacterium *Bacillus subtilis*." *Mater. Lett.*, 65(17-18), 2745–2747.

Vithiya, K., Kumar, R., and Sen, S. (2014). "Antimicrobial activity of biosynthesized silver oxide nanoparticles." *J. Pure Appl. Microbiol.*, 8(4), 3263–3268

Wagstaffe, M., Hussain, H., Acres, M. J., Jones, R., Syres, K. L., and Thomas, A. G. (2017). "Structure and Reactivity of a Model Oxide Supported Silver Nanocluster Catalyst Studied by Near Ambient Pressure X - ray Photoelectron Spectroscopy." *The Journal of Physical Chemistry, C*, 121, 21383–21389.

Wang, G., Ma, X., Huang, B., Cheng, H., Wang, Z., Zhan, J., Qin, X., Zhang, X., and Dai, Y. (2012). “Controlled synthesis of Ag<sub>2</sub>O microcrystals with facet-dependent photocatalytic activities.” *J. Mater. Chem.*, 22(39), 21189–21194.

Wang, C., Wang, H., Chen, Q., Ren, B., Duan, R., and Guan, R. (2019). “Synchronous regulation of morphology and crystal phase of TiO<sub>2</sub> via a facile green hydrothermal approach and their photocatalytic activity.” *Mater. Res. Bull.*, 109, 90–97.

Wang, T., Xiao, H., Gao, Y., Xu, J., Zhang, Z., Bian, H., and Sun, T. (2020). “Ag<sub>2</sub>O/TiO<sub>2</sub> hollow microsphere heterostructures with exposed high-energy {001} crystal facets and high photocatalytic activities.” *J. Mater. Sci. Mater. Electron.*, 31(14), 11496–11507

Wang, W., Zhang, J., Chen, F., He, D., and Anpo, M. (2008). “Preparation and photocatalytic properties of Fe<sup>3+</sup>-doped Ag@TiO<sub>2</sub> core – shell nanoparticles.” *Journal of Colloid and Interface Science* 323, 182–186.

Wei, J., Lei, Y., Jia, H., Cheng, J., Hou, H., and Zheng, Z. (2014). “Controlled in situ fabrication of Ag<sub>2</sub>O/AgO thin films by a dry chemical route at room temperature for hybrid solar cells.” *Dalt. Trans.*, 43(29), 11333–11338.

Wei, N., Cui, H., Song, Q., Zhang, L., Song, X., Wang, K., Zhang, Y., Li, J., Wen, J., and Tian, J. (2016). “Ag<sub>2</sub>O nanoparticle/TiO<sub>2</sub> nanobelt heterostructures with remarkable photo-response and photocatalytic properties under UV, visible and near-infrared irradiation.” *Appl. Catal. B Environ.*, 198, 83–90.

Wei, T., Zhu, Y., An, X., Liu, L., Cao, X., Liu, H., and Qu, J. (2019). “Defect Modulation of Z - Scheme TiO<sub>2</sub>/Cu<sub>2</sub>O Photocatalysts for Durable Water Splitting.” *ACS Catal.*, 9, 8346–8354

Wei, X., Luo, M., Li, W., Yang, L., Liang, X., and Xu, L. (2012). “Bioresource Technology Synthesis of silver nanoparticles by solar irradiation of cell-free *Bacillus amyloliquefaciens* extracts and AgNO<sub>3</sub>.” *Bioresour. Technol.*, 103(1), 273–278.

Wright, M. H., Farooqui, S. M., White, A. R., and Greene, C. (2016). "Production of Manganese Oxide Nanoparticles by *Shewanella* Species." *Appl Environ Microbiol.*, 82(17), 5402–5409.

Wu, T., Lin, T., Zhao, J., Hidaka, H., and Serpone, N. (1999). "TiO<sub>2</sub>-assisted photodegradation of dyes. 9. Photooxidation of a squarylium cyanine dye in aqueous dispersions under visible light irradiation." *Environmental science & technology*, 33(9), 1379-1387.

Xing, C., Zhang, Y., Liu, Y., Wang, X., Li, J., Mart, P. R., Spadaro, M. C., Guardia, P., Arbiol, J., Llorca, J., and Cabot, A. (2021). "Photodehydrogenation of Ethanol over Cu<sub>2</sub>O/TiO<sub>2</sub> Heterostructures." *Nanomaterials.*, 11, 1399.

Xiong, L., Li, J., Yang, B., and Yu, Y. (2012). "Ti 3 + in the Surface of Titanium Dioxide: Generation , Properties and Photocatalytic Application." *Journal of Nanomaterials*, 831524.

Xu, M., Han, L., and Dong, S. (2013). "Facile fabrication of highly efficient g-C<sub>3</sub>N<sub>4</sub>/Ag<sub>2</sub>O heterostructured photocatalysts with enhanced visible-light photocatalytic activity." *ACS Appl. Mater. Interfaces.*, 5, 12533–12540

Xu, Y., Li, C., Zhu, X., Huang, W. E., and Zhang, D. (2014). "Application of magnetic nanoparticles in drinking water purification." *Environ. Eng. Manag. J.*, 13(8), 2023–2029.

Yang, C., Dong, W., Cui, G., Zhao, Y., Shi, X., and Xia, X. (2017). "Highly-efficient photocatalytic degradation of methylene blue by PoPD-modified TiO<sub>2</sub> nanocomposites due to effect of TiO<sub>2</sub> with PoPD." *Scientific Reports*, 7, 1–12.

Yang, X. H., Fu, H. T., Wang, X. C., Yang, J. L., Jiang, X. C., and Yu, A. B. (2014). "Synthesis of silver-titanium dioxide nanocomposites for antimicrobial applications." *J. Nanoparticle Res.*, 16(8).

Yang, Y., Waterhouse, G. I. N., Chen, Y., Sun-Waterhouse, D., and Li, D. (2022). "Microbial-enabled green biosynthesis of nanomaterials: Current status and future prospects." *Biotechnol. Adv.*, 55, 107914.

Yazhini, K. B., Savitha, K. U., and Prabu, H. G. (2015). "Photocatalytic Degradation of Dyes using Rutile TiO<sub>2</sub>-Pani Composite Prepared by One Pot Method." *Environmental Pollution and Control Research*, 1, (1), 1-6.

Younas, H., Qazi, I. a, Hashmi, I., Awan, M. A., Mahmood, A., and Qayyum, H. A. (2014). "Visible light photocatalytic water disinfection and its kinetics using Ag-doped titania nanoparticles." *Environ. Sci. Pollut. Res. Int.*, 21(1), 740–52.

Yu, J., Jimmy, C. Y., Leung, M. K.-P., Ho, W., Cheng, B., Zhao, X., and Zhao, J. (2003). "Effects of acidic and basic hydrolysis catalysts on the photocatalytic activity and microstructures of bimodal mesoporous titania." *J. Catal.*, 217, 69– 78.

Yu, J., Jimmy, C. Y., Yu, J., Ho, W., and Zhang, L. (2001). "Preparation of highly photocatalytic active nano-sized TiO<sub>2</sub> particles via ultrasonic irradiation." *Chem. Commun.*, 1942– 1943

Yu, J., Jimmy, C. Y., Ho, W., and Jiang, Z. (2002). "Effects of calcination temperature on the photocatalytic activity and photo-induced super-hydrophilicity of mesoporous TiO<sub>2</sub> thin films." *New J. Chem.*, 26, 607– 613.

Yuan, Q., Bomma, M., and Xiao, Z. (2019). "Enhanced silver nanoparticle synthesis by escherichia coli transformed with candida albicans metallothionein gene." *Materials (Basel)*, 12(24).

Yuan, W. T., Meng, J., Zhu, B. E., Gao, Y., Zhang, Z., Sun, C. H., and Wang, Y. (2018). "Unveiling the atomic structures of the minority surfaces of TiO<sub>2</sub> nanocrystals." *Chem. Mater.*, 30, 288– 295.

Yuan, W. T., Wang, Y., Li, H. B., Wu, H. L., Zhang, Z., Selloni, A., and Sun, C. H. (2016). "Real-time observation of reconstruction dynamics on TiO<sub>2</sub>(001) surface

under oxygen via an environmental transmission electron microscope.” *Nano Lett.*, 16, 132– 137.

Yusof, H. M., Aini, N., Rahman, A., and Mohamad, R. (2020). “Biosynthesis of zinc oxide nanoparticles by cell - biomass and supernatant of *Lactobacillus plantarum* TA4 and its antibacterial and biocompatibility properties.” *Sci. Rep.*, 10, 19996.

Zhang, F., Yuan, C. Lu, L., Zhang, L., Che, Q., and Zhang, X. (2012). "Facile growth of mesoporous  $\text{Co}_3\text{O}_4$  nanowire arrays on Ni foam for high performance electrochemical capacitors." *Journal of Power Sources*, 203, 250-256.

Zhang, L., Xia, D., and Shen, Q. (2006). “Synthesis and characterization of  $\text{Ag@TiO}_2$  core-shell nanoparticles and  $\text{TiO}_2$  nanobubbles.” *Journal of Nanoparticle Research*, 23–28.

Zhao, W., and Liu, C. (2020). “Mesoporous  $\text{Cu-Cu}_2\text{O@TiO}_2$  heterojunction photocatalysts derived from metal–organic frameworks.” *RSC Adv.*, 10, 14550

Zhao, Y., Tao, C., Xiao, G., and Su, H. (2017). “Controlled synthesis and wastewater treatment of  $\text{Ag}_2\text{O/TiO}_2$  modified chitosan-based photocatalytic film.” *RSC Adv.*, 7(18), 11211–11221

Zhou, W., Liu, H., Wang, J., Liu, D., Du, G., & Cui, J. (2010).  $\text{Ag}_2\text{O/TiO}_2$  nanobelts heterostructure with enhanced ultraviolet and visible photocatalytic activity. *ACS applied materials & interfaces*, 2(8), 2385-2392.

## RESEARCH PUBLICATIONS

### Journal articles

- Kulal, D., and Shetty, K.V. (2021). “Visible light mediated photocatalytic dye degradation using Ag<sub>2</sub>O/AgO-TiO<sub>2</sub> nanocomposite synthesized by extracellular bacterial mediated synthesis - An eco-friendly approach for pollution abatement.” *Journal of Environmental Chemical Engineering*, 9, 105389.  
<https://doi.org/10.1016/j.jece.2021.105389>
- Deekshitha., and Shetty, K.V. (2021). “Solar light active biogenic titanium dioxide embedded silver oxide (AgO/Ag<sub>2</sub>O@TiO<sub>2</sub>) nanocomposite structures for dye degradation by photocatalysis.” *Materials Science in Semiconductor Processing*, 132, 105923.  
<https://doi.org/10.1016/j.mssp.2021.105923>

### Conference Proceedings

- Deekshitha K and Vidya Shetty K, “Greener and environment friendly process of synthesis of Ag-TiO<sub>2</sub> nanocomposite for Reactive Blue 220 removal from dye contaminated water.” National Symposium on *Environmental Pollution Prevention and Control : Future perspective* (EPPC:FP.:2019), August 23-25, 2019, NITK Surathkal.

### Book Chapters

- Kulal, D., and Shetty, K.V. (2022). “Insights into Pathways of Biodegradation of Endocrine Disrupting Chemicals by Microbes.” *Omics for Environmental Engineering and Microbiology Systems*, ISBN 9781003247883.

### Patent Published

- Bacterial Based Synthesis of Core Shell AgO@TiO<sub>2</sub> Nanoparticles for Photocatalytic Water Disinfection and Dye Degradation, Application Number: 201741044068 dtd. 08/12/2017, Publication date 14/06/2019.

## BIO-DATA

**Deekshitha**

**Email ID :** [deekshithakulal27@gmail.com](mailto:deekshithakulal27@gmail.com)

**Contact No :** +91 9845258667

### Personal Details

Name	Deekshitha
Father's name	Ganesh Ram B
Date of birth	07/04/1991
Gender	Female
Marital status	Single
Nationality	Indian
Address	Mangala Engineering Works, Near Govt High School, Bockapatna, Mangalore 575003 Karnataka, India

### Educational Qualification:

- **Phd** (Pursuing), in the Department of Chemical Engineering, National Institute of Technology Karnataka (NITK) Surathkal, Mangalore.
- **Master of Science** (Biotechnology) from the Department of Biotechnology, St Aloysius College, Mangalore with 68.8% in 2014.
- **Bachelor of Science** (Biotechnology) Department of Biotechnology, St Aloysius College, Mangalore with 78.9 % in 2012.
- **Pre-university Education** from St. Agnes PU College, Mangalore with 77.3 % in 2009.
- **SSLC** from Sri Narayana Guru English Medium High School, Mangalore with 83.3% in 2007.

## Research Publications

### Journal articles

- Kulal, D., and Shetty, K.V. (2021). “Visible light mediated photocatalytic dye degradation using Ag<sub>2</sub>O/AgO-TiO<sub>2</sub> nanocomposite synthesized by extracellular bacterial mediated synthesis - An eco-friendly approach for pollution abatement.” *Journal of Environmental Chemical Engineering*, 9, 105389.  
<https://doi.org/10.1016/j.jece.2021.105389>
- Deekshitha., and Shetty, K.V. (2021). “Solar light active biogenic titanium dioxide embedded silver oxide (AgO/Ag<sub>2</sub>O@TiO<sub>2</sub>) nanocomposite structures for dye degradation by photocatalysis.” *Materials Science in Semiconductor Processing*, 132, 105923.  
<https://doi.org/10.1016/j.mssp.2021.105923>

### Conference Proceedings

- Deekshitha K and Vidya Shetty K, “Greener and environment friendly process of synthesis of Ag-TiO<sub>2</sub> nanocomposite for Reactive Blue 220 removal from dye contaminated water.” National Symposium on *Environmental Pollution Prevention and Control : Future perspective* (EPPC:FP.:2019), August 23-25, 2019, NITK Surathkal.

### Book Chapters

- Kulal, D., and Shetty, K.V. (2022). “Insights into Pathways of Biodegradation of Endocrine Disrupting Chemicals by Microbes.” *Omic for Environmental Engineering and Microbiology Systems*, ISBN 9781003247883.

### Patent Published

- Bacterial Based Synthesis of Core Shell AgO@TiO<sub>2</sub> Nanoparticles for Photocatalytic Water Disinfection and Dye Degradation, Application Number: 201741044068 dtd. 08/12/2017, Publication date 14/06/2019.

### **Technical Skills**

- Having hands on experience in synthesis of nanomaterials using microbial method.
- Proficient in tissue culture, Gel electrophoresis, PCR
- Proficient in handling equipments like ICP-OES, UV-Vis spectrophotometer, Centrifuge, Sonicator, muffle furnace etc.

### **Work Experience**

- Worked as a scientific analyst in Molecular Connections, Bangalore for the period of May 2014 – May 2015.

### **Achievements**

- Qualified GATE with a score of 879 in 2014.
- Has been a student resource person in one day “Workshop on Biotechnology Techniques for High School Teachers” sponsored by Pilikula Regional Science Center Society, 2012.
- Secured 1<sup>st</sup> place in “Biomolecules & Biocatalysts in Bioprocesses” poster presentation, March 2012.

**Languages Known** – English, Kannada, Hindi and Tulu

### **Declaration**

I hereby declare that the above mentioned details are true to the best of my knowledge.

Place : Surathkal, Karnataka

Deekshitha

Date :